

# Ordered Nanomaterials for Electron Field Emission

Clare Melissa Collins



UNIVERSITY OF  
CAMBRIDGE

Hughes Hall

August 2017

This dissertation is submitted for the Degree of Doctor of Philosophy to the Department of Engineering at the University of Cambridge.



*“Science and everyday life cannot and should not be separated”*

Rosalind Franklin - 1940



# Declaration

This thesis is submitted in fulfilment of the requirements for the Degree of Doctor of Philosophy as stipulated by the Department of Engineering, University of Cambridge.

The content of this report has been, in its entirety, written by the author on whose original work is herein documented, except where references are made and due credit is given in the acknowledgements. This dissertation is the result of my own work and includes nothing which is the outcome of work done in collaboration except as declared in the Preface and specified in the text.

It is not substantially the same as any that I have submitted, or, is being concurrently submitted for a degree or diploma or other qualification at the University of Cambridge or any other University or similar institution except as declared in the Preface and specified in the text. I further state that no substantial part of my dissertation has already been submitted, or, is being concurrently submitted for any such degree, diploma or other qualification at the University of Cambridge or any other University or similar institution except as declared in the Preface and specified in the text.

In accordance with Cambridge University regulations, this report contains less than 65,000 words and 150 figures.

*Clare M Collins*

(August 2017)



# Acknowledgements

Without the academic guidance, support and general provision of care from a wide ranging number of individuals, this thesis would not have been nearly as fulfilling or as enjoyable as I have found the experience to be.

Firstly, and most importantly, I cannot express my gratitude enough for my (at least for the majority of the time) supervisor, Dr. Matt Cole; I could not have asked for better. Throughout my time in Cambridge, Matt has provided excellent and insightful academic knowledge, as well as encouragement and personal guidance. For this I believe myself to be truly lucky. Our weekly meetings have ensured the swift development of my research and have truly shaped it into what it has become. He has pushed me to become a better scientist and artist in equal measures, for which my gratitude is unbounded. Due appreciation must also be made to Prof. Bill Milne, my original supervisor, with whom I had somewhat more sporadic, though no less insightful or influential, contact with owing to his being in high demand across the globe. As part of a very small research group I have been lucky to receive near sole attention at times from my superiors. I must also note the other members of the group that have come and gone throughout my time, all of whom have been both helpful and kind. None more so than Mr. Richard Parmee, with whom I have collaborated most closely with academically and who has never failed to provide the most exciting and exotic anecdotes. Prof. John Robertson must also be duly thanked for agreeing to be my final, short-lived, supervisor.

Secondly, I must thank all those on the Ultra Precision DTC from the Course Director Prof. Bill O'Neill and the wonderful Sophie Fuller who makes sure everything runs smoothly, to my MRes cohort, in particular Yoanna Shams, Chris Wright and Sam Brown who have become great friends as well as colleagues. The incredible people that have passed through the DTC, and the amazing experiences I have had whilst being part of it myself, would not have existed without the generous support given by EPSRC, without which I could not be here.

I am most grateful to the exceptional technicians in CAPE that work tirelessly to assure the smooth running of the clean rooms and the workshop. I have been greeted at every encounter by a smile; they have each brightened my wanderings around the building, helped me whenever I have needed without hesitation and indeed the Christmas meals would not have been the same without them. In particular I must thank Neil Lawrence for his patience and kindness.

To my family, my mother Alison, who has offered invaluable wisdoms and to whom I owe everything from my surely inherited talents as a scientist to her infallible dedication to the smooth running of my existence. My father, David, for his unwavering support and belief in me, without which I surely would not be where or who I am today. Finally, to my sister, Katy, who understands me like nobody else; thank you for everything.

My experience at the University of Cambridge would not have been the same without the staff and students at Hughes Hall. Throughout my time at Cambridge Hughes has provided not just

a source for all my non-academic and sporting outlets, of which there have been many, but has helped shape and expand my horizons through the incredible diversity of students it attracts.

# Contents

<b>List of Figures and Tables</b>	IV-V
<b>Abstract</b>	VI
<b>List of Symbols and Abbreviations</b>	VII-X
<b>Publications and Presentations</b>	XI
<b>Chapter 1: Introduction</b>	<b>1</b>
1.1 Motivation.....	3
1.2 Objectives.....	6
1.3 Thesis Structure.....	6
References.....	7
<b>Chapter 2: Field Emission from Carbon Nanotubes</b>	<b>9</b>
2.1 Introduction.....	11
2.2 Electron Emission.....	11
2.2.1 The History of Field Emission.....	13
2.3 Fowler Nordheim Theory.....	16
2.3.1 Field Emission from Nanomaterials.....	20
2.4 Carbon Allotropes.....	22
2.4.2 Carbon Nanotubes.....	23
2.5 Carbon Nanotube and Emitter Fabrication.....	25
2.6 Carbon Nanotube Field Emission Applications.....	27
2.6.1 Field Emission Displays.....	27
2.6.2 X-Ray Sources.....	28
2.6.3 Other Applications.....	30
2.7 Patterned Carbon Nanotube Field Emitter Devices.....	30
2.8 Summary.....	37
References.....	37
<b>Chapter 3: High Performance Field Emitter Characteristics</b>	<b>43</b>
3.1 Introduction.....	45
3.2 Classification by Material.....	45
3.3 Field Emission Performance Metrics.....	46
3.3.1 Data Extraction.....	48
3.4 Material Work Function and the Effect Performance.....	48

3.4.1	Limitations of Acquired Data .....	52
3.4.2	Conclusions on the Influence of Work Function .....	53
3.5	The Importance of Morphology.....	54
3.5.1	Shortcomings of Field Enhancement Factor.....	54
3.5.2	Surface Roughness Metric .....	57
3.6	Summary .....	59
	References.....	60
 <b>Chapter 4: Emitter Morphology for Enhanced Maximum Current</b>		<b>67</b>
4.1	Introduction.....	69
4.2	Emitter Fabrication .....	69
4.2.1	Techniques and Equipment .....	69
4.2.1.1	Electron Beam Photolithography: <i>NanoBeam EBL</i> .....	70
4.2.1.2	Direct Current Magnetron Sputtering.....	72
4.2.1.3	CNT Growth: <i>Aixtron “Black Magic”</i> .....	73
4.2.2	Fabrication Methodology .....	74
4.2.3	Emitter Design.....	75
4.3	Scanning Anode Field Emission Microscopy .....	80
4.3.1	Measuring Field Emission: Methodology .....	82
4.3.2	Field Emission Mapping .....	83
4.3.3	Tip Height from the Emitting Surface.....	84
4.3.4	Instabilities, Difficulties and Inaccuracies of Meaningful Data Collection.....	86
4.3.5	Limitations and Conclusions .....	87
4.4	Parallel Plate Field Emission.....	89
4.4.1	Experimental Procedure .....	90
4.4.2	Results.....	91
4.4.3	Conclusions .....	98
4.5	Future Work .....	99
4.6	Summary .....	100
	References.....	100
 <b>Chapter 5: Hysteretic Behaviour of Carbon Nanotube Field Emitters</b>		<b>103</b>
5.1	Introduction.....	105
5.2	Background.....	105
5.2.2	Adsorption and Desorption.....	108
5.3	Data Collection and Processing.....	110
5.4	Parallel Plate Emission Performance .....	111

5.4.1 Repeatability .....	111
5.4.2 Raman Spectroscopy .....	112
5.4.3 Optical Excitation .....	114
5.4.4 Vacuum Pressure Dependence .....	117
5.5 In-Situ Residual Gas Analysis.....	119
5.5.1 Results and Discussions .....	121
5.5.2 Limitations and Future Work .....	125
5.6 Stability .....	126
5.6.1 Future Work .....	132
5.7 Hysteresis Onset .....	133
5.8 Effect of Dwell Time on Hysteresis .....	134
5.8.1 Limitations and Future Work .....	137
5.9 A Model Describing the Emission Process and Resultant Hysteretic Behaviour.....	138
5.9.1 Explaining the Causes of Hysteresis: Trapped, Surface and Intermediate States from Adsorbed Molecules .....	140
5.9.2 Evidence from Results .....	144
5.10 Summary .....	146
References.....	147
<b>Chapter 6: Conclusion and Summary</b>	<b>151</b>
6.1 Conclusions .....	153
6.2 Summary .....	156

# List of Figures and Tables

Figure 2.1   Emission Mechanisms Schematic.....	11
Figure 2.2   Developments in Field Emission; Reducing the curvature of radius of emitters.....	14
Figure 2.3   Field Emission Schematic Diagrams.....	15
Figure 2.4   The Nanocarbons.....	23
Figure 2.5   Emitter Patterning.....	31
Figure 3.1   Performance metric definition.....	47
Figure 3.2   Material Performance by Work Function.....	49
Figure 3.3   Distribution of Interelectrode Distance, $d$ .....	52
Figure 3.4   Comparing Literature Values of Local Field Enhancement Factor, $\beta$ , Work Function, $\phi$ , and Aspect Ratio, AR.....	57
Figure 3.5   Morphology Metric Definition.....	59
Table 3.1   Average performance of FE materials according to dimensionality.....	50
Table 3.2   Definitions of $\beta$ found in literature.....	55
Figure 4.1   Beam Exposure and Dosage.....	71
Figure 4.2   Emitter Fabrication.....	75
Figure 4.3   Pillar Array Scanning Electron Micrograph.....	76
Figure 4.4   Emitter Pattern Design.....	77
Figure 4.5   Emitter CAD Design.....	78
Figure 4.6   Geometrical Inverse Pillars.....	78
Figure 4.7   Geometrical Pillars.....	79
Figure 4.8   CNT Edge Growth.....	79
Figure 4.9   SAFEM and Parallel Plate Schematic.....	81
Figure 4.10   SAFEM Mapping.....	83
Figure 4.11   SAFEM Data Spread.....	84
Figure 4.12   SAFEM Data Plots.....	85
Figure 4.13   Field Emission Map.....	87
Figure 4.14   Parallel Plate Emitters.....	90
Figure 4.15   Results from Parallel Plate Experiments.....	93
Figure 4.16   Average I-V Curves for the Different Geometries.....	95
Figure 4.17   Fowler Nordheim Plots.....	96
Figure 4.18   $\beta$ values.....	97
Table 4.1   Surface area coverage of CNTs across fabricated samples as measured from the pattern file.....	92
Table 4.2   $\beta$ values for each of the geometries.....	97
Figure 5.1   Hysteretic Behaviour of Field Emission.....	106
Figure 5.2   Repeatability Results.....	112
Figure 5.3   Raman Spectroscopy.....	113
Figure 5.4   Optical Excitation Map.....	115

Figure 5.5   Peak at $\lambda = 650$ nm.....	116
Figure 5.6   Optical Turn-On Values .....	117
Figure 5.7   Dependence of Maximum Current on Vacuum Pressure .....	118
Figure 5.8   Gas Species in Vacuum.....	122
Figure 5.9   RGA Results .....	123
Figure 5.10   Stability Data .....	127
Figure 5.11   Evolution of Hysteresis over Exposure to 50 Voltage Cycles .....	129
Figure 5.12   I-V Curves of Grouped Loops .....	130
Figure 5.13   I-V Curve Evolution over 50 Cycles .....	132
Figure 5.14   Results of Varying the Maximum Applied Current .....	134
Figure 5.15   Fowler Nordheim Plots for Sweep Speed Results. ....	135
Figure 5.16   Sweep Speed: Unfolding the I-V Curve.....	137
Figure 5.17   Field Emission Model .....	139
Figure 5.18   Sources of Additional Electrons .....	141
Table 5.1   $\beta$ calculated for the different dwell times .....	136

# Ordered Nanomaterials for Electron Field Emission

Clare M Collins

In the quest for reliable, repeatable and stable field electron emission that has commercial potential, whilst many attempts have been made, none yet has been truly distinguishable as being successful. Whilst I do not claim within this thesis to have uncovered the secret to success, fundamental issues have been addressed that concern the future directions towards achieving its full potential.

An exhaustive comparison is made across the diverse range of materials that have, over the past 40-50 years, been postulated and indeed tested as field emitters. This has not previously been attempted. The materials are assessed according to the important metrics of turn on voltage,  $E_{on}$ , and maximum current density,  $J_{max}$ , where low  $E_{on}$  and high  $J_{max}$  are seen as desirable. The nano-carbons, carbon nanotubes (CNTs), in particular, perform well in both these metrics. No dependency was seen between the material work function and its performance as an emitter, which might have been suggested by the Fowler Nordheim equations.

To address the issues underlying the definition of the local enhancement factor,  $\beta$ , a number of variations of surface geometry using CNTs were fabricated. The field emission of these emitters was measured using two different approaches. The first is a Scanning Electrode Field Emission Microscope, SAFEM, which maps the emission at individual locations across the surface of the emitter, and the parallel plate that is more commonly encountered in field emission measurements.

Finally, an observed hysteretic behaviour in CNT field emission was explored. The field emitters were subjected to a number of tests. These included; in-situ residual gas analysis of the gas species in the emitter environment, a stability study in which the emitters were exposed to a continuing voltage loop for 50 cycles, differing applied voltage times to analyse the effects on the emitted current, and varying maximums of applied field in a search for hysteresis onset information. These studies revealed the candidate in causing the hysteresis is likely to be water vapour that adsorbs on the CNT surface. A six step model of the emission process was made that details how and when the hysteresis is caused.

## List of Symbols and Abbreviations

Throughout this thesis S.I. units have been used, except in the case of gas flow rates, which are quoted in standard cubic centimeters per minute (1 sccm =  $1.67 \times 10^{-8}$  m<sup>3</sup>/s) and pressure (mbar, 1 mbar = 100 Pa).

In the first instance, all abbreviations are explicitly written in the text and are denoted in parenthesis immediately following the first usage.

Unless stated otherwise the notation and symbols have the following meanings;

$\alpha$	Morphology Metric	$I_{up}$	Up Sweep Current (A)
$\beta$	Field Enhancement Factor	$J$	Current Density (mA/cm <sup>2</sup> )
$\beta_{lit}$	Literature Values of $\beta$	$J_{max}$	Maximum Current Density (mA/cm <sup>2</sup> )
$d$	Inter-Electrode Vacuum Gap (m)	$\lambda$	Wavelength (nm)
$E$	Electric Field (V/ $\mu$ m)	$m$	Gradient (dx/dy)
$E_0$	Conduction Band Energy (eV)	$m_e$	Electron Mass (kg)
$E_f$	Fermi Energy (eV)	$P$	Pressure (mbar)
$E_{on}$	Turn On Electric Field (V/ $\mu$ m)	$R$	Pillar Pitch ( $\mu$ m)
$E_{thr}$	Threshold Electric Field (V/ $\mu$ m)	$r$	Tip Radius (nm)
$e$	Electron Charge (C)	$S$	Emission Area (cm <sup>2</sup> )
$\phi$	Work Function (eV)	$T$	Temperature ( $^{\circ}$ C/K)
$G$	Unit Cell Geometry	$t$	Time (s)
$H$	Height (m)	$\nu$	Frequency (Hz)
$h$	Planck's Constant	$V$	Voltage (V)
$I$	Current (A)	$V_{on}$	Turn On Voltage (V)
$I_{down}$	Down Sweep Current (A)	$w$	Wall Width ( $\mu$ m)
$I_{max}$	Maximum Current (A)	$x$	Geometry Spacing ( $\mu$ m)
		$xyz$	Directions
		$z$	Tip Height ( $\mu$ m)

Abbreviations used throughout this thesis have the following meanings;

1D	One Dimensional	2D	Two Dimensional
----	-----------------	----	-----------------

3D	Three Dimensional	GaN	Gallium Nitride
<i>a</i> -C	Amorphous Carbon	GPIB	General Purpose Interface Bus
a.m.u	Atomic Mass Unit	GUI	Graphical User Interface
Al/Fe	Aluminium/Iron	H	Hydrogen
AlN	Aluminium Nitride	h-BN	Hexagonal Boron Nitride
Alq <sub>3</sub>	Tris(8 hydroxyquinolato)aluminium	H <sub>2</sub> O	Water
AR	Aspect Ratio	HDTV	High Definition Television
B	Boron	HOMO	Highest Occupied Molecular Orbital
BaO	Barium Oxide	InGaN	Indium Gallium Nitride
C	Carbon	IP	Inverse Pillar
C <sub>2</sub> H <sub>2</sub>	Acetylene	ITO	Indium Tin Oxide
CAD	Computer Aided Drawing	LaB <sub>6</sub>	Lanthanum Hexaboride
CAPE	Centre for Advanced Photonics and Electronics	LED	Light Emitting Diode
cBN	Cubic Boron Nitride	MgO	Magnesium Oxide
CbO	Niobium Oxide	MoO <sub>2</sub>	Molybdenum Dioxide
CdS	Cadmium Sulphide	MoS <sub>2</sub>	Molybdenum Disulphide
CNF	Carbon Nanofiber	MWNTs	Multi-walled Carbon Nanotubes
CNTs	Carbon Nanotubes	N <sub>2</sub>	Nitrogen
CO <sub>2</sub>	Carbon Dioxide	NASA	National Aeronautics and Space Administration
Cu	Copper	NH <sub>3</sub>	Ammonia
CuO	Copper Oxide	NO <sub>2</sub>	Nitrogen Dioxide
CuPC	Copper Phthalocyanine	O	Oxygen
CuTCNQ	Copper Tetracyanoquinodimethane	P	Pillar
CVD	Chemical Vapour Deposition	PE	Photoemission
DC	Direct Current	PECVD	Plasma Enhanced Chemical Vapour Deposition
DLC	Diamond Like Carbon	PMMA	Poly(methylmethacrylate)
DOS	Density Of States	PPy	Polypyrrole
FE	Field Emission	RGA	Residual Gas Analysis
FED	Field Emission Display	RGO	Reduced Graphene Oxide
FWHM	Full-Width-Half-Maximum	SAFEM	Scanning Anode Field Emission Microscope
FN	Fowler Nordheim		

Si	Silicon	TWT	Travelling Wave Tube
SiC	Silicon Carbide	UHV	Ultra-High-Vacuum
SEM	Scanning Electron Microscopy	W	Tungsten
SMU	Source-Measurement Unit	WKB	Wentzel-Kramers-Brouillon
SnO <sub>2</sub>	Tin Dioxide	WO	Tungsten Oxide
SnS <sub>2</sub>	Tin Disulphide	WS <sub>2</sub>	Tungsten Disulphide
SWNTs	Single-Walled Nanotubes	ZnMgO	Zinc Magnesium Oxide
<i>ta</i> -C	Tetrahedral Amorphous Carbon	ZnO	Zinc Oxide
TE	Thermionic Emission	ZnS	Zinc Sulphide
TEM	Transmission Electron Microscopy	ZnSe	Zinc Selenide

## Publications

- [1] Cole, M. T., Parmee, R. J., Kumar, A., **Collins C. M.**, Kang, M. H., Xiao, J., Cepek, C., Yuan, X., Milne, W. I., Conjugated polyelectrolyte nano field emission adlayers. *Nanoscale Horizons* **1**, 304-312, (2016).
- [2] Cole, M. T., **Collins, C. M.**, Parmee, R., Li, C. & Milne, W. I. Chemical Functionalization of Carbon Nanomaterials. *Chemistry and Applications*, **1**, 1034 - 1061 (CRC Press, 2015).
- [3] **Collins, C. M.**, Parmee, R. J., Milne, W. I. & Cole, M. T. High Performance Field Emitters. *Advanced Science*, **3**, 5 (2015).
- [4] Ding, S., Cole, M. , Li, C. , Zhou, Y. , **Collins, C. M.** , Kang, M. H. , Parmee, R. J. Towards Graphane Field Emitters. *RSC Advances* **5**, 105111-105118 (2015).
- [5] Parmee, R., **Collins, C. M.**, Milne, W. & Cole, M. X-ray generation using carbon nanotubes. *Nano Convergence* **2**, 1 (2015).
- [6] Rawson, F. J., Cole, M. T., Hicks, J. M., Aylott, J. W., Milne, W. I., **Collins, C. M.**, Jackson, S. K., Silman, N. J., Mendes, P.M., Electrochemical communication with the inside of cells using micro-patterned vertical carbon nanofibre electrodes. *Scientific Reports* **6**, 37672 (2016).

## Presentations

- [1] Clare. M. Collins. William. I. Milne, Matthew. T. Cole (Oral and Poster), *Ultra Precision Manufacturing Conference*, Cambridge, May 2015
- [2] Clare. M. Collins, Richard. J. Parmee, William. I. Milne, & Matthew. T. Cole (Poster), *MRS Fall Meeting*, Boston, December 2015
- [3] Clare. M. Collins, William. I. Milne, Matthew. T. Cole (Poster), *Cambridge CDT joint event*, Cambridge, March 2017
- [4] Clare. M. Collins (Oral and Poster), *Ultra Precision Conference*, Cranfield, April 2017

# **1. Introduction**



## 1.1 Motivation

Cold cathode field electron emission from nanomaterials is an enduring area of academic and technological interest. Applications of this technology primarily are considered to be the replacement of electron sources, which are commercially, at present, generated through thermionic emission. The most widely investigated applications include displays<sup>1-3</sup>, travelling wave tubes<sup>4,5</sup>, microwave amplifiers<sup>6,7</sup>, electron microscopy<sup>8,9</sup>, parallel electron beam lithography<sup>2,10,11</sup>, field emission lamps<sup>2,12</sup> and X-ray sources<sup>2,13,14</sup>.

The benefits gained by using cold cathodes are numerous. The first, as the name suggests, is the operation of devices at cold temperatures compared to thermionic rivals. The application of heat is essential in thermionic technologies as electrons require large amounts of kinetic energy to escape the surface and contribute to a current. This is negated by the use of electric fields in electron field emission. Application of an electric field results in the triangulation and narrowing of the tunnelling barrier between the emitter surface and vacuum, allowing, at fields of sufficient strength, the tunnelling of electrons at the Fermi energy. This provides a more energy efficient solution to generating an electron source, as well as offering potentially longer lifetimes as current thermionic devices have typical lifetimes of up to just one year<sup>15</sup>. By removing the heating element needed for thermionic emission this also permits more compact constructions as the need for cooling apparatus is eliminated.

Of further importance are the fast temporal responses and higher control of the emitted beam on offer when using field emission over thermionic. As a result of the tunnelling process, fast response times have been measured down to less than 50  $\mu\text{s}$  in field emission<sup>3</sup>. Slow response times in thermionic emission systems are driven by the nature of the feedback loops that mitigate current fluctuation. Electrons tunnelling through at the Fermi energy, rather than over a potential barrier, have further benefits including a narrow energy distribution. Carbon nanotubes, CNTs, have small energy distribution with full-width-half-maximum, FWHM, of approximately 0.1 – 0.3 eV reported<sup>16</sup>. Control of a broad beam, as seen in thermionic emission, necessitates architectures that focus the beam and reduce spot size, which can be cumbersome, adding to the size, and complexity, adding to expense. Cold cathode designs offer reductions in both scale and price of necessary additional features required in applications and offer the added advantage of miniaturisation.

## 1. Introduction

A number of drawbacks have limited the acceptance of technologies utilising cold cathode field emission devices, and they are thus yet to become widely commercially available. Addressing fundamental flaws, notably fabrication, reliability, temporal and spatial stability and reproducibility<sup>17</sup>, is essential in the pursuit of commercial viability. This thesis attempts to combat, or at least better understand, some of the current issues, with particular efforts concentrated on improving reliability and stability of current output. The intended application of the findings made herein is aimed principally towards field emission from CNTs as X-ray sources, though this is not exclusive as there exists a continuity between many of the other applications noted above.

The Fowler Nordheim equation, derived according to the behaviour of classical bulk metals, accordingly rearranged to be of use with nanomaterials, is given by:

$$J = \left( \frac{A_{FN}\beta^2 E^2}{\phi} \right) \exp \left( - \frac{B_{FN}\phi^{\frac{3}{2}}}{\beta E} \right) \quad (1)$$

where  $J$  is the emission current density,  $A_{FN}$  and  $B_{FN}$  are constants,  $E$  is the applied electric field,  $\phi$  is the material surface work function and  $\beta$  is the local field enhancement around the tip. Investigating the behaviour of nanomaterials as field emitters, which do not conform to bulk metal behaviours, is explored within this thesis in reference to this equation, specifically the factors  $\phi$  and  $\beta$ .

Low  $\phi$  has been repeatedly touted as a primary driver towards achieving high performance field electron emitters<sup>18,19</sup>. However, detailed analysis of this material characteristic and relation to field emission capabilities has not yet been fully or comprehensively studied across a diverse range of materials. Fowler Nordheim theory suggests that low work function materials result in higher current densities relative to those materials with high work functions, though proof of this is lacking. As a result of this widely, perhaps incorrectly, adopted theory, many have strived to develop low work function materials, composites, or coatings for enhancing the performance of their field emitters<sup>20-22</sup>. Confirmation of the relative merits of low work function is somewhat elusive and thus absent in completion. The effect of material  $\phi$  has not yet been considered on a large material-to-material basis. By performing this task, across an extensive and exhaustive collection of materials, clearer understanding of the effect of surface  $\phi$  on field emission can be extracted.

High  $\beta$  has similarly been suggested as a route to achieving successful field emission achieved through increasingly small dimensions and sharp tips. There is no way in which to directly

measure or isolate the local field enhancement around an emitting tip, or indeed an array of emitting tips, under experimental conditions and thus many ambiguities surround this value. Traditionally, values are calculated using  $\beta = (h/r)^{23-25}$ , where  $h$  is the emitter height or length and  $r$  is the radius of curvature at the tip, this is more commonly seen in bulk cone-like geometries. With nanowires, however, this becomes superfluous and insufficient in defining  $\beta$ . Most opt, instead, to calculate  $\beta$  from the measured and known quantities, by working backwards using the Fowler Nordheim equation. This can be achieved through calculation of the gradient of a Fowler Nordheim plot showing  $\ln(1/V)$  against  $\ln(I/V^2)$ . Whilst this is a commonly accepted and used practice within the field emission community, deeper understanding of the explicit factors affecting  $\beta$  are not universally understood in detail. Further investigation into the effects of characteristics including surface coverage, degree of alignment, and the screening effect by surrounding neighbours is paramount in progressing the field further.

Another practical flaw limiting the viability of materials, particularly CNTs and carbon derivatives, is the hysteretic current behaviour observed under emission conditions. A number of theories have been linked to causing this phenomenon, including suggestions such as improvement under electrostatic alignment<sup>26</sup>, additional emission from intermediary electron states<sup>27</sup> and adsorption and desorption of gas molecules<sup>28-30</sup> from the material surface. The hysteresis is observed when the current emitted under increasing electric fields differs to that measured at the same electric field strengths under a decreasing applied field. Characteristically, at higher applied fields the measured current is larger in the increasing fields compared to decreasing<sup>28-30</sup>. Molecular adsorption on the CNT surface has been shown to directly influence surface work function, with electronegative species such as oxygen<sup>31</sup> increasing  $\phi$ , whilst others, such as nitrogen<sup>32</sup>, lower it. This could be of importance in the field emission cycle. Other impacts of adsorbates include additional tunnelling states resulting in additional electron emission<sup>33</sup>. Studying the emission from custom-built emitters under a number of different subjected tests will allow further study into the causes of hysteretic behaviour, which in turn will be required in mitigation.

## 1.2 Objectives

The research aims of this thesis are as follows:

- To address the suitability of materials as field emitters across an exhaustive range of materials spanning one, two and three dimensional varieties with the intention to bring to light dependencies of field emission performance on material  $\phi$ .
- To explore and give guidance on the highly influential parameters  $\phi$  and  $\beta$  governing electron field emission by thorough investigation of material and emitter properties to promote the development of devices that reliably show high current output at low field values.
- Fabrication of high performance carbon nanotube field electron emitters for the use in applications such as X-ray sources.
- Through experimentation examine the hysteretic behaviour of electron field emission from fabricated CNTs with a view to determine its origin and potential mitigation.

## 1.3 Thesis Structure

This thesis documents studies undertaken by the author to better understand the underlying processes pertaining to the field emission of electrons from ordered nanomaterials, CNTs in particular, for the eventual use as X-ray sources. The chapters of the thesis are grouped according to subject matter, primarily concerning an introduction to the field, the influential factors behind the emission process of both  $\phi$  and  $\beta$ , hysteretic behaviour in field emission from carbon nanotubes and conclusions that can be drawn from the studies.

In Chapter 2, an introduction to and history of both field emission and CNTs, and indeed the combination of the two, is addressed. Field emission, as discovered around the turn of the 20<sup>th</sup> Century after the significant developments made in the domain of quantum mechanics, has been governed predominantly by the Fowler Nordheim equations, derived in 1928<sup>34</sup>. Knowledge of CNTs and their manufacture, properties, application and structure has, however, been a far more recent undertaking, accelerated principally after the discovery by Iijima<sup>35</sup>. Iijima *et al* discovered the fabrication of CNTs in isolation, encountered by accident as a by-product of an arc discharge method. Available literature on these subjects is detailed in this chapter, and a need for further investigations into the combining of the pre-existing Fowler-

Nordheim equations and their appropriateness for materials of nanoscale dimensions are identified.

An exhaustive range of nanomaterials are compared in Chapter 3. Using data collected from other sources, a novel and comprehensive set of data is displayed and analysed according to the seemingly important material property: surface  $\phi$ . The importance of  $\beta$  is introduced, and an attempt at determining a morphology metric,  $\alpha$ , is made, to be used in conjunction with the aforementioned work function studies.

Chapter 4, leading on from the conclusions made in Chapter 3, details the fabrication of CNT emitters and results of experiments conducted in pursuit of a deeper understanding of the influence of morphology on electron field emission from CNTs, driven by questions concerning  $\beta$ . Two different methods of measuring field emission from in house fabricated samples are presented, with discussions made on the resulting data from each.

The phenomenon of hysteretic behaviour observed in field emission from CNTs is the focus of Chapter 5. In this chapter, experiments are conducted that attempt to pin down the underlying causes of this observed hysteresis. CNT emitters are subjected to changes in environmental and procedural conditions highlighting behaviours that can be utilised to determine a model of the emission process. A model and justification describing the behaviour seen in the experimental results is also presented here.

The final Chapter 6 summarises the findings made from the work undertaken throughout the project.

## References

- 1 Wang, Q. H. *et al.* A nanotube-based field-emission flat panel display. *Applied Physics Letters* **72**, 2912-2913 (1998).
- 2 de Jonge, N. & Bonard, J. M. Carbon nanotube electron sources and applications. *Philosophical Transactions of the Royal Society a-Mathematical Physical and Engineering Sciences* **362**, 2239-2266 (2004).
- 3 Lei, W. *et al.* A graphene-based large area surface-conduction electron emission display. *Carbon* **56**, 255-263 (2013).
- 4 Jensen, K. L. Field emitter arrays for plasma and microwave source applications. *Physics of Plasmas* **6**, 2241-2253 (1999).
- 5 Whaley, D. R., Gannon, B. M., Smith, C. R., Armstrong, C. M. & Spindt, C. A. Application of field emitter arrays to microwave power amplifiers. *Ieee Transactions on Plasma Science* **28**, 727-747 (2000).
- 6 Milne, W. I. *et al.* Carbon nanotubes as field emission sources. *Journal of Materials Chemistry* **14**, 933-943 (2004).
- 7 Temple, D. Recent progress in field emitter array development for high performance applications. *Materials Science & Engineering R-Reports* **24**, 185-239 (1999).
- 8 Bauer, E. Low-energy-electron microscopy. *Reports on Progress in Physics* **57**, 895-938 (1994).
- 9 Pawley, J. The development of field-emission scanning electron microscopy for imaging biological surfaces. *Scanning* **19**, 324-336 (1997).

## 1. Introduction

- 10 Milne, W. I. *et al.* Carbon films for use as the electron source in a parallel e-beam lithography system. *New Diamond and Frontier Carbon Technology* **11**, 235-247 (2001).
- 11 Milne, W. I. *et al.* Investigating carbon materials for use as the electron emission source in a parallel electron-beam lithography system. *Current Applied Physics* **1**, 317-320 (2001).
- 12 Saito, Y. Field emission from carbon nanotubes and its application to electron sources. *Carbon (New York)* **38**, 169-182 (2000).
- 13 Xia, Y. N. *et al.* One-dimensional nanostructures: Synthesis, characterization, and applications. *Advanced Materials* **15**, 353-389 (2003).
- 14 Cole, M. T. *et al.* in *Conference on Carbon Nanotubes, Graphene, and Associated Devices V.* (2012).
- 15 Gonzales, B. Rectangular Fixed-Gantry CT Prototype: Combining CNT X-Ray Sources and Accelerated Compressed Sensing-Based Reconstruction. *IEEE access* **2**, 971-981 (2014).
- 16 Liang, S.-D. *Quantum Tunneling and Field Electron Emission Theories.* (World Scientific Publishing Co. Pte. Ltd., 2014).
- 17 Parmee, R., Collins, C., Milne, W. & Cole, M. X-ray generation using carbon nanotubes. *Nano Convergence* **2**, 1 (2015).
- 18 Qian, X., Liu, H., Guo, Y., Song, Y. & Li, Y. Effect of aspect ratio on field emission properties of ZnO nanorod arrays. *Nanoscale Research Letters* **3**, 303-307 (2008).
- 19 Lee, M.-B. Aspect Ratio of Nanosized Field Emitters for Optimized Emission Current. *Journal of the Korean Physical Society* **44**, 800-806 (2004).
- 20 Yamamoto, S. Electron emission and work function - Past, present and future. *Applied Surface Science* **251**, 4-13 (2005).
- 21 Nakamoto, M. & Moon, J. Extremely environment-hard and low work function transfer-mold field emitter arrays. *Applied Surface Science* **275**, 178-184 (2013).
- 22 Xu, J. *et al.* Excellent Field-Emission Performances of Neodymium Hexaboride (NdB<sub>6</sub>) Nanoneedles with Ultra-Low Work Functions. *Advanced Functional Materials* **23**, 5038-5048 (2013).
- 23 Menaka, Patra, R., Ghosh, S. & Ganguli, A. K. Manipulating the anisotropy and field emission of lanthanum hexaboride nanorods. *Rsc Advances* **2**, 7875-7885 (2012).
- 24 Jha, M., Patra, R., Ghosh, S. & Ganguli, A. K. Vertically aligned nanorods of lanthanum hexaboride with efficient field emission properties. *Solid State Communications* **153**, 35-39 (2013).
- 25 Ng, K. L., Yuan, J., Cheung, J. T. & Cheah, K. W. Electron field emission characteristics of electrochemical etched Si tip array. *Solid State Communications* **123**, 205-207 (2002).
- 26 Cahay, M., Murray, P.T., Back, T.C., Fairchild, S., Boeckl, J., Bulmer, J., Koziol, K.K.K., Gruen, G., Sparkes, M., Orozco, F. and O'Neill, W. Hysteresis during field emission from chemical vapor deposition synthesized carbon nanotube fibers. *Applied physics letters* **105**, 173107 (2014).
- 27 Arkhipov, A. V., Mishin, M. V., Sominski, G. G. & Parygin, I. V. Hysteresis of pulsed characteristics of field emission from nanocarbon films. *Technical Physics* **50**, 1353-1359 (2005).
- 28 Chen, J. *et al.* The hysteresis phenomenon of the field emission from the graphene film. *Applied Physics Letters* **99**, 173104 (2011).
- 29 Zuo, Y., Ren, Y., Wang, Z., Han, X. & Xi, L. Enhanced field emission and hysteresis characteristics of aligned carbon nanotubes with Ti decoration. *Organic Electronics* **14**, 2306-2314 (2013).
- 30 Li, C. *et al.* Effect of adsorbates on field emission from flame-synthesized carbon nanotubes. *Journal of Physics D-Applied Physics* **41**, 195401 (2008).
- 31 Akdim, B. The Effects of O Adsorbates on Field Emission Properties of Single-Wall Carbon Nanotubes: A Density Functional Theory Study. *Nano letters* **3**, 1209-1214 (2003).
- 32 Pinto, H. Electronic and electrochemical doping of graphene by surface adsorbates. *Beilstein journal of nanotechnology* **5**, 1842-1848 (2014).
- 33 Dean, K. A. The environmental stability of field emission from single-walled carbon nanotubes. *Applied physics letters* **75**, 3017-3019 (1999).
- 34 Fowler, R. H. & Nordheim, L. Electron emission in intense electric fields. *Proceedings of the Royal Society of London Series a-Containing Papers of a Mathematical and Physical Character* **119**, 173-181 (1928).
- 35 Iijima, S. Helical microtubules of graphitic carbon. *Nature* **354**, 56 (1991).

## **2. Field Emission from Carbon Nanotubes**



## 2.1 Introduction

Whilst developments in field emission, FE, have been significant over the last century, the introduction of nanomaterials as prime candidates has only been made in recent years with carbon nanotubes, CNTs, as the prime candidate. A vast diversity of research has been conducted in the area of nanomaterial-based FE, though significant progress regarding the commercialisation of these materials and technologies based on them remains continually on the horizon.

## 2.2 Electron Emission

Electron emission is defined as the transmission of electrons from an electron dense, solid or liquid material into vacuum. There are principally three types of electron emission processes: photoemission, PE, thermionic emission, TE, and FE. PE relies on absorption of energy from a photon by an electron, exciting it to a higher state thereby allowing the electron to pass over the surface potential barrier with incident energy  $h\nu \geq \phi$ , where  $h$  is Planck's constant ( $6.63 \times 10^{-34}$  Js),  $\nu$  is the frequency of the wavelength of light and  $\phi$  is the work function of the material. Typically, to gain sufficient energy, the incident light must lie in the ultraviolet part of the electromagnetic spectrum. Whilst physically interesting, with fast response times down to nanoseconds<sup>1,2</sup>, practically it is the least explored of the emission mechanisms and is not greatly relied upon for use in applications as achieving high currents is challenging.

TE, comparatively, is used extensively. To liberate electrons demands high temperatures ( $> 1000$  K) in order that they acquire sufficient kinetic energy greater than the restraining surface potential barrier. The quantity of kinetic energy required is defined by work function,  $\phi$ , of the material, which for most metals is between 2 – 5 eV. Strictly speaking,  $\phi$  is determined by the amount of energy an electron needs to overcome the ionisation potential. Factors that influence work function magnitude are the intrinsic partial free energy of electrons as well as surface electrostatic effects<sup>3</sup>. In the presence of an electric field, the surface potential barrier required for electrons to emit lowers, whilst the shape of the potential barrier also changes from nominally quadrilateral to more triangular. When the principle emission method is thermionic, with electrons passing over the newly lowered barrier, this is termed Schottky emission. Figure

## 2. Field Emission from Carbon Nanotubes

2.1 shows the essential differences, in terms of energy required, between thermionic, Shottky and field emission.

Both PE and TE entail classical physics principles of excitation to pass over a barrier, whereas FE enters the domain of quantum mechanics. FE of electrons necessitates an applied electric field only, without heating, and is accordingly termed cold emission. Electrons tunnel through the vacuum barrier potential at the Fermi energy,  $E_f$ , which is significantly narrowed in the presence of an electric field. This sources the emission current. With increasing fields, the barrier narrows further and emission current increases with an observed exponential relationship. In semiconductors, electrons from the conduction band are promoted to the valence band by field induction<sup>4</sup>. Huge advances in FE were seen throughout the 20<sup>th</sup> century, from conception<sup>5</sup> through to commercially available devices including the first prototype<sup>6</sup> in 1985, which lead to developments of commercial devices by Pixtech and Futaba by 2001<sup>7</sup> and a 38" HDTV from Samsung<sup>8</sup> in 2003.

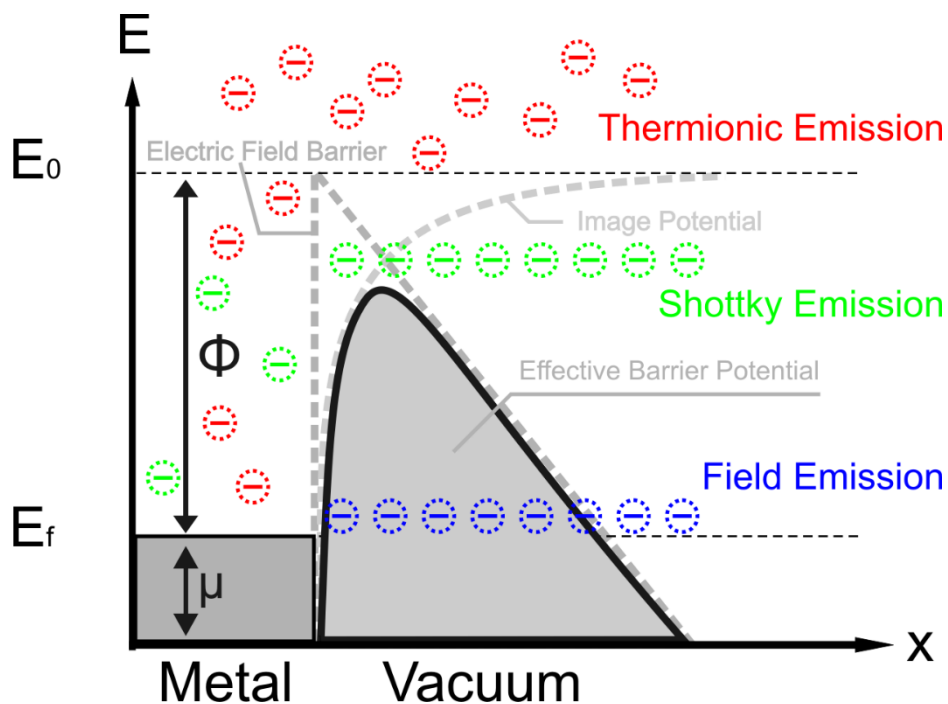


**Figure 2.1 | Emission Mechanisms Schematic.** Field emission at the Fermi energy (blue), thermionic emission over the classical electric field barrier (red) and Shottky emission (green) of electrons (negative circles) and the effective potential barrier seen in Shottky emission as a result of the triangular barrier and image potential.

### 2.2.1 The History of Field Emission

FE devices, or so called cold cathode devices, operate at room temperature and are an exciting avenue of technological development. The developments in FE are synchronous with vacuum microelectronics. The first evidence of what appeared to be an FE device was reported by Winkler<sup>9</sup> in 1744, where electrical discharge from a wire electrode was described, though the terminology to explain the phenomenon did not yet exist. The discovery of the electron in 1897 by J. J. Thomson<sup>10</sup> was a crucial step in developing a comprehensive understanding of the underpinning physical mechanisms. At the beginning of the 20<sup>th</sup> Century, dramatic advances in modern science were made in the field of quantum mechanics<sup>11</sup>. Quantum tunnelling was explained via the Heisenburg uncertainty principle coupled to wave-particle duality. Post 1922, experimental interest in the emission of electrons under high fields came into play from separate individuals, primarily including Millikan<sup>12</sup>, Gossling<sup>13</sup> and Oppenheimer<sup>14</sup>. In 1928, Fowler and Nordheim<sup>5</sup> derived a set of extensive equations describing quantum tunnelling of electrons from a bulk metal through a two dimensional barrier, and therein predicting the current-field dependence during FE. The equations proved difficult to verify experimentally, however, because of high voltage requirements, poor control or reproducibility of experimental conditions at the time alongside, then imperceptible, surface defects and sample-to-sample microstructural variations. They were often also impeded by destructive vacuum arcing at high voltages. In 1937, Müller<sup>15</sup> etched a tungsten wire, which emitted radially within a spherical glass vessel, and in doing so initiated what would be the first Field Emission Electron Microscope. This set up was used to verify the findings of Fowler and Nordheim by Good and Müller<sup>16</sup> and Dyke and Dolan<sup>17</sup>. The evolution of field emitters since has been driven, primarily, by the capabilities of nanotechnology to reduce the radius of emitting tips. The first field emitters consisted of a single sharp tipped needle with radii of a few hundred nanometres, and were created through conventional wet etching techniques. Between 1950 and 1970, field emission needles were implemented in microwave amplifiers<sup>18</sup>, cathode ray tubes<sup>19</sup>, electron microscopes<sup>20</sup>, electron beams<sup>21</sup> and flash X-ray photography<sup>22,23</sup>. They were functionally restricted, however, by the necessary ultra-high vacuum conditions ( $10^{-9}$  mbar), limited lifetimes, and high voltages (several thousand V). Further technological improvements were needed.

In 1968, a significant breakthrough, with a new emitter design, was published by Charles Spindt<sup>6</sup> and was accordingly termed a Spindt cathode. Figures 2.2a and b show an example of a Spindt cathode array in cross-section. In contrast to original field emitters, Spindt cathodes are made of many thousands of tips made by high precision thin film vacuum deposition

## 2. Field Emission from Carbon Nanotubes

techniques distributed in precise arrays operating at hundreds, not thousands, of volts. Commonly commercially available Spindt type emitters are an example of FE devices to successfully reach market<sup>6</sup> where they have been chiefly employed in display technologies. They consist of a sharp-tipped cone or pyramid of a metallic material (typically a refractory metal) set into a substrate, where the cone has a typical radius of 50 - 200 nm, though radii as small as 2.6 nm have been reported<sup>24</sup>, and have shown high current densities<sup>25</sup> of up to 20 A/cm<sup>2</sup>. A number of bulk metals with cone-like geometry have been tested for field emission including copper<sup>26</sup> and nickel<sup>27-29</sup>, as well as semi-conductor metals such as silicon<sup>30,31</sup>, and compound materials such as gallium nitride<sup>32</sup>, gallium arsenide<sup>33</sup> and cubic boron nitride<sup>34</sup>. Wet<sup>29,31</sup> and dry<sup>26,30</sup> etching are used to create these micro-conical structures, as well as direct growth<sup>27</sup>. Figure 2.2c shows gallium arsenide grown in a pyramidal structure<sup>33</sup>. Despite this revolution, high current densities at low fields remains challenging due to high demands on the emitting materials, with poor vacuum conditions leading to individual or large area tip degradation by tip rounding, reduction in the tips aspect ratio, AR, emitter poisoning<sup>35,36</sup> or vapourisation<sup>37</sup>. Nevertheless, Spindt cathodes were implemented in display technologies such as flat panel displays<sup>38</sup>.

From 1994 onwards there was a move towards nanomaterials, largely the nano-carbons, particularly carbon nanotubes, CNTs, and diamond-based materials, exploiting the sharp tips available. Cold cathode devices and FE from nanomaterials have been enduring areas of academic and technological interest since this shift in focus. Nanomaterials, in general, offer increased FE performance compared to Spindt-type cone shaped emitters with high AR and unique electronic properties. Whilst Spindt cathodes can offer a sharp tip, nanomaterials have the additional benefit of comparable nano-sized diameter from tip to base, which leads to dramatically enhanced local electric fields, increasing emitter performance. Successful devices have yet to reach commercial availability, due to lack of sophistication and repeatability<sup>39</sup>, although some specialist devices by Siemens<sup>40</sup>, XinRay<sup>41</sup> and Oxford Instruments<sup>42</sup> have been designed. CNTs in particular are promising, showing a degree of stability over long times and at large currents<sup>43,44</sup>, fast reaction times<sup>45,46</sup>, large AR<sup>47</sup>, high conductivity (up to 1000 times that of copper<sup>48</sup>) and mechanical and chemical stability<sup>49</sup>. The first published use of CNTs employed in FE was in 1995<sup>50,51</sup>, where individual CNTs were mounted onto a metal supporting tip as seen in Figure 2.2d. It took a further few years before nanotube powders and solutions were used to make films, glued or pasted onto metal supports. This lead further onto the growth of nanotubes is a bottom-up fashion on planar substrate surfaces, as shown in Figure

2.2e. Figure 2.2f shows the pinnacle of reducing emitter diameter with individually grown and spaced CNTs grown from 100 nm wide catalyst dots by Milne *et al*<sup>52</sup>. The complexities, and prices, surrounding this design, however, means that attaining the smallest emitting radius may not be the simplest route to market. Desired high current densities and low operating fields have been recorded, although a number of problems with CNT FE devices have been encountered. Limitations, resulting in the prevention of current commercial availability include: lack of cost effective and reliable emitter fabrication, time stability inconsistencies, spatial uniformity, and reproducibility. In the last 20 years, struggles to achieve commercial viability with these limitations have been vast, but widespread global interest in the potential that CNTs hold for the future has continued to advance the technology.

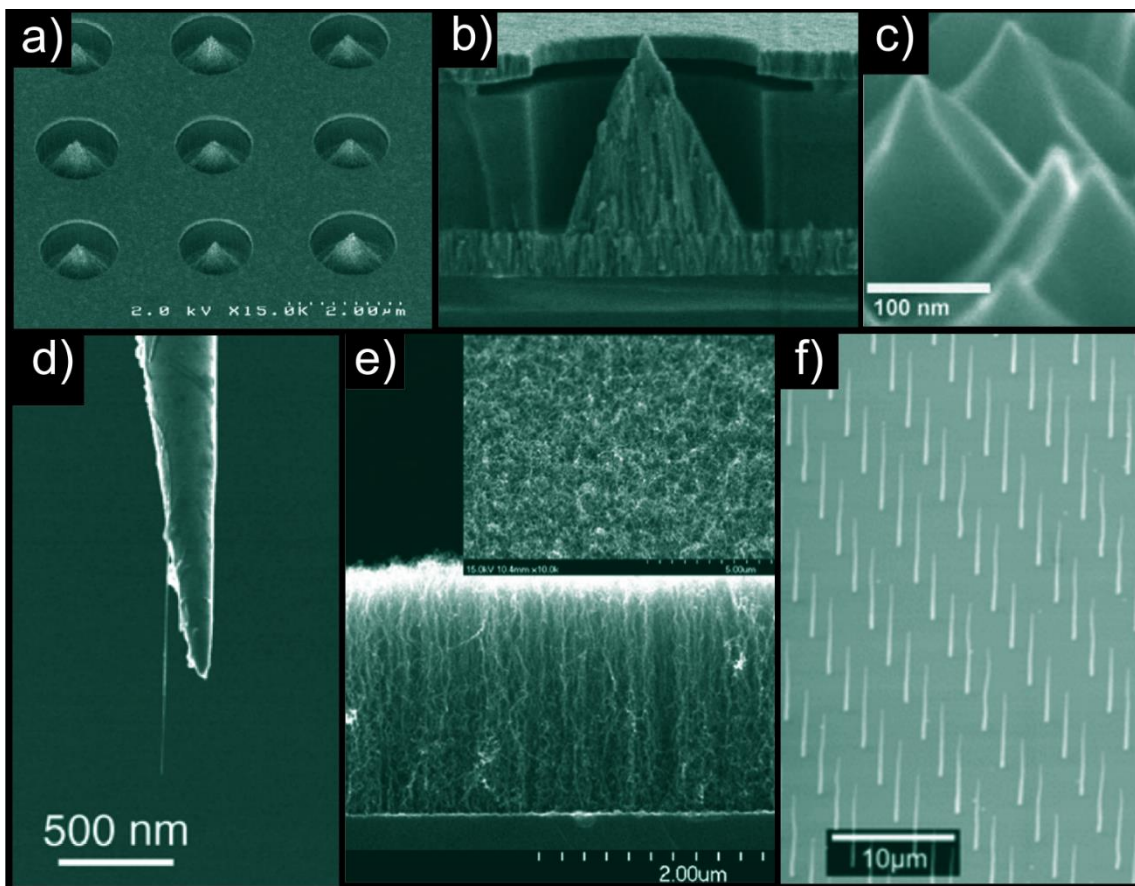


**Figure 2.2 | Developments in Field Emission; Reducing the curvature of radius of emitters.** a) Spindt emitter top down view b) Cross section of Spindt cones (both Motorola)<sup>53</sup> c) pyramidal bulk GaN cones<sup>33</sup> d) Single CNT on gold wire support<sup>54</sup> e) Aligned forest of CNTs grown on planar silicon surface, side view (inset top view)<sup>55</sup> f) Individually grown CNTs in a controlled fabrication process<sup>53</sup>.

## 2.3 Fowler Nordheim Theory

The most commonly used theory to investigate FE to date, is the Fowler Nordheim, FN, Theory<sup>5</sup> first published in 1928. Fowler and Nordheim developed a theory, and complementing equations, that successfully predicted electron emission from metals. A number of general assumptions are made in the process of deriving the equations. (1) It is assumed that emission occurs at the tip, neglecting substrate effects. (2) The emitter has an atomically smooth surface and a planer tip model can be used<sup>56</sup>. (3) That a triangular barrier potential exists at the metal-vacuum interface. (4)  $\phi$  is independent of the electric field. (5) Electrons are thermally equilibrated and obey a Fermi-Dirac distribution. (6) One dimensional tunnelling in a single direction occurs due to a sharp tip. (7) Application of the Sommerfeld or free electron model, which is only strictly correct for electrons in bulk metals. The free electron model assumes electrons are detached from ions and describes the behaviour of valence electrons in a metallic crystal structure. The zero temperature approximation works well for room temperature emission<sup>3</sup>.

Figure 2.3a shows a parallel plate field emitting device operating in diode mode as is typically referenced in literature. The emitting material, under high vacuum conditions ( $< 10^{-7}$  mbar), is negatively biased and exposed to a high voltage on the anode. The inter-electrode vacuum gap,  $d$ , defines the apparent electric field. A triangular barrier assumption is used in both bulk and nanomaterials. Whilst for bulk metals this is a good approximation, it is possible it does not well represent the surface-vacuum barrier for many nanomaterials. Figure 2.3b shows the triangular surface potential barrier at the interface between an emitting material and the vacuum, where conduction band energy,  $E_0 = E_f + \phi$ , where  $E_f$  is Fermi energy and  $\phi$  is the work function. Intuitively, less energy is required for emission from materials with low  $\phi$ , and indeed studies have been made on low  $\phi$  materials such as amorphous-diamond (bulk)<sup>57,58</sup> ( $\phi = 1.33$  eV), barium oxide, BaO,<sup>59</sup> nanowires ( $\phi = 1.65$  eV) and lanthanum hexaboride, LaB<sub>6</sub>,<sup>60</sup> nanowires ( $\phi = 2.57$  eV). Due to intricacies of the underlying physics, they have not, in fact, shown distinctly improved behaviour compared to other materials.

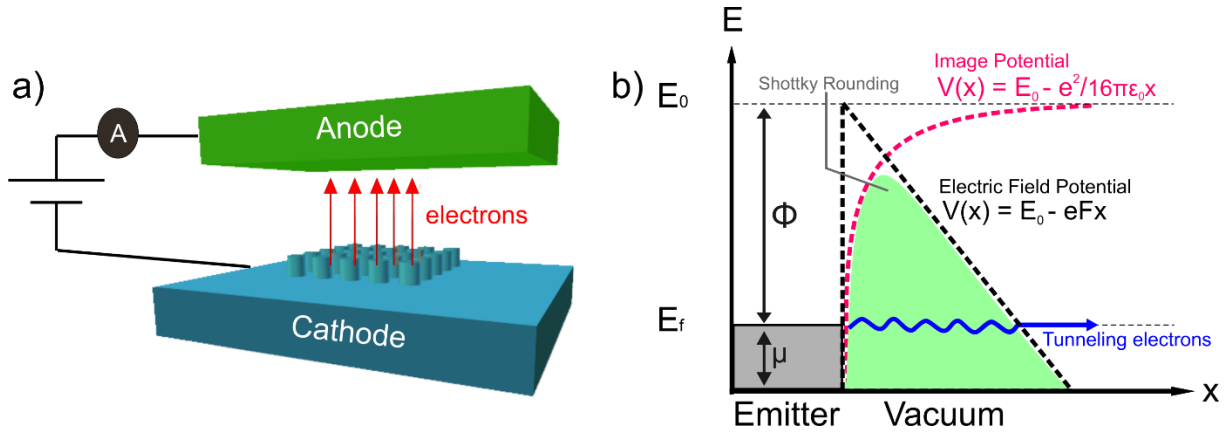


**Figure 2.3 | Field Emission Schematic Diagrams.** Typical FE device with nanomaterials grown on cathode, operating in diode mode b) schematic of the potential barrier induced by an electric field including Shottky corrections and image potential.

To estimate the current density,  $J$ , the emission current formula for emission in the  $x$  direction from an emitter in the  $yz$ -plane is given by:

$$J_x = \int_0^{\infty} N(E_x)D(E_x)dE_x \quad (1)$$

where  $N(E_x)dE_x$  is the electron supply function, giving the number of electrons crossing the barrier in a direction parallel to the substrate plane (from emitter bulk); and  $D(E_x)$  gives the transmission coefficient or tunnelling probability. To calculate  $D(E_x)$ , the Wentzel-Kramers-Brouillon, WKB, approximation is used. Tunnelling occurs when the barrier is significantly thinned by the electric field to less than a few nanometers, with a relationship between increasing emitted electrons and decreasing barrier thickness. For metals, the emission tip is modelled as a semi-infinite quantum well with work function,  $\phi$ , and local electric field,  $F$ , approximated as a linear potential. Application of the Fermi-Dirac distribution, which assumes electrons follow the free electron model and hence obey the Pauli Exclusion Principle, and WKB approximation, gives the FN equation, as <sup>39</sup>:

$$J = A_{FN} \frac{F^2}{\phi} \exp\left(-\frac{B_{FN}\phi^2}{F}\right) \quad (2)$$

where the constant  $A_{FN}$  is derived from the supply function  $N(E_x)dE_x = dE_x \int_{E_x}^{\infty} n(E, E_x)dE$  according to the free electron model and  $B_{FN}$  from the transmission

## 2. Field Emission from Carbon Nanotubes

coefficient  $D(E_x) = D_F \exp\left(\frac{E_x - E_F}{dF}\right)$  of the barrier using the solution to the Schrödinger equation and WKB approximation:

$$A_{FN} = \frac{e^3}{16\pi^2\hbar} = 1.54 \times 10^{-6} \text{ A eV V}^{-2}$$

$$B_{FN} = \frac{4\sqrt{2m_e}}{3\hbar e} = 6.83 \times 10^9 \text{ eV}^{-3/2} \text{ V m}^{-1}$$

where  $e$  is the electron charge,  $m_e$  is the mass of an electron and  $\hbar$  is Planck's constant  $h/2\pi$ .

The electron supply function is dependent on the relationship between the back contacts and the emission material. For nanomaterials and non-metallic materials, further considerations are required. Beyond the triangular barrier, equations derived for a Shottky-Nordheim barrier includes corrections from the effects of image potentials giving:

$$J = \lambda_M A_{FN} \frac{F^2}{\phi} \exp\left(-\frac{\nu_F B_{FN} \phi^{\frac{3}{2}}}{F}\right) \quad (3)$$

where  $\lambda_M$  is a pre-exponential correction factor and  $\nu_F$  is a correction factor given at a particular value of the principle Shottky-Nordheim barrier function.

A reduced version of the standard FN equation, commonly used in calculations with experimental data, is given by:

$$J = \frac{I}{S} = \left(\frac{A_{FN} \beta^2 E^2}{\phi}\right) \exp\left(-\frac{B_{FN} \phi^{\frac{3}{2}}}{\beta E}\right) \quad (4)$$

where  $I$  is the total emission current,  $S$  is the effective area of emission, defined by the effective area from which electron liberation occurs from the cathode, which is somewhat dubious and difficult to measure and is commonly mistaken as the area of the substrate onto which the field emitting materials are deposited,  $E$  is the local electric field, and  $\beta$  is the field enhancement factor relating to an increase in the observed local field around sharp tips.  $E$  can be approximated using the anode-cathode voltage,  $V$ , and inter-electrode separation,  $d$ , by  $E = \beta(V/d)$ , where  $\beta$  is a proxy metric for AR or tip sharpness. The quantities  $I$  and  $S$  can be directly measured under experimental conditions, and give rise to the calculation of factors such as  $\beta$  and, of course,  $J$ . According to the general WKB approximation and subsequent transmission models, low  $\phi$  and high  $\beta$  typically manifest as high maximum current density.

The reduced FN equation is commonly used to calculate FN behaviours from a nanomaterial emitter. A linear fit to a plot of  $\ln (J/E^2)$  (y-axis) against  $1/E$  (x-axis), typically called an FN plot, indicates that a material follows Fowler-Nordheim theory well. A linear rearrangement here gives:

$$\ln \left( \frac{J}{E^2} \right) = \left( -\frac{B_{FN}\phi^{\frac{3}{2}}}{\beta} \right) \frac{1}{E} + \ln \left( \frac{A_{FN}\beta^2}{\phi} \right) \quad (5)$$

The local field enhancement factor,  $\beta$ , is related, in part, to the emitter geometry, with high AR materials, such as CNTs, proving to be excellent candidates by exhibiting very large values. The value of  $\beta$  is measured by inference of known quantities including  $J$ ,  $E$  and  $\phi$ . Due to complexities arising in accurately assessing  $E$  and indeed  $\phi$ , however, calculated values of  $\beta$  are wildly disparate with values from 1 to 10,000 stated in literature<sup>61,62</sup>, although it should be noted that emitter morphology can also vary wildly within a sample and is of high influence in defining  $\beta$ .

Experimentally, the gradient,  $m$ , from a Fowler Nordheim plot ( $\ln (J/E^2)$  against  $1/E$ ) is commonly used to derive the local field enhancement factor,  $\beta$ , when  $\phi$  is known, given by:

$$\beta = -\frac{B_{FN}\phi^{3/2}}{m} \quad (6)$$

Calculating  $\phi$  can be performed using ultraviolet photoelectron spectroscopy, Kelvin probe microscopy, or other similar surface sensitive techniques and has different values for individual materials.

Theoretically, the maximum current density of an emitter can be calculated using the Fermi energy of the material, from where the majority of electrons are emitted, when the potential barrier is transparent to electrons<sup>3</sup> ( $D(E_x) = 1$ ):

$$J_{max} = \frac{em_e}{(2\pi)^2\hbar^3} E_F^2 = 80.83 E_F^2 \text{ eV}^{-2} \mu\text{A nm}^{-2}$$

In the Sommerfeld model, where  $\phi \sim 1.5 \text{ eV} - 15 \text{ eV}$ ,  $J_{max}$  can take values between  $180 \mu\text{A nm}^{-2}$  and  $18,000 \mu\text{A nm}^{-2}$ .

### 2.3.1 Field Emission from Nanomaterials

Despite being derived for classical bulk metals, the Fowler Nordheim equations have continued to be extensively used with the introduction of newly discovered one dimensional, 1D, and two

## 2. Field Emission from Carbon Nanotubes

dimensional, 2D, materials that neither behave classically, nor in the same way as bulk materials<sup>63</sup>. There are, therefore, ambiguities. In contrast to bulk metals, emission from both single-walled nanotubes, SWNTs, and multi-walled nanotubes, MWNTs, has been accredited to originate from discrete energy states<sup>64-67</sup> and continuous electronic bands<sup>68</sup>. The density of states at the tip deviates from metallic behaviour, with localised states that have well-defined energy levels<sup>54</sup>. Uncertainties on the validity of application of FN theory in these circumstances<sup>69</sup> have surfaced, however, a more relevant or universally accepted theory has not yet appeared. Nanomaterial FE analysed using standard FN theory has consequently continued to dominate and has been in use by scientists for some decades now.

A number of the assumptions made in FN theory come into question when considering nanomaterials. From the numbered assumptions mentioned above (Section 2.3), the following inaccuracies arise, which could affect the use of FN: Nanomaterials do not, in general, have atomically smooth surfaces, for example, at the tip of a CNT or nanowire. A planar boundary may not exist in nanomaterials, where the radii of curvature are especially high and close to, or less than, the barrier width, and the electric field near the surface becomes inhomogeneous. The approximation of a planar barrier becomes incorrect, with solutions to the three dimensional Schrödinger equation required; yet to be solved completely<sup>70</sup>. The tunnelling barrier corrected for atomically sharp tips requires image charge interaction and interaction between tunnelling charge and applied field to be known<sup>71</sup>. It is plausible that the electric field could penetrate some nanomaterials, changing the emission character, and indeed has been shown to do so in CNTs<sup>72,73</sup>. Zheng *et al*<sup>74</sup> used density functional theory to model this effect, finding that penetration at the tip leads to a deep potential well causing a non-linear decrease of the potential barrier and could explain the, elsewhere observed, low turn on voltages. The free electron model is not representative of electrons in all nanomaterials or in fact for any material used in FE that is not a metal. Filip *et al*<sup>75</sup> propose that a 2D free electron model is appropriate in “bulk” cases of emission from CNT films, where electrons show free movement in the space of 2D graphene sheet, subjected to a transverse confinement due to tight rolling into a nanotube. Fursey and Glazanov<sup>70</sup> suggest that the constant  $A_{FN}$  is connected to Fermi surface geometry that is material dependent and arises from approximations in the WKB model. They suggest that the difference between experimentally found values and free-electron model derived values can differ by up to 20%. The significant difference in the atomic structure of nanomaterials compared to bulk metals is characterised by: energy band structure beyond what is classically described by the Sommerfeld model; shape and size of material affecting

the electric potential distribution close to the surface and shape of the vacuum barrier potential; quantum confinement effects in nanowires; impurities and defects causing localised states near the Fermi energy and adsorption of foreign molecules altering emission of electrons. In 1D materials, it is the transmission coefficient that is most widely refuted because the WKB approximation falls apart at high fields, preventing a strict solution to the Schrödinger equation.

Often in 1D and 2D materials, a high and low field approximation is chosen, where nanomaterial  $I$ - $V$  characteristics diverge from bulk metallic in experimental results. In high field regions a deviation between 10% and 30% from linear FN behaviour is seen in CNTs<sup>65</sup>. Two values of  $\beta$  are often quoted, found by two gradients of two straight lines exhibited in plotted data often coarsely fitted according to classical FN theory<sup>76,77</sup>. In some cases straight line behaviour is not exhibited at all<sup>71</sup>. The explanation of these two values is attributed simply to the difference in emission between high and low field. Many suggest that  $\beta$  is a result of a combination of the emitter geometry; such as AR, surface roughness, the size of the vacuum gaps, crystal structure and spatial distribution of emitters<sup>78-80</sup> yet fail to intimately describe the exact relationship.

CNTs exhibit further unusual behaviour, often highly desirable, that cannot be fully explained by Fowler Nordheim theory alone. In CNTs explicitly, the saturation of emission current occurs at values of approximately 1  $\mu$ A, larger than those of metallic emitters. In macroscopic metallic emitters, the energy distribution is limited to around 0.3 eV and is dependent on the tunnelling barrier<sup>81</sup>. Increased narrow energy distribution, at least half that of metallic emitters, with FWHM approximately 0.1 – 0.3 eV has been shown at room temperature due to the energy distribution being also governed by the localised band structure<sup>82</sup>. These are two of the main benefits seen over bulk metals. Individual nanotubes can accommodate currents between 0.1 and 0.2 mA per tube<sup>3</sup>. Electrons originating from a number of energy bands result in an energy distribution with multiple peaks as opposed to a metallic continuum. Despite having a reported work function of between 4.3 – 5.1 eV<sup>83</sup>, which is larger than conventional FE materials, these excellent properties have proven influential in driving popularity of CNTs in FE research. FN equations specifically for CNTs have been derived<sup>3</sup> that take into account the linear energy dispersion relation, with Dirac Fermion behaviour, which differs to common metals that follow the Sommerfeld model and have a parabolic energy dispersion relation. However, this is not normally accepted or used.

## 2. Field Emission from Carbon Nanotubes

Some inaccuracies have been identified when considering emission from nanomaterials, however, sophisticated understanding or indeed widely accepted alternative solutions are lacking. Thus classical FN theory remains predominant in describing and predicting FE behaviour.

## 2.4 Carbon Allotropes

Carbon, in all forms, is of significant prominence and importance in the study of field electron emission, showing desirable characteristics such as high measured current densities. As the fourth most abundant element, the supply of carbon is large and subsequent research potential is vast. Whilst many forms of carbon have been used in FE, including diamond, graphite and amorphous-carbon,  $a$ -C, of particular interest are the 1D and 2D allotropes: graphene and CNTs.

### 2.4.1 Graphene

Graphene has been termed a wonder material, displaying a combination of unique and exciting properties. Discovered through observation of the lamella structure of graphite, graphene refers to a freestanding single atomic layer of  $sp^2$  hexagonally covalent bonded carbon, seen in Figure 2.4a, and is recognised as a 2D material because of its planar geometry. A carbon atom has six electrons occupying  $1s^2$ ,  $2s^2$  and  $2p^2$  electronic orbitals. In graphene,  $sp^2$  hybrids form in the  $xy$ -plane and  $p_z$  states in the plane normal to this, forming  $\sigma$  and  $\pi$  bonds in a tight binding approximation. Isolation of graphene sheets is relatively recent compared to its discovery by Wallace<sup>84</sup> in 1947, taking place in Manchester in 2004. The Nobel Prize in Physics was awarded for this in 2010 to Andre Geim and Konstantin Novoselov “*for ground-breaking experiments regarding the two-dimensional material graphene*”<sup>85</sup>.

Noteworthy reported properties are: high tensile strength<sup>86</sup>, high conductivity<sup>87</sup>, chemical inertness, optical transparency<sup>88</sup>, and high thermal conductivity<sup>89,90</sup>. There has been a diverse array of experiments to verify and utilise these unique properties. Numerous issues, however, have been encountered that as yet inhibit it from achieving the speculatively prophesised potential in the commercial market.

### 2.4.2 Carbon Nanotubes

CNTs were first considered to be an exciting material in a paper published in 1991 by Iijima *et al*<sup>91</sup>, though their discovery pre-dates this to as early as 1952 by Radushkevich and

Luckyanovich<sup>92</sup>. They are known as a 1D material, showing an extreme AR, with radius often up to  $10^6$ , times smaller than their length. Structurally, they are described as a graphene sheet seamlessly rolled into a tube-like geometry and hence demonstrate many of the attractive properties of graphene. Figure 2.4a exhibits a planar graphene structure; carbon nanotubes rolled from this plane can be seen in Figure 2.4b. There are typically three types of single walled nanotubes defined by the appearance of bonds around the diameter, which correspond to the methods of manipulation in achieving a rolled graphene lattice from a single plane. These are armchair, zigzag and chiral. Armchair configurations are exclusively metallic, whilst zigzag and chiral can be metallic or semi-conductor like with a range in measured band gap depending on diameter, typically between 0 and 2 eV<sup>66</sup>. Characteristics such as high electrical conductivity<sup>52</sup>, quick response times<sup>45</sup>, low driving voltages<sup>93</sup>, and resilience to electromigration<sup>94</sup> have made them an important contender for the use in FE applications.

Single wall nanotubes, SWNTs, entail a single tube and can be open or capped at the tip depending on their means of manufacture. Multi-wall nanotubes, MWNTs, are defined by a number of tubes concentrically nested. As seen between layers of graphene in graphite, layers between graphene-like sheets in MWNTs are bound by weak Van der Waals forces. The diameter of SWNTs have been reported to range from  $\sim 0.4$  nm to  $> 3$  nm, and MWNTs from  $\sim 1.4$  nm to 100 nm at least<sup>66</sup>, variations of which are significantly influenced by fabrication method and particle size of metal catalysts from which they can be grown. Due to easier fabrication, in FE applications, MWNTs are more commonly utilised than SWNTs and are quasi-metallic (with band gap close to 0 eV<sup>95</sup>).

There is great diversity seen when evaluating the characteristics of CNTs, particularly MWNTs, apart from size and shape. The purity of nanotubes is chiefly governed by the amount of carbon to undesired materials present, and is significantly affected by synthesis and distribution. Disorder and crystallinity describe the fundamental structure of the CNT. Packing density, as well as length of CNTs, can be highly variable depending on fabrication conditions, and indeed intended output. The CNT cap, which can take a number of forms, can be influential in FE. When modelling their behaviour, CNTs are regularly represented by a cylinder with a hemispherical cap. Due to experimental variation a smooth, clean hemispherical cap is rarely fabricated, specifically in MWNTs. The tip may be tapered, flat, open or show protrusions. Deviation from a hemispherical shape, however, can lead to an increase in field enhancement factor and resultant higher current, up to ten times larger<sup>96,97</sup>.

## 2. Field Emission from Carbon Nanotubes

Defects can alter morphology and the function of CNTs, occurring through a variety of means and can have a pronounced effect on FE capabilities. Most commonly defects arise in the form of vacancies, interstitials (free atoms trapped in graphitic sheet layers), adatoms, and pentagon-hexagon pairs (Figure 2.4d). A pentagon-hexagon pair, whilst changing the physical shape and appearance of the CNT, maintains the connectivity of the  $sp^2$  hybrid lattice<sup>98</sup> and is of insignificant importance to FE, with little effect on emission performance. Other types of defect, however, can interrupt the lattice and have been implicated in affecting FE in a number of ways from encouraging contamination by foreign molecules<sup>99</sup> to additional emission centres<sup>100</sup>. Non- $sp^2$  defects, such as dangling bonds, adatoms, vacancies and interstitials can be formed in post-process treatments and where adsorption of non-carbon atoms has been seen, this has been implicated in causing hysteretic  $I$ - $V$  behaviour<sup>101</sup>. Defects can be deliberately induced by doping, where substitutional atoms are embedded in the lattice with the intent of changing the CNT properties. For example, doped N and B atoms have been shown to increase the chemical reactivity<sup>98</sup>, where this is a desired outcome.

Other 1D carbon forms, not strictly tubular, exist that are otherwise remarkably similar. A carbon nanotube is defined by a fully hollow core. A carbon nanofiber, CNF, exhibited in Figure 2.4c, on the other hand, has a solid centre but maintains many similarities to a CNT. Instead of a rolled cylindrical configuration, the graphene layers in CNFs can be stacked in vertical layers, herringbones or cups, and horizontal layers<sup>102</sup>. Analysis of the graphitic, G, band in Raman spectroscopy can reveal the difference in CNFs and CNTs, with CNFs showing higher defect densities<sup>103</sup> owing to the closer packaging of graphene sheets. CNTs are affected by Van der Waals forces more than CNFs due to the larger surface area to volume ratio. A higher stiffness than CNTs make CNFs robust against movement caused by local electric fields in FE. CNTs can bend in electric fields, due to torque induction caused by metallic catalyst, whereas CNFs have a higher stability.

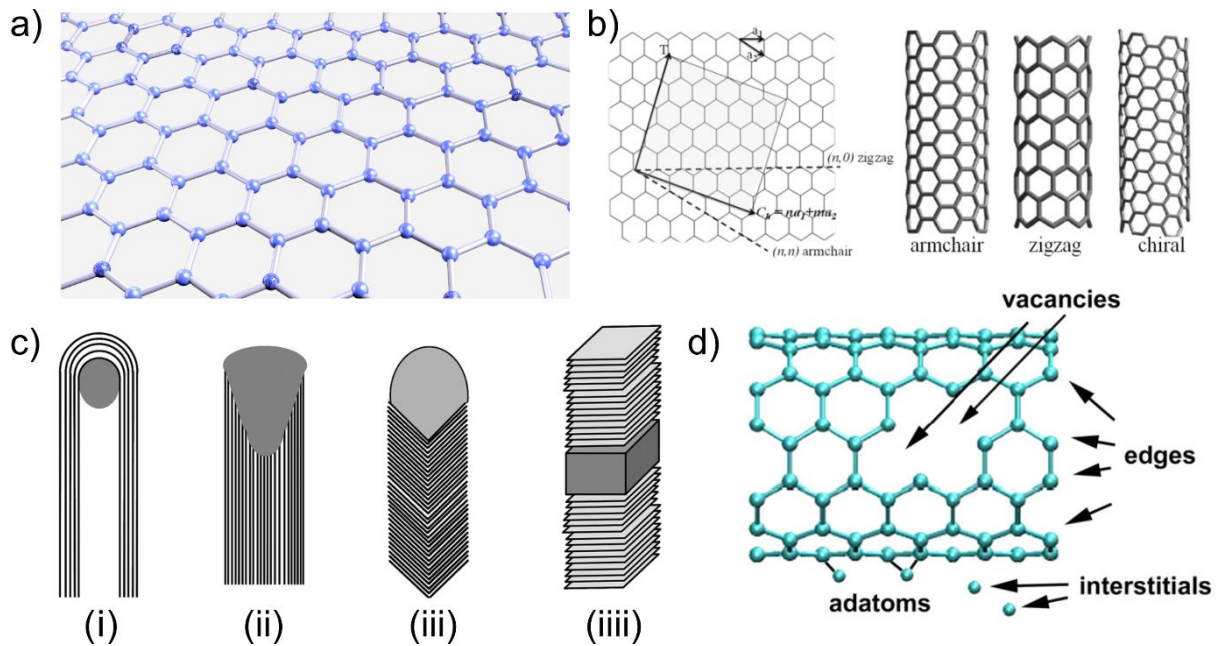


**Figure 2.4 | The Nanocarbons.** Structure of a) Graphene b) CNT configurations from a rolled graphene sheet<sup>104</sup> c) CVD grown carbon structures<sup>102</sup> i) multi-walled CNT (ii) carbon nanofiber ribbon (iii) fishbone carbon nanofiber (iiii) platelet carbon nanofiber d) common defects found in grown carbon nanotubes<sup>98</sup>.

## 2.5 Carbon Nanotube and Emitter Fabrication

CNTs are fabricated either by vaporisation methods, such as arc discharge or laser ablation, or by catalytic decomposition of hydrocarbons over metal catalysts<sup>96</sup> in a bottom-up process where materials are built from molecular components into more complex structures. A number of techniques can be used for the fabrication of CNTs, with difference in cost, process complexity, need for catalyst deposition, commercial availability, repeatability of CNT structure, and CNT alignment. Vaporisation methods, including electric arc discharge<sup>91</sup> and laser ablation<sup>105</sup> require high temperatures,  $> 3000$  °C, whereas catalytic decomposition methods can be performed at relatively lower temperatures.

The first process, by which they were discovered by Iijima *et al*, was arc discharge. Aggressive CNT degrading acids are used in purifying the CNTs grown by vaporisation methods, however. A typical yield<sup>106</sup> of  $\leq 10\%$  is seen using arc discharge, with the resulting materials requiring post growth processing. The purity of CNTs produced in laser ablation is high (up to 90% with additional treatments<sup>107</sup>), though many other by products are also made (such as fullerenes and amorphous carbon). Vaporisation fabricated CNT emitters can be realised through dispersion as a powder or in a solution. Drop, cast and spray techniques are quick and cost effective,

## 2. Field Emission from Carbon Nanotubes

requiring an easy to manipulate CNT ink. Many have chosen this method for this reason. Drawbacks, however, include poor performance in FE applications due to misalignment and non-uniformity in such deposited CNTs as well as instability of surfactants in a vacuum environment. Electrophoresis deposits ink in a more controlled manner via the motion of charged particles<sup>108</sup>, though issues with alignment and repeatability are still problems. Vacuum filtration<sup>109</sup> is cheap and easy, achieved by sieving and consequent rinsing of a CNT ink through an evacuated filter. CNTs are transferred to a substrate using heat (200 °C) with an applied pressure (2 kg over an area of 10 mm × 10 mm). Large area processing and the low cost of this technique make it popular. However, with all above methods, agglomeration of CNTs caused by Van der Waals forces, as well as random orientation of CNTs on the substrate, cause non-uniformity which leads to poor emission currents and problems with device repeatability.

Chemical vapour deposition, CVD, offers high repeatability and allows a degree of control over CNT length, diameter, alignment and growth position. Temperatures, often  $500\text{ °C} < T < 1200\text{ °C}$ , are required in the growth process, though the lowest recorded temperature is 320 °C<sup>110</sup>. Growth on catalyst sites is initiated using a hydrocarbon feedstock gas (often CH<sub>4</sub> or C<sub>2</sub>H<sub>2</sub>) and an amorphous carbon etchant gas (H<sub>2</sub> or NH<sub>3</sub>)<sup>109</sup>. Plasma enhanced chemical vapour deposition, PECVD, employs a plasma that enhances the catalyst and exhibits further alignment of the CNTs. Lower temperatures can be achieved with PECVD, giving rise to the potential for use on plastic substrates and future flexible devices, though this remains a challenge<sup>111-113</sup>. A key advantage of CVD growth mechanisms is that transition metal sputtered catalysts can be patterned using lithographic processes to give precise control over the location at which the CNTs are grown. This is highly desirable in the study of FE and has shown increased FE capabilities discussed in further detail in Section 2.7. In this work, CNTs are grown exclusively through CVD methods by the author since the equipment and growth methods were well established and the nature of alignment and patterning ability were superior relative to other methods of fabrication.

In a study by the author on the published works of CNT field emitters, it was found that most of the fabrication methods above had been used to grow CNTs for FE. Some studies, trying to maximise emission currents and minimise cost, implemented inexpensive deposition methods, such as screen printing of CNTs in a paste, followed occasionally by post processing such as plasma treatment<sup>114,115</sup>. Others focused on investigating the science of emission and have

attempted to reach high current densities and/or low turn on voltages often associated with CVD and well aligned CNTs using CVD techniques primarily.

## 2.6 Carbon Nanotube Field Emission Applications

Proposed applications of CNT FE include graphical displays<sup>96,116,117</sup>, travelling wave tubes<sup>118,119</sup>, microwave amplifiers<sup>53,120</sup>, electron microscopy<sup>121,122</sup>, parallel electron beam lithography<sup>96,123</sup>, and X-ray sources<sup>96,123-125</sup>. Essentially, any device where an electron beam is required, for example in surface science microscopy, or where TE is used, FE from CNTs can replace existing technologies. There are few suggestions of truly innovative uses, focussing mainly on replacing existing technologies. This has perhaps inhibited the penetration of CNT, and indeed FE, products into the commercial market. The first marketable device made with a CNT cathode was a field emission lamp<sup>96,126</sup>, which is still available today, employed in outdoor lighting and in agriculture, however, other energy saving technologies have dominated commercially. Historically, the most popular applications in research, because of the large potential markets, are field emission displays, FEDs, and X-ray sources.

### 2.6.1 Field Emission Displays

At the turn of 21<sup>st</sup> century, it seemed that FEDs held the key to the most promising future for CNT FE devices by replacing liquid crystal technologies, which in 1999 accounted for 75% of the flat panel display market<sup>7</sup>. An FED is made from a matrix of cathode ray tubes, each tube contributing to a single pixel. Electrons with high energy are projected towards a phosphor plate at the anode of the field emitter, where red green and blue sub-pixels can be individually addressed to generate any coloured image. Unlike liquid crystal technologies, each colour pixel can be individually addressed, saving up to 50% in energy consumption<sup>49</sup>. Other benefits include high brightness, wider viewing angle, high dynamic range and operating temperature. Spindt emitters with electron beam evaporated molybdenum cones were most commonly used in FEDs. Samsung were the first to create a sealed FED prototype made using a CNT paste in 1999<sup>127,128</sup>. Competition peaked between Samsung, Motorola and a number of Japanese companies in the late 1990s. However, mass production and efficiency issues of FEDs saw light emitting diode, LED, technologies develop to fill the gap in this market using a more effective, approach also addressing individual pixels. A number of other difficulties were hard to overcome including charging effect at the isolation spacers between anode and cathode, device outgassing, high costs of operation caused by the comparatively large required voltages,

## 2. Field Emission from Carbon Nanotubes

lack of emission uniformity and array fabrication yield as well as long term stability issues<sup>129,130</sup>. The success of LEDs meant that from 2010 onwards, there were far fewer publications on FEDs and the efforts of the competing companies had changed focus.

### 2.6.2 X-Ray Sources

X-rays were discovered in 1895 by Rontgen<sup>131</sup>. These electromagnetic waves can be used to generate an image that reveals the fine inner structure of an object by utilising differences seen in absorption and ionisation in materials with different chemistry. Dyke and Dolan<sup>17</sup>, in 1956, were the first to use FE as an X-ray source using linear tungsten pins to strike a copper target. The first X-ray system was made by Hoffmans<sup>132</sup> in 1896 and was used to image the human anatomy. The first field emission X-ray tube was invented in 1975 by Charbonnier *et al*<sup>133</sup>. An X-ray tube consists most basically of a cathode and anode in a vacuum tube. High energy electrons from the cathode hit the anode to generate X-rays. Where TE is used, other elements including beam focussing and cooling are often required. The ability to distinguish materials of varying density, invisible to the naked eye, has proven popular in medical applications from a very early stage in the identification of broken bones and foreign metals, bullets for example<sup>134</sup>, within the body. Further to this, they have proven invaluable to the security industry, with inspection technologies employed globally in airports and homeland security, as well as in industrial inspection.

X-rays are generated by bombarding a metal target with high energy electrons causing deep electronic shell displacement of the target atom. When the atom relaxes an X-ray is emitted, which is characteristic of the target material. Of the three electron emission methods, TE was the first to reach commercial availability in X-ray devices. It relies on heating of a filament, usually tungsten, giving free electrons enough energy to pass over the surface potential barrier at the metal-vacuum interface. High power consumption is required to resistively heat the filament to temperatures  $> 1000\text{ }^{\circ}\text{C}$ <sup>135</sup>. Due to high temperatures, the filament lifetime is limited and cumbersome, mandatory heating power supplies impose a size limitation. Typically, the lifetime of an X-ray tube in a conventional machine is less than a year<sup>135</sup>. Thermal instability due to increased atomic mobility at elevated temperatures allows for significant electro-migration. Emitted electrons have random energy distribution and direction. Despite focussing electrons in an electric field, beam intensity distribution remains non-Gaussian, which ultimately limits image resolution. As a result of the high temperature and power needs, only single pixel devices are used and are physically much larger than equivalent

FE devices. A slow temporal response, with switching times of 10 ms<sup>136</sup>, also results in motion blurring, reducing the image quality.

FE offers benefits over TE, by operating at room temperature and demonstrating fast switching times, down to nanoseconds<sup>137</sup>, with the potential for longer device lifetimes due to lower operating temperatures. Other benefits include: device miniaturisation, possibility of pulsed emission, the ability to be nano-engineered, control over the generated beam energy and direction, and negligible cathode sputtering. Cathode sputtering is a function of both the emitting material and operating temperature. Carbon has a low sputter cross-section, which is increased by heating, making FE, principally from CNTs and carbon materials, preferable to thermal emission. Carbon has also proven to have higher stability in non-ultra-high-vacuum, non-UHV, conditions compared with metallic alternatives<sup>138</sup>. Other materials, including zinc oxide, ZnO, nanowires<sup>139</sup>, silicon<sup>140</sup> and diamond<sup>141,142</sup> have also been utilised in the miniaturisation of X-ray sources, though CNTs are most prevalent.

CNT based cold cathodes have been fabricated and used in X-ray devices. Sugie *et al*<sup>138</sup> (2001) directly compared images taken with thermionic and field emission and found higher detail was available with CNT field emitter due to increased resolution. The focal spot size, determining spatial resolution, is partly influenced by the area of emitted electrons. The intensity of the X-rays is proportional to the electron beam current and the square of the acceleration voltage<sup>39</sup>. Focussing is required in TE because the filament is typically 2 mm in diameter and 10 mm long<sup>109</sup>, whereas, FE can be far more compact. Yue *et al*<sup>135</sup> (2002) built a SWNT emitter and took an X-ray image with an acceleration voltage of 14 kV, smaller than normally used in medical imaging (50 – 100 kV). Efforts to miniaturise X-ray tubes have been performed by Haga *et al*<sup>143</sup> (2004) and a digital X-ray tube by Kim *et al*<sup>144</sup> (2013). In 2016, Choi *et al*<sup>145</sup> developed a miniature device using a point contact CNT deposition method. A tungsten tip with 5 µm radius of curvature was dipped into CNT paste. The adhered CNTs were then deposited in dots by lowering the probe to the surface. Employed as an X-ray source, feature sizes of 2-3 µm were resolved.

Despite lack of widespread commercial availability, there are a number of specialised CNT X-ray based products in use. XinRay Systems have developed CNT X-ray machines with the specific purpose of diagnosing breast cancer and have recently branched into dentistry. A high resolution image is acquired by sequencing CNT X-ray pixels at a number of angles<sup>146,147</sup>.

## 2. Field Emission from Carbon Nanotubes

Miniature, micro-focused CNT X-ray sources have also been developed by NASA and Microwave Power Technology for use in mineralogical analyses of matter in space<sup>42</sup>.

### 2.6.3 Other Applications

Parallel electron beam lithography aims to speed up the currently used slow standard e-beam equipment eliminating the need to raster scan and pattern during writing. In research and development, electron beam lithography is a widely used tool that permits mask-less lithography directly writing a pattern from a computer generated file, allowing intricate details and easily manipulated patterns to be realised in an ad hoc fashion. However, a severe disadvantage is the slow exposure over large areas compared to photolithography. Parallelisation of the beam is one solution to increasing process speed. The feasibility of this has been tested by Chang *et al*<sup>148</sup> and Muray *et al*<sup>149</sup> with field emission behaviour investigated by Milne<sup>123</sup>.

Other electron beam instruments are potential applications of CNT FE. In scanning electron microscopy, SEM, and transmission electron microscopy, TEM, improvement of energy resolution can be achieved by utilising the lower energy spread offered with high resolutions owing to small emission area and reduced beam diameter. Additional advantages include decreased acquisition times and increased processing speeds<sup>96</sup>. In electron microscopes, field emission guns offer high brightness and longer lifetime to thermionic alternatives<sup>49</sup>.

In long-range telecommunications, microwave links are used. FE CNTs can provide the electron source in a travelling wave tube, TWT, which amplifies radio frequency signals in the microwave range. Current technologies are cumbersome, based on thermionic cathodes. FE offers lightweight and fast switching as well as miniaturisation that could be particularly beneficial in satellites given the significant weight savings, and therefore financial savings<sup>49,150</sup>.

## 2.7 Patterned Carbon Nanotube Field Emitter Devices

Through growing developments in precision engineered lithography, manipulation of surface emitter morphology has become increasingly popular. Patterning CNT cathodes is essential for device applications such as flat panel displays requiring defined pixels. In early years, patterned emitter fabrication was primarily through vaporisation methods, namely arc discharge and laser ablation, manipulated in a paste<sup>96</sup>. Wang *et al*<sup>116</sup> developed the first flat panel CNT FE display by etching a glass substrate, pressing a nanotube/epoxy solution into the etched grooves and polishing the surface to expose the microchannels. Deposition of CNTs in a paste or solution

presents limitations in precision over fine features. This led to an increase in the use of CVD methods, where higher precision can be achieved. Use of lithography to pattern CNT anodes was introduced, growing nanotubes only where metal catalysts are present on the substrate surface. Morphology of the emitter surface controls the local enhancement factor and screening effect around CNTs. A number of lithographic processes have been employed to pattern CNT growth regions including photo<sup>151</sup>/e-beam<sup>152</sup> lithography and shadow masking<sup>153</sup>. A great variety of geometries can be synthesised to achieve high performing field emitters that yield high currents at low electric field values.

An influential characteristic of nanomaterials on their commercial viability is the temporal stability of their emission current. Increased emission current can be seen by dramatic local field enhancement around the, sometimes, atomically sharp tips of 1D materials. Ideal surface morphology entails indistinguishable CNT structures; the ability to grow CNTs to an identical height and width as each of its neighbours, however, is not a simple, or indeed feasible, task. Even in the most controlled environmental growing conditions, statistical variability in the growth mechanisms of the nanomaterial results in CNT-to-CNT disparities. To date the very best uniformities of carbon nanofibers achieved is around 6.3 % variation in height and variation in tube diameter of 4.1 %<sup>154</sup>. Burn out is a phenomenon that occurs when a longer CNT than its surrounding neighbours dominates emission current, significantly contributing to FE until thermal degradation destroys it<sup>155</sup>. This is particularly problematic when CNTs are deposited using pastes where large height variations are manifested<sup>156</sup>. The maximum current density an individual CNT can reportedly accommodate prior to burn out has been stated<sup>157</sup> to be as high as 100, 000 A/cm<sup>2</sup>. The occurrence of burn out can be minimised by CVD fabrication, which gives relatively consistent CNT height compared to other methods, with variations of just a few percent seen<sup>154</sup>. Successful FE devices require burn out to be significantly minimised, if not totally eradicated, achieved through carefully controlled nano-engineering of emitter geometry.

A substantial number of publications describe the use of patterned nanotube structures. A few are named here though the list is by no means exhaustive. A significant discovery on the importance of vertical alignment of CNTs and consequent improvement on emission performance was realised, followed logically by further manipulation of emitter geometry. Before settling predominantly on growth of CNTs from sputtered catalysts in CVD, other techniques included that seen by Kind *et al*<sup>158</sup>, who stamped gel-like catalyst in predetermined areas using micro-contact printing. Bonard *et al*<sup>159</sup> in 2001, also used this method, professing

## 2. Field Emission from Carbon Nanotubes

catalyst control and subsequent control over CNT density. Early issues arose concerning adhesion. In 1999, Fan *et al*<sup>160</sup> used a combination of shadow masking and deposition of an Fe catalyst by electron beam evaporation to grow “towers” of carbon nanotubes in  $38\ \mu\text{m} \times 38\ \mu\text{m}$  blocks, 130  $\mu\text{m}$  tall. Further evidence of CNT patterning using shadow masking was seen in 2001, by Choi *et al*<sup>153</sup>. Circular deposition of the metal catalyst, with a diameter of 250  $\mu\text{m}$  and pitch of 750  $\mu\text{m}$ , was achieved, seen in Figure 2.5a. A current density of 397  $\text{mA}/\text{cm}^2$  at 4  $\text{V}/\mu\text{m}$  was recorded, and current saturation (Section 2.3.1) was observed above fields of 2  $\text{V}/\mu\text{m}$ . Sohn *et al*<sup>161</sup> chose a different technology and used an optical mask to expose selected areas of a photoresist to light before catalyst sputtering. The sputtered catalyst was subsequently removed in regions where the resist remained on the surface after optical exposure by ‘lift-off’. Figure 2.5b and c show the geometry, where  $30\ \mu\text{m} \times 30\ \mu\text{m}$  squares were attained. At 3  $\text{V}/\mu\text{m}$ , a maximum current density of 80  $\text{mA}/\text{cm}^2$  was measured. Optical masking can be advantageous over shadow masks in reducing edge blurring.

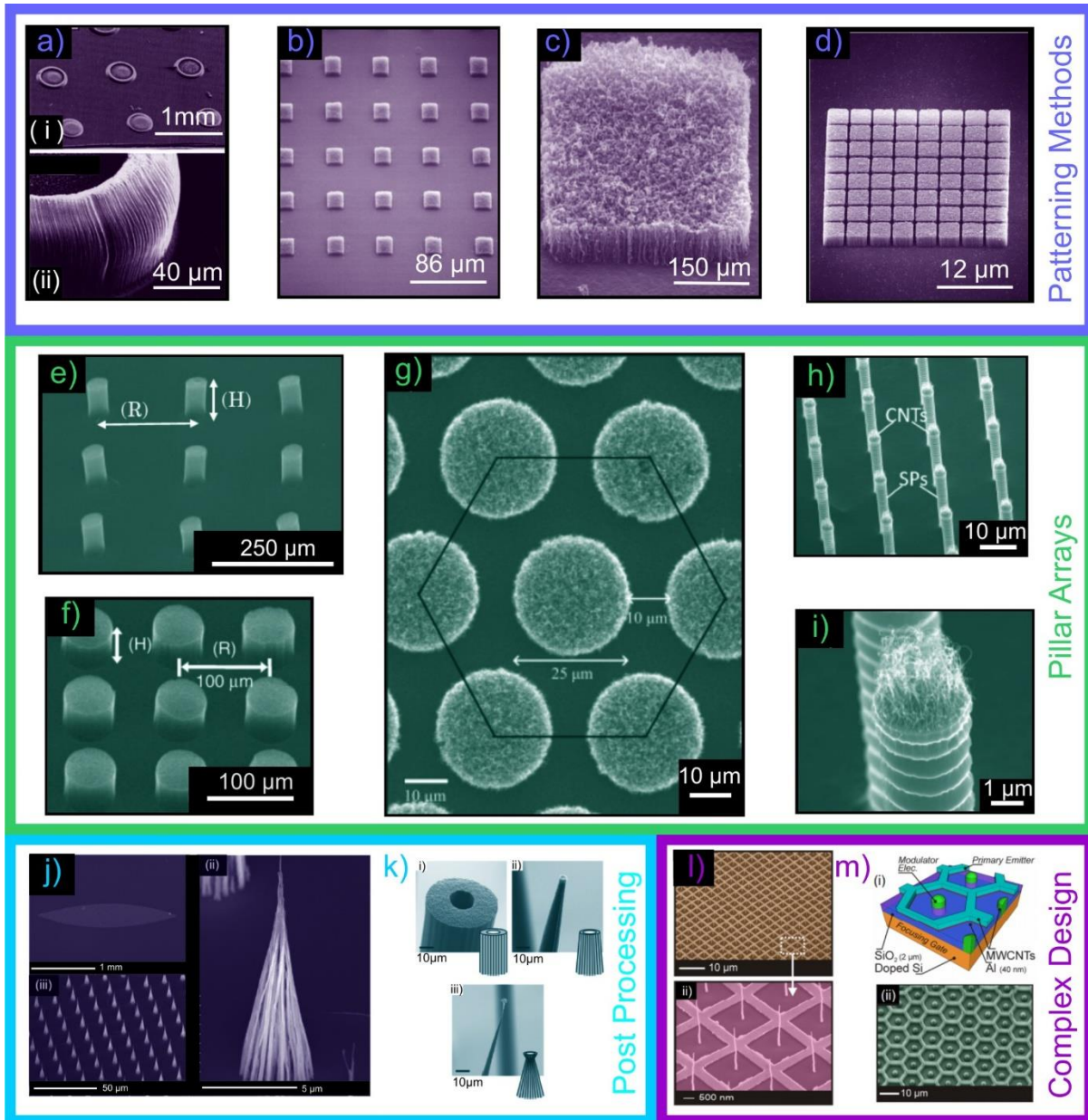


**Figure 2.5 | Emitter Patterning.** Early patterning of CNTs a) Choi et al<sup>153</sup> discs patterned using stainless steel mask b) Sohn et al<sup>161</sup> squares patterned using an optical mask c) closer view of optical mask patterned sample d) Sohn et al<sup>162</sup> laser patterned CNTs in grid of squares. CNT Pillar Arrays e) Katayama et al<sup>163</sup> optimal ratio between the height of the CNTs (H) and the pitch (R)  $R/H = 2$  f) Fujii et al<sup>164</sup>  $R/H = 6$  g) Chen et al<sup>165</sup> reduced pillar diameter of  $25\mu\text{m}$ , and pitch of  $10\mu\text{m}$  h) Li et al<sup>166</sup> silicon pillars, SP, with CNT on top i) single SP-CNT. CNT morphologies created using post process treatments j) Ryu et al<sup>167</sup> cone-shape CNTs fabricated by resist-assisted patterning process k) Aria et al<sup>168</sup> show i) untreated ii) moderate iii) heavy exposure of  $\text{O}_2$  plasma. Finally, complex emitter designs patterned using electron beam lithography l) Li et al<sup>155</sup> isolated single ballast CNT with square drain m) Cole et al<sup>169</sup> with hexagonal drain.

## 2. Field Emission from Carbon Nanotubes

As well as the ability to pattern, the growth methods have also developed with time. After initial studies, Sohn *et al*<sup>162</sup>, in 2002 used laser deposition to manipulate catalytic Fe before growth of CNTs in a  $25\ \mu\text{m} \times 25\ \mu\text{m}$  array, as seen in Figure 2.5d, in attempt to control both the pattern and ensure high degrees of vertical alignment of CNTs. The thickness of the Fe catalyst was varied, controlled by exposure time of a KrF laser with pulse energy of 300 mJ and a repetition rate of 10 Hz. This method offered good adhesion between the catalyst and Si substrate due to high kinetic energies of iron and was essential in determining the size of the catalyst nanoparticles from which the CNTs grew. The Van der Waals force has proven influential in attainment of vertical alignment, with high sensitivity to catalyst nanoparticle density. From nanoparticles of between 10 nm and 50 nm, well aligned CNTs were grown. In 2005, SiO<sub>2</sub> and Si substrates were etched to create patterned trenches from which CNT arrays were synthesised by Huh *et al*<sup>170</sup>. In 2015 this technique was still in use; Cui *et al*<sup>171</sup> directly patterned a silicon substrate by etching to create honeycomb structures.

Electrostatic screening between emitters comes into play when considering emission from an ensemble of close packed CNTs. With increasing packing density, the electric field at the CNT tips decreases. To study this, individual standing CNTs and arrays of CNT pillars became of much interest. De Heer *et al*<sup>172</sup>, in 1995 began aligning CNTs in a preferential direction by drawing a nanotube suspension through a filter. In 2001, Chhowalla *et al*<sup>173</sup> grew a number of different carbon nanotube samples with varying densities and heights, finding the less densely packed emitters to perform better as a result of the reduced screening effect. In 2002, Teo *et al*<sup>174</sup> compared field emission further testing different densities and finding that a sparse forest ( $10^7$  nanofibers/cm<sup>2</sup>) and an array of individual nanofibers spaced twice their height apart had a similar  $\beta$  as a result of a similar screening effect. These were generally grown from a photolithographically patterned catalyst followed by CVD. Figures 2.5e-i show examples of such arrays. In 2004, Katayama *et al*<sup>163</sup> found that the optimal ratio between the height of the CNTs,  $H$ , and the pitch,  $R$ , defined by centre-to-centre distance, was  $R/H = 2$ . Figure 2.5e shows the pillar diameter of  $50\ \mu\text{m}$  and a pitch of  $250\ \mu\text{m}$ . In the same year, with advances in precision and resolution of lithography, and progress in growth mechanisms, Milne *et al*<sup>53</sup> were able to grow individual CNF structures from a 100 nm dot of Ni catalyst (Seen in Figure 2.1f). However, studies on the more easily fabricated pillars continued to dominate research. The  $R/H$  ratio was scrutinised, with revisions resulting in  $R/H \approx 6$  by Fujii *et al*<sup>164</sup> in 2008, seen in Figure 2.5f. This was performed by the same research group as the previously discovered optimal value of 2. Pillar diameters of  $50\ \mu\text{m}$  were used again in these findings. Electron beam

lithography was used by Chen *et al*<sup>165</sup> in 2010 to further reduce the pillar dimensions to a diameter of 25  $\mu\text{m}$ , and pitch to 10  $\mu\text{m}$  as shown in Figure 2.5g. A hexagonal arrangement of the pillars has been further shown to decrease the screening effect compared to a square configuration by Harris *et al*<sup>175</sup> because of equal separation distances. In 2014, Cole *et al*<sup>125</sup> devised an experiment to assess the local field enhancement factor and how it was affected by electrostatic screening by growing individual 5  $\mu\text{m}$  tall nanotubes at intervals of 1, 2, 6, 8 and 10  $\mu\text{m}$ . Validation of the original findings, that the  $\beta$  ratio saturates when  $R/H = 2$ , was made. In 2015, Li *et al*<sup>166</sup> took the pillar arrays a step further in attempt to reduce the screening effect by growing CNTs on top of silicon pillars. The silicon pillars, seen in Figure 2.5h, have a diameter of 3  $\mu\text{m}$  and are spaced at 15  $\mu\text{m}$  intervals. High current densities of over 1.65  $\text{A}/\text{cm}^2$  at a field of 5.8  $\text{V}/\mu\text{m}$  were recorded in this way.

Further manipulation of emitter morphology has been undertaken in the quest for ever higher performance. A number of post growth treatments of emitters have been considered that attempt to further improve the measured FE by addressing issues including simplicity of manufacturing and increasing defect site numbers to promote emission. Ryu *et al*<sup>167</sup> grew and patterned arrays in a cone-like formation, shown in Figure 2.5j. A resist-assisted patterning process, designed to grow CNTs without a diffusion barrier metal, along with a hydrofluoric acid treatment was implemented, producing 3  $\mu\text{m}$  cone shape islands of CNTs with a pitch of 15  $\mu\text{m}$ . A low turn on field of 3  $\text{V}/\mu\text{m}$  was found for an emission current of 0.1  $\text{mA}/\text{cm}^2$ . The central thesis behind the study was to aid manufacturability by simplification of the growth process. However, the process required the use of hydrofluoric acid which is a dangerous substance to handle and thus limits the viability of this approach.

Another approach utilising complex emitter geometry was presented by Li *et al*<sup>155</sup> (2012) in an attempt to reduce the effect of burn out. Shown in Figure 2.5i, an isolated single ballasted CNT emitter is surrounded by a square CNT drain electrode with a pitch of  $2.5 \mu\text{m} \times 2.5 \mu\text{m}$  and a width of 0.5  $\mu\text{m}$ , this precision was achieved with electron beam lithography. The individual current contributions of CNTs is decreased through the integration of a ballast resistance (the upper most Si layer), which is in series with individual CNT emitters. This results in reduced local electric field in proportion to the current emitted. Cole *et al*<sup>169</sup> modified the square electrode array to a hexagonal variation to improve the current, which is attributed to a higher enhanced local electric field created using this edge morphology. They also changed the central singular CNT to a controlled diameter pillar. Hexagonal, honeycomb, emitters have shown

## 2. Field Emission from Carbon Nanotubes

greater current densities than the square or circular pillar variations as shown by Liu *et al*<sup>176</sup>. Figure 2.5m shows a schematic of this array and an SEM micrograph.

Post process plasma treatments can be used to enhance the field emitting capabilities of a material by changing its structure. These produce an increased number of locations from where the electrons can be emitted by increasing the atomic defect density. This is particularly successful in graphitic carbon allotropes. Chau *et al*<sup>177</sup> attribute the increased FE from tetrahedral amorphous carbon, *ta*-C to the lowering of the work function produced by use of a hydrogen microwave plasma. Other benefits including sharpening of edges<sup>178</sup> and removal of particles in a cleaning process<sup>179,180</sup>. Aria *et al*<sup>168</sup> have shown that morphology manipulations by densification of CNTs can be also be achieved through use of an oxygen plasma. Figure 2.5k shows the resulting geometry, although emission was not measured in this case. Further specifics associated with the effects of plasma operating conditions on FE was investigated by the author using existing data on the topic. Four main categories were investigated consisting of material (CNT, graphene or CNF), plasma operating power, plasma precursor gas and exposure time of the material to the plasma. The most significant enhancements to the emitted current density and operating fields, found from a total of 22 papers<sup>114,178-198</sup>, were found with a pre-cursor gas of nitrogen on a graphene emitter using a plasma power of < 200 W, exposed for 1 - 3 minutes. A general trend of increased FE performance with plasma treatment was seen with an average 20% reduction in turn on electric field (to achieve a measured current density of 0.01 mA/cm<sup>2</sup>) using plasma treatments. This work is published in <sup>199</sup>.

In an ideal emitter, all CNTs have the same height and diameter, and equal spacing, emitting a relatively small, similar current to one another, prolonging lifetime and averaging current fluctuations<sup>96</sup>. Despite fruitful and thorough investigations, some major drawbacks inhibit FE from CNTs becoming truly viable for use in applications. Without considering influential factors such as cost and manufacturability, most prominent is the vast continuous nature of grown CNTs and the effects on current and stability, the control over both of which remains a challenge. Efforts to overcome drawbacks have primarily focussed on patterning in a number of unique ways, though a widely accepted high performance emitter geometry remains absent. With questions still to answer on the true effect of emitter morphology and the direct influence of patterning and dimensions, there remains a gap in current research; issues on which this thesis focusses.

## 2.8 Summary

In this chapter, a review of the literature concerning field emission, carbon nanotubes and the history and complications of field emission from carbon nanotubes has been presented, with a review of possible applications. It is evident that the physics underpinning the emission process in nanomaterials differs somewhat to that of bulk metallic emitters and that many have tried to explain this deviation. Concurrently, advances in deposition techniques and photolithographical precision have seen increases in emitted current density and lower turn on voltages from carbon nanotubes. There is still, however, significant improvements to be made and further processes to be fully understood.

## References

- 1 Wong, T.-H. Nanosecond laser pulse-induced electron emission from multiwall carbon nanotube film. *Nanotechnology* **18**, 135705 (2007).
- 2 Li, C. Edge effect enhanced photo-thermionic emission from a carbon nanotubes array. *Applied physics letters* **110**, 093105 (2017).
- 3 Liang, S.-D. *Quantum Tunneling and Field Electron Emission Theories*. (World Scientific Publishing Co. Pte. Ltd., 2014).
- 4 Stratton, R. Theory of Field Emission from Semiconductors. *Physical review* **125**, 67-82 (1962).
- 5 Fowler, R. H. Electron Emission in Intense Electric Fields. *Proceedings of the Royal Society. A, Mathematical, physical, and engineering sciences* **119**, 173-181 (1928).
- 6 Spindt, C. A. A Thin-Film Field-Emission Cathode. *Journal of Applied Physics* **39**, 3504-3505, (1968).
- 7 Talin, A. A., Dean, K. A. & Jaskie, J. E. Field emission displays: a critical review. *Solid-State Electronics* **45**, 963-976, (2001).
- 8 Eichmeier, J. A. & Thumm, M. *Vacuum electronics: components and devices*. (Springer Science & Business Media, 2008).
- 9 Winkler, J. H. *Gedanken von den Eigenschaften, Wirkungen und Ursachen der Electricität: nebst einer Beschreibung zweo neuer electrischen Maschinen*. (In Verlag Bernhard Christoph Breitkopfs, 1744).
- 10 Thomson, J. J. XL. *The London, Edinburgh and Dublin philosophical magazine and journal of science* **44**, 293-316 (1897).
- 11 Casimir, H. B. G. The historical development of quantum theory. *Contemporary physics* **24**, 631-634 (1983).
- 12 Millikan, R. A. & Lauritsen, C. C. Dependence of electron emission from metals upon field strengths and temperatures. *Physical Review* **33**, 0598-0604, (1929).
- 13 Gossling, B. S. The emission of electrons under the influence of intense electric fields. *Philosophical Magazine* **1**, 609-635 (1926).
- 14 Oppenheimer, J. R. On the quantum theory of the capture of electrons. *Physical Review* **31**, 0349-0356, (1928).
- 15 Müller, E. W. Elektronenmikroskopische Beobachtungen von Feldkathoden. *Zeitschrift für Physik* **106**, 541-550 (1937).
- 16 Good Jr, R. H. & Müller, E. W. in *Electron-Emission Gas Discharges I* 176-231 (Springer, 1956).
- 17 Dyke, W. & Dolan, W. Field emission. *Advances in electronics and electron physics* **8**, 89-185 (1956).
- 18 Charbonnier, F. M. Basic and applied studies of field emission at microwave frequencies. *Proceedings of the IEEE* **51**, 991-1004 (1963).
- 19 Latham, R. V. The development of a high-definition cathode-ray tube using a carbon-fibre field-emission electron source. *Journal of physics. E, Scientific instruments* **15**, 1083-1092 (1982).
- 20 Crewe, A. V. A High-Resolution Scanning Transmission Electron Microscope. *Journal of applied physics* **39**, 5861-5868 (1968).
- 21 Crewe, A. V. Electron Gun Using a Field Emission Source. *Review of scientific instruments* **39**, 576-583 (1968).

## 2. Field Emission from Carbon Nanotubes

- 22 Dyke, W. P. & Grundhauser, F. J. X-ray tube having field emission cathode and evaporative anode in combination with electrical pulser means. (1967).
- 23 Denley, O. W. (Google Patents, US, 1970).
- 24 Nakamoto, M. & Moon, J. Stable, ruggedized, and nanometer-order size transfer mold field emitter array in harsh oxygen radical environment. *Journal of vacuum science and technology. B, Nanotechnology & microelectronics* **33**, 03C107 (2015).
- 25 Barasch, E. F. *et al.* Gated field-emitter cathodes for high-power microwave applications. *Cover Layout: Linda Blimkie Data Base: Fred P. Adams, John Hulbert Photographs: Javid Sheikh, with contributions from Blair Smith True Tran-Ngoc*, 519 (1992).
- 26 Song, X., Zhao, C. X., Wu, J. Q., Chen, J. & Ieee. in *25th International Vacuum Nanoelectronics Conference (IVNC)*. 376-377 (2012).
- 27 Wang, J. *et al.* Controlled growth of nickel nanocrystal arrays and their field electron emission performance enhancement via removing adsorbed gas molecules. *Crystengcomm* **15**, 1296-1306, (2013).
- 28 Le Shim, E. *et al.* in *25th International Vacuum Nanoelectronics Conference (IVNC)*. 198-199 (2012).
- 29 Joo, S. W. & Banerjee, A. N. Field emission characterization of vertically oriented uniformly grown nickel nanorod arrays on metal-coated silicon substrate. *Journal of Applied Physics* **107**, (2010).
- 30 Gunther, B. *et al.* Uniformity and stability of field emission from bare and metal coated Si tip arrays. *Journal of Vacuum Science & Technology B* **21**, 427-432 (2003).
- 31 Ng, K. L., Yuan, J., Cheung, J. T. & Cheah, K. W. Electron field emission characteristics of electrochemical etched Si tip array. *Solid State Communications* **123**, 205-207, (2002).
- 32 Sharma, R. B., Pal, S. & Joag, D. S. Field electron emission from GaN/W tips. *Materials Science and Engineering B-Advanced Functional Solid-State Materials* **168**, 36-39 (2010).
- 33 Shih, C. F., Chen, N. C., Chang, P. H. & Liu, K. S. Field emission properties of self-assembled InN nanostructures: Effect of Ga incorporation. *Journal of Crystal Growth* **281**, 328-333, (2005).
- 34 Ooi, N. & Adams, J. B. Ab initio studies of the cubic boron nitride surface. *Surface Science* **574**, 269-286 (2005).
- 35 Chalamala, B. R., Wallace, R. M. & Gnade, B. E. Poisoning of Spindt-type molybdenum field emitter arrays by CO<sub>2</sub>. *Journal of Vacuum Science & Technology B* **16**, 2866-2870, (1998).
- 36 Xie, C. G. & Dworsky, L. Rate equation of current degradation of the spindt-type field emitter array. *Ieee Transactions on Electron Devices* **51**, 644-647, (2004).
- 37 Cochran, J. K. Low-voltage field emission from tungsten fiber arrays in a stabilized zirconia matrix. *Journal of materials research* **2**, 322-328 (1987).
- 38 Phillips, P. M., Spindt, C. A., Holland, C. E., Schwoebel, P. R. & Brodie, I. in *4th International Conference on Millimeter and Submillimeter Waves and Applications*. 90-97 (1998).
- 39 Saitō, Y. *Carbon nanotube and related field emitters : fundamentals and applications*. (Wiley-VCH, 2010).
- 40 Graefelfing, H. H., Bittorf, H. & Veith, W. Flat Color TV tube. (Filed in 1968, Published 16 November 1971).
- 41 Qian, X. *et al.* High resolution stationary digital breast tomosynthesis using distributed carbon nanotube x-ray source array. *Medical Physics* **39**, 2090-2099, (2012).
- 42 Sarrazin, P. *et al.* Carbon-nanotube field emission X-ray tube for space exploration XRD/XRF instrument. *Adv X Ray Anal* **47**, 232-239 (2004).
- 43 Gamo, H. *et al.* Field Emission Current Uniformity and Stability of Well-Aligned Carbon Nanotubes Synthesized in Methanol. *Japanese Journal of Applied Physics* **47**, 6606-6609 (2008).
- 44 Zou, R. J. *et al.* Carbon Nanotubes as Field Emitter. *Journal of Nanoscience and Nanotechnology* **10**, 7876-7896 (2010).
- 45 Lei, W. *et al.* High-current field-emission of carbon nanotubes and its application as a fast-imaging X-ray source. *Carbon* **94**, 687-693 (2015).
- 46 Jeong, J.-W. A digital miniature x-ray tube with a high-density triode carbon nanotube field emitter. *Applied physics letters* **102**, 023504 (2013).
- 47 Wang, X. Fabrication of Ultralong and Electrically Uniform Single-Walled Carbon Nanotubes on Clean Substrates. *Nano letters* **9**, 3137-3141 (2009).
- 48 Bin, Y. Development of Highly Oriented Polyethylene Filled with Aligned Carbon Nanotubes by Gelation/Crystallization from Solutions. *Macromolecules* **36**, 6213-6219 (2003).
- 49 Li, Y. H., Sun, Y. H. & Yeow, J. T. W. Nanotube field electron emission: principles, development, and applications. *Nanotechnology* **26**, (2015).
- 50 Rinzler, A. G. *et al.* Unraveling nanotubes - field-emission from an atomic wire *Science* **269**, 1550-1553, (1995).

- 51 Chernozatonskii, L. A. Electron field emission from nanofilament carbon films. *Chemical physics letters* **233**, 63-68 (1995).
- 52 Milne, W. I. Carbon nanotubes as field emission sources. *Journal of materials chemistry* **14**, 933 (2004).
- 53 [Image] Milne, W. I. *et al.* Carbon nanotubes as field emission sources. *Journal of Materials Chemistry* **14**, 933-943 (2004).
- 54 [Image] Bonard, J. M., Salvetat, J. P., Stockli, T., Forro, L. & Chatelain, A. Field emission from carbon nanotubes: perspectives for applications and clues to the emission mechanism. *Applied Physics a-Materials Science & Processing* **69**, 245-254 (1999).
- 55 [Image] Uh, H. S. & Park, S. Improved field emission properties from carbon nanotubes grown onto micron-sized arrayed silicon pillars with pyramidal bases. *Diamond and Related Materials* **54**, 74-78, (2015).
- 56 Cutler, P. H. *et al.* Theory Of Electron-Emission in High Fields from Atomically Sharp Emitters - Validity of the Fowler Nordheim Equation. *Progress in Surface Science* **42**, 169-185 (1993).
- 57 Yang, Y. H., Wang, C. X., Wang, B., Xu, N. S. & Yang, G. W. ZnO nanowire and amorphous diamond nanocomposites and field emission enhancement. *Chemical Physics Letters* **403**, 248-251, (2005).
- 58 Kan, M.-C., Huang, J.-L., Sung, J. C., Chen, K.-H. & Yau, B.-S. Thermionic emission of amorphous diamond and field emission of carbon nanotubes. *Carbon* **41**, 2839-2845, (2003).
- 59 Cui, Y. *et al.* Stable field emission lamps based on well-aligned BaO nanowires. *Rsc Advances* **4**, (2014).
- 60 Menaka, Patra, R., Ghosh, S. & Ganguli, A. K. Manipulating the anisotropy and field emission of lanthanum hexaboride nanorods. *Rsc Advances* **2**, 7875-7885, (2012).
- 61 Robertson, J. Mechanisms of electron field emission from diamond, diamond-like carbon, and nanostructured carbon. *Journal of Vacuum Science & Technology B* **17**, 659-665,
- 62 Yan, H. *et al.* Synthesis, property and field-emission behaviour of amorphous polypyrrole nanowires. *Nanotechnology* **17**, 3446-3450, doi:10.1088/0957-4484/17/14/017 (2006).
- 63 Forbes, R. G., Fischer, A. & Mousa, M. S. Improved approach to Fowler-Nordheim plot analysis. *Journal of Vacuum Science & Technology B* **31**, (2013).
- 64 Bonard, J.-M. Field-Emission-Induced Luminescence from Carbon Nanotubes. *Physical review letters* **81**, 1441-1444 (1998).
- 65 Bonard, J.-M., Kind, H., Stöckli, T. & Nilsson, L.-O. Field emission from carbon nanotubes: the first five years. *Solid-State Electronics* **45**, 893-914, (2001).
- 66 Baughman, R. H., Zakhidov, A. A. & de Heer, W. A. Carbon nanotubes - the route toward applications. *Science* **297**, 787-792 (2002).
- 67 Bonard, J. M. *et al.* Field emission properties of multiwalled carbon nanotubes. *Ultramicroscopy* **73**, 7-15, (1998).
- 68 Kan, M. C., Huang, J. L., Sung, J. & Chen, K. H. Thermally activated electron emission from nano-tips of amorphous diamond and carbon nano-tubes. *Thin Solid Films* **447**, 187-191, (2004).
- 69 Liang, S.-D. & Chen, L. Theories of field and thermionic electron emissions from carbon nanotubes. *Journal of Vacuum Science & Technology B* **28**, C2A50-C52A57, (2010).
- 70 Fursey, G. N. & Glazanov, D. V. Deviations from the Fowler-Nordheim theory and peculiarities of field electron emission from small-scale objects. *Journal of Vacuum Science & Technology B* **16**, 910-915, (1998).
- 71 Cutler, P. H., He, J., Miskovsky, N. M., Sullivan, T. E. & Weiss, B. Theory of electron-emission in high fields from atomically sharp emitters - validity of the Fowler-Nordheim equation. *Journal of Vacuum Science & Technology B* **11**, 387-391, (1993).
- 72 Peng, J. *et al.* The roles of apex dipoles and field penetration in the physics of charged, field emitting, single-walled carbon nanotubes. *Journal of Applied Physics* **104**, (2008).
- 73 Chen, C. W., Lee, M. H. & Clark, S. J. Field penetration induced charge redistribution effects on the field emission properties of carbon nanotubes - a first-principle study. *Applied Surface Science* **228**, 143-150, (2004).
- 74 Zheng, X. Quantum-Mechanical Investigation of Field-Emission Mechanism of a Micrometer-Long Single-Walled Carbon Nanotube. *Physical review letters* **92**, 106803 (2004).
- 75 Filip, V., Nicolaescu, D., Tanemura, M. & Okuyama, F. Influence of the electronic structure on the field electron emission from carbon nanotubes. *Journal of Vacuum Science & Technology B* **21**, 382-390, (2003).
- 76 Pandey, S. *et al.* Improved electron field emission from morphologically disordered monolayer graphene. *Applied Physics Letters* **100**, (2012).
- 77 Palnitkar, U. A. *et al.* Remarkably low turn-on field emission in undoped, nitrogen-doped, and boron-doped graphene. *Applied Physics Letters* **97**, (2010).
- 78 Zhai, T. *et al.* Characterization, Cathodoluminescence, and Field-Emission Properties of Morphology-Tunable CdS Micro/Nanostructures. *Advanced Functional Materials* **19**, 2423-2430, (2009).

## 2. Field Emission from Carbon Nanotubes

- 79 Fang, X. *et al.* Ultrathin ZnS nanobelts as field emitters. *Advanced Materials* **19**, 2593, (2007).
- 80 Xu, J. *et al.* Fabrication of vertically aligned single-crystalline lanthanum hexaboride nanowire arrays and investigation of their field emission. *Npg Asia Materials* **5**, (2013).
- 81 Bonard, J. M. Field emission from carbon nanotubes: perspectives for applications and clues to the emission mechanism. *Applied physics. A, Materials science & processing* **69**, 245-254, (1999).
- 82 Purcell, S. T. 64 meV measured energy dispersion from cold field emission nanotips. *Applied physics letters* **67**, 436-438 (1995).
- 83 Ago, H. Work Functions and Surface Functional Groups of Multiwall Carbon Nanotubes. *The journal of physical chemistry. B* **103**, 8116-8121 (1999).
- 84 Wallace, P. R. The Band Theory of Graphite. *Physical review* **71**, 622-634 (1947).
- 85 [Webpage] *The 2010 Nobel Prize in Physics - Press Release*,  
<[https://www.nobelprize.org/nobel\\_prizes/physics/laureates/2010/press.html](https://www.nobelprize.org/nobel_prizes/physics/laureates/2010/press.html)> (2010).
- 86 Wang, D. W. *et al.* Fabrication of Graphene/Polyaniline Composite Paper via In Situ Anodic Electropolymerization for High-Performance Flexible Electrode. *Acs Nano* **3**, 1745-1752, (2009).
- 87 Novoselov, K. S. *et al.* Two-dimensional gas of massless Dirac fermions in graphene. *Nature* **438**, 197-200, (2005).
- 88 Stankovich, S. *et al.* Graphene-based composite materials. *Nature* **442**, 282-286, (2006).
- 89 Geim, A. K. Graphene: Status and Prospects. *Science* **324**, 1530-1534, (2009).
- 90 Balandin, A. A. Thermal properties of graphene and nanostructured carbon materials. *Nature materials* **10**, 569-581 (2011).
- 91 Iijima, S. Helical Microtubules Of Graphitic Carbon. *Nature* **354**, 56-58, doi:10.1038/354056a0 (1991).
- 92 Lukyanovich, V. M. & Radushkevich, L. V. Elektronno-Mikroskopicheskoe Issledovanie Formy Perekhodnykh Por Aktivnykh Uglei Iz Sakhara. *Doklady Akademii Nauk Sssr* **91**, 585-587 (1953).
- 93 De, H. A carbon nanotube field-emission electron source. *Science (New York, N.Y.)* **270**, 1179 (1995).
- 94 Teo, K. B. K. Microwave devices: Carbon nanotubes as cold cathodes. *Nature (London)* **437**, 968-968 (2005).
- 95 Chang, S.-W. A Comparison of Photocurrent Mechanisms in Quasi-Metallic and Semiconducting Carbon Nanotube pn-Junctions. *ACS nano* **9**, 11551-11556 (2015).
- 96 de Jonge, N. & Bonard, J. M. Carbon nanotube electron sources and applications. *Philosophical Transactions of the Royal Society a-Mathematical Physical and Engineering Sciences* **362**, 2239-2266, (2004).
- 97 Gomer, R. *Field Emission and Field Ionisation*. 53 (Harvard University Press, 1961).
- 98 Lehman, J. H. Evaluating the characteristics of multiwall carbon nanotubes. *Carbon (New York)* **49**, 2581-2602 (2011).
- 99 Mawhinney, D. B. Surface defect site density on single walled carbon nanotubes by titration. *Chemical physics letters* **324**, 213-216 (2000).
- 100 Hazra, K. S. Improved field emission from multiwall carbon nanotubes with nano-size defects produced by ultra-low energy ion bombardment. *Carbon (New York)* **49**, 4760-4766 (2011).
- 101 Chun, L. *et al.* Effect of adsorbates on field emission from flame-synthesized carbon nanotubes. *Journal of Physics D: Applied Physics* **41**, 195401 (2008).
- 102 [Image] Serp, P. & Machado, B. Carbon (Nano)materials for Catalysis. *RSC Catalysis Series* **253**, 337-358 (2015).
- 103 Aggarwal, G., Mishra, P., Joshi, B. & Islam, S. S. Thermal carbonization of nanoporous silicon: Formation of carbon nanofibres without a metal catalyst. *Pramana-Journal of Physics* **83**, 427-434, (2014).
- 104 [Image] Choudhary, V. & Gupta, A. in *Carbon Nanotubes - Polymer Nanocomposites* Ch. 0 (InTech, 2011).
- 105 Journet, C. *et al.* Large-scale production of single-walled carbon nanotubes by the electric-arc technique. *Nature* **388**, 756-758 (1997).
- 106 Raniszewski, G. Influence of Plasma Jet Temperature Profiles in Arc Discharge Methods of Carbon Nanotubes Synthesis. *Nanomaterials (Basel, Switzerland)* **7**, 50 (2017).
- 107 Bandow, S. Purification and magnetic properties of carbon nanotubes. *Applied physics. A, Materials science & processing* **67**, 23-27 (1998).
- 108 Boccaccini, A. R. Electrophoretic deposition of carbon nanotubes. *Carbon (New York)* **44**, 3149-3160, (2006).
- 109 Parmee, R., Collins, C., Milne, W. & Cole, M. X-ray generation using carbon nanotubes. *Nano Convergence* **2**, 1 (2015).
- 110 Chen, J. S., Stolojan, V. & Silva, S. R. P. Towards type-selective carbon nanotube growth at low substrate temperature via photo-thermal chemical vapour deposition. *Carbon* **84**, 409-418, (2015).

- 111 Boskovic, B. O. *et al.* Low temperature synthesis of carbon nanofibres on carbon fibre matrices. *Carbon* **43**, 2643-2648, (2005).
- 112 Cole, M. *et al.* Dry-Transfer of Aligned Multiwalled Carbon Nanotubes for Flexible Transparent Thin Films. *Journal of Nanomaterials* **3**, (2012).
- 113 Sun, X. Y. & Sun, Y. G. Single-walled carbon nanotubes for flexible electronics and sensors. *Journal of Materials Science & Technology* **24**, 569-577 (2008).
- 114 Yu, J., Chen, J., Deng, S. Z., She, J. C. & Xu, N. S. Post-treatment of screen-printed carbon nanotube emitter by selective plasma etching. *Journal of Vacuum Science & Technology B* **25**, 552-556, (2007).
- 115 Qin, Y. & Hu, M. Effects of microwave plasma treatment on the field emission properties of printed carbon nanotubes/Ag nano-particles films. *Applied Surface Science* **254**, 1757-1762, (2008).
- 116 Wang, Q. H. *et al.* A nanotube-based field-emission flat panel display. *Applied Physics Letters* **72**, 2912-2913, (1998).
- 117 Lei, W. *et al.* A graphene-based large area surface-conduction electron emission display. *Carbon* **56**, 255-263, (2013).
- 118 Jensen, K. L. Field emitter arrays for plasma and microwave source applications. *Physics of Plasmas* **6**, 2241-2253 (1999).
- 119 Whaley, D. R., Gannon, B. M., Smith, C. R., Armstrong, C. M. & Spindt, C. A. Application of field emitter arrays to microwave power amplifiers. *Ieee Transactions on Plasma Science* **28**, 727-747 (2000).
- 120 Temple, D. Recent progress in field emitter array development for high performance applications. *Materials Science & Engineering R-Reports* **24**, 185-239, (1999).
- 121 Bauer, E. Low-energy-electron microscopy. *Reports on Progress in Physics* **57**, 895-938, (1994).
- 122 Pawley, J. The development of field-emission scanning electron microscopy for imaging biological surfaces. *Scanning* **19**, 324-336 (1997).
- 123 Milne, W. I. *et al.* Investigating carbon materials for use as the electron emission source in a parallel electron-beam lithography system. *Current Applied Physics* **1**, 317-320, (2001).
- 124 Xia, Y. N. *et al.* One-dimensional nanostructures: Synthesis, characterization, and applications. *Advanced Materials* **15**, 353-389, (2003).
- 125 Cole, M. T. *et al.* Deterministic Cold Cathode Electron Emission from Carbon Nanofibre Arrays. *Scientific Reports* **4**, (2014).
- 126 Saito, Y. Field emission from carbon nanotubes and its application to electron sources. *Carbon (New York)* **38**, 169-182 (2000).
- 127 Choi, W. B. *et al.* Fully sealed, high-brightness carbon-nanotube field-emission display. *Applied Physics Letters* **75**, 3129-3131, (1999).
- 128 Lee, N. S. Application of carbon nanotubes to field emission displays. *Diamond and related materials* **10**, 265-270 (2001).
- 129 Hunt, C. & Chakhovskoi, A. Phosphor Challenge for Field-Emission Flat-Panel Displays. *Journal of Vacuum Science & Technology B* **15**, 516-519 (1997).
- 130 Fan, Y. C. & Rose, M. Field Emission Displays (FEDs). *Handbook of Visual Display Technology, Vols 1-4*, 1071-1104, (2012).
- 131 Rontgen, W. C. On a new kind of rays. *Science (New York, N.Y.)* **3**, 227-231, (1896).
- 132 Hoffmans, H. J. *Proefnemingen met de Röntgen'sche stralen in het laboratorium der Hoogere Burgerschool te Maastricht*. Vol. 1 (Leiter-Nypels, 1896).
- 133 Charbonnier, F. M., Barbour, J. P. & Dyke, W. P. Resolution of field-emission x-ray sources. *Radiology* **117**, 165-172 (1975).
- 134 Slack, C. M. Field Emission X-Ray Tube. *Journal of applied physics* **12**, 165-168 (1941).
- 135 Yue, G. *et al.* Generation of continuous and pulsed diagnostic imaging x-ray radiation using a carbon-nanotube-based field-emission cathode. *Applied Physics Letters* **81**, 355-357, (2002).
- 136 Zhang, J. A nanotube-based field emission x-ray source for microcomputed tomography. *Review of scientific instruments* **76**, 094301 (2005).
- 137 Cheng, Y. Dynamic radiography using a carbon-nanotube-based field-emission x-ray source. *Review of scientific instruments* **75**, 3264-3267 (2004).
- 138 Sugie, H. *et al.* Carbon nanotubes as electron source in an x-ray tube. *Applied Physics Letters* **78**, 2578-2580, (2001).
- 139 Ooki, S. *et al.* X-ray source with cold emitter fabricated using ZnO conductive whiskers. *Japanese Journal of Applied Physics* **47**, 7303-7307, (2008).
- 140 Basu, A., Swanwick, M. E., Fomani, A. A. & Velasquez-Garcia, L. F. A portable x-ray source with a nanostructured Pt-coated silicon field emission cathode for absorption imaging of low-Z materials. *Journal of Physics D-Applied Physics* **48**, (2015).

## 2. Field Emission from Carbon Nanotubes

- 141 Fukumoto, S. *et al.* Development of an evaluation system for electron emission characteristics and generation of X-rays using a needle type semiconductor diamond electron emitter. *Diamond and Related Materials* **17**, 764-767, (2008).
- 142 Ribbing, C., Rangsten, P. & Hjort, K. Diamond membrane based structures for miniature X-ray sources. *Diamond and Related Materials* **11**, 1-7, (2002).
- 143 Haga, A. A miniature x-ray tube. *Applied physics letters* **84**, 2208-2210 (2004).
- 144 Kim, J. W. *et al.* in *Conference on Medical Imaging - Physics of Medical Imaging*. (2013).
- 145 Choi, Y. C. *et al.* Preparation of a miniature carbon nanotube paste emitter for very high resolution X-ray imaging. *Carbon* **100**, 302-308 (2016).
- 146 [Webpage] Xinray Systems. <<http://xinraysystems.com/index.php/carbon-nanotube-cathodes/>>
- 147 Gonzales, B. Rectangular Fixed-Gantry CT Prototype: Combining CNT X-Ray Sources and Accelerated Compressed Sensing-Based Reconstruction. *IEEE access* **2**, 971-981 (2014).
- 148 Chang, T. H. P. & Chang, T. H. P. Arrayed miniature electron beam columns for high throughput sub-100 nm lithography. *Journal of vacuum science & technology. B, Microelectronics processing and phenomena* **10**, 2743 (1992).
- 149 Muray, L. P. *J. Vac. Sci. Technol., B* **18**, 3099 (2000).
- 150 Milne, W. I. & Cole, M. T. 8-11.
- 151 Huang, S. M., Dai, L. M. & Mau, A. Controlled fabrication of aligned carbon nanotube patterns. *Physica B-Condensed Matter* **323**, 333-335, (2002).
- 152 Merkulov, V. I., Lowndes, D. H., Wei, Y. Y., Eres, G. & Voelkl, E. Patterned growth of individual and multiple vertically aligned carbon nanofibers. *Applied Physics Letters* **76**, 3555-3557, (2000).
- 153 Choi, Y. C. *et al.* Patterned growth and field emission properties of vertically aligned carbon nanotubes. *Diamond and Related Materials* **10**, 1457-1464, (2001).
- 154 Teo, K. B. K. *et al.* Plasma enhanced chemical vapour deposition carbon nanotubes/nanofibres - how uniform do they grow? *Nanotechnology* **14**, 204-211, (2003).
- 155 Li, C. *et al.* Hot Electron Field Emission via Individually Transistor-Ballasted Carbon Nanotube Arrays. *Acs Nano* **6**, 3236-3242, (2012).
- 156 Lee, H. *et al.* Ozone electrical trimming of carbon nanotubes to improve their field-emission lifetime and uniformity. *Journal of Korean Physical Society* **54**, 185 (2009).
- 157 Song, L. *et al.* Sharp burnout failure observed in high current-carrying double-walled carbon nanotube fibers. *Nanotechnology* **23**, (2012).
- 158 Kind, H. *et al.* Printing gel-like catalysts for the directed growth of multiwall carbon nanotubes. *Langmuir* **16**, 6877-6883, (2000).
- 159 Bonard, J. M. *et al.* Tuning the field emission properties of patterned carbon nanotube films. *Advanced Materials* **13**, 184-188, (2001).
- 160 Fan, S. S. Self-oriented regular arrays of carbon nanotubes and their field emission properties. *Science (New York, N.Y.)* **283**, 512 (1999).
- 161 Sohn, J. I. *et al.* Patterned selective growth of carbon nanotubes and large field emission from vertically well-aligned carbon nanotube field emitter arrays. *Applied Physics Letters* **78**, 901-903, (2001).
- 162 Sohn, J. I., Nam, C. & Lee, S. Vertically aligned carbon nanotube growth by pulsed laser deposition and thermal chemical vapor deposition methods. *Applied Surface Science* **197**, 568-573, (2002).
- 163 Katayama, M., Lee, K. Y., Honda, S., Hirao, T. & Oura, K. Ultra-low-threshold field electron emission from pillar array of aligned carbon nanotube bundles. *Japanese Journal of Applied Physics Part 2-Letters & Express Letters* **43**, L774-L776, (2004).
- 164 Fujii, S. *et al.* Effect of arrangement of pillar array of aligned carbon nanotube bundles on its field-emission characteristic. *Diamond and Related Materials* **17**, 556-558, (2008).
- 165 Chen, Y. M., Chen, C. A., Huang, Y. S., Lee, K. Y. & Tiong, K. K. Characterization and enhanced field emission properties of IrO<sub>2</sub>-coated carbon nanotube bundle arrays. *Nanotechnology* **21**, (2010).
- 166 Li, Z. *et al.* High current field emission from individual non-linear resistor ballasted carbon nanotube cluster array. *Carbon* **89**, 1-7, (2015).
- 167 Ryu, J. H., Kang, J. S. & Park, K. C. Carbon Nanotube Electron Emitter for X-ray Imaging. *Materials* **5**, (2012).
- 168 Aria, A. I., Lyon, B. J. & Gharib, M. Morphology engineering of hollow carbon nanotube pillars by oxygen plasma treatment. *Carbon* **81**, 376-387, (2015).
- 169 Cole, M. T. *et al.* in *Conference on Carbon Nanotubes, Graphene, and Associated Devices V*. (2012).
- 170 Huh, Y., Lee, J. Y. & Lee, C. J. Growth of vertically aligned carbon nanotube emitters on patterned silicon trenches for field emission applications. *Thin Solid Films* **475**, 267-270, (2005).
- 171 Cui, L. F., Chen, J. T., Yang, B. J. & Jiao, T. F. High Current Emission from Patterned Aligned Carbon Nanotubes Fabricated by Plasma-Enhanced Chemical Vapor Deposition. *Nanoscale Research Letters* **10**, (2015).

- 172 Deheer, W. A. *et al.* Aligned carbon nanotube films - production and optical and electronic-properties. *Science* **268**, 845-847, (1995).
- 173 Chhowalla, M., Ducati, C., Rupesinghe, N. L., Teo, K. B. K. & Amaratunga, G. A. J. Field emission from short and stubby vertically aligned carbon nanotubes. *Applied Physics Letters* **79**, 2079-2081, (2001).
- 174 Teo, K. B. K. *et al.* Field emission from dense, sparse, and patterned arrays of carbon nanofibers. *Applied Physics Letters* **80**, 2011-2013, (2002).
- 175 Harris, J. R., Jensen, K. L. & Shiffler, D. A. Dependence of optimal spacing on applied field in ungated field emitter arrays. *Aip Advances* **5**, (2015).
- 176 Liu, P. Enhanced field emission from imprinted carbon nanotube arrays. *Applied physics letters* **89**, 073101 (2006).
- 177 Chua, D. H. C. *et al.* Effects and thermal stability of hydrogen microwave plasma treatment on tetrahedral amorphous carbon films by in situ ultraviolet photoelectron spectroscopy. *Journal of Applied Physics* **106**, (2009).
- 178 Qi, J. L. *et al.* Ar plasma treatment on few layer graphene sheets for enhancing their field emission properties. *Journal of Physics D-Applied Physics* **43**, (2010).
- 179 Weng, C. H. *et al.* Structural transformation and field emission enhancement of carbon nanofibers by energetic argon plasma post-treatment. *Applied Physics Letters* **85**, 4732-4734, (2004).
- 180 Lee, S. H., Lin, C. H., Chiou, J. M. & Kuo, C. T. Effects of post treatment on the field emission properties of CNTs grown by ECR-CVD. *Diamond and Related Materials* **15**, 854-858, (2006).
- 181 Wang, B. B., Cheng, Q. J., Chen, X. & Ostrikov, K. Enhancement of electron field emission of vertically aligned carbon nanotubes by nitrogen plasma treatment. *Journal of Alloys and Compounds* **509**, 9329-9334, (2011).
- 182 Tsai, C.-H. Effect of field emission property of carbon-like nanofiber treated by using a fluorocarbon/oxygen plasma. *Surface and Interface Analysis* **44**, 573-577, (2012).
- 183 Liu, J., Zeng, B., Wu, Z., Zhu, J. & Liu, X. Improved field emission property of graphene paper by plasma treatment. *Applied Physics Letters* **97**, (2010).
- 184 Kimura, C., Yamamuro, Y., Aoki, H. & Sugino, T. Improved field emission characteristics of carbon nanofiber treated with nitrogen plasma. *Diamond and Related Materials* **16**, 1383-1387, (2007).
- 185 Ali, J. Enhancement of Field Emission Properties of Carbon Nanotubes by ECR-Plasma Treatment. *Chemical physics letters* **373**, 1-5 (2014).
- 186 Lee, J. A. *et al.* Improvement of field-emission properties of screen printed carbon nanotube films via argon plasma treatment. *Journal of the Electrochemical Society* **153**, H111-H114, (2006).
- 187 Chen, G., Neupane, S., Li, W., Chen, L. & Zhang, J. An increase in the field emission from vertically aligned multiwalled carbon nanotubes caused by NH<sub>3</sub> plasma treatment. *Carbon* **52**, 468-475, (2013).
- 188 Choi, H., Shin, Y. J., Cha, S. I., Kang, I. H. & Bahng, W. Enhanced field-emission capacity by density control of a CNT cathode using post-plasma treatment. *Solid State Communications* **171**, 50-54, (2013).
- 189 Feng, T. *et al.* Effects of plasma treatment on microstructure and electron field emission properties of screen-printed carbon nanotube films. *Physica E-Low-Dimensional Systems & Nanostructures* **36**, 28-33, (2007).
- 190 Kyung, S. J., Park, J. B., Lee, J. H. & Yeom, G. Y. Improvement of field emission from screen-printed carbon nanotubes by He/(N<sub>2</sub>,Ar) atmospheric pressure plasma treatment. *Journal of Applied Physics* **100**, (2006).
- 191 Qin, Y.-X. & Hu, M. Ar microwave plasma treatment of carbon nanotubes film by electrophoretic deposition. *Journal of Inorganic Materials* **23**, 515-518 (2008).
- 192 Wang, W.-P. *et al.* Field emission characteristics of carbon nanotubes post-treated with high-density Ar plasma. *Applied Surface Science* **256**, 2184-2188, (2010).
- 193 Yu, K., Zhu, Z., Li, Q. & Lu, W. Electronic properties and field emission of carbon nanotube films treated by hydrogen plasma. *Applied Physics a-Materials Science & Processing* **77**, 811-817, (2003).
- 194 Juan, C. P., Tsai, C. C., Chen, K. H., Chen, L. C. & Cheng, H. G. C. Effects of high-density oxygen plasma posttreatment on field emission properties of carbon nanotube field-emission displays. *Japanese Journal of Applied Physics Part 1-Regular Papers Brief Communications & Review Papers* **44**, 8231-8236, (2005).
- 195 Soin, N. Enhanced and Stable Field Emission from in Situ Nitrogen-Doped Few-Layered Graphene Nanoflakes. *Journal of physical chemistry. C* **115**, 5366-5372 (2011).
- 196 Mathur, A. *et al.* Oxygen plasma assisted end-opening and field emission enhancement in vertically aligned multiwall carbon nanotubes. *Materials Chemistry and Physics* **134**, 425-429, (2012).
- 197 Kumar, A. *et al.* Effect of oxygen plasma on field emission characteristics of single-wall carbon nanotubes grown by plasma enhanced chemical vapour deposition system. *Journal of Applied Physics* **115**, (2014).

## 2. Field Emission from Carbon Nanotubes

- 198 Kumar, A. *et al.* A comparative study of nitrogen plasma effect on field emission characteristics of single wall carbon nanotubes synthesized by plasma enhanced chemical vapor deposition. *Applied Surface Science* **322**, 236-241, (2014).
- 199 Ding, S. Towards graphane field emitters. *RSC advances* **5**, 105111-105118 (2015).

# **3. High Performance Field Emitter Characteristics**



## 3.1 Introduction

Fowler Nordheim theory suggests two methods to maximise the output current density; by striving for low work function,  $\phi$ , and high field enhancement factor,  $\beta$ . Isolation of one of these variables predicts a measured response. The most convenient variable to isolate is surface  $\phi$  since it takes on a measurable value, as allowing for a classification by material. Confidently quantifying  $\beta$  is a far harder task. In this chapter, to study the effect of  $\phi$  on field emission, an exhaustive meta study comparison is made between materials, gathered by collecting data from numerous sources. The complications of studying  $\beta$  are also detailed.

## 3.2 Classification by Material

A large variety of materials of all dimensionalities, namely one dimensional, 1D, two dimensional, 2D and three dimensional, 3D, or bulk, have been studied in regards to their field emitting capabilities. This work has been published in <sup>1</sup>. 1D materials are characterised by a very high aspect ratio, AR. 1D emitters are diverse in structure, though often consist of aligned or disordered forests of 1D nanowires where the density of these 1D materials can be controlled by their growth conditions. In the present study, the majority of the 2D materials are carbon based but also include the broader family of transition metal dichalcogenides. All are atomically thin, with typical single grains ranging in diameter from a few tens of nanometers, to many hundreds of micrometers. All 2D materials to date are polycrystalline, and are either grown directly, or deposited additively on various substrates, much like 1D nanomaterials. 3D and bulk nanomaterial emitters often have micro-cone geometry. They possess structures that consist of more complex atomic and macroscopic arrangements; they can be crystalline, amorphous, disordered or structured. A primary defining trait is a characteristically low AR, which is typically  $< 10$ . To date, whilst a diverse variety of materials have been studied, a comprehensive comparison between them has seldom been performed and certainly to no great extent. This chapter documents a thorough comparison with the purpose of identifying specific traits to be able to effectively design a high performing field emitter.

Using published data, comparisons can be made between a vast range of materials. Results on popular and well established nanomaterials, such as CNTs and graphene, proved numerous in literature, whereas only single papers were published for other materials such as cubic boron nitride, cBN <sup>2</sup>. For a long established field of research, ambiguities and inconsistencies become

### 3. High Performance Field Emitter Characteristics

clear when an exhaustive range is studied. This includes principally; a lack of clear definition of FE performance metrics employed and a universal definition of  $\beta$ .

All work herein has been performed by the author. The data has been extracted from existing publications, however, all graphs and analysis have been made personally.

## 3.3 Field Emission Performance Metrics

Key parameters for the success of a material as a field emitter are often depicted as a low turn on electric field,  $E_{on}$ , a low threshold electric field,  $E_{thr}$ , and a high maximum current density,  $J_{max}$ . These characteristics are essential in combination for most applications of FE to allow optimum performance at low working energies. Though key in assessing the emission performance, the metrics  $E_{on}$  and  $E_{thr}$  have been, to date, inconsistently defined, varying dramatically between publications<sup>3-7</sup>, with many apparently almost arbitrary definitions.  $E_{on}$  is best described by the electric field at which a current can be measured. The need for some coherence surrounding this has traditionally led to a specific current density output, usually 0.01 mA/cm<sup>2</sup>, beyond which emission is sufficiently high, or increasing, to be deemed “on” from an initial starting condition where no applied field results in no emitted current. Just under half of the papers studied herein give a value for  $E_{on}$ .  $E_{thr}$  is stated less frequently, by approximately 20% of authors, at common, yet varying values of 0.1 mA/cm<sup>2</sup>, 10 mA/cm<sup>2</sup> and 1 mA/cm<sup>2</sup>. Historically,  $E_{thr}$  was defined by the emission current density required to visualise electron emission patterns on phosphorescent screens<sup>8</sup>, with a value of 10 nA/cm<sup>2</sup>, though this meaning has since become seemingly irrelevant and a formal replacement has not followed it. 10 mA/cm<sup>2</sup> is broadly quoted as a “figure of merit”<sup>9,10</sup>, particularly with regards to flat panel displays, though with no clear reasoning given as to why. The use of these frequently seen values in other FE applications appears undefined, however, and they are not exclusively quoted. Indeed, some acknowledge that there are no strict rules, with some groups opting to define their own metrics<sup>11-14</sup>. Due to such arbitrary definitions and apparent lack of consistency, it has proven, to date, prohibitively challenging to draw direct valid comparisons between differing materials and morphologies. Here we attempt to resolve this inconsistency by introducing globally applicable definitions for  $E_{on}$ ,  $E_{thr}$  and  $J_{max}$ .

Figure 3.1 shows a typical  $J$ - $E$  curve and novel generalised definitions for  $E_{on}$  and  $E_{thr}$ , defined as 10% and 30% respectively of a normalised total measured current density,  $J' = J/J_{max}$ , when

subjected to an applied electrostatic field,  $E$ . Defining both  $E_{on}$  and  $E_{thr}$  allows fitting and Fowler-Nordheim-like curves to be readily extracted given only two parameters.

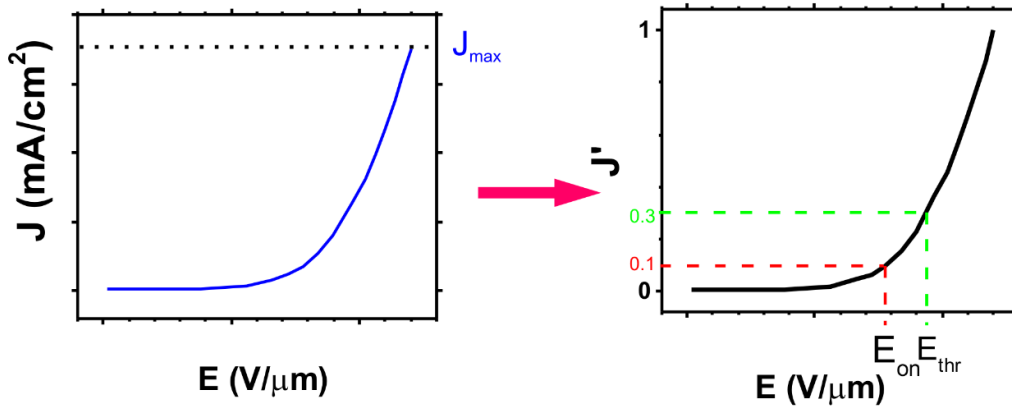


**Figure 3.1 | Performance metric definition.** The raw data showing the exponential behaviour of the measured current (left) is converted into a function of the maximum current density,  $J_{max}$ , from which  $E_{on}$  and  $E_{thr}$  are extracted at 10% and 30% respectively of  $J'$ , where  $J' = J/J_{max}$ .

This redefinition of  $E_{on}$ , however, is flawed. When  $J$  is normalised, the reading of 10% gives a value of  $J$  and  $E$  for each emitter that depends directly on  $J_{max}$ . Whilst redefining parameters allowed a direct comparison to be made between materials, a similar comparison can be made by simply defining  $E_{on}$  at a fixed  $J$  value. The two methodologies resulted in similar data sets, however, the latter approach was chosen, given its simplicity and consistency with existing literature. The most commonly used value seen in the literature was 0.01 mA/cm<sup>2</sup>, thus justifying this otherwise arbitrarily chosen figure. Not all materials could be measured, due to some not reaching a current density of 0.01 mA/cm<sup>2</sup>, however, this was only around 2% of published works. Due to absence of a clear reason for or definition of  $E_{thr}$ , this was dropped entirely from further study as  $E_{on}$  is considered to be the only metric with distinctive meaning.

$J_{max}$  represents maximum current density shown on published graphs, though most authors also state it within the main body of text and often in the abstract of published works. This highlights the importance of the figure and indeed the desired outcomes, where in most cases an anticipated high value is required. A definition of  $J_{max}$  is subject to some uncertainties; whether the tip was run until it failed, maximum applied field, or maximum current extraction under the experimental conditions it is exposed to. In most cases, the value is assumed to be represented by maximum current extracted without encountering a failure.

### 3.3.1 Data Extraction

A digital extraction tool (GetData Graph Digitizer, Vs 2.26.0.20) was used to digitise, gather and verify data from sources using  $J$  as a function of  $E$ . In some cases, where current,  $I$ , or voltage,  $V$ , were given instead of  $J$  or  $E$  along an axis, data was converted into the correct form on the condition that total emitting area or cathode-anode separation,  $d$ , was disclosed. The vast majority of data ( $\approx 95\%$ ), however, was directly extracted from  $J$ - $E$  curves. This data was re-plotted, where necessary, to be able to extract defined parameters, usually  $E_{on}$ , that were neither mentioned in the text nor measured using a different metric definition.

## 3.4 Material Work Function and the Effect on Performance

The Fowler Nordheim equation given in calculating the current density,  $J$ , is given by  $J = \left( \frac{A_{FN}\beta^2 E^2}{\phi} \right) \exp\left( -\frac{B_{FN}\phi^{3/2}}{\beta E} \right)$ . The emitter  $\phi$  is central to defining emission from a material and has thus been a source of potential improvement in emitter design. It is often implied that lower values enhance electron emission performance by reducing surface potential and increasing tunnelling probability. Whilst  $\phi$  is herein regarded as a quantity shared by emitters of the same material, strictly speaking surface  $\phi$  can be altered by surface effects, which change this value<sup>15</sup>. Where different values of  $\phi$  are stated for a single material, the average of these values is given in the results.

Ordering the extracted  $E_{on}$  and  $J_{max}$  performance metrics according to increasing  $\phi$  highlights the dependency of material properties on FE performance, if indeed one exists. Figure 3.2 compares materials ordered by  $\phi$  only, with no consideration to  $\beta$  or surface morphology of emitter. For each material standard errors are shown.

The materials considered, arranged by increasing  $\phi$ , include 1D nanowires: barium oxide<sup>16</sup>, BaO, lanthanum hexaboride<sup>17</sup>, LaB<sub>6</sub>, copper tetracyanoquinodimethane<sup>18</sup>, CuTCNQ, tris(8 hydroxyquinolinato)aluminium<sup>19-22</sup>, Alq<sub>3</sub>, silicon<sup>23-27</sup>, Si, magnesium oxide<sup>28,29</sup>, MgO, aluminium nitride<sup>30-32</sup>, AlN, cadmium sulphide<sup>4,5,33-35</sup>, CdS, silicon carbide<sup>36,37</sup>, SiC, tungsten<sup>38-40</sup>, W, indium tin oxide<sup>41</sup>, ITO, copper phthalocyanine<sup>42,43</sup>, CuPc, boron<sup>44-46</sup>, B, polypyrrole<sup>47-51</sup>, PPy, tin dioxide<sup>52</sup>, SnO<sub>2</sub>, indium gallium nitride<sup>13,53,54</sup>, InGaN, CNTs<sup>6,55-62</sup>, copper<sup>3,63,64</sup>, Cu, zinc selenide<sup>65</sup>, ZnSe, diamond<sup>66</sup>, gallium nitride<sup>67,68</sup>, GaN, zinc oxide<sup>23,69-76</sup>,

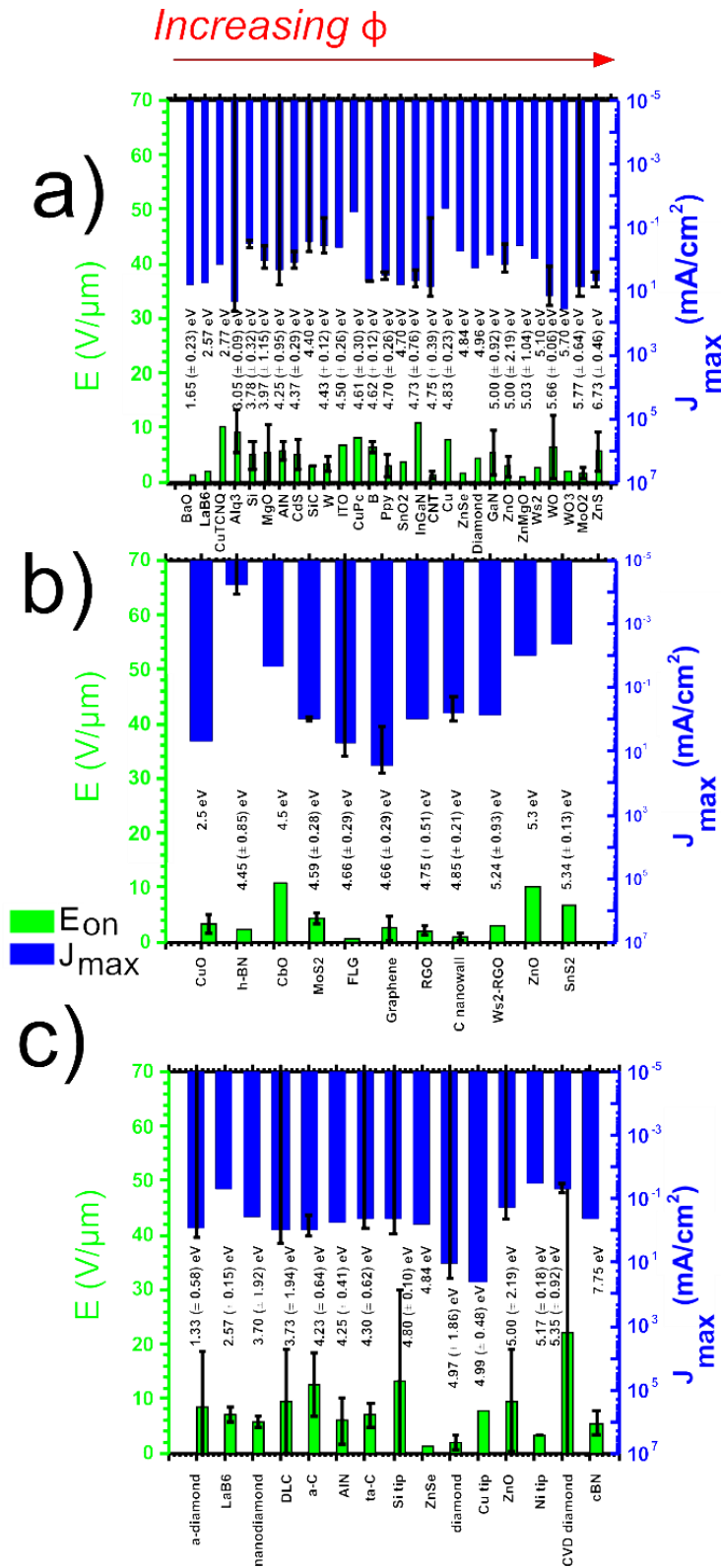


**Figure 3.2 | Material Performance by Work Function.**  $E_{on}$  (green) and  $J_{max}$  (blue) for a) 1D, b) 2D and c) 3D/bulk materials ordered by increasing work function (written above material). Materials showing low  $E_{on}$  (shorter green bars) and large  $J_{max}$  (longer blue bars) are deemed to perform well. No distinctive trends were noted, suggesting that work function ( $\phi$ ) does not influence, to any great extent, a materials field emitting performance.

### 3. High Performance Field Emitter Characteristics

ZnO, zinc magnesium oxide<sup>77</sup>, ZnMgO, tungsten disulphide<sup>78</sup>, WS<sub>2</sub>, tungsten oxide<sup>79-82</sup>, WO, tungsten trioxide<sup>83</sup>, WO<sub>3</sub>, molybdenum dioxide<sup>84-86</sup>, MoO<sub>2</sub> and zinc sulphide<sup>23,87-91</sup>, ZnS; the 2D platelets: copper oxide<sup>92,93</sup>, CuO, hexagonal boron nitride<sup>94-97</sup>, h-BN, niobium oxide<sup>98</sup>, CbO, molybdenum disulphide<sup>99-101</sup>, MoS<sub>2</sub>, graphene (monolayer, vertically standing, clustered and few layer)<sup>7,102-113</sup>, reduced graphene oxide<sup>107,114</sup>, RGO, carbon nanowall<sup>115-117</sup>, WS<sub>2</sub>-RGO<sup>118</sup>, ZnO<sup>119</sup> and tin disulphide<sup>120-122</sup>, SnS<sub>2</sub>; and finally the 3D/bulk materials: *a*-diamond<sup>73,123</sup>, LaB<sub>6</sub><sup>124-127</sup>, nanodiamond<sup>128,129</sup>, diamond like carbon<sup>130,131</sup>, DLC, amorphous carbon<sup>14,132</sup>, *a*-C, AlN<sup>133</sup>, tetrahedral amorphous carbon<sup>134-137</sup>, *ta*-C, Si tips<sup>138-140</sup>, ZnSe<sup>65</sup>, diamond<sup>141-144</sup>, Cu tips<sup>63,64,145</sup>, ZnO<sup>74,146</sup>, Ni tips<sup>147-150</sup>, chemical vapour deposition, CVD, diamond<sup>151-153</sup>, and cBN<sup>2,154</sup>.

Figure 3.2 summarises a variety of FE materials, considered across an intentionally diverse range of emitter geometries and morphologies in order to allow for a valid comparison of intrinsic material properties. Comparisons can be drawn with ease from Figure 3.2, both in regards to  $\phi$  and on a material-to-material basis. Work function and standard deviation were calculated using an average of authors quoted values, no attempt was made to verify the values found. When categorised according to dimensionality, results shown in Table 3.1, it can be seen that the 1D and 2D materials have very similar general performances, whilst the calculated value of  $E_{on}$  for 3D/bulk is nearly twice that of 1D and 2D materials. This is likely due to very sharp edges seen in these materials, with sizes down to atomic range in some cases<sup>155</sup>. A similar average  $\langle J_{max} \rangle$  is seen across all materials, suggesting that this quantity does not strictly depend on dimensionality, and should be compared on an individual emitter basis.

**Table 3.1** | Average performance of FE materials according to dimensionality.

	$\langle E_{on} \rangle$ (V/ $\mu$ m)	$\langle J_{max} \rangle$ (mA/cm <sup>2</sup> )
1D	4.66	4.85
2D	4.21	3.31
3D/bulk	8.09	3.70

The graphitic allotropes, including CNTs and graphene, show promising performance. CNTs show a low value of  $E_{on} = 1.29 \pm 0.72$  V/ $\mu$ m compared to the average for 1D ( $\langle E_{on} \rangle = 4.66$

V/ $\mu\text{m}$ ), as well as high maximum emission current density of  $6.92 \pm 6.87 \text{ mA/cm}^2$ . Similarly,  $E_{on} = 2.52 \pm 2.16 \text{ V}/\mu\text{m}$  was recorded for graphene, with a high  $J_{max} = 26.7 \pm 24.9 \text{ mA/cm}^2$ . Some materials such as ZnMgO nanowires and ZnSe (bulk) show promising values, with low  $E_{on}$  of  $0.78 \text{ V}/\mu\text{m}$  and  $1.40 \text{ V}/\mu\text{m}$ , respectively, but exhibit a poor comparison to the average of their respective dimensionalities with regards to  $J_{max}$  ( $0.35 \text{ mA/cm}^2$  and  $0.63 \text{ mA/cm}^2$ ). In contrast to this, Alq<sub>3</sub> nanowires and WO nanowires show remarkably high  $J_{max}$ , where Alq<sub>3</sub> nanowires have  $\langle J_{max} \rangle = 20.5 \pm 22.9 \text{ mA/cm}^2$  and WO nanowires  $\langle J_{max} \rangle = 13.8 \pm 12.3 \text{ mA/cm}^2$  compared to CNTs with  $6.76 \pm 7.45 \text{ mA/cm}^2$ . However, they do not consistently perform this well across all metrics, exhibiting higher than average values of  $E_{on}$ , with Alq<sub>3</sub> nanowires showing  $9.23 \pm 3.93 \text{ V}/\mu\text{m}$  and WO nanowires with  $6.92 \pm 6.87 \text{ V}/\mu\text{m}$ . An ideal emitter has low  $E_{on}$  and high  $J_{max}$ ; having the best combination of these qualities is important. 2D materials, in particular the carbon derivatives, show largely similar performance to one another. This is likely due to similarity in their atomic structure, comparable  $\phi$ , or indeed reduced noise in the analysis given the higher volumes of data.

Notable discrepancies were observed with claimed values of  $J_{max}$  varying widely within a single material. For example, the data for CVD diamond (polycrystalline)<sup>151</sup>, showed  $E_{on} = 4.42 \text{ V}/\mu\text{m}$ , with  $J_{max} = 0.11 \text{ mA/cm}^2$ , whilst another (which was hydrogen doped)<sup>152</sup> evidenced  $E_{on} = 58.40 \text{ V}/\mu\text{m}$ , and  $J_{max} = 0.01 \text{ mA/cm}^2$ . The results for the polycrystalline sample are a factor of ten larger than the hydrogen doped emitter material. An abnormally large standard deviation of  $32.4 \text{ V}/\mu\text{m}$  ( $E_{on}$ ) is consequently seen, which has a greater value than the mean of  $21.9 \text{ V}/\mu\text{m}$ . This is indicative of other factors affecting FE capabilities other than emitter material and corresponding  $\phi$ . In this case the doping may have some effect on  $\phi$ , though this dramatic shift is unlikely to be caused for this reason; it is more likely associated with experimental conditions or indeed sample geometry.

It is apparent from Figure 3.2, that materials ordered according to increasing  $\phi$  in this manner indicate no clear trend on an expected exponential fitting, displaying no seeming direct correlation between  $\phi$  and  $E_{on}$  or  $J_{max}$ . It seems highly likely that work function arguments alone do not correctly represent field emitting capabilities, and that other material characteristics may have a more profound effect than first considered. It is conceivable, however, that in combination with other characteristics, such as emitter morphology and surface geometry, a clearer trend may appear.

### 3.4.1 Limitations of Acquired Data

A number of factors potentially affecting the validity of collected data are considered. Firstly, whilst in many reported cases,  $\phi$  is a defined bulk characteristic, surface  $\phi$  of a material can be readily tuned to maximise emission. In practice, surface  $\phi$  may not be strictly constant, depending critically on the ambient and local electric fields<sup>156,157</sup>. Surface  $\phi$  is suggested to be particularly sensitive to adsorbates, with subsequent hysteretic field electron emission studies observed<sup>158-160</sup>, which have been particularly implicated in CNTs and porous nanomaterials. Since there may consequently be fluctuations in  $\phi$ , drawing clear conclusions would be a complex process. Further complications are introduced by the inability to actually measure  $\phi$  as, or in fact if, it changes during the emission process.

Just 50% of authors reported  $d$ , the distribution of which is shown in Figure 3.3a. Of those that gave a value, the average  $\langle d \rangle = 209 \pm 207 \mu\text{m}$  with a modal value of  $d = 100 \mu\text{m}$  found. 86% of values were within one standard deviation of the mean, giving rise to the conclusion that the data is largely unaffected by variation in  $d$ .

The interelectrode distance,  $d$ , has a direct influence on measured  $J$ . Higher  $J$  is measured when  $d$  is smallest, this is shown in Figure 3.3b. The closer the plates are, the lower the electric threshold for generating a voltage.

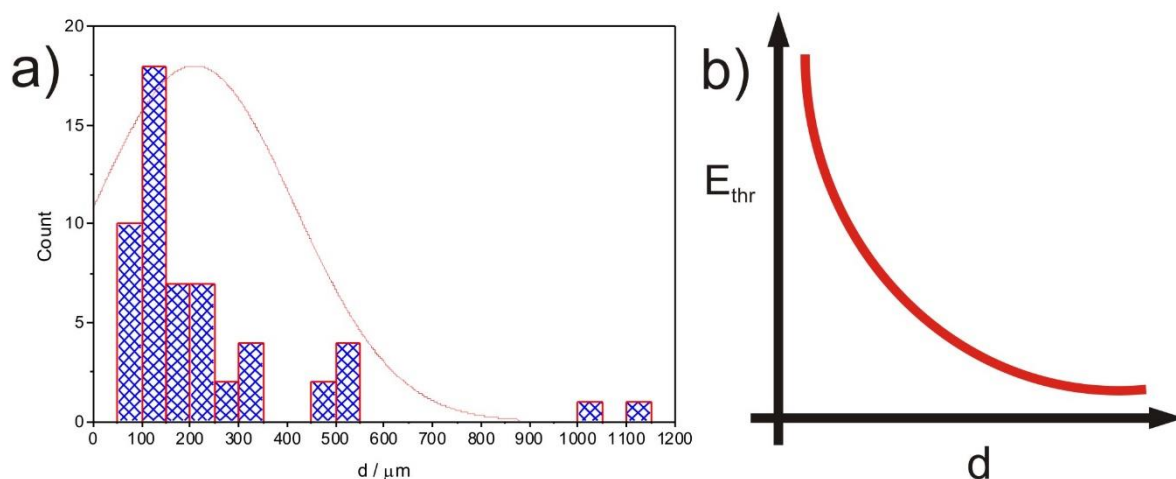


**Figure 3.3 | Interelectrode Distance,  $d$ .** a) Distribution of values of  $d$  stated by 50 % of authors that reported field emission from any material b) Change in threshold field with distance.

The large data set size will likely induce some statistical scatter in the data. Chief amongst which is the length (or height in the case of 2D and bulk materials) of the emitters. This is

unlikely, however, to have a dramatic effect as the heights are usually within a degree of magnitude of one another. A further, more potentially significant, factor affecting the emission properties is the fabrication method, which just two thirds of authors mention. Over the expanse of materials studied, the number of fabrication techniques reported reaches over 15. Some materials (e.g. CNTs) can be synthesised using a number of techniques, as described in Chapter 2. Within these materials different FE behaviour could be seen. Across all dimensionalities the most frequently mentioned was chemical vapour deposition, CVD, including plasma enhanced and microwave plasma enhanced CVD. The high numbers seen using this fabrication technique is due largely to the various carbon based materials where synthesis has been heavily researched.

Additional limitations include potential crystalline damage caused by cleaning processes such as ultrasonication during synthesis, different surfactants used in fabrication giving variations in dispersion and surface  $\phi$ , as well as experimental conditions such as vacuum, temperature and pressure levels, driving conditions and applied electrostatic fields, all of which have not been considered herein. In addition, it is possible that doping and subsequent changes in the electronic properties of the material occur when CVD and wet chemistry methods are coupled. Even if fabrication methods are similar, factors such as material composition, lattice configuration and alignment could all be different and may well affect emission performance dramatically. Nevertheless, the vast data set was selected to reduce implications of these issues on the study. Independent studies from different research groups were assessed to form a fair representation of each material; the focus here was on  $\phi$ .

#### **3.4.2 Conclusions on the Influence of Work Function**

Previous ambiguities in definitions of performance metrics  $E_{on}$  and  $E_{thr}$  led to new definitions, ensuring comparability between studies, where  $E_{thr}$  was disposed with altogether. It was found that ordering materials by increasing  $\phi$  did not result in a clear trend, suggesting other factors are of higher influence when predicting field emitting capabilities of a material and indeed emitter. General observations that can be made on a material-to-material comparison basis, disregarding the work function argument, show that few materials seem more promising than the nanocarbons. Further benefits of these materials are that they can be grown, aligned, and engineered at sub-micron scale, which is not true for many other materials. CNTs in particular unite ultra-precision engineering with detailed materials science, resulting in the realisation of

### 3. High Performance Field Emitter Characteristics

highly functional electron emitters. Similarly, 1D materials, with large AR, show benefits over 2D and bulk materials, with the potential for very high fields around sharp emitting tips. Along with the vertical alignment seen through CVD, CNTs are perhaps one of the most promising materials for enhanced FE and have proven to mediate desirable high current densities at low fields.

## 3.5 The Importance of Morphology

The other influential term in Fowler Nordheim theory is  $\beta$ . Material  $\phi$  can be measured using techniques such as Kelvin Probe Force Microscopy and Ultraviolet Photoelectron Spectroscopy. As a more abstract concept, however, no standard definition and therefore no standard measurement procedure exist for  $\beta$ . Herein lies the crux of the problem. Visual assessment of surface morphology through scanning electron microscopy, SEM, or atomic force microscopy, AFM, can give some clue to surface geometry, though no quantitative worth can be assigned. To provide a value,  $\beta$  is generally calculated using FN theory from the gradient,  $m$ , of an FN plot where  $\beta = -\frac{B_{FN}\phi^{3/2}}{m}$ . A number of factors impact morphology including surface coverage, AR, surface roughness, degree of patterning, vertical alignment, packing density and electronic screening effect. The combined and individual effects of these factors are both hard to quantify and to measure. An effort to compare devices according to geometry is made herein, using a new morphology metric,  $\alpha$ .

### 3.5.1 Shortcomings of Field Enhancement Factor

A problem encountered in defining morphology is the validity of  $\beta$  calculated experimentally, which is determined primarily using conventional Fowler-Nordheim theory defined for bulk materials.  $\beta$  relates the local electric field surrounding the emitter apex,  $E_0$ , to the linearly approximated macroscopic electric field,  $E$ , where  $\beta = E_0/E$ , and can be extracted, empirically, from FN fits. This requires a linear dependency, which is not always noted, although many authors do see this and subsequently use this to calculate  $\beta$ . Some of the previously mentioned ambiguities with Fowler Nordheim (Section 2.3.1) for nanomaterials can cause a lack of definitive understanding of nanomaterial behaviour. In some cases, two  $\beta$  values can be measured corresponding to two linear dependencies at high and low fields<sup>11,109,112</sup>, which is not easily explained.

Around 70% of the papers studied actually state any value of  $\beta$ , highlighting the first inconsistency in the field; some report extremely high<sup>134</sup> (order of 10,000)  $\beta$  values, and others very low<sup>51</sup> (order of 1). It is hard to have confidence in the validity of these extreme values. Numerous discrepancies in the definition of  $\beta$  were seen, with some quoting it as the value of height,  $h$ , of the emitter over the radius of curvature,  $r$ , of the tip:  $(h/r)$ ,<sup>127,138</sup> or some linearly scaled variation of this, varying between 1 and 25<sup>12,13,23,125,131</sup>. Many others calculate  $\beta$  by extracting it from a selected gradient on a measured FN plot. It has become commonplace to use this method in more recent years, as seen by 100% of 1D materials, where any value was given. However, as little as 50% usage for 2D and 3D was noted. Some 7.5% of studied works provide an empirical validation of such values by comparing them with  $\beta$  estimates using other methods<sup>13,19,20,131</sup>. Others, 2.5%, simply quote a value and suggest that  $\beta$  is a result of an unknown combination of factors; such as AR, surface roughness, the size of the vacuum gaps, crystal structure and spatial distribution of emitters<sup>17,87,161</sup>. It is not known, nor is any attempt often made, to understand in these cases, how each of these contributors affects  $\beta$  or indeed the emission properties in any great detail. Table 3.2 shows an exhaustive list of definitions of  $\beta$  throughout the literature of which there are nine in total.

**Table 3.2** | Definitions of  $\beta$  found in literature.

<i><math>\beta</math> as defined in literature</i>		<i>Ref.</i>	<i>Geometry</i>
$\beta = (l/r)$	$l = \text{emitter length}$ $r = \text{emitter radius}$	162 131	1D/3D
$\beta = (h/r)$	$h = \text{emitter height}$ $r = \text{radius of curvature of tip or radius at apex}$	125 127 138	3D
$\beta = \left( \frac{d}{kr_{\text{tip}}} \right)$	$d = \text{inter-electrode distance}$ $k = \text{constant} (= 5 \text{ for long thin geometry})$ $r = \text{radius of curvature of tip}$	149	1D
$\beta = 100 \left( 1 + \sqrt{\frac{h}{2r}} \right)$	<i>Smith's model:</i> $h = \text{height}$ $r = \text{emitter radius}$	13	1D
$\beta = \beta_0 \beta_s = \beta_0 \left[ 1 - \exp\left(-\frac{cs}{h}\right) \right]$	$\beta_0 = \text{intrinsic field enhancement factor is a ratio of local and macroscopic fields} (r = \text{radius}).$	25	1D

### 3. High Performance Field Emitter Characteristics

$\beta_0 = 1.2 \left( \frac{h}{r} + 2.15 \right)^{0.9}$	$\beta =$ overall field enhancement factor, $\beta_s =$ screening factor $s =$ wire spacing $c =$ constant		
$\beta = \frac{1}{\left( \frac{h}{d} + \frac{1}{\beta_0} \right)}$	$\beta_0 =$ enhancement factor (independent of $d$ , $h$ and applied voltage)	80	1D
$\beta_0 = \left( \frac{h}{0.95 r_0} \right)$	$\beta_0 =$ geometric field enhancement factor $h =$ height $r_0 =$ average radius of tip	151	3D
$\beta \approx d^{(1-c)}$	$d =$ inter-electrode distance $c =$ constant ( $< 1$ ).	116	3D
$\beta = - \left( \frac{b\phi^2}{k} \right)$	$b =$ constant ( $= 6.83 \times 10^7 \text{ eV}^{3/2} \text{ V/cm}$ ) $k =$ Select gradient of the Fowler-Nordheim plot	All 1D that calculate	1D, 2D and 3D

Figure 3.4a investigates the relationship between  $\beta$  from the literature, herein termed  $\beta_{lit}$ , and  $\phi$  in an attempt to find a correlation.  $\beta_{lit}$  does not appear to be a function of  $\phi$  across a wide range of materials over the 1D, 2D and 3D range, which is not an unsurprising result. Figure 3.4a highlights what is expected to be seen, that the qualities most desired, and hence most commonly reported, are low  $\phi$  and high  $\beta$ , where a significant proportion of the data points lie at the top, with high  $\beta$ , and to the left of the figure, with  $\phi < 5$  eV. 1D materials show the largest spread in  $\phi$ , whereas 2D are mostly confined between 4.0 - 5.0 eV. As they are predominantly graphene or other carbon based materials, a similar  $\phi$  is expected. This finding further aids the claim that  $\beta$  lacks clear definition, showing great variety amongst what are considered to be similar materials. 3D and bulk materials, on average, show a lower  $\phi$ , but also a lower  $\beta$  than both 1D and 2D. A clear relationship cannot be seen between  $\phi$  and  $\beta_{lit}$ , despite  $\phi$  being often highly prominent in calculating  $\beta$  using the FN slope method.

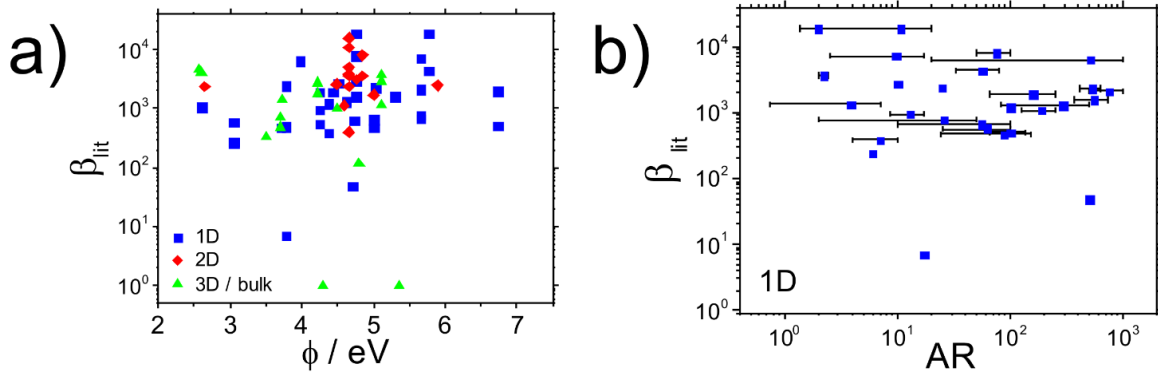


**Figure 3.4 | Comparing Literature Values of Local Field Enhancement Factor,  $\beta$ , Work Function,  $\phi$ , and Aspect Ratio, AR.** a) The relationship between  $\beta_{lit}$  and  $\phi$ , with no clear dependency seen. b) Relationship between  $\beta_{lit}$  and AR again showing little dependency.

AR is defined by emitter height divided by diameter and is of particularly high value in 1D materials. It is expected that  $\beta$  has some degree of dependency on AR, though the exact dependence is widely debated. To further investigate this, the relationship between  $\beta_{lit}$  and calculated AR (of 1D materials) is shown in Figure 3.4b. No clear dependency is noted here. The 1D materials were chosen in this instance, as their AR is most clearly defined, with 80% of papers stating material dimensions, compared to just over 10% for 2D and 3D. The error bars represent the additive range in AR from stipulated variations in diameter and length of the nanowires caused by statistical variation in fabrication. Such variations can be quite extensive. To further investigate the effects of AR on  $\beta$ , the alignment and orientation of the emitters must be considered, as well as emitter density and emitter patterning. Indeed, electrostatic screening dramatically alters the measured emission profiles. For example, an individual nanowire with high AR lying parallel to the emission direction will manifest a lower  $\beta$  compared to the same nanowire in a vertically orientated configuration even though they have identical length and diameter. This distinction is very important, however, is not considered in Figure 3.4b or even in the literature to any great extent. The exact manner in which the AR contributes to  $\beta$  is, therefore, currently unknown in detail.

### 3.5.2 Surface Roughness Metric

As a result of the shortcomings of  $\beta$  a more generalised roughness metric is defined, which manifests in the surface morphology and degree of perturbation therein. A surface morphology

### 3. High Performance Field Emitter Characteristics

metric,  $\alpha$ , is yet to be a defined function of  $\beta$ , the direct relationship to which is not fully quantified. Initial studies of the newly defined metric were measured according to perceived surface roughness, organised by SEM images of the emitting materials. Two categories of images were considered; areal and profile, categorised by orientation in which SEM images were acquired. Issues with this arose twofold. Firstly, there was no mathematical procedure to determine  $\alpha$  given unavoidable inconsistencies. The assessment was completed by eye and judged according to individual perceptions and became somewhat invalidated by personal opinion. Secondly, the pictures themselves, from which the measurements were made, vary from image to image in grey scale, scale and orientation between SEM images.

In order to combat the first issue, a test was conducted blind by five individuals according to perceived surface roughness from SEMs, with no access given to information of the emitter including: material, study authorship or source,  $\phi$ , emitting performance or other ranked metrics including that of our previously conducted  $\phi$  studies. SEM images of each material, which corresponded to the data extracted for that material, were ranked in order from most to least rough by each individual, where surfaces with highest perturbation are predicted to have higher current. Perceptions naturally varied; if two (or more) materials had the same rank after averaging across the five results, they were placed in order of performance. After five iterations, many of the materials had the same average scoring and thus the exercise became pointless. Despite further efforts made, this definition of  $\alpha$  was judged unsuitable.

A second attempt at defining a mathematical metric was determined by converting qualities into numerical form using automated image analysis and combining them. Figure 3.5 visualises the various measurable quantities. The vertical alignment,  $d\vartheta$ , was quantified using an average of the angle,  $\vartheta$ , between  $90^\circ$  and  $0^\circ$  at which nanowires are arranged, where perfect alignment perpendicular (with  $\vartheta = 90$ ) to the substrate gives a value of 1 and an average alignment of  $\vartheta^\circ$  from parallel to the substrate gives a value of  $\vartheta/90$ . The height distribution,  $dH$ , was defined as the variation in taller nanowires compared to the average. The spacing between nanowires,  $dP$ , relates to packing density. AR and surface coverage possess numerical value and were also considered. Unfortunately, the problem remains that images used to collect this data show large variation, and there was little comprehension from plotting graphs as a function of a combination of these qualities and this method was similarly disregarded.

To be able to look into the effect of morphology, a more controlled and comparable method is required. An experimental method whereby morphology can be carefully monitored and

inconsistencies encountered in imaging can be overcome is required to combat present issues surrounding classification of surface geometry.

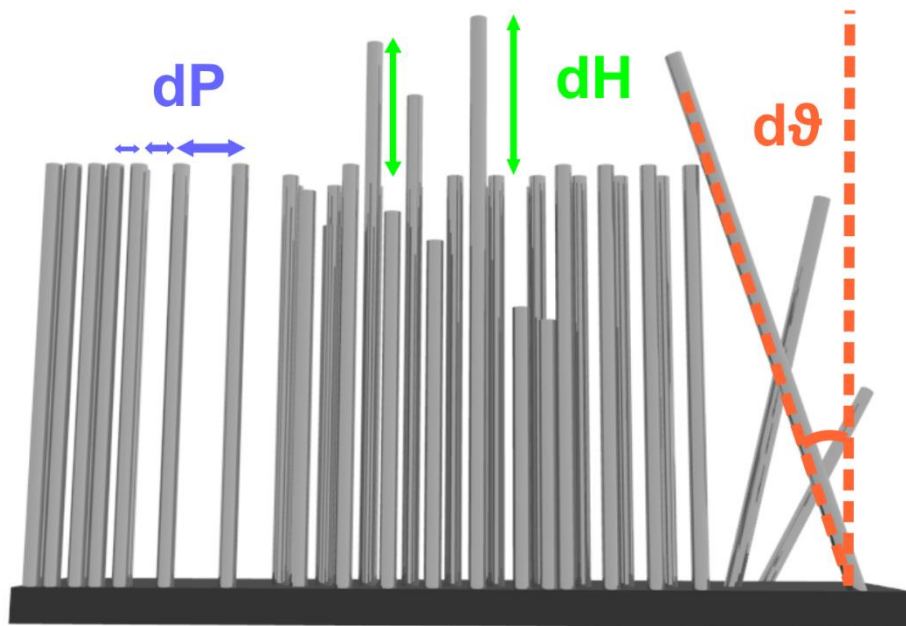


**Figure 3.5 | Morphology Metric Definition.** Definitions of values of density or difference in pitch ( $dP$ ), variation in height distribution ( $dH$ ) and alignment ( $d\theta$ ).

### 3.6 Summary

Inaccuracies in Fowler Nordheim become clear when considering electron emission from nanomaterials. According to theory, work function and field enhancement factor are influential in determining emitter performance. It was expected, therefore, that when arranged according to work function, some dependency would be seen. This was not true. What was strikingly evident, however, was that 1D and 2D materials show turn on electric field values, for a measured current density of  $0.01 \text{ mA/cm}^2$ , at half that of 3D and bulk materials. This is indicative of the significance of field enhancement factor around very sharp tips. The graphitic nanocarbons perform well; nevertheless, a number of other nanomaterials also show promise. It can be concluded that emitter material, and work function, are not the most significant factors in determining success of a material as a field emitter when solely considered, although dimensionality, and indeed sharp tip morphology, does appear to have a strong influence.

Understanding field enhancement factor further is crucial in attaining information to design field emitters that reliably produce high emission at low fields. To accurately measure

### 3. High Performance Field Emitter Characteristics

morphology has proven to have a number of inaccuracies and thus dependency of performance on emitter geometry is a challenging study. Whilst it can be generally agreed that certain aspects are desirable (e.g. high aspect ratio or vertical alignment), these quantities are notoriously difficult to quantise effectively. The study of emitter geometry therefore requires a more systematic and controlled approach.

## References

- 1 Collins, C. M., Parmee, R. J., Milne, W. I. & Cole, M. T. High Performance Field Emitters. *Advanced Science*, **3** (2015).
- 2 Teii, K. & Matsumoto, S. Low threshold field emission from high-quality cubic boron nitride films. *Journal of Applied Physics* **111**, 093728 (2012).
- 3 Zheng, K. *et al.* Enhanced field emission and patterned emitter device fabrication of metal-tetracyanoquinodimethane nanowires array. *Applied Surface Science* **256**, 2764-2768 (2010).
- 4 Chavan, P. *et al.* CdS nanowires: Ultra-long growth and enhanced field emission properties. *Vacuum* **101**, 38-45 (2014).
- 5 Ge, T., Kuai, L. & Geng, B. Solution-phase chemical route to branched single-crystalline CdS nanoarchitectures and their field emission property. *Journal of Alloys and Compounds* **509**, 353-358 (2011).
- 6 Bonard, J. M., Salvetat, J. P., Stockli, T., Forro, L. & Chatelain, A. Field emission from carbon nanotubes: perspectives for applications and clues to the emission mechanism. *Applied Physics a-Materials Science & Processing* **69**, 245-254 (1999).
- 7 Hallam, T., Cole, M. T., Milne, W. I. & Duesberg, G. S. Field Emission Characteristics of Contact Printed Graphene Fins. *Small* **10**, 95-99 (2014).
- 8 Gomer, R. *Field Emission and Field Ionisation*. 53 (Harvard University Press, 1961).
- 9 Shang, N. *et al.* Self-Assembled Growth, Microstructure, and Field-Emission High-Performance of Ultrathin Diamond Nanorods. *Acs Nano* **3**, 1032-1038 (2009).
- 10 Bonard, J. M. *et al.* Field emission properties of multiwalled carbon nanotubes. *Ultramicroscopy* **73**, 7-15 (1998).
- 11 Banerjee, D. & Chattopadhyay, K. K. Enhanced field emission properties of PECVD synthesized chlorine doped diamond like carbon thin films. *Surface & Coatings Technology* **253**, 1-7 (2014).
- 12 Shih, C. F., Chen, N. C., Chang, P. H. & Liu, K. S. Field emission properties of self-assembled InN nanostructures: Effect of Ga incorporation. *Journal of Crystal Growth* **281**, 328-333 (2005).
- 13 Smith, R.C, Carey, J. D., Forrest, R.D. & Silva, S.R.P. Effect of aspect ratio and anode location on the field emission properties of a single tip based emitter. *J. Vac. Sci. Technology* **23**, 632 (2005).
- 14 Banerjee, D., Jha, A. & Chattopadhyay, K. K. Low-temperature synthesis of amorphous carbon nanoneedle and study on its field emission property. *Physica E-Low-Dimensional Systems & Nanostructures* **41**, 1174-1178 (2009).
- 15 Halas, S. & Durakiewicz, T. Is work function a surface or a bulk property? *Vacuum* **85**, 486-488 (2010).
- 16 Cui, Y. *et al.* in *27<sup>th</sup> International Vacuum Nanoelectronics Conference*, 188-189 (Engelberg, Switzerland, 2014).
- 17 Xu, J. *et al.* Fabrication of vertically aligned single-crystalline lanthanum hexaboride nanowire arrays and investigation of their field emission. *Npg Asia Materials* **5** (2013).
- 18 Liu, H. *et al.* Fabrication of large-area hybrid nanowires arrays as novel field emitters. *Journal of Materials Chemistry* **19**, 1031-1036 (2009).
- 19 Chiu, J. J. *et al.* Room temperature vibrational photoluminescence and field emission of nanoscaled tris-(8-hydroxyquinoline) aluminum crystalline film. *Applied Physics Letters* **83**, 4607-4609 (2003).
- 20 Cho, C.-P. & Perng, T.-P. On the dendritic growth and field emission of amorphous AlQ<sub>3</sub> nanowires. *Organic Electronics* **11**, 115-122 (2010).
- 21 Chiu, J. J., Kei, C. C., Perng, T. P. & Wang, W. S. Organic semiconductor nanowires for field emission. *Advanced Materials* **15**, 1361 (2003).
- 22 Xu, G. *et al.* Facile solution synthesis without surfactant assistant for ultra long Alq<sub>3</sub> submicrowires and their enhanced field emission and waveguide properties<sup>†</sup>. *Journal of Materials Chemistry* **20**, 3006-3010 (2010).

- 23 Fang, X., Bando, Y., Gautam, U. K., Ye, C. & Golberg, D. Inorganic semiconductor nanostructures and  
their field-emission applications. *Journal of Materials Chemistry* **18**, 509-522 (2008).
- 24 Au, F. C. K. *et al.* Electron field emission from silicon nanowires. *Applied Physics Letters* **75**, 1700-1702  
(1999).
- 25 Hung, Y., Jr. *et al.* Relaxing the electrostatic screening effect by patterning vertically-aligned silicon  
nanowire arrays into bundles for field emission application. *Thin Solid Films* **556**, 146-154 (2014).
- 26 Fang, X. *et al.* Si nanowire semisphere-like ensembles as field emitters. *Chemical Communications*, **40**,  
4093-4095 (2007).
- 27 Devarapalli, R. R. *et al.* Vertical arrays of SiNWs-ZnO nanostructures as high performance electron field  
emitters. *Journal of Materials Chemistry* **22**, 22922-22928 (2012).
- 28 Ma, L. A. *et al.* Large-scale growth of ultrathin MgO nanowires and evaluate their field emission  
properties. *Physica E-Low-Dimensional Systems & Nanostructures* **41**, 1500-1503 (2009).
- 29 Tan, H., Xu, N. & Deng, S. Synthesis and electron emission properties of MgO nanowires. *Journal of  
Vacuum Science & Technology B* **28**, C2B20-C2B23 (2010).
- 30 He, J. H. *et al.* Aligned AlN nanorods with multi-tipped surfaces - Growth, field-emission, and  
cathodoluminescence properties. *Advanced Materials* **18**, 650 (2006).
- 31 Ji, X., Chen, P., Deng, J., Zhou, W. & Chen, F. Field Emission Properties of AlN Nanostructures. *Journal  
of Nanoscience and Nanotechnology* **12**, 6531-6533 (2012).
- 32 Pelletier, J., Gervais, D. & Pomot, C. Application of wide-gap semiconductors to surface ionization:  
Work functions of AlN and SiC single crystals. *Journal of Applied Physics* **55**, 994-1002 (1984).
- 33 Chavan, P. G., More, M. A., Joag, D. S., Badadhe, S. S. & Mulla, I. S. in *27<sup>th</sup> International Vacuum  
Nanoelectronics Conference* 83-84 (Engelberg, Switzerland 2014).
- 34 Lin, Y., Hsu, Y., Lu, S. & Kung, S. Non-catalytic and template-free growth of aligned CdS nanowires  
exhibiting high field emission current densities. *Chemical Communications*, 2391-2393 (2006).
- 35 Li, L. *et al.* Single-Crystalline CdS Nanobelts for Excellent Field-Emitters and Ultrahigh Quantum-  
Efficiency Photodetectors. *Advanced Materials* **22**, 3161-3165 (2010).
- 36 Wang, H., Li, Z., Kang, L. & Li, X. Synthesis and field emission of beta-SiC nanowires on silicon  
nanoporous pillar array. *Applied Surface Science* **259**, 79-82 (2012).
- 37 Zhou, W. M. *et al.* Field emission from nonaligned SiC nanowires. *Applied Surface Science* **253**, 2056-  
2058 (2006).
- 38 Lee, Y. H. *et al.* Tungsten nanowires and their field electron emission properties. *Applied Physics Letters*  
**81**, 745-747 (2002).
- 39 Wang, S. *et al.* Structure and Field-Emission Properties of Sub-Micrometer-Sized Tungsten-Whisker  
Arrays Fabricated by Vapor Deposition. *Advanced Materials* **21**, 2387-2392 (2009).
- 40 Yeong, K. S. & Thong, J. T. L. Field-emission properties of ultrathin 5 nm tungsten nanowire. *Journal  
of Applied Physics* **100**, 114325 (2006).
- 41 Wan, N. *et al.* Broadband anti-reflection and enhanced field emission from catalyst-free grown small-  
sized ITO nanowires at a low temperature. *Acta Materialia* **58**, 3068-3072 (2010).
- 42 Komolov, A. S. *et al.* Electronic properties of the interface between hexadecafluoro copper  
phthalocyanine and unsubstituted copper phthalocyanine films. *Semiconductors* **47**, 956-961 (2013).
- 43 Tong, W. Y., Li, Z. X., Djuricic, A. B., Chan, W. K. & Yu, S. F. Field emission from copper  
phthalocyanine and copper hexadecafluorophthalocyanine nanowires. *Materials Letters* **61**, 3842-3846  
(2007).
- 44 Gan, H., Jin, S., Guo, T., Deng, S. & Xu, N. in *27<sup>th</sup> International Vacuum Nanoelectronics Conference*  
180-181 (Engelberg, Switzerland, 2014).
- 45 Liu, F. *et al.* Fabrication and field emission properties of boron nanowire bundles. *Ultramicroscopy* **109**,  
447-450 (2009).
- 46 Wu, C.-H., Juang, Z.-Y. & Hsieh, C.-K. Electron field emission characteristics of boron nanowires grown  
by ultralow pressure CVD. *Japanese Journal of Applied Physics* **53** (2014).
- 47 Andreoli, E., Liao, K.-S., Haldar, A., Alley, N. J. & Curran, S. A. PPy:PSS as alternative to PEDOT:PSS  
in organic photovoltaics. *Synthetic Metals* **185-186**, 71-78 (2013).
- 48 Duong Ngoc, H., Nguyen Trong, T., Tran Dinh, V. & Nguyen Duc, T. Synergistic Effects in the Gas  
Sensitivity of Polypyrrole/Single Wall Carbon Nanotube Composites. *Sensors* **12**, 7965-7974 (2012).
- 49 Joo, J., Lee, S. J., Park, D. H., Lee, J. Y. & Lee, T. J. Field-Emission Characteristics of Electrochemically  
Synthesized Polypyrrole Nanotubes Prepared by SDC. *Electrochemical and solid-state letters* **8**, 39-41  
(2005).
- 50 Patil, S. S., Harpale, K. & More, M. A. in *27<sup>th</sup> International Vacuum Nanoelectronics Conference* 239-  
240 (Engelberg, Switzerland, 2014).
- 51 Yan, H. *et al.* Synthesis, property and field-emission behaviour of amorphous polypyrrole nanowires.  
*Nanotechnology* **17**, 3446-3450 (2006).

### 3. High Performance Field Emitter Characteristics

- 52 Fang, X., Yan, J., Hu, L., Liu, H. & Lee, P. S. Thin SnO<sub>2</sub> Nanowires with Uniform Diameter as Excellent Field Emitters: A Stability of More Than 2400 Minutes. *Advanced Functional Materials* **22**, 1613-1622 (2012).
- 53 Jang, S.-H. & Jang, J.-S. Schottky Barrier Characteristics and Carrier Transport Mechanism for Ohmic Contacts to Strained p-Type InGaN/GaN Superlattice. *Electrochemical and Solid State Letters* **13**, 403-405 (2010).
- 54 Seo, T. H. *et al.* Graphene network on indium tin oxide nanodot nodes for transparent and current spreading electrode in InGaN/GaN light emitting diode. *Applied Physics Letters* **98** (2011).
- 55 Lee, J. *et al.* High-performance field emission from a carbon nanotube carpet. *Carbon* **50**, 3889-3896 (2012).
- 56 Nguyen, D. D., Lai, Y.-T. & Tai, N.-H. Enhanced field emission properties of a reduced graphene oxide/carbon nanotube hybrid film. *Diamond and Related Materials* **47**, 1-6 (2014).
- 57 Shiraishi, M. & Ata, M. Work function of carbon nanotubes. *Carbon* **39**, 1913-1917 (2001).
- 58 Ago, H. *et al.* Work functions and surface functional groups of multiwall carbon nanotubes. *Journal of Physical Chemistry B* **103**, 8116-8121 (1999).
- 59 Shin, D. H. *et al.* in *27<sup>th</sup> International Vacuum Nanoelectronics Conference* 230-231 (Engelberg, Switzerland, 2014).
- 60 Kato, S., Chouhan, V., Noguchi, T. & Tsujinno, S. in *27<sup>th</sup> International Vacuum Nanoelectronics Conference* 132-133 (Engelberg, Switzerland, 2014).
- 61 Yang, X. *et al.* Enhanced Field Emission from a Carbon Nanotube Array Coated with a Hexagonal Boron Nitride Thin Film. *Small* **11**, 3710-3716 (2015).
- 62 Yang, J., Yan, X.-B., Chen, J.-T., Sun, D.-F. & Xue, Q.-J. Synthesis and field emission properties of carbon nanotube films modified with amorphous carbon nanoparticles by a simple electrodeposition method. *Chinese Chemical Letters* **25**, 375-379 (2014).
- 63 Auciello, O. *et al.* Review of synthesis of low-work function Cu-Li alloy coatings and characterization of the field emission properties for application to field emission devices. *Journal of Vacuum Science & Technology B* **19**, 877-883 (2001).
- 64 Glatzel, T., Steigert, H., Sadewasser, S., Klenk, R. & Lux-Steiner, M. C. Potential distribution of Cu(In,Ga)(S,Se)<sub>2</sub>-solar cell cross-sections measured by Kelvin probe force microscopy. *Thin Solid Films* **480**, 177-182 (2005).
- 65 Zeng, Q. Z. Synthesis, field emission and optical properties of ZnSe nanobelts, nanorods and nanocones by hydrothermal method. *Materials science in semiconductor processing* **31**, 189-194 (2015).
- 66 Panda, K., Sankaran, K. J., Panigrahi, B. K., Tai, N.-H. & Lin, I. N. Direct Observation and Mechanism for Enhanced Electron Emission in Hydrogen Plasma-Treated Diamond Nanowire Films. *Acs Applied Materials & Interfaces* **6**, 8531-8541 (2014).
- 67 Ng, D. K. T., Hong, M. H., Tan, L. S., Zhu, Y. W. & Sow, C. H. Field emission enhancement from patterned gallium nitride nanowires. *Nanotechnology* **18** (2007).
- 68 Wang, Y. Q. *et al.* Structure and surface effect of field emission from gallium nitride nanowires. *Applied Surface Science* **285, Part B**, 115-120 (2013).
- 69 Ding, S., Cui, H., Lei, W., Zhang, X. & Wang, B. in *27<sup>th</sup> International Vacuum Nanoelectronics Conference* 178-179 (Engelberg, Switzerland, 2014).
- 70 Jamali Sheini, F., Joag, D. S. & More, M. A. Field emission studies on electrochemically synthesized ZnO nanowires. *Ultramicroscopy* **109**, 418-422 (2009).
- 71 Sun, X. Designing efficient field emission into ZnO. *Nanotechnology, SPIE* (2006).
- 72 Tampo, H. *et al.* Band profiles of ZnMgO/ZnO heterostructures confirmed by Kelvin probe force microscopy. *Applied Physics Letters* **94**, 242107 (2009).
- 73 Yang, Y. H., Wang, C. X., Wang, B., Xu, N. S. & Yang, G. W. ZnO nanowire and amorphous diamond nanocomposites and field emission enhancement. *Chemical Physics Letters* **403**, 248-251 (2005).
- 74 Zhang, Z. P., Chen, W. Q., Li, Y. F. & Chen, J. in *27<sup>th</sup> International Vacuum Nanoelectronics Conference* 78-79 (Engelberg, Switzerland, 2014).
- 75 Song, J. *et al.* Epitaxial ZnO Nanowire-on-Nanoplate Structures as Efficient and Transferable Field Emitters. *Advanced Materials* **25**, 5750-5755 (2013).
- 76 Ye, C., Bando, Y., Fang, X., Shen, G. & Golberg, D. Enhanced field emission performance of ZnO nanorods by two alternative approaches. *Journal of Physical Chemistry C* **111**, 12673-12676 (2007).
- 77 Yousefi, R., Sheini, F. J., Muhamad, M. R. & More, M. A. Characterization and field emission properties of ZnMgO nanowires fabricated by thermal evaporation process. *Solid State Sciences* **12**, 1088-1093 (2010).
- 78 Viskadourous, G. *et al.* Enhanced Field Emission of WS<sub>2</sub> Nanotubes. *Small* **10**, 2398-2403 (2014).
- 79 Agiral, A. & Gardeniers, J. G. E. *On-Chip Tungsten Oxide Nanowires Based Electrodes for Charge Injection*. Ch. 9 (Intech, 2010).

- 80 Huang, K., Pan, Q., Yang, F., Ni, S. & He, D. The catalyst-free synthesis of large-area tungsten oxide nanowire arrays on ITO substrate and field emission properties. *Materials Research Bulletin* **43**, 919-925 (2008).
- 81 Kojima, Y. *et al.* Effects of oxidation during synthesis on structure and field-emission property of tungsten oxide nanowires. *Japanese Journal of Applied Physics Part 1-Regular Papers Brief Communications & Review Papers* **46**, 6250-6253 (2007).
- 82 Yue, S. *et al.* Amazing ageing property and in situ comparative study of field emission from tungsten oxide nanowires. *Nanotechnology* **22** (2011).
- 83 Li, L. *et al.* WO<sub>3</sub> nanowires on carbon papers: electronic transport, improved ultraviolet-light photodetectors and excellent field emitters. *Journal of Materials Chemistry* **21**, 6525-6530 (2011).
- 84 Khademi, A., Azimirad, R., Zavarian, A. A. & Moshfegh, A. Z. Growth and Field Emission Study of Molybdenum Oxide Nanostars. *Journal of Physical Chemistry C* **113**, 19298-19304 (2009).
- 85 Zhou, J. Large-Area Nanowire Arrays of Molybdenum and Molybdenum Oxides: Synthesis and Field Emission Properties. *Advanced materials (Weinheim)* **15**, 1835-1840 (2003).
- 86 Liu, J. *et al.* Enhanced field emission properties of MoO<sub>2</sub> nanorods with controllable shape and orientation. *Materials Letters* **58**, 3812-3815 (2004).
- 87 Fang, X. *et al.* Ultrathin ZnS nanobelts as field emitters. *Advanced Materials* **19**, 2593 (2007).
- 88 Fang, X., Bando, Y., Ye, C. & Golberg, D. Crystal orientation-ordered ZnS nanobelt quasi-arrays and their enhanced field-emission. *Chemical Communications*, **29**, 3048-3050 (2007).
- 89 Fang, X., Wu, L. & Hu, L. ZnS Nanostructure Arrays: A Developing Material Star. *Advanced Materials* **23**, 585-598 (2011).
- 90 Fang, X. *et al.* Multiangular branched ZnS nanostructures with needle-shaped tips: Potential luminescent and field-emitter nanomaterial. *Journal of Physical Chemistry C* **112**, 4735-4742 (2008).
- 91 Gautam, U. K., Fang, X., Bando, Y., Zhan, J. & Golberg, D. Synthesis, structure, and multiply enhanced field-emission properties of branched ZnS nanotube - In nanowire core-shell heterostructures. *Acs Nano* **2**, 1015-1021 (2008).
- 92 Liao, A.-Z., Zhu, W.-D., Chen, J.-B., Zhang, X.-Q. & Wang, C.-W. Vertically aligned single-crystalline ultra-thin CuO nanosheets: Low-temperature fabrication, growth mechanism, and excellent field emission. *Journal of Alloys and Compounds* **609**, 253-261 (2014).
- 93 Zhao, X., Wang, P. & Li, B. CuO/ZnO core/shell heterostructure nanowire arrays: synthesis, optical property, and energy application. *Chemical Communications* **46**, 6768-6770 (2010).
- 94 Yamada, T., Masuzawa, T., Ebisudani, T., Okano, K. & Taniguchi, T. Field emission characteristics from graphene on hexagonal boron nitride. *Applied Physics Letters* **104**, 5 (2014).
- 95 Yamada, T. *et al.* in *27<sup>th</sup> International Vacuum Nanoelectronics Conference* 182-183 (Engelberg, Switzerland, 2014).
- 96 Preobrajenski, A. B., Vinogradov, A. S. & Martensson, N. Monolayer of h-BN chemisorbed on Cu(111) and Ni(111): The role of the transition metal 3d states. *Surface Science* **582**, 21-30 (2005).
- 97 Ohtani, S. *et al.* Electron emission from h-BN films codoped with Mg and O atoms. *Thin Solid Films* **546**, 53-57 (2013).
- 98 Yu, T. *et al.* Controlled growth and field-emission properties of cobalt oxide nanowalls. *Advanced Materials* **17**, 1595-1599 (2005).
- 99 Kashid, R. V. *et al.* Enhanced Field-Emission Behavior of Layered MoS<sub>2</sub> Sheets. *Small* **9**, 2730-2734 (2013).
- 100 Yun, J.-M. *et al.* Efficient work-function engineering of solution-processed MoS<sub>2</sub> thin-films for novel hole and electron transport layers leading to high-performance polymer solar cells. *Journal of Materials Chemistry C* **1**, 3777 (2013).
- 101 Zhang, Q. *et al.* Synthesis of a MoS<sub>2</sub>@MWNT nanostructure with enhanced field emission and electrochemical properties. *Rsc Advances* **3**, 10994-11000 (2013).
- 102 Jiang, L. *et al.* Controlled Synthesis of Large-Scale, Uniform, Vertically Standing Graphene for High-Performance Field Emitters. *Advanced Materials* **25**, 250-255 (2013).
- 103 Malesev, A. *et al.* Field emission from vertically aligned few-layer graphene. *Journal of Applied Physics* **104** (2008).
- 104 Zhao, N. *et al.* in *27<sup>th</sup> International Vacuum Nanoelectronics Conference* 153-154 (Engelberg, Switzerland, 2014).
- 105 Wu, Z.-S. *et al.* Field Emission of Single-Layer Graphene Films Prepared by Electrophoretic Deposition. *Advanced Materials* **21**, 1756-1760 (2009).
- 106 Wu, C., Li, F., Zhang, Y. & Guo, T. Field emission from vertical graphene sheets formed by screen-printing technique. *Vacuum* **94**, 48-52 (2013).
- 107 Jeong, H. J. *et al.* Flexible Field Emission from Thermally Welded Chemically Doped Graphene Thin Films. *Small* **8**, 272-280 (2012).

### 3. High Performance Field Emitter Characteristics

- 108 Li, L. *et al.* Floral-clustered few-layer graphene nanosheet array as high performance field emitter. *Nanoscale* **4**, 6383-6388 (2012).
- 109 Pandey, S. *et al.* Improved electron field emission from morphologically disordered monolayer graphene. *Applied Physics Letters* **100** (2012).
- 110 Li, J., Chen, J., Luo, B., Yan, X. & Xue, Q. The improvement of the field emission properties from graphene films: Ti transition layer and annealing process. *Aip Advances* **2** (2012).
- 111 Yin, Y., Liu, W., Tian, K., Wei, X. & Wang, X. in *27<sup>th</sup> International Vacuum Nanoelectronics Conference* 46-47 (Engelberg, Switzerland, 2014).
- 112 Palnitkar, U. A. *et al.* Remarkably low turn-on field emission in undoped, nitrogen-doped, and boron-doped graphene. *Applied Physics Letters* **97** (2010).
- 113 Chen, W. *et al.* in *27<sup>th</sup> International Vacuum Nanoelectronics Conference* 36-37 (Engelberg, Switzerland, 2014).
- 114 Rout, C. S. *et al.* Superior Field Emission Properties of Layered WS<sub>2</sub>-RGO Nanocomposites. *Scientific Reports* **3** (2013).
- 115 Chuang, A. T. H., Robertson, J., Boskovic, B. O. & Koziol, K. K. K. Three-dimensional carbon nanowall structures. *Applied Physics Letters* **90** (2007).
- 116 Banerjee, D., Mukherjee, S. & Chattopadhyay, K. K. Synthesis of amorphous carbon nanowalls by DC-PECVD on different substrates and study of its field emission properties. *Applied Surface Science* **257**, 3717-3722 (2011).
- 117 Wu, Y. H. *et al.* Carbon nanowalls and related materials. *Journal of Materials Chemistry* **14**, 469-477 (2004).
- 118 Rout, C. S. *et al.* Superior Field Emission Properties of Layered WS<sub>2</sub>-RGO Nanocomposites. *Scientific Reports* **3**, 1-8 (2013).
- 119 Young, S.-J. & Liu, Y.-H. Enhanced Field Emission Properties of Two-Dimensional ZnO Nanosheets Under UV illumination. *IEEE Journal of Selected Topics in Quantum Electronics* **21**, 9100304 (2015).
- 120 Schroeder, P. G., Nelson, M. W., Parkinson, B. A. & Schlaf, R. Investigation of band bending and charging phenomena in frontier orbital alignment measurements of para-quaterphenyl thin films grown on highly oriented pyrolytic graphite and SnS<sub>2</sub>. *Surface Science* **459**, 349-364 (2000).
- 121 Schroeder, P. G., France, C. B., Park, J. B. & Parkinson, B. A. Orbital alignment and morphology of pentacene deposited on Au(111) and SnS<sub>2</sub> studied using photoemission spectroscopy. *Journal of Physical Chemistry B* **107**, 2253-2261 (2003).
- 122 Joshi, P. D., Joag, D. S., Rout, C. S. & Late, D. J. in *27<sup>th</sup> International Vacuum Nanoelectronics Conference* 241-242 (Engelberg, Switzerland, 2014).
- 123 Kan, M.-C., Huang, J.-L., Sung, J. C., Chen, K.-H. & Yau, B.-S. Thermionic emission of amorphous diamond and field emission of carbon nanotubes. *Carbon* **41**, 2839-2845 (2003).
- 124 Yutani, A., Kobayashi, A. & Kinbara, A. Work functions of thin LaB<sub>6</sub> films. *Applied Surface Science* **70-71, Part 2**, 737-741 (1993).
- 125 Menaka, Patra, R., Ghosh, S. & Ganguli, A. K. Manipulating the anisotropy and field emission of lanthanum hexaboride nanorods. *Rsc Advances* **2**, 7875-7885 (2012).
- 126 Xu, J. *et al.* Fabrication of vertically aligned single-crystalline lanthanum hexaboride nanowire arrays and investigation of their field emission. *NPG Asia Materials* **5**, 1-9 (2013).
- 127 Jha, M., Patra, R., Ghosh, S. & Ganguli, A. K. Vertically aligned nanorods of lanthanum hexaboride with efficient field emission properties. *Solid State Communications* **153**, 35-39 (2013).
- 128 Huang, B.-R. *et al.* Field emission property of arrayed nanocrystalline diamond. *Diamond and Related Materials* **20**, 314-317 (2011).
- 129 Raina, S., Kang, W. P. & Davidson, J. L. Field emission from nanodiamond grown with 'ridge' type geometrically enhanced features. *Diamond and Related Materials* **17**, 790-793 (2008).
- 130 Jung, H. S., Park, H. H., Pang, S. S. & Lee, S. Y. The structural and electron field emission characteristics of pulsed laser deposited diamond-like carbon films with thermal treatment. *Thin Solid Films* **355**, 151-156 (1999).
- 131 Zanin, H., May, P. W., Hamanaka, M. H. M. O. & Corat, E. J. Field Emission from Hybrid Diamond-like Carbon and Carbon Nanotube Composite Structures. *Acs Applied Materials & Interfaces* **5**, 12238-12243 (2013).
- 132 Tripathi, R. K., Panwar, O. S., Srivastava, A. K., Rawal, I. & Chockalingam, S. Structural, nanomechanical, field emission and ammonia gas sensing properties of nitrogenated amorphous carbon films deposited by filtered anodic jet carbon arc technique. *Talanta* **125**, 276-283 (2014).
- 133 Sun, W. *et al.* Morphology inducing selective plasma etching for AlN nanocone arrays: tip-size dependent photoluminescence and enhanced field emission properties. *Journal of Materials Chemistry C* **2**, 2417-2422 (2014).

- 134 Robertson, J. Mechanisms of electron field emission from diamond, diamond-like carbon, and nanostructured carbon. *Journal of Vacuum Science & Technology B* **17**, 659-665 (1999).
- 135 Hart, A., Satyanarayana, B. S., Milne, W. I. & Robertson, J. Effect of surface treatment and back contact material on field emission from tetrahedral amorphous carbon. *Diamond and Related Materials* **8**, 809-813 (1999).
- 136 Ilie, A., Hart, A., Flewitt, A. J., Robertson, J. & Milne, W. I. Effect of work function and surface microstructure on field emission of tetrahedral amorphous carbon. *Journal of Applied Physics* **88**, 6002-6010 (2000).
- 137 Milne, W. I. Field emission from tetrahedrally bonded amorphous carbon. *Applied Surface Science* **146**, 262-268 (1999).
- 138 Ng, K. L., Yuan, J., Cheung, J. T. & Cheah, K. W. Electron field emission characteristics of electrochemical etched Si tip array. *Solid State Communications* **123**, 205-207 (2002).
- 139 Pan, Z. X., She, J. C., Deng, S. Z. & Xu, N. S. in *27<sup>th</sup> International Vacuum Nanoelectronics Conference* 74-75 (Engelberg, Switzerland, 2014).
- 140 Chen, S. X., Li, J. J., Gu, C. Z. & Ieee. Field Emission from the Composite Structure of Silicon Tips and Vertical Carbon Nanotubes. *2007 7th Ieee Conference on Nanotechnology, Vol 1-3*, 367-370 (2007).
- 141 Glesener, J. W., Lin, H. B. & Morrish, A. A. Field emission from cleaved diamond fibers. *Thin Solid Films* **308**, 204-208 (1997).
- 142 Cheng, H.-F. *et al.* Bias enhanced nucleation and growth processes for improving the electron field emission properties of diamond films. *Surface & Coatings Technology* **228**, 175-178 (2013).
- 143 Zhao, F., Zhao, D.-d., Wu, S.-l., Cheng, G.-a. & Zheng, R.-t. Diamond-like carbon decoration enhances the field electron emission of silicon nanowires. *Surface and Coatings Technology* **228**, **Supplement 1**, S349-S353 (2013).
- 144 Abbott, P., Sosa, E. D. & Golden, D. E. Effect of average grain size on the work function of diamond films. *Applied Physics Letters* **79**, 2835-2837 (2001).
- 145 Song, X., Zhao, C. X., Wu, J. Q., Chen, J. & Ieee. in *25th International Vacuum Nanoelectronics Conference (IVNC)*. 376-377 (2012).
- 146 Gautam, U. K. *et al.* Solvothermal Synthesis, Cathodoluminescence, and Field-Emission Properties of Pure and N-Doped ZnO Nanobullets. *Advanced Functional Materials* **19**, 131-140 (2009).
- 147 Wang, J. *et al.* Controlled growth of nickel nanocrystal arrays and their field electron emission performance enhancement via removing adsorbed gas molecules. *Crystengcomm* **15**, 1296-1306 (2013).
- 148 Le Shim, E. *et al.* in *25th International Vacuum Nanoelectronics Conference (IVNC)*. 198-199 (2012).
- 149 Joo, S. W. & Banerjee, A. N. Field emission characterization of vertically oriented uniformly grown nickel nanorod arrays on metal-coated silicon substrate. *Journal of Applied Physics* **107** (2010).
- 150 Nakane, T. *et al.* Field-emission barrier height of an alloy tip: Possible effect of surface segregation. *Journal of Vacuum Science & Technology a-Vacuum Surfaces and Films* **15**, 1563-1567 (1997).
- 151 Wang, J. & Ito, T. Improved field emission characteristics of nano-structured carbon films deposited on polycrystalline CVD diamond. *Diamond and Related Materials* **16**, 364-368 (2007).
- 152 Cui, J. B. *et al.* Hydrogen termination and electron emission from CVD diamond surfaces: a combined secondary electron emission, photoelectron emission microscopy, photoelectron yield, and field emission study. *Diamond and Related Materials* **9**, 1143-1147 (2000).
- 153 Gröning, O. Properties and characterization of chemical vapor deposition diamond field emitters. *Solid-state electronics* **45**, 929-944 (2001).
- 154 Ooi, N. & Adams, J. B. Ab initio studies of the cubic boron nitride (111) surface. *Surface Science* **574**, 269-286 (2005).
- 155 Cutler, P. H. *et al.* Theory Of Electron-Emission in High Fields from Atomically Sharp Emitters - Validity of the Fowler Nordheim Equation. *Progress in Surface Science* **42**, 169-185 (1993).
- 156 Bundaleski, N., Trigueiro, J., Silva, A. G., Moutinho, A. M. C. & Teodoro, O. M. N. D. Influence of the patch field on work function measurements based on the secondary electron emission. *Journal of Applied Physics* **113** (2013).
- 157 Murray, P. T. *et al.* Evidence for adsorbate-enhanced field emission from carbon nanotube fibers. *Applied Physics Letters* **103** (2013).
- 158 Kar, S. *et al.* Quantitative analysis of hysteresis in carbon nanotube field-effect devices. *Applied Physics Letters* **89** (2006).
- 159 Kuznetsov, A. A., Lee, S. B., Zhang, M., Baughman, R. H. & Zakhidov, A. A. Electron field emission from transparent multiwalled carbon nanotube sheets for inverted field emission displays. *Carbon* **48**, 41-46 (2010).
- 160 Lim, S. C. *et al.* Field-emission properties of vertically aligned carbon-nanotube array dependent on gas exposures and growth conditions. *Journal of Vacuum Science & Technology a-Vacuum Surfaces and Films* **19**, 1786-1789 (2001).

### 3. High Performance Field Emitter Characteristics

- 161 Zhai, T. *et al.* Characterization, Cathodoluminescence, and Field-Emission Properties of Morphology-Tunable CdS Micro/Nanostructures. *Advanced Functional Materials* **19**, 2423-2430 (2009).
- 162 Huang, K.-J., Hsiao, Y.-S. & Whang, W.-T. Selective growth and enhanced field emission properties of micropatterned iron phthalocyanine nanofiber arrays. *Organic Electronics* **12**, 1826-1834 (2011).

# **4. Emitter Morphology for Enhanced Maximum Current**



## 4.1 Introduction

In this chapter, emitter morphology and the associated field enhancement factor,  $\beta$ , are experimentally investigated. A number of CNT surface geometries are studied herein in an attempt to better understand the primary influential factors driving high current output and early current onset. The conditions in which they were made and measured were carefully controlled. CNTs proved promising in the previous work function study, thus justifying their use for these studies. Using just one material, fabrication method, and measurement process allows minimisation of the variables seen in the meta-analysis of the previous chapter. A scanning anode field emission microscope, SAFEM, and parallel plate set up are used to measure emission current from a number of fabricated patterned CNTs when an electric field is induced by application of a fixed voltage.

## 4.2 Emitter Fabrication

The CNTs are grown using chemical vapour deposition, CVD, which allows both aligned fabrication and selected area growth. Previous effort, by Dr M. T. Cole, to optimise the growth progress was performed and has been adopted herein. Previous works that have used the following method described, used in this chapter, can be found at <sup>1,2</sup>.

In house fabrication and measurement of the devices was performed, ensuring maintained fine control of the procedure. Emitters were fabricated using several steps requiring different technical processes. In total, 52 variations of emitter were fabricated, all with different surface morphologies and heights.

### 4.2.1 Techniques and Equipment

Commercial and custom built equipment is used in the preparation of emitters. Methods used in the process include: patterning by electron beam lithography; catalyst deposition by direct current, DC, magnetron sputtering; and thermal CVD to grow CNTs. Other equipment used in the process include spinners, hot plates, microscopes and scanning electron microscopes, SEMs. The fabrication took place in the Class 10, 000, Class 1000 and Class 100 clean rooms in the Electrical Engineering Division Building at the University of Cambridge.

### **4.2.1.1 Electron Beam Photolithography: *NanoBeam EBL***

Electron beam photolithography is a high precision lithography process with a resolution down to 100 nm. To be able to mark a substrate surface, a photoresist must be applied. Electrons interact with the resist, selectively exposing predetermined areas. Common resists include poly(methyl methacrylate), PMMA, and UVIII, both of which are positive resists. A positive resist changes its chemical structure under exposure, becoming soluble in a photo developer solution, which then removes the photoresist from the patterned areas.

Prepared samples were fabricated using the *NanoBeam EBL* in the Class 100 clean room environment. An initial step consisted of manually loading the pre-prepared samples onto a chuck. Twelve 10 mm × 10 mm samples were loaded at once. The chuck, housed in a cassette, was then loaded into an airlock, a small chamber adjacent to the main chamber containing the writing electron beam. Once loaded, the system is pumped to a pressure  $< 10^{-6}$  mbar. This ensures the main chamber remains at constant high vacuum, protecting it from ambient and vastly increasing time efficiency of establishing a safe working environment. When sufficient pressure has been reached a robot arm transfers the selected chuck onto a stage under the electron gun in the main chamber. The stage moves in the *xy*-plane with an accuracy of 100 nm and is coupled with a laser interferometer that can accurately determine the location with a precision down to 1 nm. A column houses the electron gun and associated optics that direct a collimated beam of highly focussed electrons onto the sample.

Pre-determined pattern files are used to selectively remove the photoresist. Pattern files were created using computer aided drawing, CAD, software, *Draftsight*, and were converted to nanobeam pattern files, npf, using a program *nbpat*. The electron beam is raster scanned, by movement of the stage, over the substrate, interacting with the photoresist in prescribed regions.

There are a number of limitations in this process. Firstly, inconsistent average thickness of photoresist per chip and across a single chip can be caused by uneven distribution during spinning, where increased thickness is seen towards the edges. If the electron beam and developer successfully remove the photoresist from the determined locations, however, this is not problematic. Contamination or variations in photoresist can be seen depending, for example, on origin from different bottles or age of photoresist at the time of use. This can result

in lack of reaction to exposure, solved by repeating using a different resist. Furthermore, scattering of the electrons in the photoresist from backscattered electrons, known as the proximity effect<sup>3</sup>, limits the resolution, although corrections can be made for this. This is a more significant problem when fabricating dimensions close to the resolution of the beam, which for the majority of cases herein is not important.

Finally, it has been seen that faults in the patterning, from the pattern file or beam exposure, can lead to incomplete patterning or patterning in selective areas only. This is a more challenging problem as there is no simple solution. It can be impractical and lengthy to accurately determine areas of exposure. These errors can manifest in further calculations, e.g. surface coverage of CNTs, which can vary drastically from the pattern files.

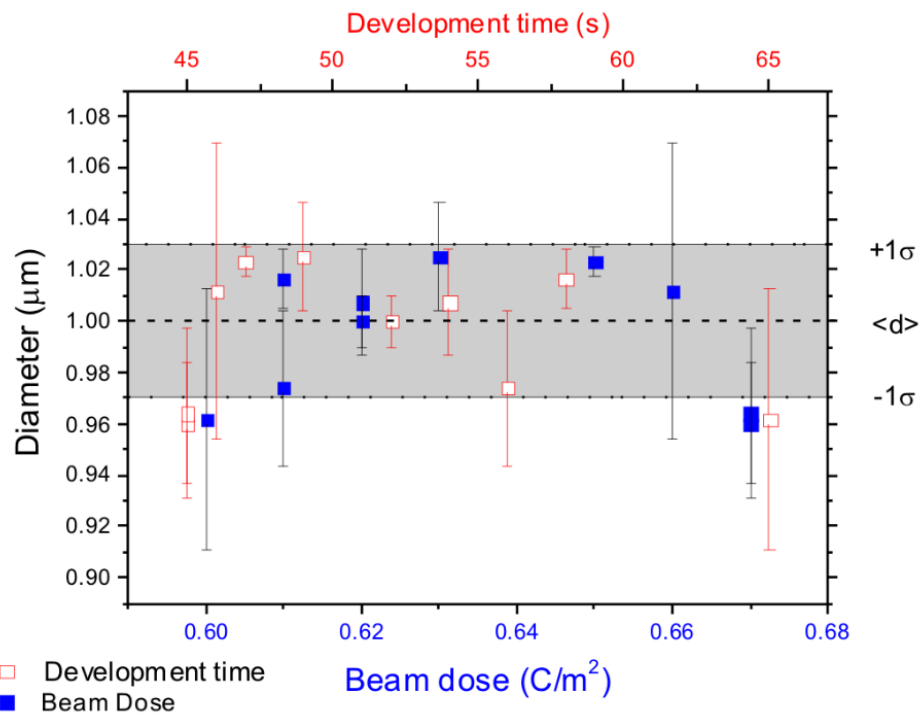


**Figure 4.1 | Beam Exposure and Dosage.** Results on the effect of circular pattern with diameter of 1  $\mu\text{m}$ .

The beam dosage is an influential parameter that can vary according to the resist used, which in this case was predominantly UVIII. To assess the required development times and appropriate electron beam dosage to attain the precision as prescribed by the pattern, a test was performed. In the experiment, samples were exposed to increasing beam dose and decreasing development time. The results of this can be seen in Figure 4.1, where the best results, closest to the desired circular pattern diameter of 1  $\mu\text{m}$ , was acquired with a beam dose of 0.62  $\text{C}/\text{m}^2$

#### 4. Emitter Morphology for Enhanced Maximum Current

and a development time of 52 seconds. The beam dose appears more influential in the final diameter of the patterned cylinder than the development time. It should be noted that the mean diameter across the different exposures and development times was equal to the intended diameter and most values fell within one standard deviation of this.

##### **4.2.1.2 Direct Current Magnetron Sputtering**

Catalyst materials are sputtered to produce a controllably thin layer, usually a few tens of atoms thick, of metal onto the substrate. The catalyst is distributed across the entire exposed surface; the photoresist acts as a barrier, preventing sputtered materials from being deposited permanently on the silicon surface, except where it has been selectively removed. After annealing, the deposited catalyst breaks down in a process termed Ostwald Ripening<sup>4</sup> to form nanoparticle nucleation sites upon which the CNTs grow or self-assemble<sup>5,6</sup>. The diameters of these nanoparticles is highly influential in determining the diameter of the nanotube given the templating nature of the process<sup>7</sup>.

During sputtering a base pressure of  $3.0 (\pm 0.3) \times 10^{-3}$  mbar is maintained under 35 sccm of argon. Magnetron power and time of exposure, both of which are chosen according to individual recipes, have been previously studied to determine a desired catalyst thickness and therein CNT growth. Shutters are used to control the exposure time by shielding the samples from an active gun, avoiding unwanted sputtering. Plasma power is monitored through a computer controlled graphical user interface, GUI, which interacts with the magnetron power source. After the sputter process, the chamber is pumped to base pressure and then vented. No vent is required between sputtering of different metals, but for cleanliness a purge down to pressures  $< 1.5 \times 10^{-5}$  mbar between sputtering was performed.

A tooling factor, resulting in uneven distribution of metal atoms across the sputtering area, can manifest as height variation in CNTs across samples. There is also a risk that conditions change between uses of the machine, resulting in inconsistent sputter depths. This will also manifest in CNT growth variations. By maintaining consistent sputter conditions (exposure, metal target, pressure) this limitation was minimised.

##### **4.2.1.3 CNT Growth: Aixtron “Black Magic”**

Once the catalyst had been deposited, CNTs were grown using thermal CVD in an *Aixtron Black Magic* CVD system. The samples, with patterned catalyst, were placed in the centre of the chamber on a thin, raised graphite heater. Ammonia,  $\text{NH}_3$ , and acetylene,  $\text{C}_2\text{H}_2$ , gases were fed into the evacuated chamber and the sample was ohmically heated through the graphite stage. Acetylene provided the carbon source from which the nanotube structure develops, whilst ammonia pyrolysis to atomic hydrogen etches *a*-C and other undesirable carbon species.

An initial annealing process breaks down the sputtered catalyst into nanoparticles from which the nanotubes are grown in a bottom-up process. Catalyst particles remain at the base of the CNT, on the substrate, in a 'base-growth' method. In a 'tip-growth' method, however, the catalyst particles reside at CNT tip and stay there throughout the growth. Initial growth steps involve absorption and decomposition of hydrocarbons onto the catalyst nanoparticle surface and diffusion of carbonic atoms into the catalyst bulk from the supersaturated catalyst surface<sup>8</sup>.

A manually operated valve controls the aperture between the vacuum pump and the CVD chamber. Control of the aperture allows control over the chamber pressure, which can be adjusted according to individual recipes. An Al/Fe bilayer catalyst requires pressures of 25 mbar, achieved through constant small manual adjustments of the primary pump valve. The samples were placed on an elevated heating element in the centre of the chamber that can reach temperatures of up to 1000 °C. The thermal ramp rate was maintained at a constant of 5 °C/s for the full extent of the experiments. After CNT growth, the chamber was pumped down to  $10^{-1}$  mbar to purge the chamber of ammonia and acetylene, followed by a vent to ambient. PECVD can also be achieved using this apparatus, enhancing the linear alignment of CNTs whilst simultaneously augmenting the growth kinetics<sup>9</sup>. In PECVD, the pressure is kept lower, at around 3 mbar, with the aperture fully open.

It is currently impossible to grow a forest, a term that refers to the high packing density in which CNTs grow from a homogeneously deposited catalyst, with identical properties of height and diameter throughout the forest. In the FE process this leads to preferential emission from tips that are taller than their surrounding neighbours. This can be minimised by growing aligned CNTs using a CVD process. Exact replication of average heights, and indeed height distribution, is not guaranteed due to factors including catalyst deposition, gas flow kinetics, statistical variation and continuous nature of the growth. The tooling factor associated with

#### 4. Emitter Morphology for Enhanced Maximum Current

sputtering results in inhomogeneous catalyst deposition resulting in density and height variations of CNTs across a single sample. Manual control of pressure results in fluctuations ( $\pm 0.5$  mbar), likely also affected the way the CNTs grew, particularly with regards to their height.

### 4.2.2 Fabrication Methodology

Preparation of the chips and growth of CNTs is undertaken using the following general procedure:

1. Diamond dice silicon wafer into  $10 \text{ mm} \times 10 \text{ mm}$  samples.
  - a. The type of silicon used had the following properties: test grade, *n* type, with an antimony dopant, 4" diameter, thickness =  $515 \pm 15 \text{ }\mu\text{m}$ , orientation  $\langle 100 \rangle \pm 0.5^\circ$ , and resistivity  $0.1 - 0.25 \text{ }\Omega \text{ cm}$ .
2. Coat the wafer in UVIII photoresist using a spinner at 5000 rpm for 30 s, for a typical thickness of around 100 nm, then bake at  $120^\circ\text{C}$  for 90 s using a hot plate.
3. Write the desired pattern into the photoresist using electron beam lithography with a beam dose of  $0.62 \text{ C/m}^2$ .
4. After patterning, an additional bake is required before developing of 90 s at  $120^\circ\text{C}$ .
5. Develop using MFCD – 26 Developer with a 52 s exposure time.
6. Sputter metal catalyst. An Al/Fe catalyst is sputtered, depositing Al first at 50 W for 120 s, followed by Fe at 20 W for 150 s. This results in  $10 \pm 1 \text{ nm}$  Al and  $1.0 \pm 0.1 \text{ nm}$  Fe deposition.
7. Lift off the photoresist in acetone for a minimum of 3 hours. Ultrasonication can be used on patterns with a micron-range scale, anything smaller can result in movement of the catalyst particles about the chip.
8. Grow CNTs using CVD process detailed above. During the growth process, a pressure of  $25.0 \pm 0.5 \text{ mbar}$  is maintained with a temperature of  $520^\circ\text{C}$ . CVD is used to grow the CNTS, with a ratio of  $\text{NH}_3$  to  $\text{C}_2\text{H}_2$  of 192:8 sccm.

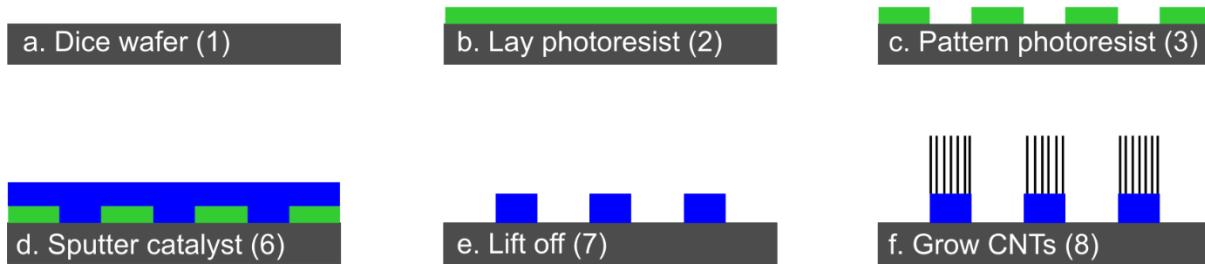


**Figure 4.2 | Emitter Fabrication.** Steps detailing fabrication of patterned CNT emitters (numbers in brackets refer to the fabrication steps detailed above).

Figure 4.2 depicts the processes involved in growing the patterned emitters for the steps detailed above. Typical growth times are between  $t_0 = 0$  s and  $t_0 = 240$  s, where  $t_0$  is defined as the point at which an arbitrary temperature of  $475$  °C is reached. CNTs start to grow across a range of temperatures, so some growth is seen at  $t_0 = 0$  s; it is simply used as a marker to ensure consistency and repeatability. The grown CNTs are  $25.4 \pm 13.3$  nm diameter, with between 2 and 5 walls. A calibration curve of growth time and resulting height was determined by altering the exposure time of the samples to the growth conditions. A maximum height of  $5$   $\mu\text{m}$  was found using this recipe.

### 4.2.3 Emitter Design

In order to competently study the effect of emitter morphology on FE performance, a range of designs were developed and fabricated. Designs were produced using *Draftsight* (CAD software). In order to reduce the measurement time, since only one sample can be measured at a time and a day pumping to vacuum is required, designated zones on a sample containing variations according to wall thickness and spacing are designed to gain as much information as possible at once. Previous studies using different morphologies, by Cole<sup>10</sup> and Li<sup>11</sup>, were conducted without rigorous investigation of the influence of the direct geometry. Herein the aim is to build on this work, resulting in the hopeful optimisation of the arrays.

#### 4.2.3.1 Pillar Arrays and Aspect Ratio

Emitter morphology was split into two different studies; aspect ratio, AR, and unit cell geometry. Conducting an AR study focusses on determining screening effect using CNT pillars. AR has been implicated in  $\beta$  in relation to Fowler Nordheim theory discussed earlier<sup>12-15</sup>, although intimate workings are not fully known. The electron screening effect occurs

#### 4. Emitter Morphology for Enhanced Maximum Current

between neighbouring CNTs and results in reduced local electric fields at high CNT densities, often dramatically affecting emission. The morphology of the chips was deliberately designed to include a number of different ratios, Figure 4.3 shows one of these ratios; the diameter of the pillars was kept at a constant  $10\ \mu\text{m}$  but the pitch was varied. The pitch is defined as the distance between pillars, centre-to-centre, and was given nine values per chip, gathered into nine distinct zones. Growing the samples at a number of different heights introduced a further variable.

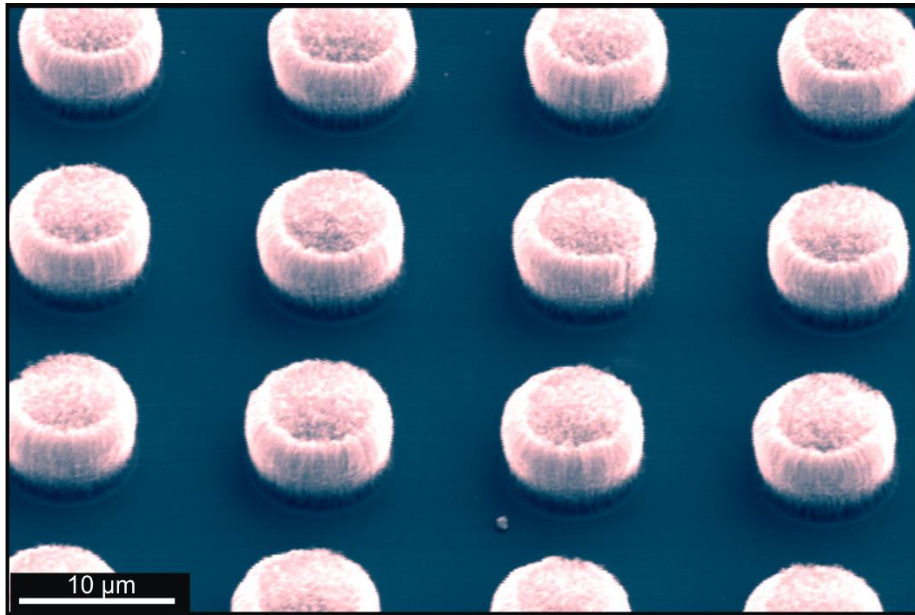


**Figure 4.3 | Pillar Array Scanning Electron Micrographs.** Example of the aspect ratio study pillars with a pitch of  $15\ \mu\text{m}$ .

It can be seen from Figure 4.3 that densification occurs around the edges of the pillar, additional growth can also sometimes happen at the edges. This observation has previously also been reported by others<sup>16,17</sup>. Increased growth at the edges could be attributed to a greater quantity of gas present at the edges in fabrication compared to the central region. Gas flow within the growth chamber and exposure could likely affect where the longer CNTs grow. This could be attributed to Knudsen diffusion<sup>18</sup> or diffusion limited growth kinetics<sup>19</sup>, where diffusion of the feedstock gases through to the central areas is prohibited after a certain growth height has been achieved. Where CNTs grew significantly longer than their neighbours, they became unable to support themselves and collapsed, usually towards the centre where other CNTs are grown.

### 4.2.3.2 Unit Cell Geometry

To investigate the theory that emission occurs with increased probability from the edges and apexes of CNT bundles, here a number of geometries are tested. If emission is indeed more prevalent at an edge, defined by the outside limit of the CNTs, an increase in emission is expected to be seen in a geometry with eight edges (octagonal unit cell), compared to three (triangular unit cell). Figure 4.4 shows the designs for which CAD models were developed and then fabricated. It is expected that the number of increasing emission sites, with increasing number of edges and apexes, positively affects FE. Four parameters are defined: geometry of the unit cell,  $G$ , wall width,  $w$ , diameter or spacing,  $x$ , and growth height,  $h$ , of the CNTs. On a  $10\text{ mm} \times 10\text{ mm}$  sample, patterns have the same  $G$  and  $h$ , with zones of varying  $w$  and  $x$ , Figure 4.5 visualises two example CAD designs. Fabrication of both pillar,  $P$ , and inverse pillar,  $IP$ , formations were designed and fabricated. This variable maintains the same number of edges whilst changing emitting area. In addition, the screening effect is expected to be minimised in pillar formations. On each sample,  $x$  is scaled from  $5\text{ }\mu\text{m}$  to  $100\text{ }\mu\text{m}$  and  $w$  from  $1\text{ }\mu\text{m}$  to  $200\text{ }\mu\text{m}$ .

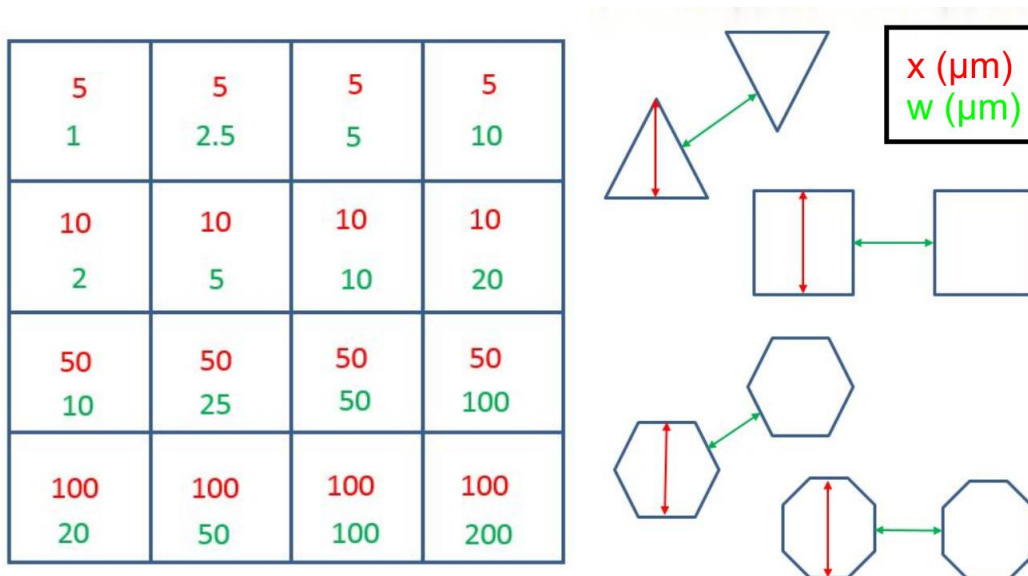


**Figure 4.4 | Emitter Pattern Design.** Dimensions of the grid on which inverse pillar,  $IP$ , arrays are designed, with wall width,  $w$ , (green) and diameter or spacing,  $x$ , (red). To the right hand side is a visualisation of  $w$  (green) and  $x$  (red) in context of each unit cell geometry.

#### 4. Emitter Morphology for Enhanced Maximum Current

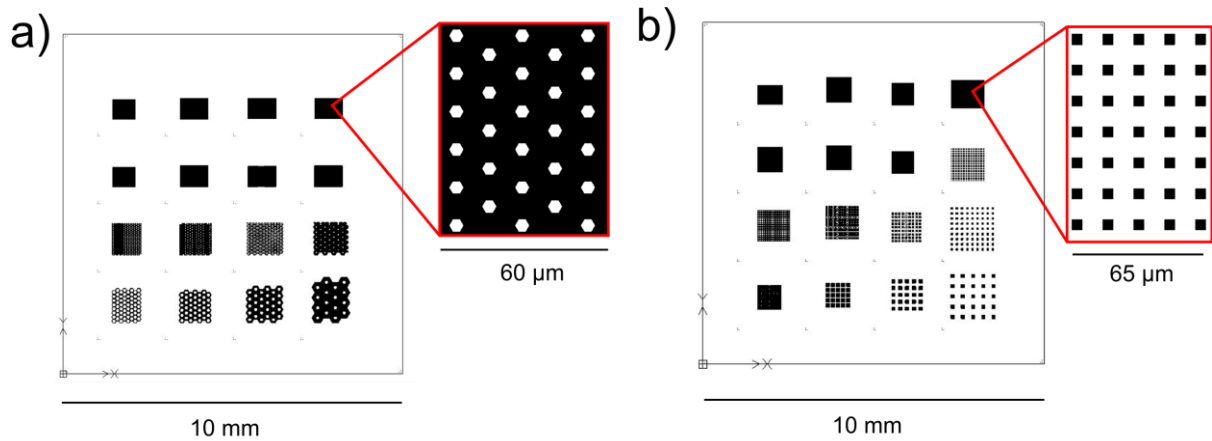


**Figure 4.5 | Emitter CAD Design.** a) Example of an inverse pillar array using a hexagonal geometry, dark regions show areas where CNTs are grown during fabrication. b) Example of a pillar array using a square geometry. Dark regions show CNT growth again.

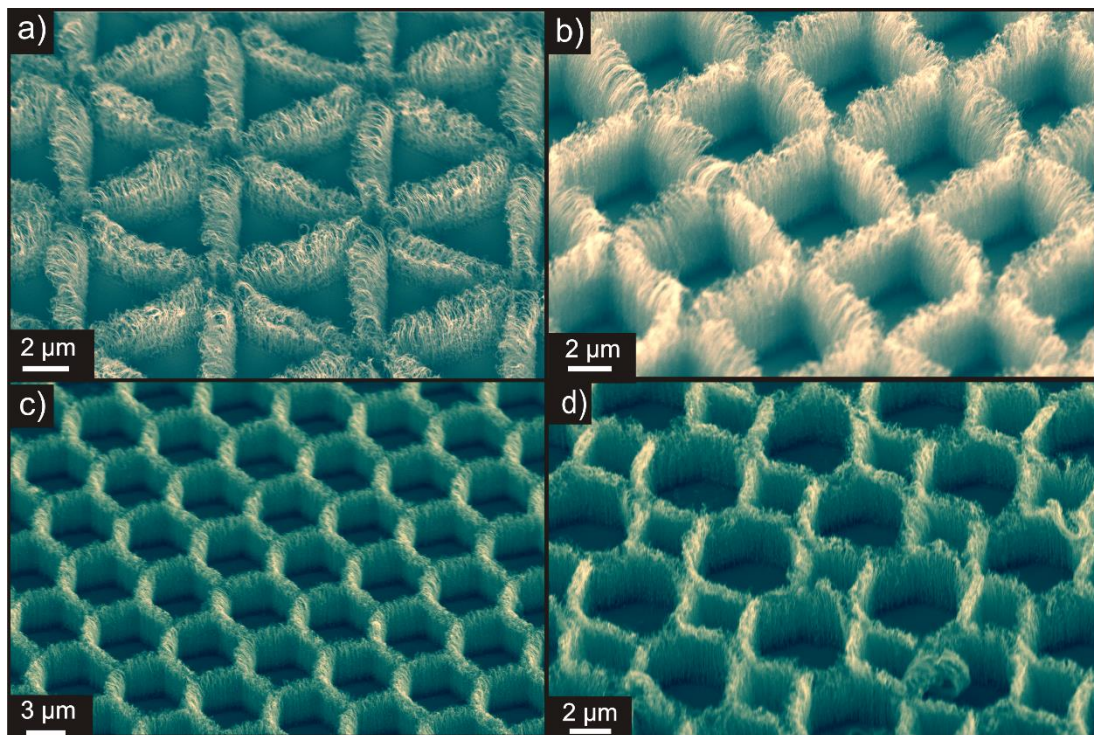


**Figure 4.6 | Geometrical Inverse Pillars.** Example scanning electron micrographs of different zones from a) Triangle b) Square c) Hexagon d) Octagon, where the lighter areas are CNT and darker are Si substrate.

Figures 4.6 and 4.7 show example scanning electron micrographs of the fabricated emitters from different regions across the *IP* and *P* geometries respectively, showcasing a variety of the

$w$  and  $x$  values used. Once again, as seen in Figure 4.3, some edges show densification and longer growth of CNTs at the edges. This is principally highlighted when the growth times are long, and  $x$  and  $w$  are small, e.g.  $x = 5 \mu\text{m}$ ,  $w = 1 \mu\text{m}$  and  $h$  is large, exemplified in Figure 4.8. There exists a notable imbalance in location of the longer CNTs, the effects on which, as they pertain to enhanced FE, could be influential. The growth time is influential in determining the difference in height between the edge and centre of the nanotube region, where greater growth times result in a larger difference.

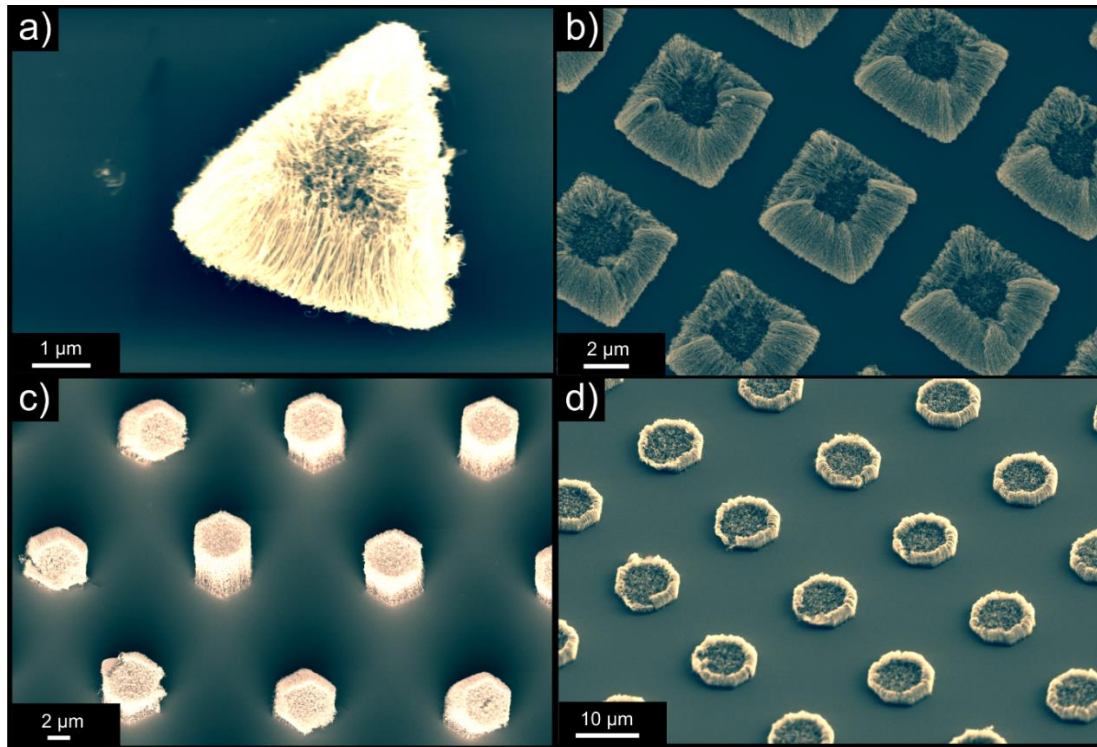


**Figure 4.7 | Geometrical Pillars.** Example scanning electron micrographs of the geometrical pillar patterns for a) Triangle b) Square c) Hexagon d) Octagon.

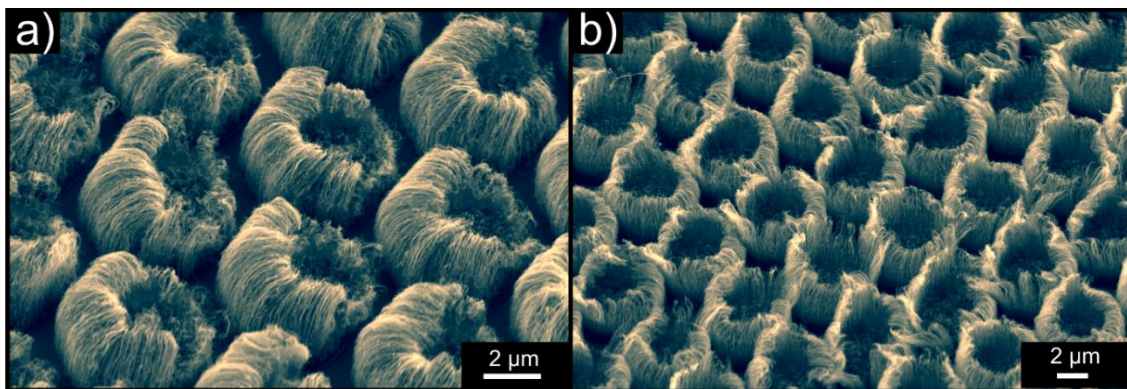


**Figure 4.8 | CNT Edge Growth.** Scanning electron micrographs showing edges grown to lengths much greater than central zones a) hexagon array and b) octagon array where  $x = 5$ ,  $w = 1$ .

### 4.3 Scanning Anode Field Emission Microscopy

A SAFEM was designed to measure and resolve the FE from a surface. Though FE itself is not unusual, it is usually measured in a parallel plate set up, where the entire emitting area of the sample contributes to emitted current. Far fewer numbers of researchers have published data collected using SAFEM technology, though it has been previously reported<sup>20-23</sup>. To measure FE from the surface necessitates a probe, or anode, that scans across the surface, building an emission map. Analysis of the resulting data shows areas of higher or lower emitted current across the surface, allowing direct comparisons to be made on the different fabricated morphologies and zones per chip as seen in Section 4.2.3 above.

The interaction of the probe with the surface is important to consider and has been reported by Thien Binh *et al*<sup>23</sup> and Semet *et al*<sup>22</sup> from the same research group. Comparisons were made between a conical and ball probe tip by mathematical modelling. Field distribution from a conical probe was dependent on cone angle, apex radius and distance to the cathode. Combining these factors into a comprehensive numerical solution proved challenging. Other complications, including contributions from the shank in the conical tip, lead to conclusions that the ball shaped probe presented the preferred tip structure to use in these measurements. A 250  $\mu\text{m}$  PtIr wire is melted by Semet *et al* to create the 350  $\mu\text{m}$  ball radius from which measurements were made. The field distribution induced by the ball probe across the emitting surface is non-uniform. To convert experimental data, from collected *I-V* into *J-E*, the field distribution must be known and can be calculated more efficiently using the ball probe.

The SAFEM has been custom built to measure spatially resolved FE. Figure 4.9 shows a photograph of the SAFEM and parallel plate in the laboratory. The right hand inserts (b and c) show the moving stages and the tip above one of the fabricated samples in the SAFEM side of the machine. A map of the electric field distribution is generated using a custom-built 3-axis stage ( $x, y, z$ ), where  $x$  and  $y$  move the chip in one plane and  $z$  moves the tungsten tip perpendicular to the  $xy$ -plane. The  $x$  and  $y$  piezo actuated stage (*Physik Instrumente LPS-45*) has a step size (in  $x$  and  $y$ ) of 40 nm with a maximum range of 13 mm. The  $z$  axis is made using a potassium hydroxide etched tungsten tip, which has a tip diameter of 100 nm, and a controllable step height of 1  $\mu\text{m}$ . The tip scans using a further piezo stage (*Physik Instrumente P-601.4S* piezo motor equipped with strain gauge and controlled using an *E-609* module) with

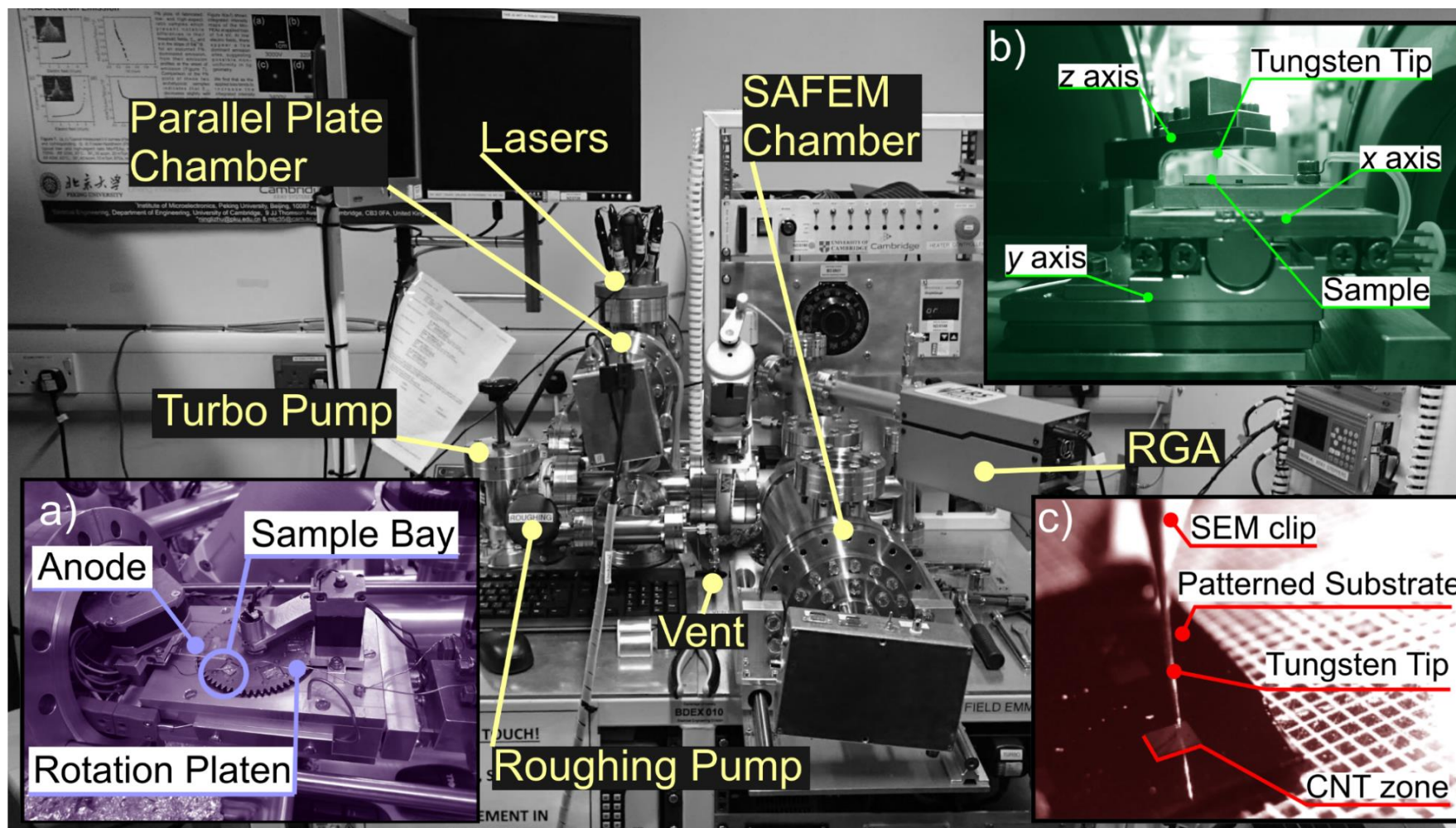


**Figure 4.9 | SAFEM and Parallel Plate Schematic.** Inserts show inside vacuum chambers of a) Parallel Plate b) SAFEM and c) close up of measurement area in SAFEM.

#### 4. Emitter Morphology for Enhanced Maximum Current

a range of 400  $\mu\text{m}$  and a resolution of 0.2 nm. Measurements are taken in a diode mode, with the tungsten tip positively biased between 0 V and 1100 V using a computer controlled high voltage supply (*Keithley 237*). Current is monitored using a source-measurement unit, SMU (*Keithley 485*). Measurements take place at ultra-high vacuum, UHV, between  $10^{-7}$  mbar and  $10^{-8}$  mbar.

### 4.3.1 Measuring Field Emission: Methodology

Samples were loaded onto the stage and fixed in position using SEM clips. Location of distinctive features was made at ambient pressure, determined by moving the tip and recording the corresponding coordinates. As no camera was available inside the chamber with a clear view of stage and tip location, these coordinates were relied upon to provide details on location of different zones and CNTs. Vacuum was achieved through use of roughing and turbomolecular pumps connected to the chamber.

A *LabView* program controls the measurement process. Variables entered into the GUI are as follows:  $x$ ,  $y$ ,  $z$ , and  $V$  range;  $\Delta x$ ,  $\Delta y$ ,  $\Delta z$ ,  $\Delta V$  step lengths; settling time at each voltage; and number of measurements at each voltage (3). The program follows the following procedure:

1. Home tip.
2. Move tip to measurement location  $x_1, y_1, z_1$ .
3. Perform FN sweep:
  - a. Increase voltage from 0 V to 1100 V and back down to 0 V in 100 V steps.
  - b. Measure the current three times at each voltage.
4. Move tip to  $x_2, y_1, z_1$ , where  $x_2 = x_1 + \Delta x$ , and repeat FN sweep.
5. Repeat  $x$  increment by  $n$  steps until the  $x$  range has been scanned, performing FN sweeps at each location.
6. Move tip to  $x_n, y_2, z_1$ , where  $y_2 = y_1 + \Delta y$ , and perform the measurements in the reverse  $x$  direction. Repeat this process over entire  $xy$ -plane.
7. Move tip to  $x_1, y_1, z_2$ , where  $z_2 = z_1 + \Delta z$ .
8. Repeat steps 2 - 5 to map a second plane.
9. Repeat until  $z_n$  heights have been mapped, and an effective 3D map of the electric field has been measured.

### 4.3.2 Field Emission Mapping

In this section, two geometries are mapped. The first is a tessellated hexagon pattern as seen in Figure 4.6c, and the second a cylindrical pillar as seen in Figure 4.3. Single  $xy$ -planes are shown here.

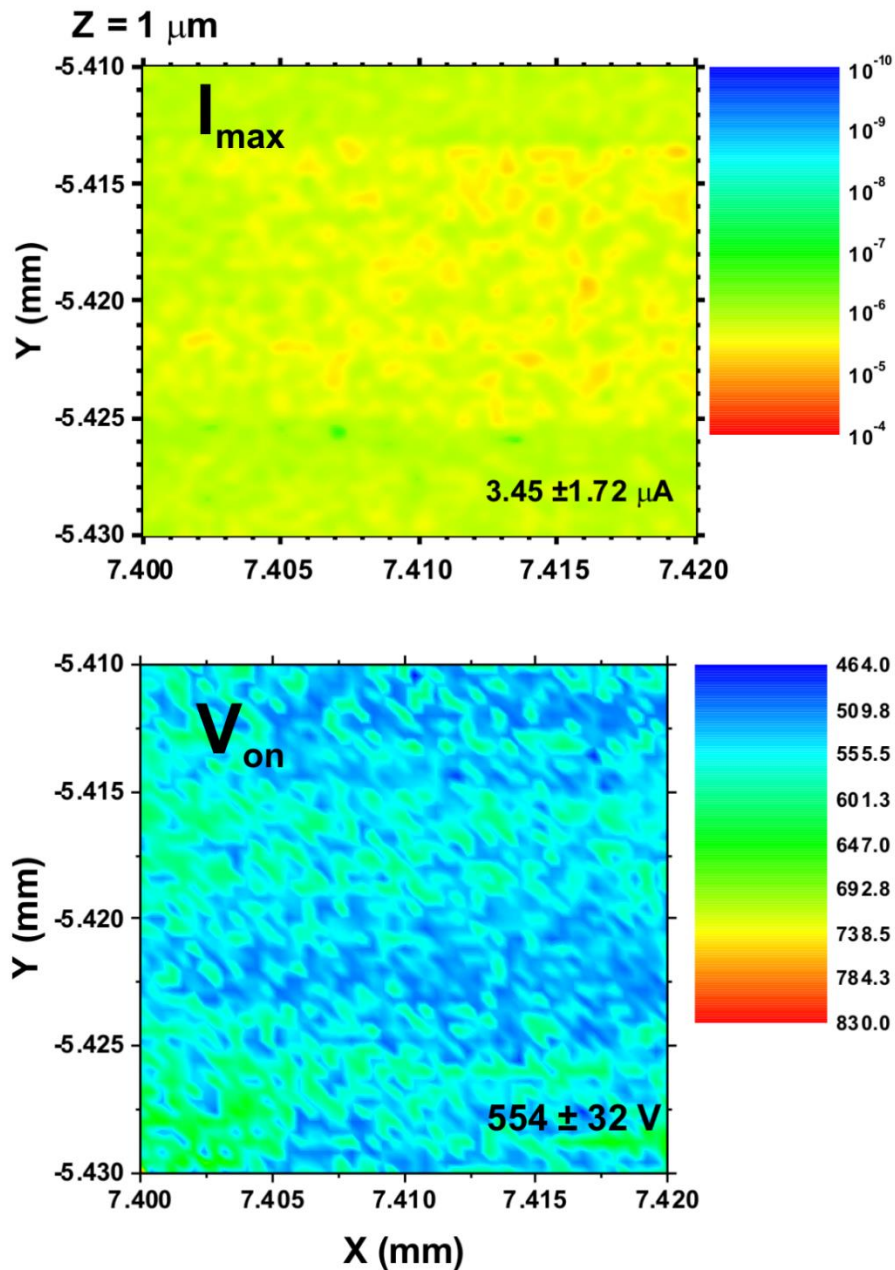


**Figure 4.10 | SAFEM Mapping.** Map of  $I_{\text{max}}$  and  $V_{\text{on}}$  of  $20 \mu\text{m} \times 20 \mu\text{m}$  area of hexagonal pattern at a height of  $1 \mu\text{m}$  from the surface.

#### 4. Emitter Morphology for Enhanced Maximum Current

Figure 4.10 shows the map of a hexagon patterned CNT substrate with a  $20\ \mu\text{m} \times 20\ \mu\text{m}$  area.  $I_{max}$  and  $V_{on}$  are plotted across the area by current measurements taken at  $4\ \mu\text{m}$  spacing across the region with the tip at a height of  $1\ \mu\text{m}$ .  $I_{max}$  is defined by the current measured at a voltage of  $1100\ \text{V}$ , and  $V_{on}$  is determined by the voltage at which a current of  $1\ \text{nA}$  is measured. There is a region of higher  $I_{max}$  between  $y = -5.425\ \text{mm}$  and  $y = -5.414\ \text{mm}$ . This is likely to be a region populated by CNTs. The same definition cannot be seen in the  $V_{on}$  map, suggesting that when the tip is over a CNT region, this does not affect when a current is measured, i.e.  $V_{on}$  remains somewhat constant and gives no indication to how high the current will reach ( $I_{max}$ ). A standard deviation of  $6\%$  of the measured average  $V_{on}$  versus nearly  $50\%$  for  $I_{max}$  shows that  $I_{max}$  is far more susceptible to immediate local surroundings (CNT/substrate), exhibiting a wider distribution about the mean.

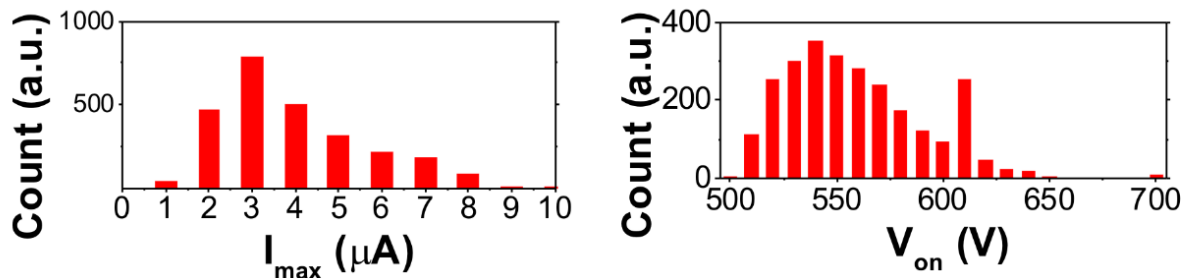


**Figure 4.11 | SAFEM Data Spread.** Distribution of measured values of a)  $I_{max}$  and b)  $V_{on}$ .

Histograms showing the distribution of  $I_{max}$  and  $V_{on}$  are shown in Figure 4.11. The distribution is skewed towards the lower end of the spectrum in both cases. This suggests that, according to previous postulations on variations in CNT heights, that a few CNTs contribute to FE more significantly than others<sup>20</sup>, around which  $\beta$  is locally enhanced. To verify that two materials are detected by their relative FE capabilities, two peaks would be expected to be seen when the data is arranged in this way. Here, however, the second, small peak seen in  $V_{on}$  is likely attributed to noise. This finding could also suggest that the assumed observed CNT strip could also just be noise in the system.

### 4.3.3 Tip Height from the Emitting Surface

In the far field, the electric field,  $E$ , has a direct relationship with separation,  $d$ , by  $E = V/d$ . It is not strictly known how  $d$  and  $I$  are related. The height of the tip,  $z$ , from the surface is predicted to have an influence on the measured current, or indeed the mapped output. Mapping across five different heights over a constant  $20\ \mu\text{m} \times 20\ \mu\text{m}$  area was performed.

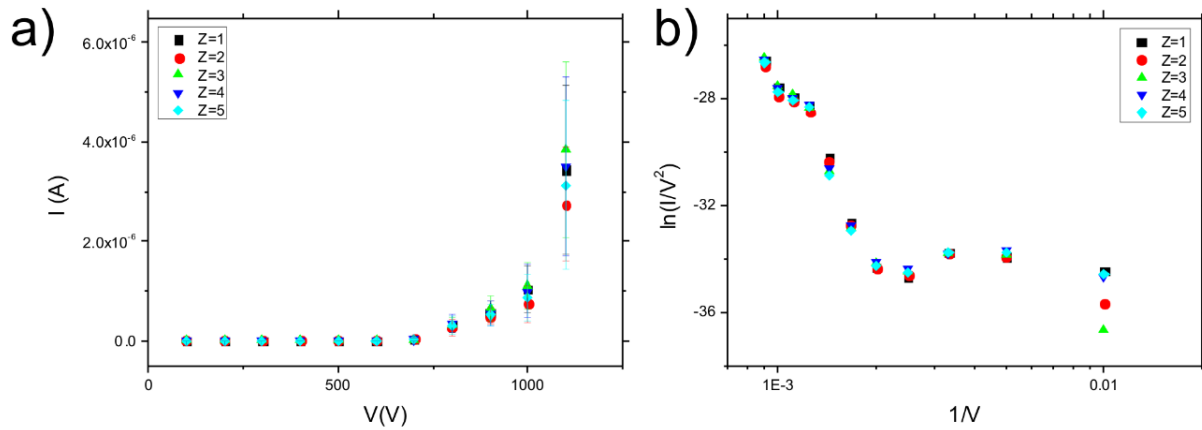


**Figure 4.12 | SAFEM Data Plots.** a) Average  $I$ - $V$  curves across a plane at tip heights of 1  $\mu\text{m}$  to 5  $\mu\text{m}$  and b) the Fowler-Nordheim plots associated with these measurements.

The average current-voltage,  $I$ - $V$ , and Fowler Nordheim characteristics are shown in Figure 4.12. Figure 4.12a shows that there is no strict dependence of the tip height on measured current across the whole measured region with  $z = 2 \mu\text{m}$  showing the lowest average at the maximum voltage and  $z = 3 \mu\text{m}$  showing the highest. The  $I$ - $V$  curves show that the current is turned on at a consistent voltage, around 700 V. As the current does not begin to saturate at 1100 V, this suggests that at larger voltages higher currents could be drawn out<sup>24</sup>. Figure 4.12b shows the Fowler Nordheim, FN, plots, clearly showing deviation from linear classical metallic behaviour with distinctive curvature expressed. A low and high field could be said to interchange at 0.002  $V^{-1}$ , although again neither of these regions show a linear relationship. Calculating  $\beta$  using the usual slope method would, therefore, here be impossible. There is some debate as to whether field emission is indeed being demonstrated at all here.

Obtaining the correct height of the measuring tip is essential in being able to accurately resolve the surface geometry. The emission map outcome can be pictured as a number of individual emission site pixels on the  $xy$ -plane. When  $d$  is minimised, with the tip close to the emitting surface, a small area exists from which electrons are liberated, analogous to small pixel size and potential high resolution. As  $d$  increases, larger areas contribute to the measured current, which could result in image blurring. It was seen in the tip height study that whilst at  $z = 1 \mu\text{m}$  a seeming line of CNTs could be distinguished, Figure 4.10, this was not the case for any further tip heights over and including 2  $\mu\text{m}$ . This could, however, also be caused by noise errors, poor repeatability or tip irregularities, which unfortunately could not be tested for without opening the vacuum chamber.

#### 4. Emitter Morphology for Enhanced Maximum Current

Determination of the tip height can be performed in a number of ways. Height could be measured from the local area, from the top of the CNTs or from the substrate. If defined as a local quantity across the emission area, it must be continuously measured from the location of the tip and surrounding geometry. It could also be a fixed value, measured equivalently across the substrate surface from either the top of the CNTs or the substrate. It is far simpler, as performed here, to maintain a constant tip height across the measurement range, however, the problem still remains as to which point the distance is measured from. Whilst this may seem arbitrary, it is important to consider as the height of the tip, if measured from the substrate surface, must be of ample height to pass over the CNT areas to avoid inflicting damage. Semet *et al*<sup>21</sup> controllably retract the probe ball from a non-destructive contact with the MWNT tip, measuring the distance from the top of the CNTs. Echoing this procedure may be the best way forwards for future studies.

### 4.3.4 Instabilities, Difficulties and Inaccuracies of Meaningful Data Collection

Fundamental issues with loss of data through software crashing or tip distortion were numerous. Measurements made using the SAFEM were highly time consuming. To run a  $30\ \mu\text{m} \times 30\ \mu\text{m}$  scan, with sufficient detail as to be able to distinguish the surface geometry, took many hours and was subject to tip breakage. Some useful data can be recovered before the tip drastically distorts if the software does not crash, however.

Figure 4.13 shows the FE map of an area of  $30\ \mu\text{m} \times 16\ \mu\text{m}$  of a CNT pillar. Regrettably, the tip distorted here after traversing  $16\ \mu\text{m}$  in the  $y$  direction and the final  $14\ \mu\text{m}$  of data collected were not useful. However, from the areas where FE was measured, shown in Figure 4.13, some useful information can be extracted. Once again it is clear that more meaningful data is given in the map of  $I_{max}$  compared to  $V_{on}$ . In the measured zone, the pillar diameter was  $10\ \mu\text{m}$  and the pitch was  $15\ \mu\text{m}$ . The bright red zones ( $I_{max}$ ) show the areas of highest measured current at  $1100\ \text{V}$ . It could be concluded that this area is populated with CNTs, even the centre of a pillar, however, it cannot be known exactly the geometry of the measured area purely from this map. An SEM that worked in tandem with SAFEM measurements or a larger measurement zone could confirm these findings, where a repeatable pattern at dimensions correlating to those of the CNTs could be drawn. Complications with tip stability produced some difficulty in measuring larger mapped areas, however.

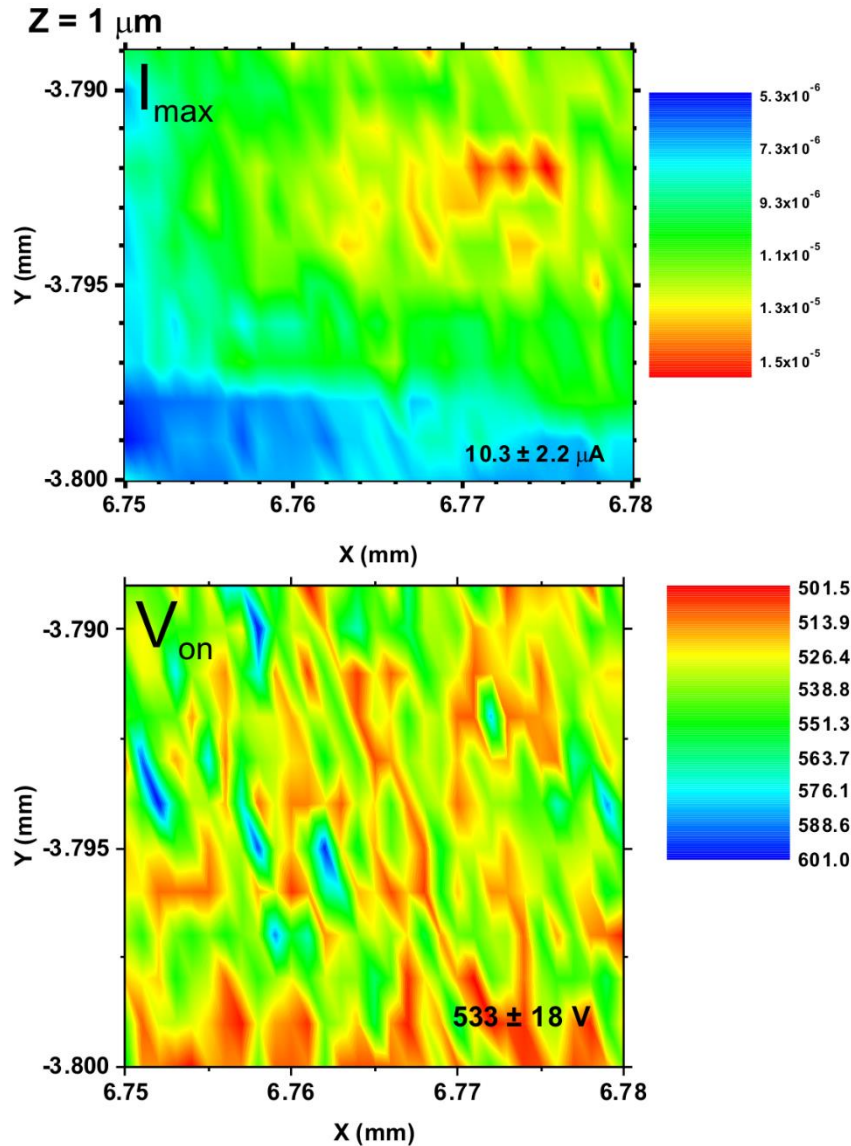


**Figure 4.13 | Field Emission Map.** CNT pillar array at a tip height of  $1 \mu\text{m}$  from emitting surface.

### 4.3.5 Limitations and Conclusions

Distance between tip and substrate was not measured to a high degree of accuracy. When the tip lands on the substrate, a jump in current is measured by the SMU. The tip is then retracted until the current drops again. The zero height of the tip is measured at the place the tip retracts to, just above the surface of the substrate, which means, consequently, that heights could likely differ between measurements. Tip deformation must also be taken into consideration, as a direct landing on the sample surface can lead to distortion, also damaging CNTs where the tip lands. The shape of the tip and the radius of curvature are subject to change in the measurement

#### 4. Emitter Morphology for Enhanced Maximum Current

process, and between measurements, therefore changing the measurement area directly affecting measured current density. This could be minimised using a ball probe tip. There is also a lack of repeatability between scans where the chip is moved in relation to the stage because coordinates are determined by stage position. If the location of the chip on the stage changes, there is no way to re-find the same spot on the chip. Arcing can also destroy the tip and the sample. Unknown precise distance,  $d$ , of tip from substrate results in poor reproducibility. Since  $d$  is expected to be between 1-2  $\mu\text{m}$ , this could be enough to blur the emission from individual locations by measuring current from a larger area, resulting in indistinguishable noise.

Data is lost if the entire scan is not run to completion, resulting in a large volume of lost data and wasted time due to numerous failures. Current and voltage information can be retained, however, post processing becomes very difficult due to large amounts of data amassed. This can be minimised by running short scans stitched together post process. Similarly, scans over large areas can result in unusable data caused by tip deformation, which cannot be discovered until post processing has been performed. In future, it may be wise to perform a scan over a large area, up to 2 mm  $\times$  2 mm with large  $\Delta x$  and  $\Delta y$  lengths, to create a general surface map from which zones of interest can then be magnified, though this would require increased tip stability.

Noise in the measurements, particularly in  $V_{on}$ , causes difficulties in determining which features were caused by FE, if it is indeed FE being measured, from the different patterned areas of the sample and what was caused by statistical variation or noise. Currently, observation inside the chamber whilst operating the SAFEM is not possible. This could be used to check or verify tip location and directly relate this to FE measurements. Comparing to a visual map, generated by SEM for example, would greatly aid in successfully concluding emission is indeed originating from the carbon nanotubes. This would require first, however, the ability to fruitfully map larger areas than reported here and a more reliable tip. The shape of the tip including the radius of curvature are subject to change in the measurement process and between measurements, therefore changing the measurement area and measured current density. Of particular importance are incidents where the tip deforms during measurement, which can lead to measurement of incalculable areas of the sample, depending on the severity of the deformation. Previous studies<sup>22,23</sup> showed that a ball probe tip was preferential, which could be implemented here to alleviate this problem.

In conclusion, using the SAFEM to measure the different geometries proved too challenging to proceed further. Issues encountered lead to inconclusive evidence in determining factors significantly influencing  $\beta$ .  $I_{max}$  was found to be of more significance when mapping FE, compared to  $V_{on}$ , due to larger range of variation and more convincing data presented. The measurement height did not appear to have a great influence on measured current, however, this could be attributed to any number of the aforementioned errors. One useful outcome of data from the SAFEM was that measurements were found to differ to classical Fowler Nordheim behaviour as was expected and has been previously reported<sup>25,26</sup>.

## 4.4 Parallel Plate Field Emission

As a result of the failure of meaningful data collection from the SAFEM, further experimentation was performed using a parallel plate set-up. Whilst this allowed FE to be measured, the current density was measured across the entire chip, and is not spatially resolved. A parallel plate measures the current emitted from the entire surface of the cathode. Electrons can be released from anywhere in the FE region to contribute to the measured current. Detailed information about where the electrons physically originate from on the cathode is lost and cannot be examined in this type of measurement; only the number of electrons, as current, can be measured.

FE from nanomaterials is typically measured in a parallel plate set up in the available literature<sup>27-31</sup>. A metal anode lies parallel to the emitting material at the cathode. When a voltage is applied to the cathode, electrons are liberated from the emitting material and are attracted to the anode producing a current. The anode is typically flat, as in this study, but can also be a ball or tip close to the surface<sup>32,33</sup>. Any conductor can be used as an anode, although commonly ITO on glass is used<sup>28,30,34,35</sup>. Here, the CNTs-on-silicon constitute the cathode, and the anode is patterned nickel-on-glass.

The current density,  $J$ , is a measure of the current that reaches the anode and the area from which it is emitted. Current density is an important parameter in FE, with high values being commonly sought after. Another important parameter is the electric field, calculated using information about the applied voltage,  $V$ , and anode-cathode spacing,  $d$ , and specifically the turn on field,  $E_{on}$ . This value is defined by the field required to obtain a current density of 0.01 mA/cm<sup>2</sup> (the validity of this discussed in the previous chapter), often required to be as low as possible, providing the lowest energies for operation.

### 4.4.1 Experimental Procedure

New geometric samples were fabricated, as outlined above, for measurement in the parallel plate device that maintained a consistent geometry per sample. To continue from the SAFEM studies, both *P* and *IP* geometries were synthesised in geometries comprising of triangular, square, hexagonal and octagonal unit cell. The chosen dimensions were intended to replicate, as much as possible, previous findings<sup>12,20</sup> of  $H/R = 2$ . For the *IP* samples  $x = 10 \mu\text{m}$  and  $w = 2 \mu\text{m}$  and for *P* samples  $x = 5 \mu\text{m}$  and  $w = 10 \mu\text{m}$  were chosen. A growth height of  $5 \mu\text{m}$  was chosen to compliment these dimensions. An example of the fabricated emitter designs can be seen in Figure 4.14.

It should be noted here that only the geometry studies are performed herein; the AR studies were not continued in the parallel plate experiments.

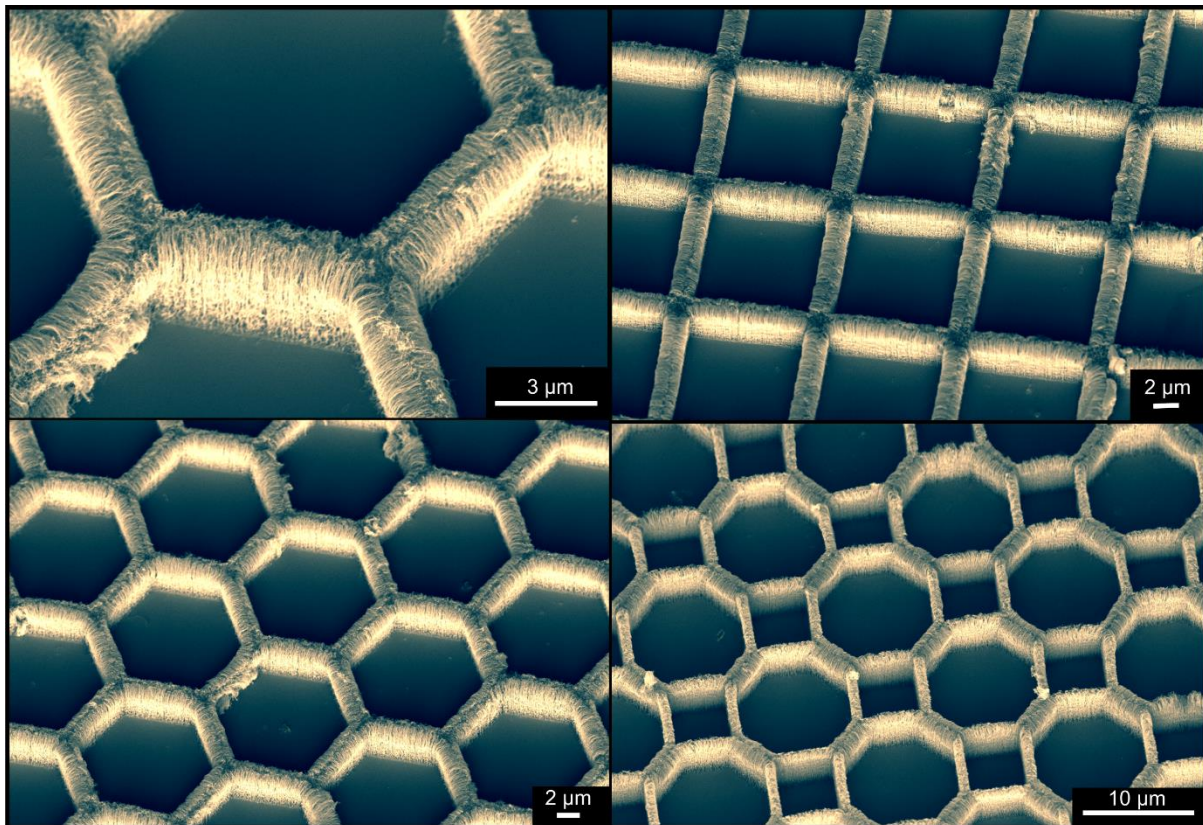


**Figure 4.14 | Parallel Plate Emitters.** Scanning electron micrographs of inverse pillar parallel plate samples in hexagon, square and octagon variations.

Samples were loaded into six bays on a computer controlled rotation platen. The anode consisted of sputtered metal (Ni) on a glass substrate, the anode was positively biased using a computer controlled variable high voltage supply and the samples were grounded. After

loading the samples into the parallel plate side of the FE rig, shown in Figure 4.9a, an ammeter was used to check for shorting. The system was then pumped down to vacuum  $< 10^{-6}$  mbar. A roughing pump was used to reach pressures  $< 10^{-1}$  mbar, followed by a turbomolecular pump. The emission current was acquired using a HP 34401A digital ammeter with a general purpose interface bus, GPIB, interface and 6.5-digit precision, which was independently confirmed using an array of, otherwise isolated, conventional galvanometric ammeters. All measurements were conducted at room temperature. To improve electrical contact between the bay and the sample, the underside of the silicon substrate was scratched using a diamond scribe to remove some of the oxidised layer and an aluminium 'spring', made by folding a small piece of aluminium foil, was placed between the sample and the bay.

The measurement procedure entailed a voltage up sweep from 0 V to 5000 V and back down to 0 V, with four current measurements taken at 50 V intervals following a 3 s settling time. The distance between the anode and cathode was kept at a constant 600  $\mu\text{m}$  with a mica spacer. A ballast resistance of  $7 \times 10^6 \Omega$  and a current limit of 0.01 A were used. A total of six CNT samples were measured in a single sitting, ensuring conditions are maintained throughout these experiments.

Typically, FE is studied using  $J$  and  $E$ , as opposed to  $I$  and  $V$ . To calculate the emission current density,  $J$ , the emitting area must be known. This can be defined by the total area covered by CNTs and the current,  $I$ , by  $J = I/S$ , where  $S$  is the surface coverage. This area can be calculated using the pattern file and the programme *nbp*. The electric field,  $E$ , is calculated using the voltage,  $V$ , and anode separation,  $d$  using  $E = V/d$ . Plotting the results as  $J$ - $E$  curves, however, was overwhelmingly affected by CNT area coverage and the calculated current densities distorted the resulting data. For consistency and accuracy, herein FE is measured solely from  $I$ - $V$  curves, using the direct measurements made in the emission process.

### 4.4.2 Results

The results of the experiments of the eight different geometries are presented in Figure 4.15. They are grouped into different categories. Firstly, they are organised either by  $I_{max}$ , calculated as the maximum current achieved at the maximum applied voltage 5000 V, or by turn on field,  $E_{on}$ , defined as the field value at which an arbitrary current of 1 nA was achieved. It is important to note here that the chosen value of the current by which  $E_{on}$  is defined is of significance for comparative purposes only, since the main focus here is on determining influential factors affecting  $\beta$ .

#### 4. Emitter Morphology for Enhanced Maximum Current

The categories of morphology are further organised into four categories. The first is geometry, defined simply by the number of edges and sides on a single unit cell without any consideration given to the area coverage of CNTs or number of units per sample. The second is the effective perimeter, calculated by finding the length of exposed CNTs, at an edge where CNT meets bare Si, of a single unit multiplied by the number of units per sample. The third variation is presented according to the number of edges present on the chip. This could also be described as number of vertices, since there are the same number of edges and vertices for each design. This is calculated as the number of edges per unit multiplied by the number of units per chip. It should be noted here that these values were calculated using the pattern file and it is assumed that all units were fabricated. This was in practice not strictly true. The final column of Figure 4.15 is organised according to the 2D surface coverage of CNTs as viewed from above.

There are two underlying investigations ongoing throughout this experimental section. Herein the geometry (triangular, square, hexagonal or octagonal) is referred to as geometry of the unit cell and micro geometry refers to *P* versus *IP* morphology.

The area of CNT coverage is thought to be influential in FE and varies between the different patterns. Table 4.1 shows the different coverage areas. The inverse pillars cover more area than pillars; the smallest area (triangle pillar) covers five times less area than the largest coverage (triangle inverse pillar). The coverage of the hexagon geometries is the most similar, with an IP:P ratio of 1.34.

**Table 4.1** | Surface area coverage of CNTs across fabricated samples as measured from the pattern file.

	<i>Inverse Pillar Area (mm<sup>2</sup>)</i>	<i>Pillar Area (mm<sup>2</sup>)</i>
<i>Triangle</i>	1.63	0.33
<i>Square</i>	1.23	0.57
<i>Hexagon</i>	1.21	0.90
<i>Octagon</i>	1.01	0.37

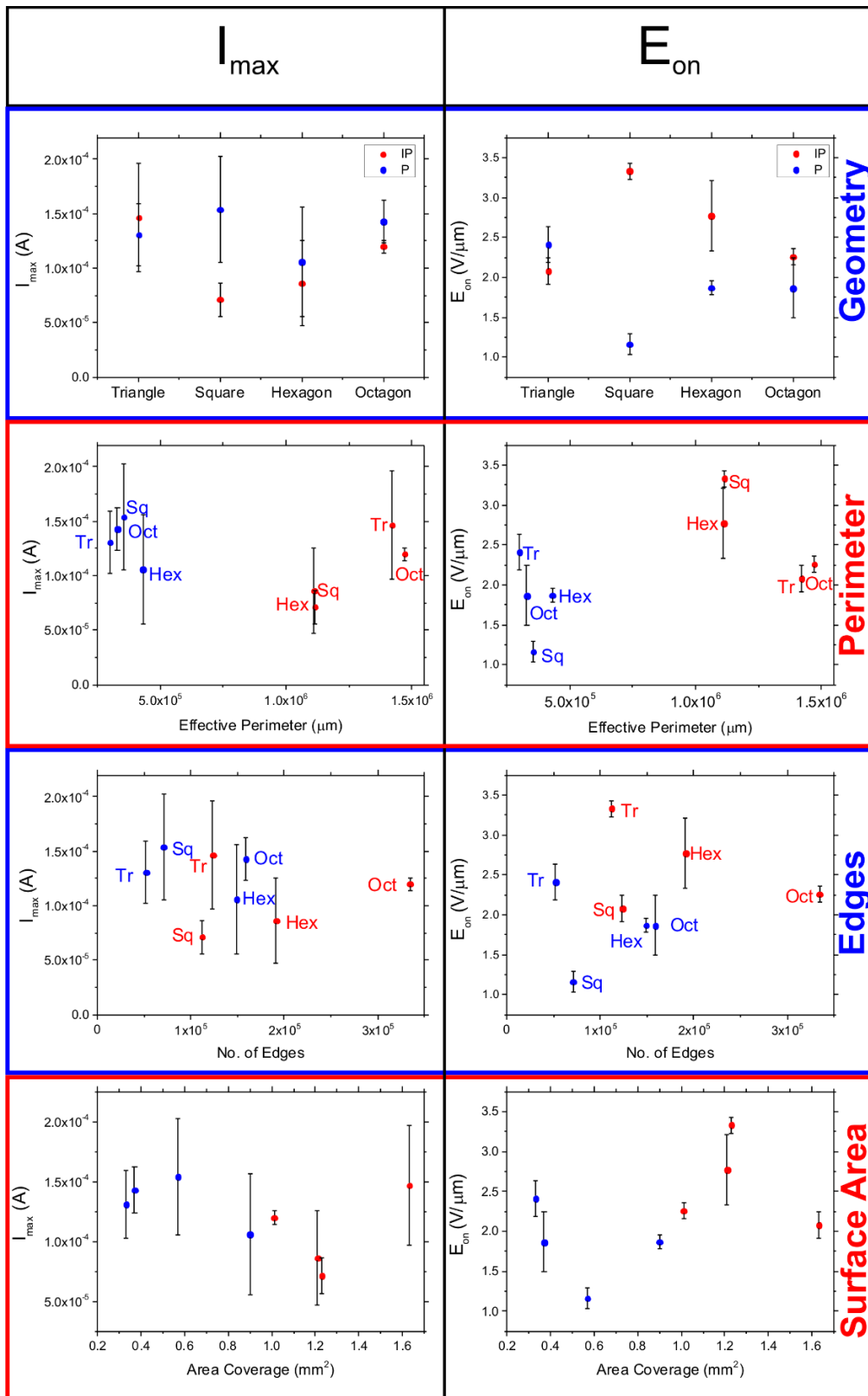


**Figure 4.15 | Results from Parallel Plate Experiments.** Studies performed on different geometries arranged according to a number of different features:  $I_{max}$  and  $E_{on}$  and geometry, perimeter, edges and surface area. Each plot is a representation of an average of three identical chips, each of which was measured three times. Blue data points represent pillar geometry and red inverse pillar.

#### 4. Emitter Morphology for Enhanced Maximum Current

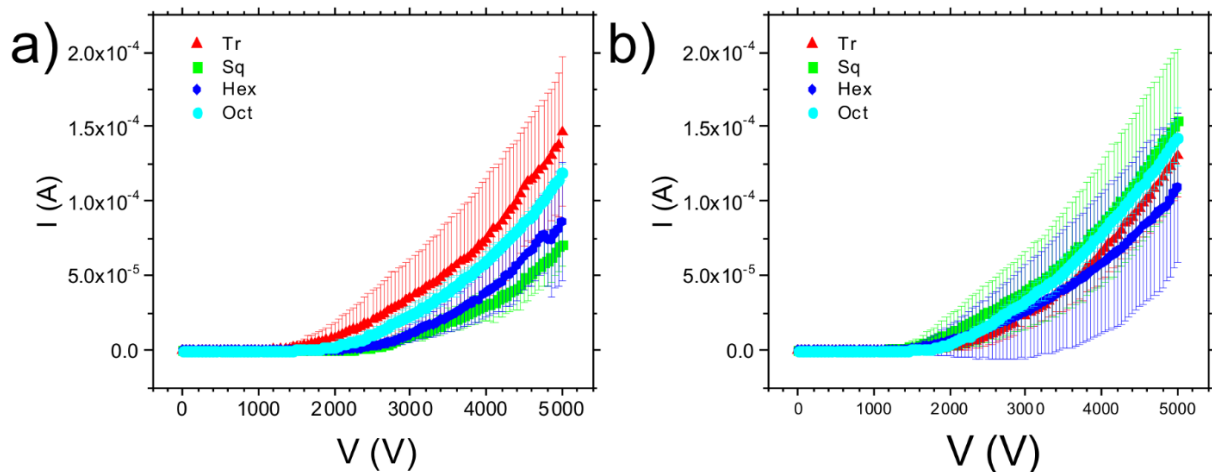
In the top row of Figure 4.15, the results are arranged by geometry. Firstly, considering contributions from  $I_{max}$ , it can be seen that the  $P$  varieties of the geometry are generally greater in value than those of the  $IP$ . Triangular geometry is an exception to this. Secondly, with the exception of square geometry, the difference between the values for each geometry is comparable and somewhat constant. There is some trend, in the inverse pillars, that suggests that the geometries with increasing edge numbers per unit cell perform better, though this does not seem to be reflected in the pillar varieties, which are somewhat consistent. For geometries arranged according to  $E_{on}$ , generally those that show high  $I_{max}$  show low  $E_{on}$  and vice versa. This is an expected result. If  $E_{on}$  (defined by a fixed current) is detected at a low electric field value, it can be expected that at any arbitrary field value, a larger current will be displayed due to greater availability of electrons. Compared to  $I_{max}$ , in  $E_{on}$  the values are not similar by unit cell geometry, however, there does appear to be a mirrored trend about  $2.25 \text{ V}/\mu\text{m}$  between the  $P$  and  $IP$  results. Interestingly, the triangle geometry is again the only point at which the pillar  $E_{on}$  is higher than that of its inverse pillar counterpart. This could be influenced by the surface area coverage of the CNTs on the substrate, which is of the greatest difference between the triangular geometry samples.

The second row in Figure 4.15 shows the results rearranged according to the effective perimeter. It is clear that the  $IP$  samples have a larger perimeter, and therefore CNT edge exposure, by the distinct separation of the data points along the  $x$ -axis. This could additionally be linked to the surface area coverage of CNTs which is likewise higher in  $IP$  samples. In  $I_{max}$ , there appears to be a linear trend, expressed in both  $P$  and  $IP$  samples, in increasing exposed perimeter and increasing  $I_{max}$ . A sharper linear relationship is seen with  $P$  geometry, excluding the hexagonal outlier. It is important to note here that this quality must be linked to both unit cell and micro geometry as the perimeter of the pillars is far smaller yet higher current is seen. This suggests that whilst the exposed edges of the CNT that make up the perimeter are important in increasing the current, it also depends strictly on the micro geometry of the chip and indeed the electronic screening factor which is expected to be smaller in  $P$  geometries. This trend is reversed in  $E_{on}$ , where greater perimeter results in decreased  $E_{on}$ . Again, this also strictly depends on micro geometry. Since this result has no correlation to unit cell, this strengthens previous findings that this has little dependence on performance. Concentration of the electric field along the CNT sidewall can result in edge emission<sup>36</sup>, which has been reported to result in poor stability, though this cannot be seen here. Studies suggest that the turn on field from the sidewalls is larger than at a tip due to higher field concentration around tip geometry

and increased local density of states<sup>37,38</sup>. At maximum applied field, contributions from the sidewall could be significant in shaping  $I_{max}$ .

The number of edges present on the emitting area does not appear to greatly affect  $I_{max}$  of the  $P$  geometries, however, a gentle trend in the  $IP$  samples could suggest that increased number of edges per chip does have some influence in increasing  $I_{max}$ . As seen above, the opposite trend is also shown with regards to  $E_{on}$  of the  $IP$  samples, with increasing number of edges resulting in decreasing  $E_{on}$ . The number of edges must be treated with some caution here as it is possible that the geometries with more vertices, particularly octagonal, could behave in a similar manner to a circular pillar, especially where CNTs have greater edge heights, which causes blurring as the outer CNTs bend towards the centre.

The surface area of exposed CNTs is plotted in Figure 4.15, final row. Greater coverage area does not directly correlate to higher current, which exemplifies the importance of the screening effect. The right balance between CNT bundle spacing and total surface area covered must be found to exploit the maximum available current. The square  $P$  geometry showed the most promising results, with the third smallest CNT surface area per sample. Throughout the measurement, increasing  $I_{max}$  is mirrored as decreasing  $E_{on}$ . This is an expected result since electrons are liberated earlier and are hence more widely available.



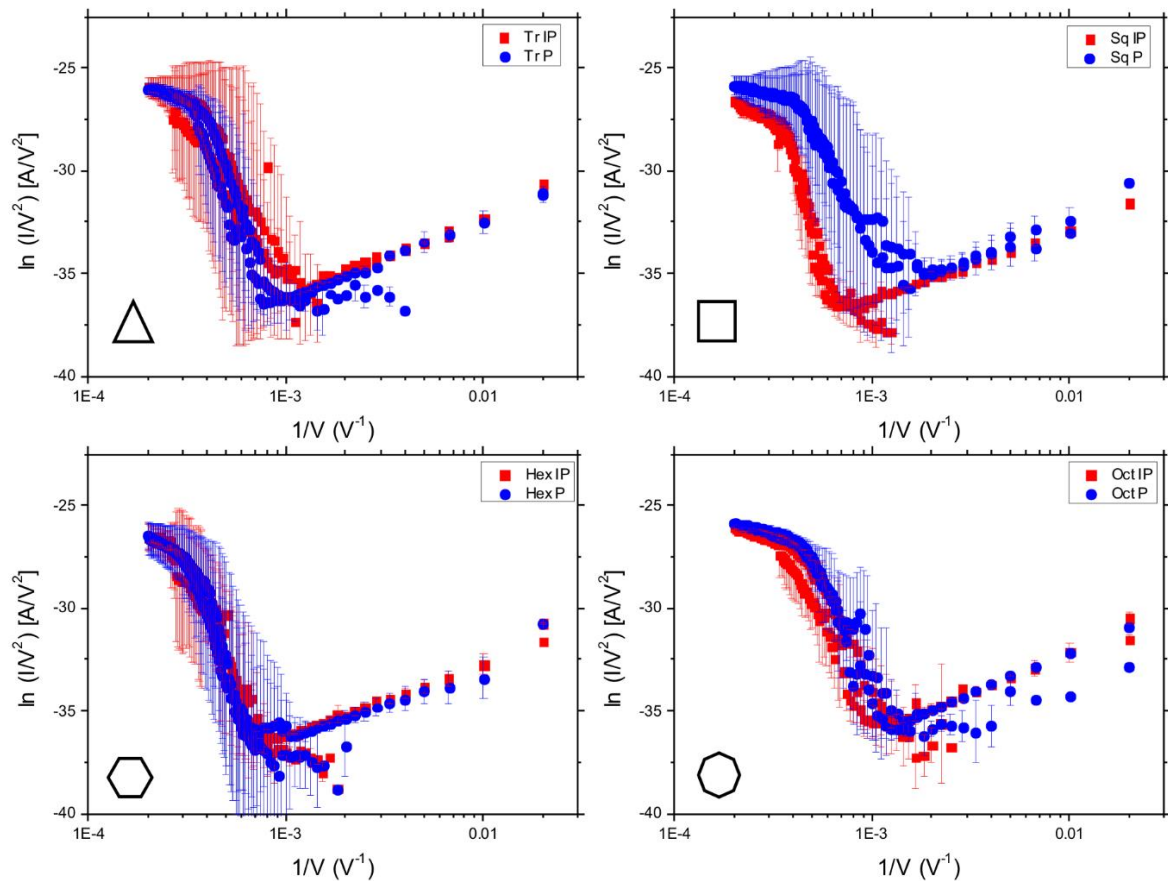
**Figure 4.16 | Average  $I$ - $V$  Curves for the Different Geometries.** Triangle, square, hexagon and octagon in a) inverse pillar and b) pillar formations.

Figure 4.16a shows the average  $I$ - $V$  curves of the different geometries in  $IP$  formation and Figure 4.16b show the  $P$  results. With the exception of triangular geometry,  $P$  samples show higher current than their  $IP$  counterparts. They also show similar curvature to one another,

#### 4. Emitter Morphology for Enhanced Maximum Current

particularly the triangle, square and hexagon results. In the *IP* results, the order of decreasing maximum current is triangle, octagon, hexagon, square, however, in *P* it is square, octagon, triangle, hexagon, which is quite different. This initially suggests that the detailed geometry, the unit cell, has less influence on the current compared to the general geometry, *P* versus *IP*.

In Figure 4.16, across both *IP* and *P* geometries, the octagon geometry appears the most stable and repeatable with very small standard deviation across the nine measurements for each morphology. Square geometry is the most variable, having the lowest current reading in *IP* geometry but the highest as a pillar. The hexagon geometry shows the poorest performance when combining comparisons across the entire geometry range.



**Figure 4.17 | Fowler Nordheim Plots.** Data from triangular, square, hexagonal and octagonal pillar (blue data points) and inverse pillar (red data points) geometries.

The FN plots of the different morphologies are shown in Figure 4.17. Although significant deviation from linear behaviour can be seen, it is clearly field emission that is being measured here, with a distinct difference to the SAFEM results found previously. Three distinct regions exist, typically the low field is between  $x < 1 \times 10^{-3} \text{ V}^{-1}$ , mid field between  $4 \times 10^{-4} \text{ V}^{-1} < x <$

$1 \times 10^{-3} \text{ V}^{-1}$ , and high field  $x < 4 \times 10^{-4} \text{ V}^{-1}$ . A mostly linear dependence is seen in each of the three regions separately.

The most similar plot between  $IP$  and  $P$  is seen by the hexagonal geometry, where the data almost entirely overlaps. The square geometry shows the largest variation, which was also previously seen in Figure 4.15 when arranged by geometry. In general, the data from each of the geometries follows a similar trend, with only small variation seen in the range of the low, mid and high fields, suggesting the shape of the curve is largely material dependent.

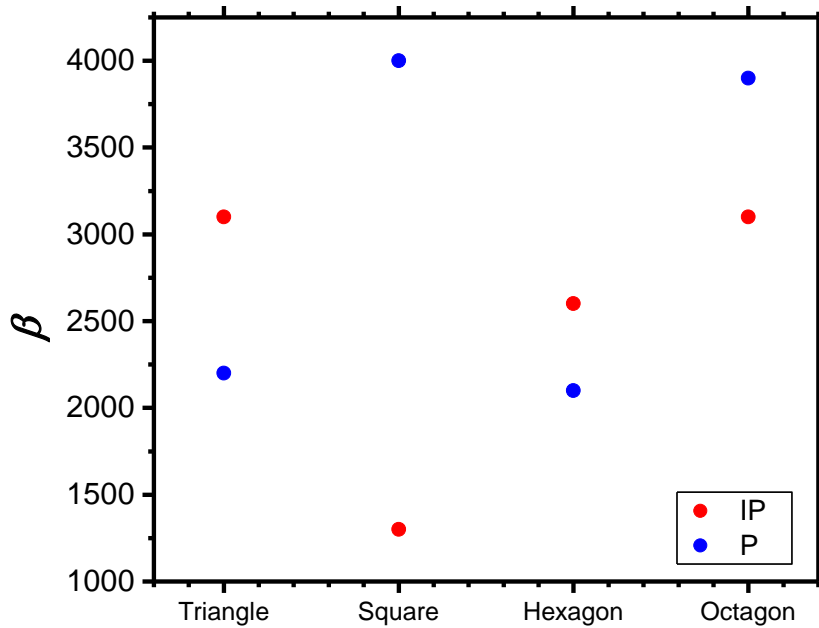


**Figure 4.18 |  $\beta$  values.**  $\beta$  values calculated for the different geometries assuming a work function of 5 eV.

**Table 4.2 |  $\beta$  values for each of the geometries.**

	<i>Inverse Pillar</i>	<i>Pillar</i>
<i>Triangle</i>	3100	2200
<i>Square</i>	1300	4000
<i>Hexagon</i>	2600	2100
<i>Octagon</i>	3100	3900

#### 4. Emitter Morphology for Enhanced Maximum Current

The value of  $\beta$  can be measured from the linear mid-field region and reflects edge enhancement. Equation 6 in Chapter 2 was used to calculate  $\beta$  using a work function of 5 eV. The low-field region is a different regime and the high-field region occurs when the field starts to saturate. Low  $\beta$  manifests as a higher gradient of the slope compared to a higher  $\beta$ . The slopes of the hexagonal and octagonal varieties are similar between the *IP* and *P* samples, with octagonal showing higher  $\beta$ , whereas triangular and square varieties show a more marked difference. The highest and lowest values of  $\beta$  across the range of geometries are found within the square geometry, with the square pillars showing the highest  $\beta$  overall. There is no clear division between *IP* being better than *P* or vice versa although *IP* are more consistent.

Comparing these values with  $E_{on}$  values for geometry in Figure 4.15, it can be appreciated that there is a reflective similarity to Figure 4.18, with those geometries that show low  $E_{on}$  showing high  $\beta$ . The hexagon geometries, particularly the pillar variety, show relatively low  $E_{on}$  and  $\beta$  which shows emission occurring from the edges of the array. The square pillars show the highest  $\beta$  value but do not have the largest perimeter or the most edges and have a mid-range surface area. The hexagon pillars, which also show high  $\beta$  have the largest number of edges amongst the pillar geometries so it follows that this high  $\beta$  reflects the edge enhancement. To further support this argument, the geometry with the lowest number of edges in the inverse pillars is the square which also shows the lowest  $\beta$ .

A separation of the data in the mid-field region between the up and down voltage sweeps is exhibited, which is particularly noticeable in both triangular geometries. This hysteresis is a frequently reported phenomenon in FE from carbon nanotubes<sup>39-43</sup>. The origin of this difference seen in the measured current is widely speculated. This will be further explored in the next chapter.

### 4.4.3 Conclusions

As the area coverage of CNTs affects emission, it would have been preferable to maintain equality throughout the study although in practice, due to statistical variations in growth, this would be difficult to achieve. From the available results, however, some important conclusions can be drawn.

Firstly, from Figure 4.15, it can be concluded, as previously predicted, that there are a number of factors that influence  $\beta$ . One evident factor was the length of exposed perimeter of CNTs. With increasing length, the perimeter was found to show increasing maximum current and

decreasing  $E_{on}$ . It is possible this effect is exaggerated by the longer grown CNTs at the edges of the CNT regions, which could help in reducing the screening effect by decreasing the density of emitting CNTs. However, this was only true within the subsets of  $IP$  and  $P$  when individually considered, since the  $P$  geometries showed better performance but had significantly less total perimeter. This highlighted the importance of combined factors affecting performance. It is thought that a reduction in the electron screening effect is of great importance on emitted current, as it is displayed here by the pillars. In general, a high  $I_{max}$  was complimented by a low  $E_{on}$ , governed by the ease of availability of electrons.

Three regions were identified when data was displayed on a classical Fowler Nordheim plot, seen in Figure 4.17. Whilst displaying somewhat linear performance within each region, this deviates from classical Fowler Nordheim behaviour. A hysteresis was observed between the up and down voltage sweeps when displayed together.

## 4.5 Future Work

To better understand the effect of the geometry, particularly the number of edges on a unit cell, repeating the experiments with bulk materials could be performed. By performing emission from structures that have well defined edges, unlike the blurred edges that can be created with CNTs, a more informative study could be made. At present, it is possible that the fabricated hexagons look very much alike the octagon geometries, which in turn could perform similar to the circular geometries under emission conditions. It would also be beneficial to include a pentagonal and/or septagonal variation.

Unfortunately, due to experienced technical difficulties, SAFEM measurements of the geometries remain, for the most part, unmeasured. Being able to use this machine to its full potential would give greater insight into the workings and effects of the surface geometry. In order for this to happen, greater tip stability is required, possible use of a melted PtIr wire, as used by Semet<sup>21,22</sup> and Thien Binh<sup>23</sup>, could be one way towards a solution to this, their calculations of field distribution from a ball probe tip could also be utilised.

## 4.6 Summary

The surface morphology has been implicated in strongly affecting field emission, though there has been some lack of clarity surrounding this. To better understand this, a number of different CNT geometries were fabricated using a combination of electron beam lithography, sputtering and chemical vapour deposition. A single chip was designed, with a number of different zones, so that as much information could be gathered as possible when measured using a scanning anode field emission microscope.

Regrettably, mainly due to machine immaturity and failures, very little useful information could be gathered in this way. Perhaps the most interesting information to be gleaned from these studies was the confirmation that CNTs do not follow classical Fowler Nordheim behaviour, showing a distinctive curvature where a linear relationship would be expected on a typical Fowler Nordheim plot.

Further investigations into the importance of surface geometry were performed in a parallel plate set up. The results of these experiments suggested that aspects of particular importance in determining the maximum achievable current and lowest activation energy were linked to the reduction of the screening factor, area coverage and increased length of exposed perimeter. Three zones were defined from the Fowler Nordheim plotted data in the low, mid and high field ranges. Within these zones the data was somewhat linear. Whilst the largest difference was seen between the results of the square pillar and inverse pillar samples, the most consistent were the hexagonal varieties and the most repeatable was found to have an octagonal unit cell. A hysteresis was observed between the up and down voltage sweeps.

## References

- 1 Cole, M. T., Doherty, M., Parmee, R., Dawson, P. & Milne, W. I. Ultra-broadband Polariser Based on Metastable Free-Standing Aligned Carbon Nanotube Membranes. *Advanced Optical Materials* **2**, 929-937 (2014).
- 2 Cole, M. *et al.* Dry-Transfer of Aligned Multiwalled Carbon Nanotubes for Flexible Transparent Thin Films. *Journal of Nanomaterials* **3** (2012).
- 3 Chang, T. H. P. Proximity effect in electron-beam lithography. *Journal of Vacuum Science & Technology* **12**, 1271-1275 (1975).
- 4 Tadros, T. in *Encyclopedia of Colloid and Interface Science* (ed Tharwat Tadros) 820-820 (Springer Berlin Heidelberg, 2013).
- 5 Xia, Y. Self-assembly growth of single-wall carbon nanotubes. *Nuclear instruments & methods in physics research. Section B, Beam interactions with materials and atoms* **155**, 395-402 (1999).
- 6 Guo, T. Self-Assembly of Tubular Fullerenes. *Journal of physical chemistry (1952)* **99**, 10694-10697 (1995).
- 7 Sohn, J. I., Nam, C. & Lee, S. Vertically aligned carbon nanotube growth by pulsed laser deposition and thermal chemical vapor deposition methods. *Applied Surface Science* **197**, 568-573 (2002).

- 8 Kong, J., Cassell, A. M. & Dai, H. Chemical vapor deposition of methane for single-walled carbon  
nanotubes. *Chemical Physics Letters* **292**, 567-574 (1998).
- 9 Cole, M. T. & Milne, W. I. Plasma Enhanced Chemical Vapour Deposition of Horizontally Aligned  
Carbon Nanotubes. *Materials* **6**, 2262-2273 (2013).
- 10 Cole, M. T. *et al.* Ballasted & electrically steerable carbon nanotube field emitters in *Conference on  
Carbon Nanotubes, Graphene, and Associated Devices*. **8462** (2012).
- 11 Li, C. *et al.* Hot Electron Field Emission via Individually Transistor-Ballasted Carbon Nanotube Arrays.  
*Acs Nano* **6**, 3236-3242 (2012).
- 12 Katayama, M., Lee, K. Y., Honda, S., Hirao, T. & Oura, K. Ultra-low-threshold field electron emission  
from pillar array of aligned carbon nanotube bundles. *Japanese Journal of Applied Physics Part 2-Letters  
& Express Letters* **43**, L774-L776 (2004).
- 13 Fujii, S. *et al.* Effect of arrangement of pillar array of aligned carbon nanotube bundles on its field-  
emission characteristic. *Diamond and Related Materials* **17**, 556-558 (2008).
- 14 Chang, C.-T., Juan, C.-P. & Cheng, H.-C. Pillar Height Dependence of Field-Emission Properties in an  
Array of Carbon Nanotube Pillars. *Japanese Journal of Applied Physics* **52** (2013).
- 15 Chen, Y. M., Chen, C. A., Huang, Y. S., Lee, K. Y. & Tiong, K. K. Characterization and enhanced field  
emission properties of IrO<sub>2</sub>-coated carbon nanotube bundle arrays. *Nanotechnology* **21** (2010).
- 16 Choi, Y. C. *et al.* Patterned growth and field emission properties of vertically aligned carbon nanotubes.  
*Diamond and Related Materials* **10**, 1457-1464 (2001).
- 17 Sohn, J. I. *et al.* Patterned selective growth of carbon nanotubes and large field emission from vertically  
well-aligned carbon nanotube field emitter arrays. *Applied Physics Letters* **78**, 901-903 (2001).
- 18 Zhu, L. Monitoring Carbon Nanotube Growth by Formation of Nanotube Stacks and Investigation of the  
Diffusion-Controlled Kinetics. *The journal of physical chemistry. B* **110**, 5445-5449 (2006).
- 19 Puretzky, A. A. Real-time imaging of vertically aligned carbon nanotube array growth kinetics.  
*Nanotechnology* **19**, 055605 (2008).
- 20 Cole, M. T. *et al.* Deterministic Cold Cathode Electron Emission from Carbon Nanofibre Arrays.  
*Scientific Reports* **4** (2014).
- 21 Semet, V. *et al.* Field electron emission from individual carbon nanotubes of a vertically aligned array.  
*Applied Physics Letters* **81**, 343-345 (2002).
- 22 Semet, V., Mouton, R. & Binh, V. T. Scanning anode field emission microscopy analysis for studies of  
planar cathodes. *Journal of Vacuum Science & Technology B* **23**, 671-675 (2005).
- 23 Binh, V. T., Semet, V., Dupin, J. P. & Guillot, D. Recent progress in the characterization of electron  
emission from solid-state field-controlled emitters. *Journal of Vacuum Science & Technology B* **19**,  
1044-1050 (2001).
- 24 Liang, S.-D. *Quantum Tunneling and Field Electron Emission Theories*. (World Scientific Publishing  
Co. Pte. Ltd., 2014).
- 25 Bonard, J.-M., Kind, H., Stöckli, T. & Nilsson, L.-O. Field emission from carbon nanotubes: the first  
five years. *Solid-State Electronics* **45**, 893-914 (2001).
- 26 Cutler, P. H. *et al.* Theory Of Electron-Emission in High Fields from Atomically Sharp Emitters -  
Validity of the Fowler Nordheim Equation. *Progress in Surface Science* **42**, 169-185 (1993).
- 27 Mao, C., Wang, X., Wu, X., Zhu, J.-J. & Chen, H.-Y. Synthesis and field emission of single-crystalline  
copper vanadate nanobelts. *Nanotechnology* **19** (2008).
- 28 Ng, D. K. T., Hong, M. H., Tan, L. S., Zhu, Y. W. & Sow, C. H. Field emission enhancement from  
patterned gallium nitride nanowires. *Nanotechnology* **18** (2007).
- 29 Liu, J. *et al.* Enhanced field emission properties of MoO<sub>2</sub> nanorods with controllable shape and  
orientation. *Materials Letters* **58**, 3812-3815 (2004).
- 30 Lee, Y. H. *et al.* Tungsten nanowires and their field electron emission properties. *Applied Physics Letters*  
**81**, 745-747 (2002).
- 31 Nayeri, F. D., Darbari, S., Soleimani, E. A. & Mohajezadeh, S. Surface structure and field emission  
properties of cost effectively synthesized zinc oxide nanowire/multiwalled carbon nanotube  
heterojunction arrays. *Journal of Physics D-Applied Physics* **45** (2012).
- 32 Chen, Z. & Zou, J. Field Emitters: ultrathin BN nanosheets protruded from BN fibers. *Journal of  
Materials Chemistry* **21**, 1191-1195 (2010).
- 33 Wu, Z.-S. *et al.* Field Emission of Single-Layer Graphene Films Prepared by Electrophoretic Deposition.  
*Advanced Materials* **21**, 1756-1760 (2009).
- 34 Yan, H. *et al.* Synthesis, property and field-emission behaviour of amorphous polypyrrole nanowires.  
*Nanotechnology* **17**, 3446-3450 (2006).
- 35 Wang, S. G. *et al.* Electron field emission from carbon nanotubes and undoped nano-diamond. *Diamond  
and Related Materials* **12**, 8-14 (2003).

#### 4. Emitter Morphology for Enhanced Maximum Current

- 36 Cheng, Y. Electron field emission from carbon nanotubes. *Comptes rendus. Physique* **4**, 1021-1033 (2003).
- 37 Yasumoto, K. *et al.* Comparison of Field Emissions from Side Wall and Tip of an Individual Carbon Nanotube. *Japanese Journal of Applied Physics* **44**, 1648 (2005).
- 38 Chai, G. Electron emission from the side wall of an individual multiwall carbon nanotube. *Carbon* **45**, 281-284 (2007).
- 39 Zuo, Y., Ren, Y., Wang, Z., Han, X. & Xi, L. Enhanced field emission and hysteresis characteristics of aligned carbon nanotubes with Ti decoration. *Organic Electronics* **14**, 2306-2314 (2013).
- 40 Cahay, M., Murray, P.T., Back, T.C., Fairchild, S., Boeckl, J., Bulmer, J., Koziol, K.K.K., Gruen, G., Sparkes, M., Orozco, F. and O'Neill, W. Hysteresis during field emission from chemical vapor deposition synthesized carbon nanotube fibers. *Applied physics letters* **105**, 173107 (2014).
- 41 Filippov, S. V., Popov, E. O., Kolosko, A. G., Romanov, P. A. & Iop. in *2nd International School and Conference Saint-Petersburg Open on Optoelectronics, Photonics, Engineering and Nanostructures* Vol. 643 *Journal of Physics Conference Series* (2015).
- 42 Arkhipov, A. V., Mishin, M. V., Sominski, G. G. & Parygin, I. V. Hysteresis of pulsed characteristics of field emission from nanocarbon films. *Technical Physics* **50**, 1353-1359 (2005).
- 43 Gorodetskiy, D. V. *et al.* Memristive model of hysteretic field emission from carbon nanotube arrays. *Journal of Nanophotonics* **10** (2016).

# **5. Hysteretic Behaviour of Carbon Nanotube Field Emitters**



## 5.1 Introduction

In this Chapter, parallel plate field emission from in-house fabricated emitters is measured under a number of different tests and conditions, exploring the effects on both the emission process and the observed hysteretic behaviour. In applications this hysteresis is undesirable. Understanding its origin is important in determining a method to mitigate it. A model to predict and describe observed hysteresis is developed herein.

## 5.2 Background

FE describes the emission of electrons into a vacuum from a material surface under an applied electric field. The main impacts and benefits derived from FE, particularly with the application as X-ray sources in mind, are a controllable electron beam with defined energy distribution, miniaturisation of devices, fast temporal response and desirable operating temperatures<sup>1</sup>. The nanocarbons, CNTs in particular<sup>2</sup>, have been recognised as promising for FE, demonstrating low field operation and high current densities<sup>2,3</sup>. CNTs offer high AR and a degree of control over emitter morphology<sup>1,4</sup>. However, time and again, hysteresis has been observed in the FE studies of many nanocarbon materials. This is a cause for concern when considering applications. The origin and physics of this phenomenon are disputed widely, with a number of varying theories. Such theories include: emission via intermediary electron energy states<sup>5</sup>, change of field enhancement factor around emitting tips due to alignment under electrostatic fields<sup>6</sup>, changes in physical morphology of the emitting material<sup>7</sup>, thermionic emission<sup>8</sup>, and most commonly implicated is the adsorption and desorption of gas molecules on the emitting surface<sup>9-12</sup>. The effect of adsorbates have been postulated to: alter the emitters electrical properties by increasing the local density of states, DOS, near the Fermi energy<sup>10</sup>, contribute to enhanced emission via electron intermediate energy states caused by adsorbates<sup>7</sup>, and to modify surface  $\phi$ , subsequently altering the tunnelling barrier<sup>9</sup>. Herein, exploration of these theories through experimentation and hypothesis is performed, proposing further insight into the hysteresis mechanisms.

### 5.2.1 Hysteresis Mechanisms

Hysteresis is observed in CNT field emitters when exposed to a symmetrical voltage loop. Figure 5.1 shows a typical  $I$ - $V$  hysteretic curve, where the current in an increasing field,  $I_{up}$ , is not equal to the current in a decreasing field,  $I_{down}$ :  $I_{up} \neq I_{down}$ . A variable in the system causes some asymmetry between the emission under increasing and decreasing applied electric field. Since the voltage loop parameters are identical in both directions, the source of the hysteresis is linked to the emitter itself rather than the measurement system to which it is attached. The occurrence and magnitude of hysteresis could, therefore, be affected by a number of factors such as CNT configuration (crystallinity, chirality, length, diameter etc.), surface and CNT morphology and geometry, or surface  $\phi$ , though specific details about influential factors are somewhat disputed<sup>6,13</sup>. There is some agreement, however, surrounding the explanation of observed hysteresis by gas species present on the CNT surface. Porous materials, such as CNTs, show high propensity to adsorb surface molecules<sup>14-16</sup>; hysteresis in adsorption and desorption isotherms has been reported<sup>17,18</sup>, which is somewhat analogous to hysteresis experienced under increasing electric fields. An isotherm shows the relationship between pressure and adsorption, with constant temperature. The adsorption isotherms for porous materials with weak interaction between adsorbate and adsorbent, such as activated carbon and water, show some hysteretic behaviour. It is thought that different sizes of these pores are fundamental in driving this hysteresis<sup>19</sup>.

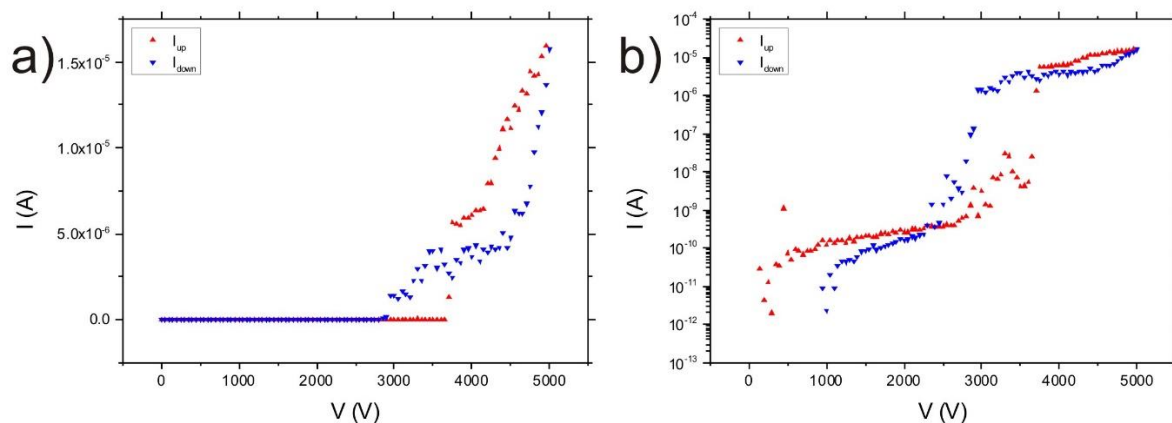


**Figure 5.1 | Hysteretic Behaviour of Field Emission.** Typical  $I$ - $V$  curve measured from CNTs with exhibited hysteresis a) linear and b) logarithmic scale.

The energies associated with adsorption and desorption differ greatly, implicating this as a strong candidate as the cause of emitter hysteresis. Initially, adsorbed molecules are released

from the surface of the emitter, or the anode, by desorption through increasing available energy imparted by the electric field and mobile electrons. Molecules are then subjected to adsorption, back on to the CNT surface, during the downward potential sweep. Arkhipov *et al*<sup>5</sup> suggested that a constancy is seen in increasing fields, whereas in decreasing fields, the current is subjected to changes, providing the source of hysteresis. This is explained by the consistent filling of surface levels with electrons in an increasing field as the surface becomes more transparent, which is asymmetric in a reducing field where the energy positions and levels vary. Increased emission, comparatively, at the trailing edge of the cycle is attributed to depopulation of intermediate states. An alternative theory of accumulation of ions at the CNT tip released by bombardment of anode molecules by electrons emitted from the cathode was postulated by Chun Li *et al*<sup>11</sup>. The positively charged removed ions are subsequently attracted to the CNT tips by strong local electric fields, consequently having the effect of enhancing tunnelling configurations by their relationship with the CNT surface. The surface coverage of adsorbates on CNTs appears directly related to emission current thus stimulating arguments regarding contribution to hysteresis<sup>10</sup>. The current is purportedly affected by adsorbed molecules through a number of proposed behaviours: changes in surface  $\phi$  requiring variable energies for emission onset; emitter impurities, influencing the local electrostatic field about the emitter; population and location of electronic band states and DOS, varying with a dependence on direction of electric field.

Field emission studies are plagued by the complexities of two highly influential parameters:  $\beta$  and  $\phi$ . The full and complete workings of these parameters are yet undetermined, as has been documented throughout this thesis. Changes in either  $\beta$  or  $\phi$  are thus often also linked to underlying impacts associated with sorption hysteresis mechanisms. Material surface  $\phi$  is inherently central to the process of FE. Adsorbates could act as an effective adlayer, changing the surface properties of a material including surface  $\phi$ . Electronegative adsorbates, such as oxygen or water, could actually increase  $\phi$  at the surface<sup>9</sup>. Composite energy bands between CNTs and adsorbates could result in intermediate electron states from which electron emission occurs.  $\phi$  is a complex entity; it is possible that it fluctuates throughout the emission process depending on adsorbed molecule species and surface coverage of adsorbates<sup>9</sup>. It was suggested by Okotrub *et al*<sup>12</sup> that physisorbed adsorbates have a more dramatic effect on fluctuating  $\phi$  due to a dynamic character with continuous influence over FE. Chemically bound molecules, in comparison, have a more simplistic relationship with CNT surface, where desorption is the result of removal from the surface under tunnelling current in a singly occurring event. It is of

crucial importance, therefore, to understand the basic influence of  $\phi$  on FE current to thoroughly explore the origin of hysteresis.

Morphology has also been implicated in affecting hysteresis. Changes in morphology are associated with changes in  $\beta$ . Cahay *et al*<sup>7</sup> suggest that back bombardment of ions can damage CNTs, causing a physical alteration to the morphology. Bombardment, which occurs as the removed species return to the surface under reducing electric fields, can supposedly open and sharpen CNT tips, which is initially beneficial for FE, though excessive etching can destroy the emitters. Larger  $\beta$  values, where  $\beta$  is defined as the ratio of emitter height,  $h$ , to radius,  $r$ , by  $\beta = h/r$ , has also been attributed to increased FE by Gorodetskiy *et al*<sup>6</sup>. Using this formula, it can be argued that in the presence of an electric field, the alignment, or straightening, of individual CNTs caused by the application of an electric field results in larger heights<sup>20</sup> and therefore higher  $\beta$ . A similar theory is suggested by Cheng *et al*<sup>21</sup> when discussing the stability of nanotube forests versus patterned or individual emitters. They claim that the effect of electrostatic screening between forests and patterned emitters is not of great difference due to random orientation of greater heights in forests of CNTs from an unaligned film under the application of an electric field. It is feasible, according to de Jonge and Bonard<sup>22</sup>, that adsorbed atoms can reach the CNT cap by surface diffusion, changing cap morphology and hence emission. However, absence of a clear definition of  $\beta$ , with many variations documented (see Chapters 3 and 4), prohibits confidence in these proposed theories. It is clear that both  $\phi$  and morphology play a key role in emission, and it is likely that each has an influence on hysteresis. The effects of each, however, are also likely to be deeply intertwined. Thorough knowledge of each quantity, detailed through both theory and experiment, is essential in giving an outlook to this effect.

### 5.2.2 Adsorption and Desorption

Molecules can be adsorbed onto the surface of a material. There are two different known mechanisms by which this can happen: chemisorption and physisorption. Chemisorption describes adsorption caused by the formation of physical chemical bonds between the surface and the molecule. Physisorption, on the other hand, is characterised by adsorption driven by weak Van der Waals type forces. Both types of adsorption result in molecules bound to the material surface, affecting surface properties. Molecules adsorb at preferential locations depending on minimisation of the energy in the system. On hexagonally bonded carbon, as

found in CNTs, molecular species adsorb at different locations: atop C atoms ( $\text{H}_2\text{O}$ ), on top of middle C-C bonds ( $\text{O}_2$ ), or on top of C hexagon centres ( $\text{H}_2$ )<sup>23</sup>.

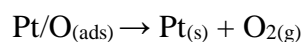
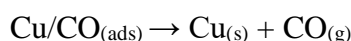
Lattice deformation, that can be caused by adsorption and desorption, is shown to be mostly insignificant on the electronic properties of a CNT<sup>23</sup>. However, the electronic properties of CNTs can be affected by certain adsorbates that act as charge acceptors. Whilst most molecules have little influence,  $\text{O}_2$  and  $\text{NO}_2$  have been seen to shift the Fermi energy into the valence band with high DOS at the Fermi level<sup>23</sup>. Undoped semiconductor CNTs can be transformed into *p*-type conductors due to predicted hybridisation between CNT valence bands and energy levels in the molecule, though such effects will have little impact on the present quasi-metallic MWNTs studied herein.

The main cause of hysteresis is frequently attributed to the difference in energies required to desorb molecules versus re-adsorption. Joule heating has been credited to have a further effect on molecular adsorption and desorption rates<sup>8,9,11</sup>, with attributed mobility of adsorbates increasing with the CNT temperature. Joule heating can occur at high fields, where higher currents are measured.

The rate of adsorption onto a surface is determined by a surface sticking probability, depending on existing coverage of adsorbed species, and the incident molecular flux<sup>24</sup>. An activation barrier may also be present, requiring a prescribed activation energy before a molecule becomes adsorbed on a surface. This activation energy may depend on the proportion of the surface already covered. In a 1D model, the distance of the molecule from the surface defines the energy in the system. Physisorption kinetics are faster than chemisorption because there is no activation energy. In general, however, the activation energies in adsorption are far smaller than energies required for a molecule to vacate the surface by desorption. For example, Zhu *et al*<sup>25</sup> measure activation energies of an  $\text{O}_2$  molecule by density functional theory to range between -0.5 eV to -0.6 eV, whilst the desorption barrier of a C-O pair was found to range between 1 eV to 2 eV.

Desorption can occur in a simple atomic process or by recombination, such as the desorption of O atoms, as  $\text{O}_2$  from a Pt surface.

For example:



where  $s$  and  $g$  denote solid and gas phases respectively.

Desorbed molecules possess higher energies than when in equilibrium with a surface. The desorption processes can include removal by thermal energy, electron or ion impact. In the case of FE from CNTs, where the thermal energy of the system varies little, it is likely that impacts affects could be of some importance when considering desorption mechanisms. Ionic movement of desorbed molecules, or indeed emitted electrons, could stimulate desorption of further species from the CNT surface, exaggerating the effect as the electric field increases.

### 5.3 Data Collection and Processing

The authors' raw data is collected in current,  $I$ , and applied voltage,  $V$ , from a *Keithley 270* SMU via custom built software and GUI. The electric field,  $E$ , can be found using  $V/d$ , where  $d$  is the spacing between the anode and cathode. This distance is maintained throughout the experiments, using a laser cut mica ceramic spacer, at 600  $\mu\text{m}$ . The current density,  $J$ , can be calculated using  $I/S$ , where  $S$  is the emitting area. Defining the emitting area should be calculated by the surface area directly covered with CNTs, an area much smaller than the 2 mm  $\times$  2 mm area over which the pattern is deposited. Measuring this area can be calculated using the pattern file, where a pattern file is used, though for a forest, it is safe to assume that the area exposed to the anode can be used as the surface area. However, throughout the fabrication process, where patterned samples are used, it is uncommon that total coverage of the calculated area is precisely equal to the area of the pattern due to some variation caused. To best represent the true results of FE measurements, it is, therefore, more accurate to plot the directly measured units of current against voltage, as was previously seen in the morphology study in Chapter 4. This is acceptable as  $I$ - $V$  graphs are commonly used to display FE data<sup>26-30</sup>, they represent the data collected and are not influenced by errors and problems encountered with emitting area calculations.

$I_{max}$  is calculated by taking the value of current recorded at 5000 V, the highest voltage that the sample is exposed to, unless otherwise stated.  $E_{on}$  is a commonly used parameter that can be accurately calculated using the constant spacing,  $d$ , and is used herein in place of  $V_{on}$ , as this is exclusively seen in literature. Typically, though some discrepancies throughout the field are seen, a value of  $J = 10 \mu\text{A}/\text{cm}^2$  is used when calculating  $E_{on}$  (see Chapter 3). This requires the

inclusion of the area calculations and is thus not often calculated in forthcoming studies, instead a value of  $I = 1$  nA is used to calculate  $E_{on}$  as a more reliable figure.

The measurement procedure and experimental set up is discussed in detail in Chapter 4, Section 4.4.1. Unless stated otherwise, the data collecting procedure remains the same.

## 5.4 Parallel Plate Emission Performance

Through a series of experiments, the complexities and workings of hysteresis can be shown and the fundamentals of its cause can be deduced. Initial studies on the performance of parallel plate FE took place to verify that the emission seen was indeed through field electron emission, as opposed to thermionic or ionic emission, and that the measurements were repeatable. Characteristics including pressure dependence and optical excitation were tested as it is important to determine whether there is a relation between the current and the vacuum pressure, and optical invariance is essential for applications as X-ray sources.

The samples measured in the majority of experiments consisted of CNT forests with a height  $h = 4.99 \pm 1.15$   $\mu\text{m}$  and a circular pillar array with dimensions:  $d = 4.94 \pm 0.11$   $\mu\text{m}$ ,  $p = 9.96 \pm 0.45$   $\mu\text{m}$ ,  $h = 3.8 \pm 0.3$   $\mu\text{m}$ . Where  $d$  is the diameter of the pillar,  $p$  is the pitch measured centre-to-centre between pillars and  $h$  is CNT height. CNTs, in pillar formation, were grown within an area  $2$  mm  $\times$   $2$  mm on a  $10$  mm  $\times$   $10$  mm Si chip. The dimensions of the pillar arrays were designed to complement previous findings to maximise emission and stability as found through literature and in the previous chapter<sup>31,32</sup>. The influence of the different morphologies was not considered herein, though each procedure maintained a single morphology for completeness.

### 5.4.1 Repeatability

The repeatability test measured FE from samples in six identically patterned pillar arrays, each measured in one of the six available bays on the rotation platen inside the vacuum chamber. Each sample was subjected to three voltage loops to a maximum of 5000 V and the same experimental conditions were experienced by each. This was the first test using the parallel plate field emitter, allowing both verification of the method and equipment used, as well as familiarisation with the procedure. Repeatability of the results gives increased confidence about the accuracy of the measurements and indeed the measuring apparatus. Although the arrays are not perfectly identical in terms of CNT height and surface coverage, measurements

## 5. Hysteretic Behaviour of Carbon Nanotube Field Emitters

were mostly consistent between samples. Some variation between results highlights the statistical variation encountered between different samples, which is not altogether unexpected.

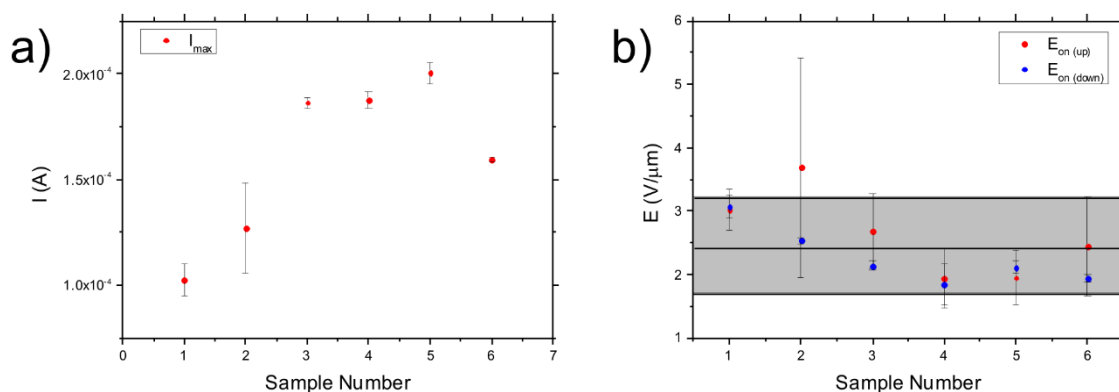


**Figure 5.2 | Repeatability Results.** Results of field emission from six identical pillar arrays, each measured three times showing a) maximum measured current and b) turn on field for up (red) and down (blue) voltage sweeps.

Figure 5.2 shows  $I_{max}$  and  $E_{on}$  calculated for each of the six samples. The average maximum current measured was  $I = 0.16 \pm 0.05$  mA over the six samples at pressure  $P = 5.7 (\pm 0.5) \times 10^{-7}$  mbar. The average  $E_{on}$  was  $2.45 \pm 0.76$  V/ $\mu m$  across both up and down sweeps. The up sweep average was  $E_{on} = 2.61 \pm 0.96$  V/ $\mu m$ , which was higher than the down sweep average of  $E_{on} = 2.27 \pm 0.45$  V/ $\mu m$ . The difference in these values is associated with the hysteresis, which will be discussed in more detail later. In Figure 5.2b the mean and one standard deviation are highlighted by the area of the grey box, within which the majority of measurements lie. Sample 2 shows some anomalous result in  $E_{on}$  found in the up sweep. In general, it was noted that the first measurements on new samples often took longer to turn on in the up sweep than in subsequent measurements. No special treatment was given to the samples before subjecting them to the experiments. This is somewhat responsible for the larger standard deviations seen in  $E_{on(up)}$ .

### 5.4.2 Raman Spectroscopy

Raman Spectroscopy is used to assess the vibrational properties of the CNTs before and after FE measurements are made. The graphitic, G, bandwidth represents the tangential vibration of carbon atoms and the disorder, D, band represents defective graphitic structures<sup>33,34</sup>. Studying the D and G peaks, the dominant peaks for CNTs and the wider family of nanocarbons, provides evidence to any changes in the graphitic structures induced during the FE process. Defects can

increase or improve the field emitting capabilities of CNTs to an extent, since FE occurs at defect sites, and the proportion of defects before and after emission measurements can be monitored using Raman techniques. Defects are not always beneficial, however, catastrophic events such as arcing can subject the emitter to very high local temperatures and can change the lattice properties as well as damage some nanotubes completely. The 2D band (also called G' or D\*) shows the degree of crystallinity of the CNTs and its position can also indicate doping<sup>35-37</sup>.

The intensity is plotted against Raman shift for samples before and after (exposure to over 60 cycles) FE measurements in Figure 5.3. A typical as-grown (pre-FE) MWNT<sup>38</sup> finds the D band at  $1350\text{ cm}^{-1}$ , G band at  $1590\text{ cm}^{-1}$  and 2D band at  $2700\text{ cm}^{-1}$ . In the post-FE measured samples, the D peak was found at  $1365 \pm 3\text{ cm}^{-1}$  and G peak at  $1590 \pm 3\text{ cm}^{-1}$ . The  $I_D/I_G$  ratio, where I is the intensity, gives an indication to the quality of the sample, where a smaller ratio indicates higher quality<sup>39</sup>.  $I_D/I_G = 0.94 \pm 0.06\text{ cm}^{-1}$  was measured. The relative similar intensity of the D and G peaks indicates the MWNTs are metallic in nature<sup>35</sup>.

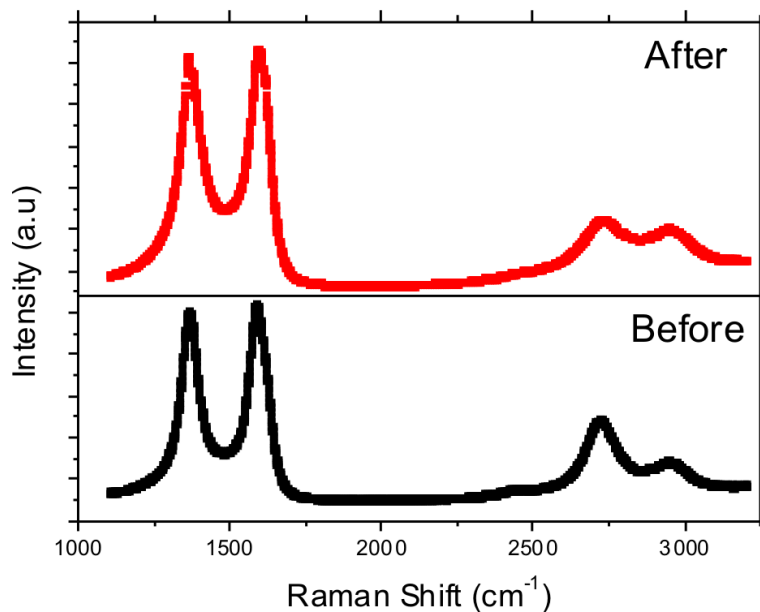


**Figure 5.3 | Raman Spectroscopy.** Results from before and after field emission measurement were performed on a CNT pillar array showing minimal changes.

Raman Spectroscopy of the CNT pillars highlighted some structural and material properties about the emitter. A change in the position of the G band, the peak associated with the graphitic nature of a carbon material, indicates doping. A (positive) shift of  $\approx 5\text{ cm}^{-1}$  is seen in the G

band after FE measurements have been performed. This is a small shift but suggests that *n*-type doping may have occurred<sup>40</sup>, though the magnitude of change is not necessarily sufficient to confidently state this. The D peak, exhibiting defects, shows no change. Similarly, the  $I_D/I_G$  ratio, giving some measure to the quality of the CNTs, doesn't change significantly, showing the lattice is not compromised by the applied fields and stresses of the FE process. The slight decrease in the ratio indicates, if anything, a decreasing number of defects. This is a positive result, proving our CNTs have the robustness to withstand the otherwise aggressive FE conditions.

The only significant change before and after FE test have been performed on an emitter is to the 2D peak, decreasing to 75% of the pre-measurement intensity and a shift of increased position by  $10\text{ cm}^{-1}$ . The 2D peak represents a term to measure and determine the type of doping in graphene<sup>41</sup>. The position of the 2D peak can discriminate between electron and hole doping. An increasing concentration of electrons in the system results in a decrease in peak position. From our data, assuming the behaviour of graphene is similar to that of CNTs, this would suggest that hole doping caused during our FE measurements. Water and oxygen are the main components of residual gas between the pressures of  $10^{-4}\text{ Pa}$  to  $10^{-7}\text{ Pa}$ , giving rise to assumptions these are the species that would be most likely to dope the emitter surface<sup>10</sup> whilst exposed to vacuum conditions. Whilst *p*-type doping has been shown for oxygen doping<sup>42</sup>, water vapour has shown conflicting evidence, though has been thought to have a minimal influence<sup>43,44</sup>. The shift seen is suggestive of *n*-type doping, which could indicate removal of electronegative species, such as oxygen. It has been suggested by Das *et al*<sup>41</sup> that whilst both G and 2D peaks give an indication to the doping of a sample, that the 2D peak is a better indicator due to lower sensitivity of the G phonon to an external electrostatic potential.

### 5.4.3 Optical Excitation

This test explores the FE as a function of optical excitation by a range of different wavelengths. CNTs can exhibit unique optical properties due to their 1D structure and Van Hove singularities that characterise their energy band structure<sup>45</sup>. Optical invariance, showing normal emission behaviour at each exposed wavelength, is important for the use of CNTs as glass-enclosed X-ray sources.

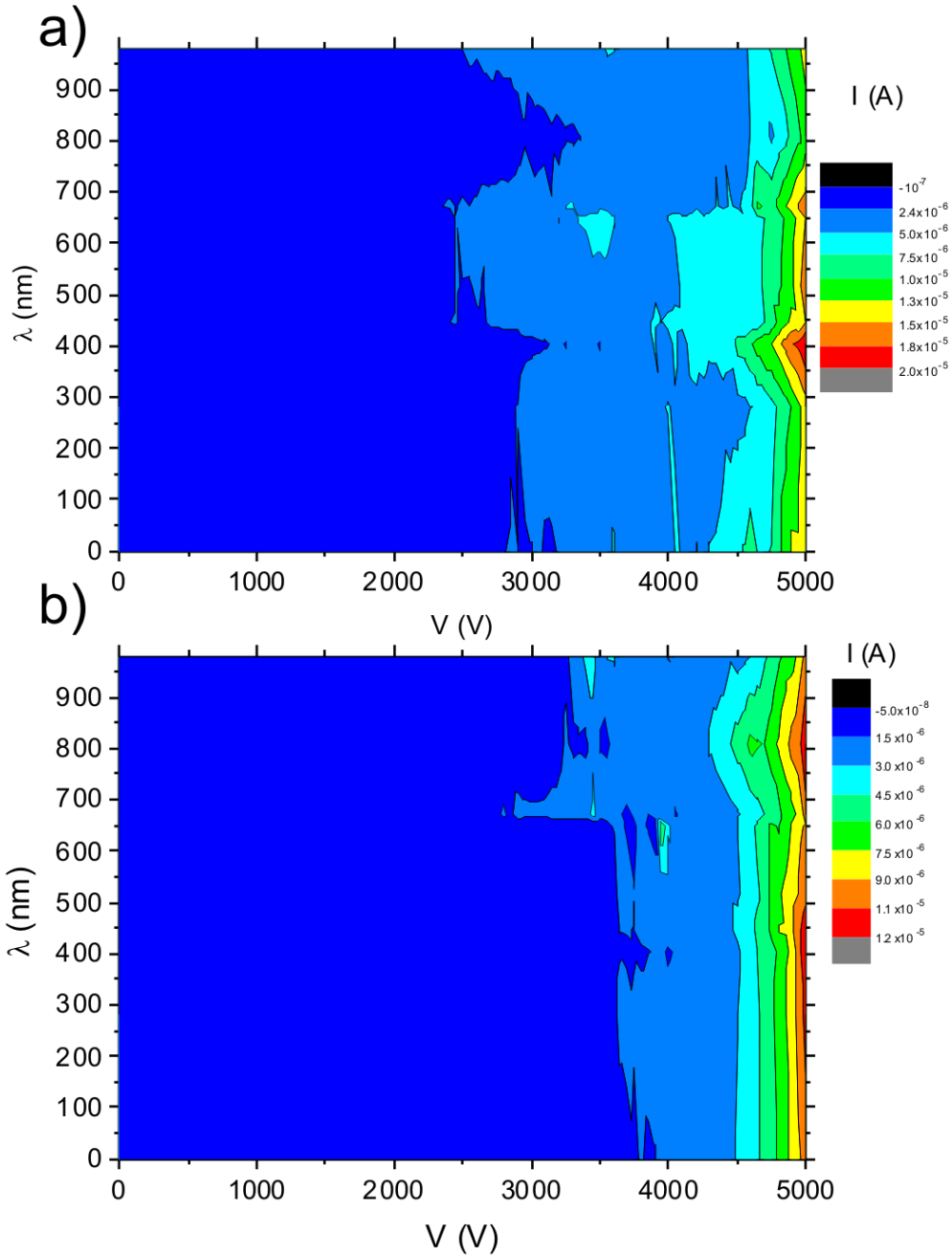


**Figure 5.4 | Optical Excitation Map.** Map of the current measured using different optical wavelengths exposed on the surface of two different, but identical, samples.

DC optical exposure FE measurements were taken using narrow band optical sources centred at (Full-Width-Half-Maximum, FWHM); 208 nm, 405 nm, 445 nm, 515 nm, 650 nm, 670 nm, 808 nm, 980 nm. This encompasses light from the infrared to ultra violet regions of the electromagnetic spectrum. All optical sources had  $< 5$  mW incident power and were mounted exterior to the vacuum chamber. The chamber was optically isolated from ambient with the

## 5. Hysteretic Behaviour of Carbon Nanotube Field Emitters

laser light passing through a quartz window. A single wavelength of light was shone on the centre of the top of the anode at a time, beneath which was the CNT sample.

Figure 5.4 shows a map of the FE at the different wavelengths from two samples with the same pillar array. The exponential nature of the FE is clear from the exponential increase seen in current towards the right hand side of the figures. The general results show that there is very little noticeable difference between the measured wavelengths of excitation and indeed the two measured samples show similar results. A small peak can be observed on both samples around 650 nm, this is reflected in the measured  $E_{on}$ , shown in Figures 5.5 and 5.6. The peak shows a current  $5.5 \mu\text{A}$ , over two times larger than the surrounding measurements, and occurs at 3950 V, where the field has a value of  $6.58 \text{ V}/\mu\text{m}$ . Resonances under optical excitation can be indicative of defects, local adsorbates or states<sup>46</sup>. The result of mostly optical invariance is positive for the use of these nanotubes in X-ray devices.

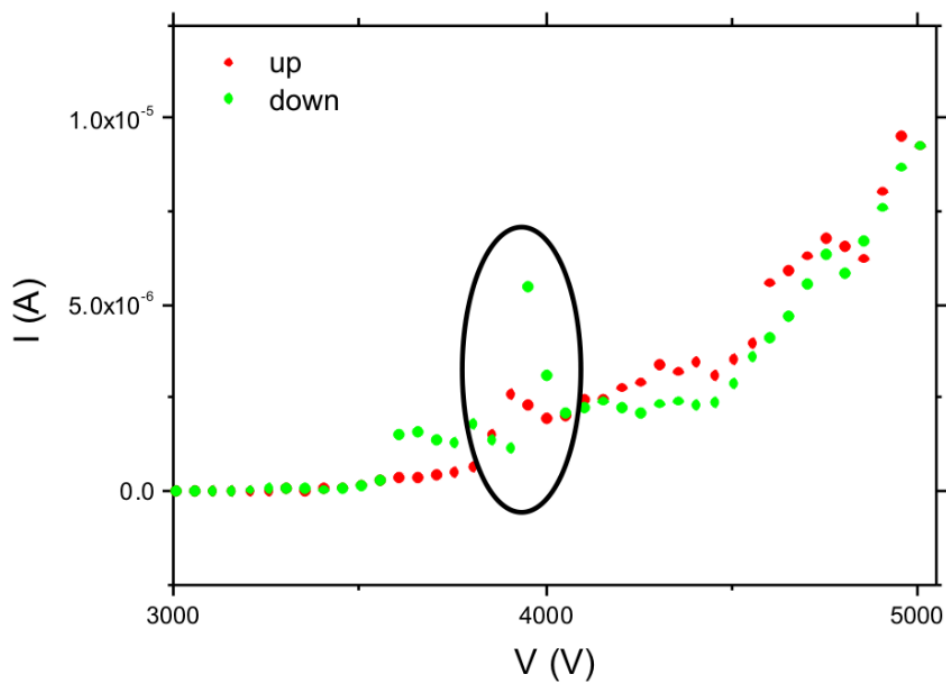


**Figure 5.5 | Peak at  $\lambda = 650 \text{ nm}$ .** Magnified view of a peak seen under optical excitation of 650 nm wavelength appearing in both up and down sweeps.

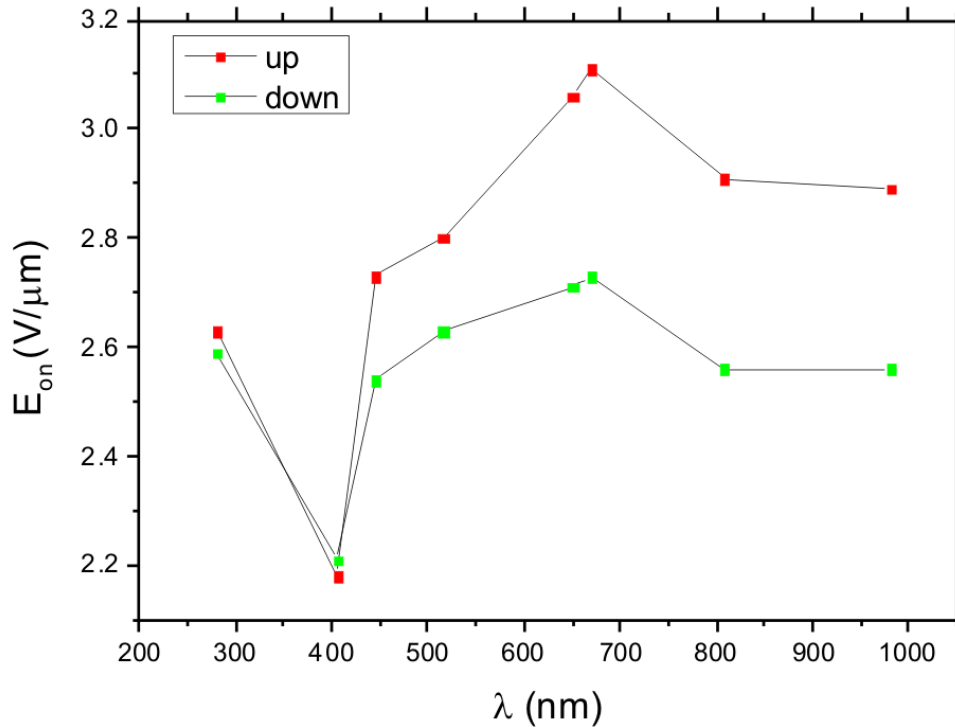


**Figure 5.6 | Optical Turn-On Values.** Turn on electric field, measured at a current of 1 nA, for each of the wavelengths a CNT sample is exposed to under field emission conditions. The resulting curve reflects the absorption edge of CNTs.

Figure 5.6 shows the measured values of  $E_{on}$  for both the up and down sweeps, a measured difference between these values is apparent. The trend, with a dip around 400 nm wavelength (ultra-violet region) seen, is characteristic of the absorption edge of carbon nanotubes, which refers to the MWNT ability to accept electrons from light irradiation in this regime<sup>47,48</sup>. Despite being metallic, with zero band gap, Rezenia and Taherkhani<sup>49</sup> have shown similar behaviour in optical conductivities of metallic and semi-conducting CNTs caused by electron-phonon coupling and the appearance of an energy gap in the density of states. The difference in values of  $E_{on}$  highlights that hysteresis is present in the measurements, with the down sweep showing mostly consistent smaller values. At smaller wavelengths the hysteresis is minimised, compared to the larger wavelength values, towards the infrared end of the spectrum. The optical excitation can be minimised by running measurements in the dark, which is performed herein.

#### 5.4.4 Vacuum Pressure Dependence

The effect on the emission process by vacuum pressure is tested here. The FE at different pressures is measured, with a single voltage loop performed at a number of intervals from high

## 5. Hysteretic Behaviour of Carbon Nanotube Field Emitters

vacuum,  $10^{-7}$  mbar, to low vacuum,  $10^{-4}$  mbar. The experiment is designed to show the influence of pressure on  $I_{max}$  and to verify it is field emission rather than ionic emission. The effect of the difference made to  $I_{max}$  and  $E_{on}$  is studied, and a safe working upper pressure is found.

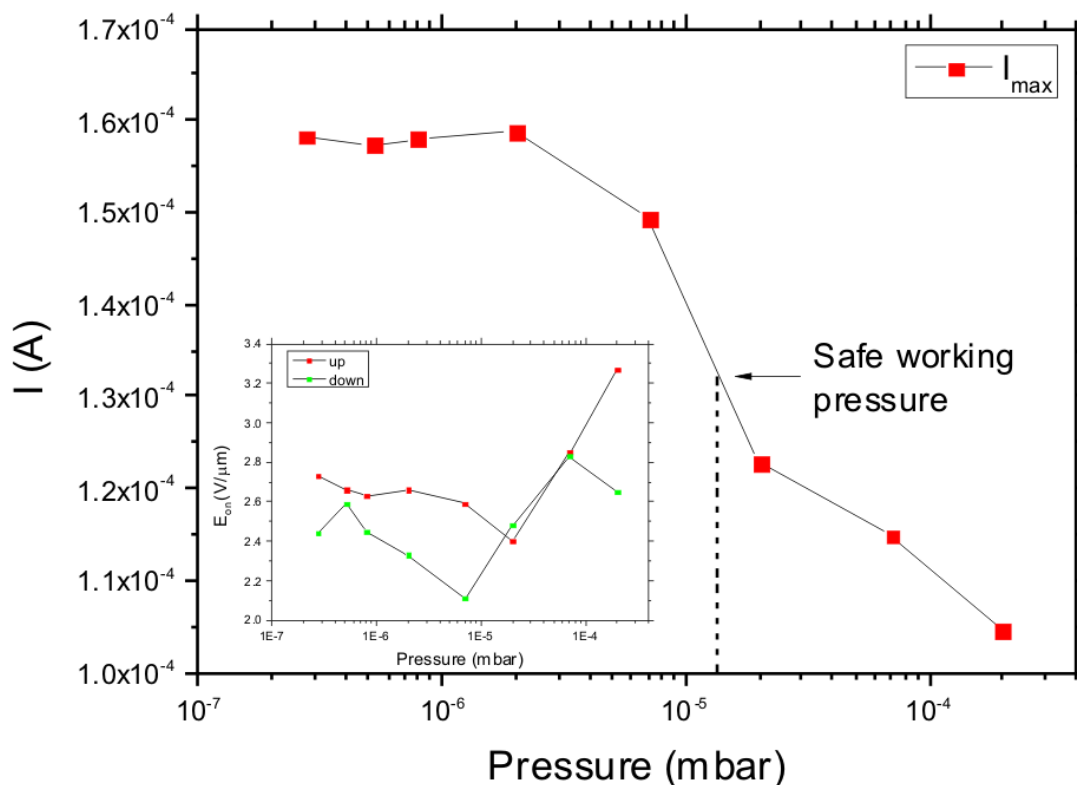


**Figure 5.7 | Dependence of Maximum Current on Vacuum Pressure.** (Insert) Dependence of  $E_{on}$  on pressure.

Differing pressures are measured at increasing air levels in the chamber, gradually leaking air into the system by slowly shutting the aperture to the turbomolecular pump. This is in order to maintain more consistent composition of molecules in the vacuum environment as different species are extracted from the chamber at different pressures:  $N_2$  is pumped first, followed by O and  $H_2O$ , where such polar species can adhere to the sides of the chamber, or indeed any surface<sup>10</sup>. By bleeding in the air, a constant gaseous composition is maintained compared to gradually releasing air from the vacuum. By determining a safe working pressure, and verifying whether fluctuations in measured current is observed under pressure variation, further experiments can be performed at a range defined by this test. The vacuum, when established, shows minor fluctuations, and can range up to  $1 \times 10^{-6}$  mbar when performing measurements

on consecutive, or indeed individual, samples, which cannot be better controlled. The safe working pressure can be defined by the point beyond which the maximum current measured is consistent, eliminating the need to maintain a constant, unfluctuating pressure across the entire measurement range. We can assume that below this value, the pressure has no effect on the measurements and it can be eliminated as an affecting variable.

The results of the experiments are shown in Figure 5.7. Figure 5.7 shows  $I_{max}$  measured at a range of pressures from  $2.8 \times 10^{-7}$  mbar to  $2.0 \times 10^{-4}$  mbar. It can be seen that at pressures below  $2 \times 10^{-6}$  mbar the value of  $I_{max}$  remains mostly constant. As the pressures exceed this, however,  $I_{max}$  drops off rapidly. The turning point is indicative of the point at which the emission regime changes from FE to other emission regimes, such as ion emission. A safe working pressure was determined by finding the mid-point value between the highest and lowest recorded  $I_{max}$ , which was found to be  $P = 1.37 \times 10^{-5}$  mbar. The consistency of the values at high vacuum show that  $I_{max}$  is not dependent on vacuum level when FE is the main emission mechanism. For future studies, this pressure was used as a point of reference, below which FE took place. In general, pressures of around  $10^{-7}$  mbar were chosen to perform experiments, to ensure the measurements were safely in the FE regime. Figure 5.7 insert shows the difference in  $E_{on}$  calculated for both up (red) and down (green) voltage sweeps. A noticeable difference between the two measurements is seen, with the down result consistently reporting a lower value. This is symbolic of an underlying hysteresis. In similarity with  $I_{max}$ ,  $E_{on}$  increases rapidly over a pressure of  $2.0 (\pm 0.8) \times 10^{-5}$  mbar. In contrast, however, the values of higher pressure show a decreasing trend before this value is reached. This is characteristic of the suppression of the liberation of electrons from the surface under higher vacuum levels.

## 5.5 In-Situ Residual Gas Analysis

In order to determine whether the underlying hysteresis mechanisms were associated with local gas species, residual gas analysis, RGA, was used to monitor the presence of a number of elsewhere implicated gas species throughout the emission exposure at different electric field values. In conjunction with the pressure studies, the collected data was also used to monitor gas species and the performance of the vacuum pumps. By analysing the gas in the vacuum chamber throughout the process, determination of gas species potentially released at different electric fields and the effect on the emission can be studied, bearing in mind the importance of

## 5. Hysteretic Behaviour of Carbon Nanotube Field Emitters

adsorption and desorption on hysteretic behaviour previously observed. It is important to detect the gas species at small intervals along the measurement loop, not just at the beginning and end, to ensure data covers the area of largest hysteresis seen in emitted current, which is primarily in the previously identified mid-field zone, and to analyse the proportion of different species at each field value.

The gases of noted importance are H<sub>2</sub>O, H, O<sub>2</sub>, N<sub>2</sub> and CO<sub>2</sub> because they have been credited with causing an effect on a number of influential properties. H, at 1 amu is, however, not reliably measured using the RGA and is thus not examined in the analysis. H<sub>2</sub>O, H and O<sub>2</sub> reportedly contribute to an increase in  $\phi$ <sup>9,50</sup>, which could increase  $E_{on}$  and measured current, whilst hysteresis is reportedly quenched by adsorption of O<sub>2</sub> or CO<sub>2</sub><sup>51</sup>. Exposure to a mixture of H<sub>2</sub>O and O<sub>2</sub> dopes, supposedly, more strongly than exposure to each individually<sup>52</sup>. H<sub>2</sub>O alone has been shown to redistribute the charge caused by the dipole moment of the H<sub>2</sub>O molecule but has also been shown to not significantly dope CNTs<sup>43</sup>. An increase in partial densities of H<sub>2</sub>, H<sub>2</sub>O, CO and CO<sub>2</sub> were reported by Okotrub *et al*<sup>12</sup> at high field strengths during the emission process, suggesting these particles were removed from the CNT surface. N has a larger electronegativity than C, which in doping has been shown to donate a  $\pi$  orbital electron. N atoms, replacing C atoms in doping, purportedly change the local DOS around the Fermi level<sup>53</sup>, which could again affect the emitted current, though this time positively. N doping raises the highest occupied molecular orbital, HOMO, above the Fermi level, with the resulting effect showing higher measured FE and lower  $\phi$  due to less energy required in electron excitation<sup>52</sup>.

An RGA analyses the composition of the molecules in the vacuum by mass spectrometry. A small sample of gas molecules is ionised positively, separated, detected and measured. The measurement made is of the mass to charge ratio:  $M/Q$ . Molecules that have the same  $M/Q$  ratio cannot be distinguished, however, assumptions can be made with some basic knowledge of the environment and general applied logic. A *Stanford Research Systems: RGA 300* is used to measure the partial pressures of molecules present in the vacuum. The mass range of 1 amu to 100 amu, was specified in the scan details, as well as scan speed. Data was collected in histogram mode and saved as a .txt file as well as a histogram .rga file.

The measurement loop was slightly different to the previously seen methods to allow for extra time to perform RGA measurements at each voltage step. The previously described pillar arrays were again used in this experiment. Pressures in the low  $10^{-6}$  mbar range were used, within the

safe working pressure. A voltage loop was run in 250 V intervals from 0 V to 5000 V in contrast to the usual 50 V intervals. This allowed larger setting times to be used without compromising the length of the experiment by too much. The settling time was set up to 60 s to allow sufficient time for RGA analysis to be made. The two files that are generated, one containing FE data the other with RGA data, can be directly compared as they correspond to each other as being made at the same time. Pressure of the chamber was monitored using the data from the RGA and additional pressure gauges that took readings within the vacuum. Three pressure gauges monitor vacuum levels in the SAFEM and parallel plate combined chambers. One in the parallel plate side and two additional ones when the chambers are connected. The RGA sits between the two sides, requiring vacuum to be established in both sections of the machine (in contrast to the other experiments in this chapter, where the parallel plate chamber only is used). This resulted in vacuum pressures of slightly higher values than were seen throughout the other tests. The chamber was baked for over an hour prior to the measurements in attempt to increase the vacuum further. The previously determined safe working pressure range was achieved.

### 5.5.1 Results and Discussions

The scan range was set to detect species with between 1 amu and 100 amu. The most common gas species, as determined by those that produced the largest peaks, were at 2 amu ( $\text{H}_2$  / deuterium), 17 amu (OH - water fragment /  $\text{NH}_3$ ), 18 amu ( $\text{H}_2\text{O}$ ), 28 amu ( $\text{N}_2$  / CO /  $\text{C}_2\text{H}_4$  / Si), 29 amu ( $\text{CH}_3\text{CH}_2$ ), 32 amu ( $\text{O}_2$  /  $\text{CH}_3\text{OH}$  / S), 43 amu (acetone fragment) and 44 amu ( $\text{CO}_2$  /  $\text{C}_3\text{H}_8$ ). Where more than one molecular ratio corresponds to the measured amu, the species in bold indicates which molecule this was assigned to. The abundances of these species in the vacuum can be seen in Figure 5.8. Amongst those considered interesting in terms of the potential effect of doping of CNTs with an effect on hysteresis are:  $\text{H}_2\text{O}$ <sup>9,43,52</sup>,  $\text{N}_2$ <sup>51-53</sup>,  $\text{O}_2$ <sup>50-52</sup> and  $\text{CO}_2$ <sup>51</sup> for reasons previously stated. These species are plotted alongside the corresponding *I-V* FE curves in Figure 5.9.

The results of hysteresis and the partial pressures of  $\text{H}_2\text{O}$ ,  $\text{N}_2$ ,  $\text{O}_2$  and  $\text{CO}_2$  can be seen in Figure 5.9. Figure 5.9a shows the *I-V* curves of the three measurements. The maximum current reached decreases with each run. Each of the measurements with the corresponding gas partial pressures are shown in Figures 5.9 b, c and d. The hysteresis is the largest in the first example, where the measured current was also the largest. In this first measurement, the level of  $\text{H}_2\text{O}$  in the chamber remains mostly constant with some change to  $\text{O}_2$  and noticeable difference in the  $\text{N}_2$  and  $\text{CO}_2$  partial pressures. This is further exemplified in Figures 5.9 e, f, g and h which

## 5. Hysteretic Behaviour of Carbon Nanotube Field Emitters

show the individual gas evolutions. Figure 5.9c shows a much tighter hysteresis and only minor variations in the gas partial pressures. Figure 5.9d, showing the smallest measured current, has the most dynamic variation of the H<sub>2</sub>O content in the vacuum, with some CO<sub>2</sub> variation as well. Subsequent measurements, seeing mostly stable pressures of H<sub>2</sub>O in the chamber, showed similar  $I_{max}$ , suggesting that when the vacuum chamber shows variations in water vapour levels, this could affect both  $I_{max}$  and the amount of hysteresis seen. The direction of the gas species, indicated by the arrows on Figures 5.9 d, e, f and g, could point to whether the water molecules are doping the surface of the CNTs or are being released. In the third field emission measurement, the levels of H<sub>2</sub>O in the chamber differ to the first two runs, increasing instead of decreasing throughout the measurement. This could show the release of these particles from the surface into vacuum, though this could also include particles measured by the RGA that were previously stuck to the chamber walls or simply signpost vacuum leakage.

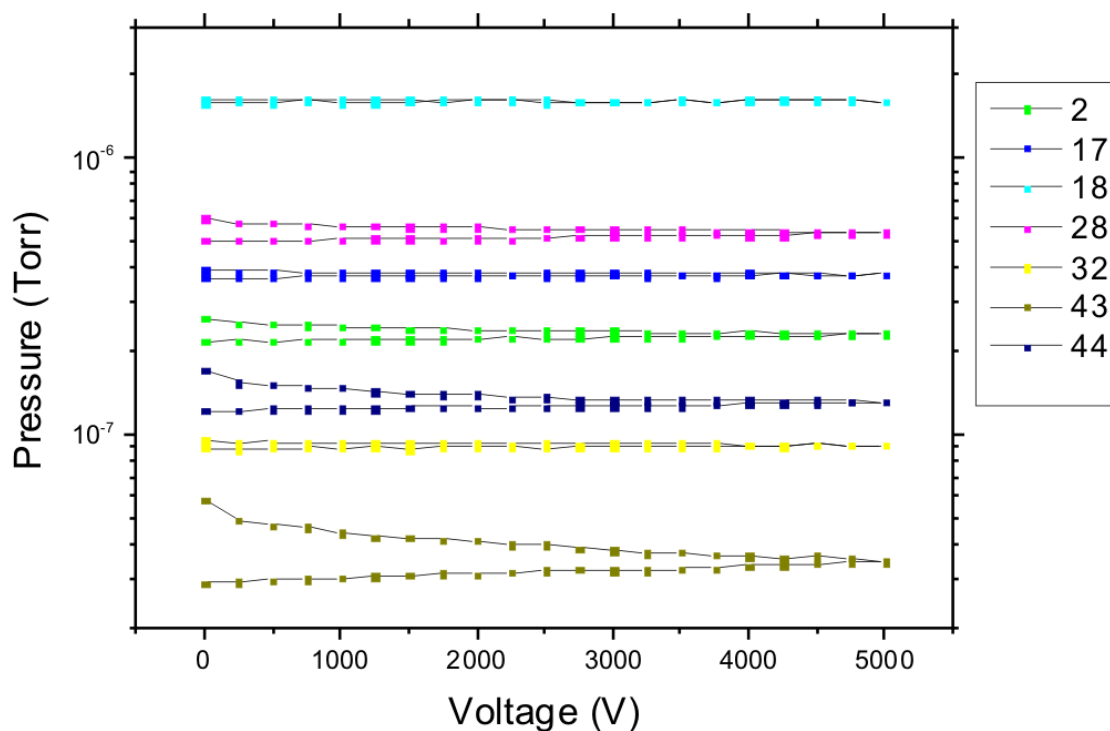


**Figure 5.8 | Gas Species in Vacuum.** Residual gas analysis results showing most prevalent partial pressures of gas species present in the vacuum between 0 and 100 amu.

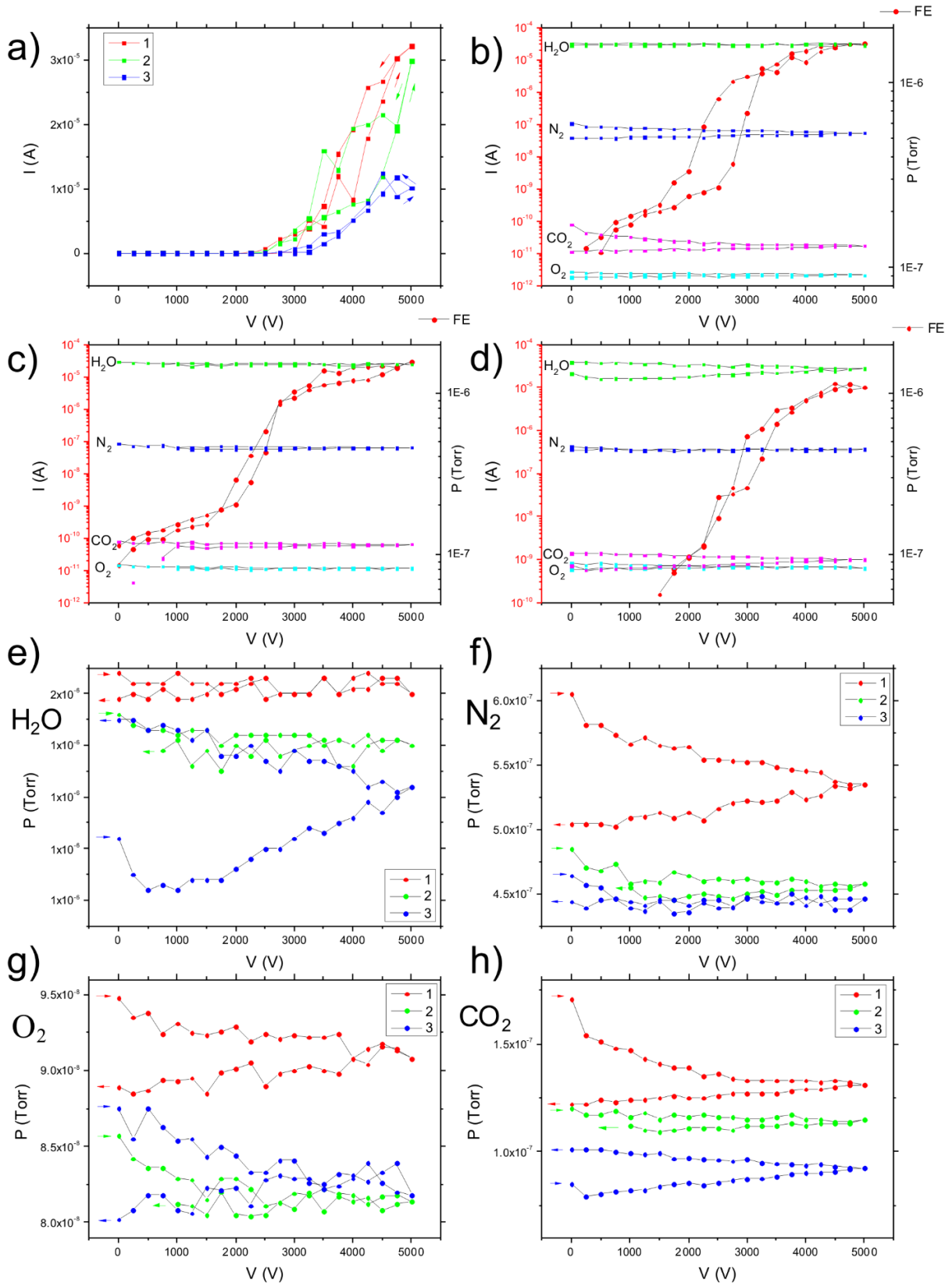


**Figure 5.9 | RGA Results.** a) Measured field emission whilst exposed to *in-situ* RGA. Emission and partial pressures of influential species of b) the first, c) the second and d) the third voltage sweep. Partial pressures for each sweep of e)  $H_2O$ , f)  $N_2$ , g)  $O_2$  and h)  $CO_2$ .

## 5. Hysteretic Behaviour of Carbon Nanotube Field Emitters

The adsorption of species from ambient air on the CNT surface before being placed into the vacuum is likely more influential on the hysteresis than those present in the vacuum. The composition of air is 78.09 % N, 20.95 % O, 0.04% CO<sub>2</sub>, with some variability on the amount of water vapour, typically 1 - 4% at the Earth's surface, and other gas species. However, it has been shown that despite the relatively low levels seen, water molecules are favourably adsorbed onto CNTs compared to N and O<sup>54</sup>, suggesting there may be higher levels of this present on the CNT before the experiment, and that water vapour species are also more likely to adsorb compared to others in the vacuum environment since they make up the highest proportion of any molecule.

The vacuum environment could be influential in determining the species adsorbed onto the surface, particularly in the down sweep, where any desorbed molecules leave likely adsorption sites vacated. Charged particles in particular are likely to be attracted by the large local electric fields to the CNT tips, increasing their likelihood of adsorbing. Even if the measured gases are not involved in the direct process of hysteresis, they could be influential in determining factors such as the maximum current. When the amount of H<sub>2</sub>O in the chamber is dynamic, this could suppress the current, as is seen in Figure 5.9d. The levels of N<sub>2</sub> or O<sub>2</sub> could be influential in determining the amount of hysteresis seen, both of which vary somewhat in relation to the amount of hysteresis.

The number of particles present, both those that make up the CNTs and those present in the vacuum, can be calculated knowing the partial pressures and volume of the chamber. The number of carbon atoms present in the CNT patterned pillar sample, as used in this experiment, was calculated to be approximately  $1 \times 10^{16}$  atoms. This was calculated using the area coverage of CNTs on the Si substrate (0.0079 m<sup>2</sup>) and a packing density ( $10^{10}$  CNT cm<sup>-2</sup>), assuming a number of five nested CNTs in an average MWNT. The grown CNTs also had a height of 4 μm and width of 25 nm. A similar value, of  $5 \times 10^{15}$  gas molecules was calculated to be present in the chamber, and assumed to be evenly distributed throughout the chamber. This value was calculated according to the ideal gas law using  $PV = nRT$ , with  $P = 3.3 \times 10^{-9}$  atmospheres,  $V = 55$  litres, under room temperature operation. The total carbon atoms present in CNTs to vacuum molecules, C:Vacuum, was therefore 1.5:1. The most abundant species, H<sub>2</sub>O, was found to have a C: H<sub>2</sub>O ratio of 4:1. Dispersed throughout the volume of the chamber, however, this ratio will be far diluted around the emitting CNTs.

## 5.5.2 Limitations and Future Work

Some limitations exist with the experimental set up. The RGA measures the partial gas pressures of the entire combined chamber of the parallel plate and SAFEM, which is large compared to the emission area. It is assumed that the dispersion of the gases inside the chamber is homogeneous, thus correctly representing the vacuum surrounding the CNTs and between the plates, where emission is measured. There is some ambiguity to the validity of this, as the RGA is placed some distance (approximately 10 cm) away from the active FE site. In future work, moving the RGA measurement location as close as is possible to the emission area may provide higher quality of information regarding any species that might escape the emitter surface and be released into the wider vacuum. Comparing results of two sets of measurements from both close to and further away from the emission zone could highlight which molecular activity in the vacuum is due to fluctuations from the pump and which is involved in the FE process.

The hysteresis is a cyclical quality. The cycle is suggestive that if species are released from the surface, they return when the field reduces, though whether the same species return to the same locations as they were released from and in the same quantities is not known, nor is it easily determined. Measuring the release into the wider vacuum chamber may not be trivial, as molecules are likely to remain in the local vicinity to be re-adsorbed, and may not possess required energies to escape the system and could also depend on the pumping rate of the chamber. Similarly, charged particles would remain within the boundaries of the electric field, when an electric field is applied, so only neutral species with enough energy could be released into the vacuum where they could then be measured by the RGA. In addition to the measurements throughout the FE cycle, measuring the RGA at intervals for some time (on the scale of a few minutes) after the end of the experiment has finished may lead to discoveries of particles that were trapped by the electric field, released to the wider vacuum, once the measurement loop has terminated, though determination of these species above a noise level may prove challenging.

Certain species are likely preferentially involved in the sorption process at defined energies and CNT locations. Allocation of signature energies or time constants of individual species is difficult to address due to the immeasurable quantities of local field enhancement around individual emitting tips, which is likely of high influence in providing the required energies for desorption. If the CNTs were to be exposed to influential gases in isolation to encourage the

## 5. Hysteretic Behaviour of Carbon Nanotube Field Emitters

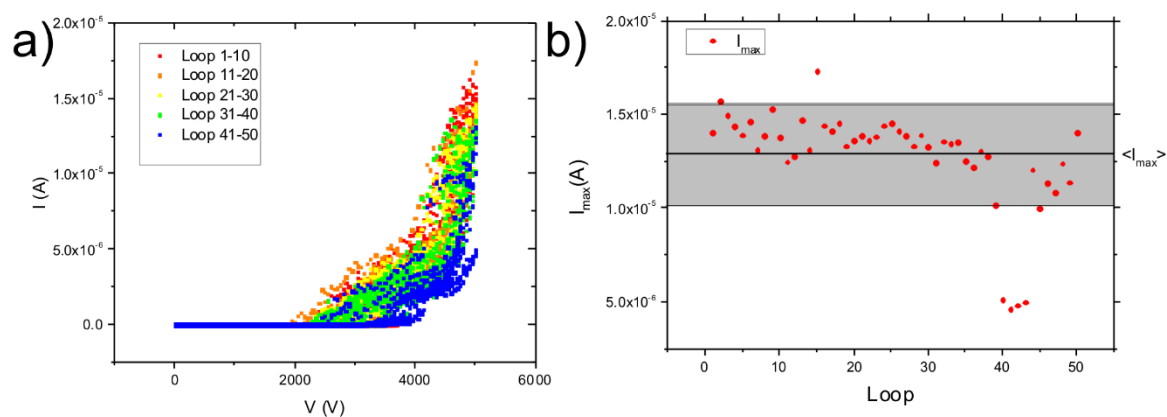
adsorption of an individual molecule species on separate emitters, without exposure to ambient before measuring the FE, it may be possible to address these energies and indeed the effects of each molecular species, and their signatures, with more clarity. This could be performed in two ways after the initial CNT growth. Firstly, the use of plasma treatments has already been seen and undertaken by some (See Chapter 2, Section 2.7). Exposure to plasmas of the influential species could, in theory, be performed in the CVD chamber, immediately after the CNT growth. This can, however, change the structural nature of the CNTs. The second way to achieve exposure to the gas molecules, which would better simulate the natural response, would be to simply flood the CVD chamber after fabrication with a single gas species for some length of time, possibly up to a few days to allow maximum adsorption to occur. This would give a better indication of which species are preferentially adsorbed onto the surface and at what quantities, as plasma treatments could be quite aggressive. Transferring these samples with minimal exposure to ambient would be desirable. Resulting FE from these emitters may then give better indications as to individual species contributions to hysteresis and reveal where in the cycle, with corresponding energies, each species desorbs and re-adsorbs onto the CNT surface.

It is important to remember that the hysteresis in this work could be directly affected by the vacuum level. If the results were collected in an environment where the vacuum levels were higher, for example  $10^{-9}$  mbar, the hysteresis may be of a different character. The initial hysteresis would likely behave the same initially, however, after the initial conditioning period, the hysteresis may become much less prominent.

### 5.6 Stability

Stability is important if FE applications are to become commercially viable. If the technology is to replace existing methods, which have current lifetimes of up to a year (X-ray sources<sup>55</sup>), this must be matched as an absolute minimum requirement. The temporal stability is measured by the ability of the emitter to maintain performance over an extended period of time. Maintaining a consistent performance is achieved, principally, by recording a constant emitted current. It has been noted by Chen *et al*<sup>9</sup> that hysteresis disappears after what is termed 'conditioning', where supposed adsorbed molecules gradually become removed and the measured current becomes repeatable between loops, purportedly increasing stability. This

experiment allows further investigation of this theory. The sample was subjected to a 0 V - 5000 V sweep at 50 V intervals (returning to previous method described in Section 4.4.1) for a total of 50 consecutive loops, totalling a period of approximately 17 hours. The sample was previously measured for FE, so it is important to note that the first loop is not the first measurement made, it is the  $n + 1^{\text{st}}$ . Also of importance to note is the exposure to ambient before the  $n + 1^{\text{st}}$  measurement.



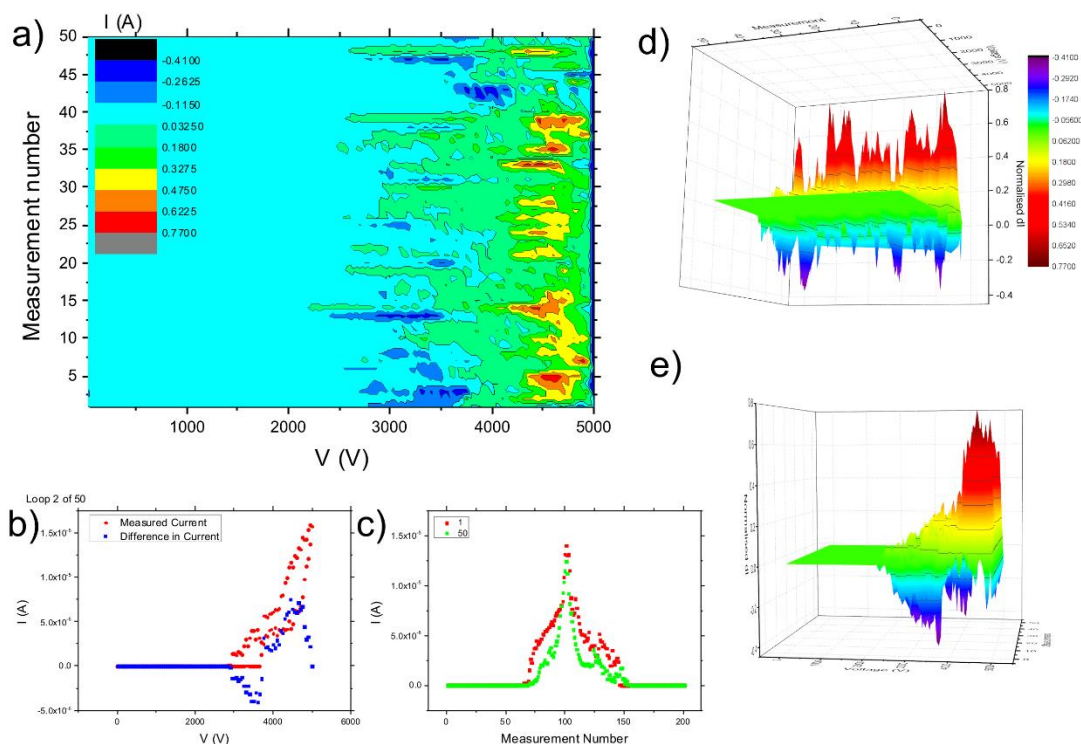
**Figure 5.10 | Stability Data.** a)  $I$ - $V$  Curves showing field emission for 50 voltage loop cycles grouped in tens to highlight gradual emitter degradation b) Maximum emitted current for each of the measured cycles.

Figure 5.10a shows the  $I$ - $V$  curves for the results of the stability experiment. Loops are grouped in tens using different colours from red to blue. This allows the gradual changes in emission to be observed, with the latter  $I$ - $V$  curves showing higher turn on fields and lower measured currents. The gradual decrease of  $I_{max}$  is shown in Figure 5.10b. The average value and one standard deviation above and below this are represented by the area within the grey box. The central measurements, between 20 and 40 loops, appear the most repeatable when assessing according to  $I_{max}$ . It has been previously suggested<sup>9,56</sup> that a conditioning period, where adsorbates are removed from the system, leads to increased stability. Although they also see the opposite trend to that seen here, with increasing  $I_{max}$ . However, these results could give further evidence to support the conditioning theory. Anomalies around the 40<sup>th</sup> loop show low  $I_{max}$ , but this is recovered towards the end of the cycle. The anomalous results could be due to arcing, which can destroy the emitter irreversibly or some change to the conditions in the vacuum chamber. It could also exemplify burn out, where significantly contributing, dominant CNTs provide a large proportion of the current and subsequently fail. The recovery seen here,

## 5. Hysteretic Behaviour of Carbon Nanotube Field Emitters

with the maximum current returning to a similar value, could be indicative of other CNTs taking on the role of emission as the first dominant ones are destroyed.

To study the evolution of hysteresis with use, the difference in current,  $\Delta I = I_{up} - I_{down}$ , is mapped across the measurement range in Figures 5.11 a, d and e. Values are normalised by dividing  $\Delta I$  by  $I_{max}$  for each loop. Figure 5.11a shows a 2D map of these values. Along with decreasing  $I_{max}$ , as the number of measurements increases, the hysteresis appears to become less exaggerated, with smaller measured  $\Delta I$  towards the end of the measurement cycle. The most exaggerated difference in the current is expressed at the beginning of the measurement process, within the first five or so measurement loops. The profile of  $\Delta I$  for a single measurement loop is shown in Figure 5.11b, and is characterised by a trough followed by a peak, formed by the regions where each of the up or down currents show higher values. In the high-mid field region values are positive, where the peak occurs,  $I_{up} > I_{down}$ . This scenario is the most prominent, with up currents generally higher than down measurements. This is opposite to the low-mid field region where  $I_{down} > I_{up}$ , resulting in negative values of  $\Delta I$ . At the end of the measurement, values converge towards  $\Delta I$ , where  $I_{up} \approx I_{down}$ . This is demonstrated in Figure 5.11b, where both the measured current, with clear hysteresis, and the difference  $\Delta I$  are displayed. At the intersection between peak and trough,  $\Delta I = 0$ . The average point at which this cross-over occurs is at  $3800 \text{ V} \pm 230 \text{ V}$ .



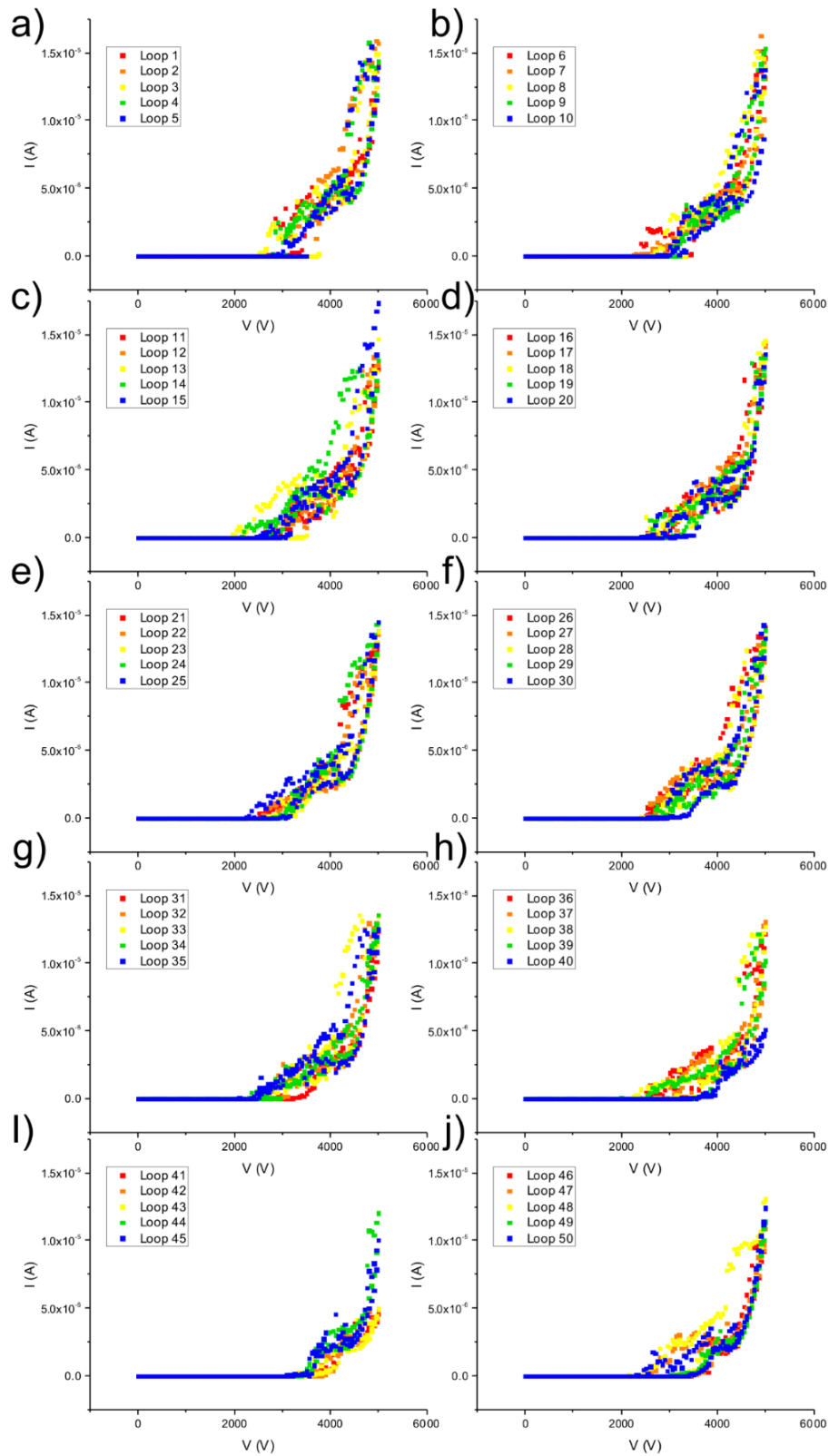
**Figure 5.11 | Evolution of Hysteresis over Exposure to 50 Voltage Cycles.** a) Normalised map of the difference between up and down measured current,  $\Delta I$ , b) example of the measured current (red) and the calculated difference in up and down sweep currents (blue), c) the difference between the current for the first (red) and final cycle (green) displayed by measurement number, d) and e) show measured current difference in 3D visualisation.

Figure 5.11 c shows the data presented in a novel way for the  $n + 1^{\text{st}}$  (red) and  $n + 50^{\text{th}}$  loop (green); the curve is opened up by arranging the measurement points by number, rather than by voltage as is traditionally seen. This allows for easier comparison between both the two sweeps in each direction and the two different measurement cycles. Displaying the data in this way highlights the narrowing of the emission curve. The FWHM of each of these curves can be measured and was found to be 2150 V and 850 V for the first and last measurements respectively. The narrowing of the FWHM marks the change in the emission current, which is reduced at all points leading up to  $I_{\text{max}}$ . Similarly, measuring the area under the curve to give an estimate of the hysteresis, the value drops to 60% of the original value, indicating a change in the amount of hysteresis. This could be attributed to permanent desorption of molecular species, correlating to the reduction in hysteresis, but could also indicate degradation of the emitter. It can be seen that on the down sweep, to the right hand side of the central peak when displayed this way, there is an agglomeration of data points in the mid-field range that show some spread in the first measurement, but narrow to more of a peak by the final measurement.

## 5. Hysteretic Behaviour of Carbon Nanotube Field Emitters

An explanation of the observed peak is the release of electrons from a source on the CNT surface. This could be caused by effects of adsorbates or trapped states from physical defects in the surface, which restrict the movement of electrons, which could show a resonance or release at certain field values. Peaks in the down sweep could possibly appear as the species are re-adsorbed, showing the permanent escape of a number of other species when the majority of adsorbates are permanently removed over the repeated cycles. The previously seen Raman spectroscopy shift (Section 5.4.2) could further support this, as this was performed after this experiment. The peak seen in the final measurement could, therefore, show that the majority of the species have been desorbed, leaving either a reduced few on the surface, or just one species of gas. Adsorbed species on the surface of the CNTs could each contribute to the emission at different field values.

Figure 5.12 shows the evolution of the FE in groups of five measurements. Initially, loops 1-5, there is consistency of the hysteresis in the mid-high field region, where it is notably defined and quite pronounced. The shape of the emission becomes less consistent with increasing measurement number after this. Between the 20<sup>th</sup> and 30<sup>th</sup> measurements, the hysteresis regains some consistency, with a narrower hysteretic behaviour than seen in the first five measurements. This is consistent with the earlier claim of stability of  $I_{max}$  in this region, and



**Figure 5.12 |  $I$ - $V$  Curves of Grouped Loops.** a) 1-5, b) 6-10, c) 11-15, d) 16-20, e) 21-25, f) 26-30, g) 31-35, h) 36-40, i) 41-45, j) 46-50.

## 5. Hysteretic Behaviour of Carbon Nanotube Field Emitters

similarly correlates to the suggested cleaning, or conditioning, process. The changes seen between these two more consistent states could be indicative of the removal of adsorbates from the surface. The smaller measured values of  $\Delta I$  in this range, indicating smaller hysteresis, seen in Figure 5.11, could be due to the removal of polar species, such as  $O_2$  or  $H_2O$ . Higher  $I_{max}$  could be caused by the removal of  $O_2$ , whose electronegativity leads to higher surface  $\phi$  (where the opposite effect is seen here) and which has been shown to be the first species to desorb in temperature studies<sup>57</sup>, suggesting this may also be the case under applied electric fields. Previously conducted experiments (by Dr. Matthew. T. Cole) have shown that the emitter does not heat during the FE process and desorption of species by thermally acquired energy is thought unlikely under the experimental conditions experienced here. Adsorption of  $O_2$  and  $CO_2$  on graphene has shown an increase in  $E_{on}$ , the latter of which also resulted in large reduction of  $I_{max}$ <sup>51</sup>. Conversely, desorption of these two species would therefore be expected to increase  $I_{max}$  and decrease  $E_{on}$ , which is indeed somewhat apparent in the results presented here. Since  $I_{max}$  is not drastically improved, it seems more likely that  $O_2$  species are removed. Towards the final measurements, the hysteresis is significantly reduced, particularly after the maximum current shows a large drop. This could be caused by significant particle desorption under the event of potential arcing that resulted from the drop in current seen previously.

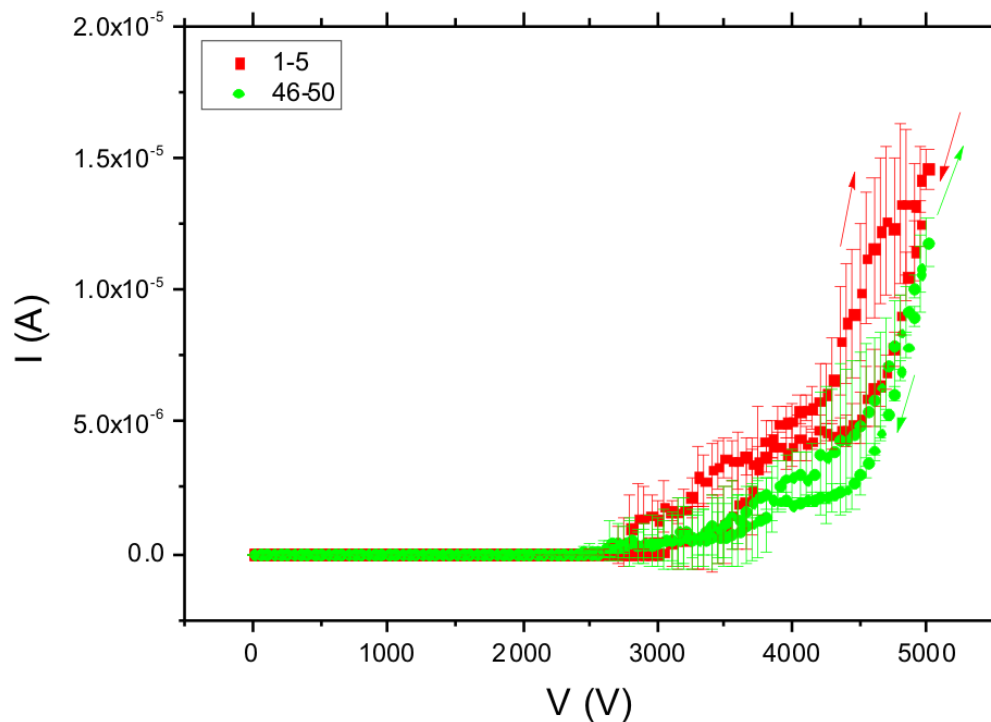


**Figure 5.13 | *I-V* Curve Evolution over 50 Cycles.** Average *I-V* curves for the first five (red) and final five (green) measurements highlighting the changes to the emission characteristics.

Figure 5.13 shows the average *I-V* curves for the first five and final five measurements of the 50 loop exposure. The cross over between up and down remains mostly consistent, but shifts from the first five sweeps (3762 V) up by 83 V (to 3845 V). The change to the emission profile, however, is quite distinct. The process resulting in this change of characteristic could be explained by a series of events. Firstly, the adsorbed molecules, from being left at ambient, contribute to the hysteresis cycle. After a conditioning period of repetitive exposure to the cycling electric field, some of these molecules are desorbed permanently at differing times according to their species and energies. Some interaction with the molecules present in the vacuum could result in further instability, or replacing of these desorbed molecules by other species (likely H<sub>2</sub>O) to which  $I_{max}$ , hysteresis and low field behaviour are sensitive. After a time, this process reaches a period of stability. This can be destabilised by further changes to the surface coverage of adsorbates caused by a change to emitter conditions such as arcing.

### 5.6.1 Future Work

Further tests could be performed over longer periods of time. This may reveal a point at which the hysteresis ceases to exist. Between the first and last measurements, the hysteresis is reduced

quite dramatically, as can be seen in Figure 5.13; should the measurement loops have continued, this could have resulted in the possible removal of hysteresis from the system. Repetition of this experiment could also highlight the behaviour of hysteresis without a seemingly destructive event, or indeed the likelihood that such an event might occur. These stability studies could be used in conjunction with the morphology studies used in the previous chapter to analyse the different geometries and their resistance to change and destructive events over long exposures.

### 5.7 Hysteresis Onset

To further understand the origin of hysteretic behaviour, it would be beneficial to understand whether the maximum voltage affects the amount of hysteresis seen and whether it is always onset at the same place in the voltage cycle. To test the effect of the maximum applied field and where in the cycle hysteresis begins to occur, an experiment was devised that reached different maximum voltages using the same sample (forest of CNTs). These voltages were 1000 V, 2000 V, 2500 V, 3000 V, 3500 V, 4000 V, 4500 V, 5000V ( $E$  (V/ $\mu\text{m}$ ) = 1.6, 3.3, 4.2, 5.0, 5.8, 6.7, 7.5 and 8.3 respectively). The same 50 V increasing applied voltage was maintained throughout the experiments.

The results are shown in Figure 5.14. Figure 5.14a shows the results in  $I$ - $V$  curve, Figure 5.14b shows the FN plots, Figure 5.14c shows the results arranged by measurement number and Figure 5.14d shows  $I_{max}$  for each voltage. Together, they show that a hysteresis typically appears for  $V > 3500$  V, after the maximum current reaches the high field regions where  $I_{max}$  begins to plateau. From Figures 5.14 a and b, it can be seen that when hysteresis appears, it follows the same trend as each previous iteration and appears independent of maximum voltage. The greatest difference in measured current does appear, however, to be when the maximum applied voltage is the largest. The main region of hysteresis is in the mid-field range. This result suggests that the same species are preferentially adsorbed and desorbed at consistent field values. It would also suggest that increasing numbers of species become mobile with increasing maximum current, as larger hysteresis is seen with increasing maximum applied field. In Figure 5.14c, it can be seen that hysteresis becomes of importance between 3500 V and 4000 V, where a change to the shape of the curve can be seen. This suggests species are

likely desorbed (mostly at one field value) between 3500 V and 4000 V. The current measured at the maximum voltage shown in Figure 5.14d follows a typical  $I$ - $V$  curve, as expected.

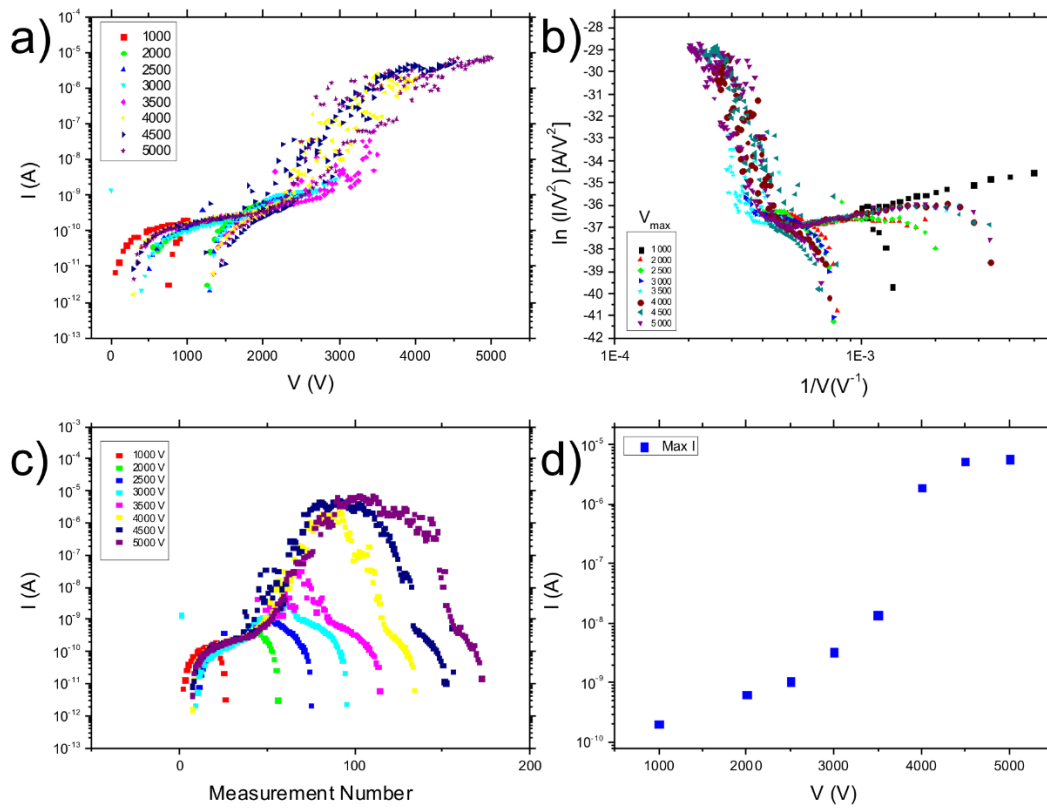


**Figure 5.14 | Results of Varying the Maximum Applied Current.** Results shown as a)  $I$ - $V$  curves, b) in a Fowler Nordheim plot, c) opened by measurement number, and d)  $I_{max}$  for each different  $V_{max}$ .

## 5.8 Effect of Dwell Time on Hysteresis

It has been postulated and observed by others<sup>9,10</sup> that the speed of the voltage sweep can be influential in altering the amount of hysteresis seen in a measurement. By altering the dwell time at each voltage, the number of electrons released is affected. When the sweep speed is faster, smaller currents are measured and the hysteresis has been reported to be somewhat quenched. To test this hypothesis, an experiment was devised that settled for different times at each voltage interval. The dwell time at each 50 V interval was set to 1 s, 2 s, 5 s and 10 s.

## 5. Hysteretic Behaviour of Carbon Nanotube Field Emitters

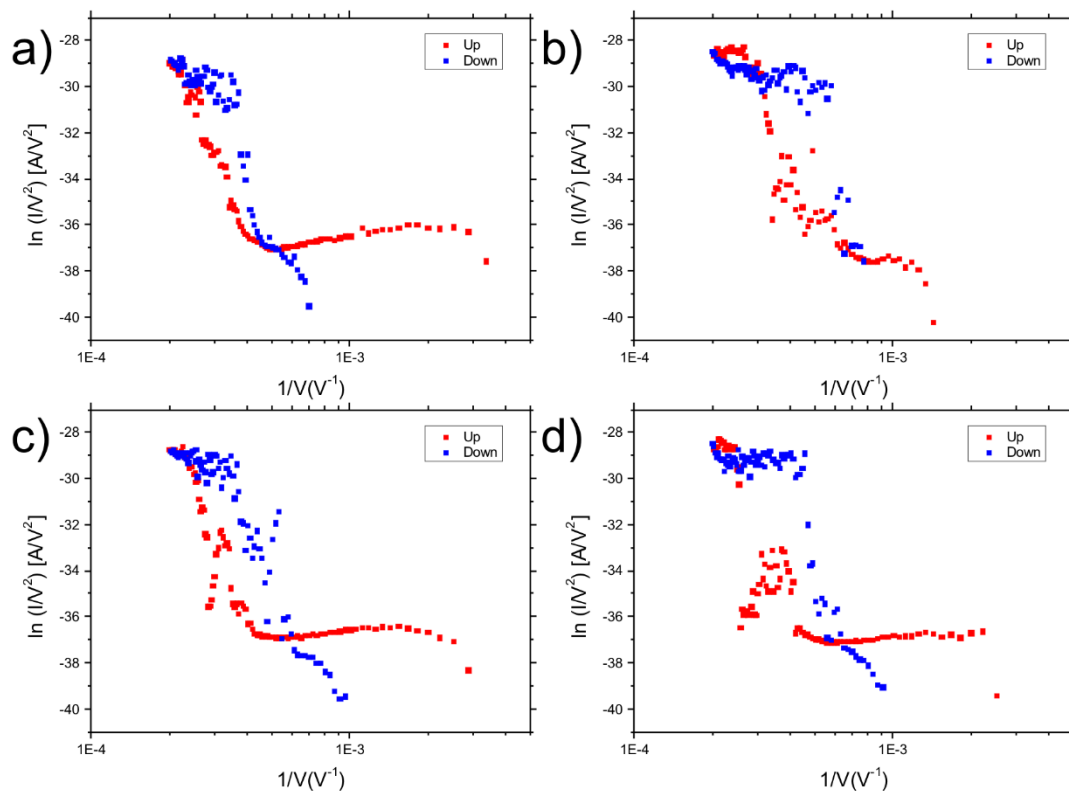


**Figure 5.15 | Fowler Nordheim Plots for Sweep Speed Results.** Hysteresis seen for measurement of field emission measured at a) 1 s, b) 2 s, c) 5 s, and d) 10 s settling time.

The results of dwelling the time at each voltage are shown in Figure 5.15. The hysteresis is clearly seen in each measurement, where the up and down sweeps do not overlap. The main differences seen tend to be related to the down sweep (blue), this was also noticed by Zuo *et al*<sup>10</sup>. The up (red) seems to remain mostly constant, though some change is noticeable in the 10 s dwell time, where a clump of measurements are seen in the mid-field range. The change exhibited in the down sweep has been attributed to adsorption recovery<sup>10,11</sup>, and indeed suppressed desorption of molecules. Lower measured current density under faster changing fields could be attributed to a filtering effect, where energy levels, particularly those altered by adsorbates, require a particular filling time before they can release electrons to vacuum, or having the conduction and valence bands shifted by adsorbates.

Table 5.1 shows the calculated values of  $\beta$  from Figure 5.15. Across the samples  $\beta$  doesn't change greatly in value, which it shouldn't. The values between up and down are mostly similar, with greater differences in the longer dwell time, which could show the effect of adsorbates on  $\beta$ .

**Table 5.1** |  $\beta$  calculated for the different dwell times.

	<i>Up</i>	<i>Down</i>
<b>1 s</b>	1200	1100
<b>2 s</b>	2000	1800
<b>5 s</b>	1100	1700
<b>10 s</b>	1100	1400

In Figure 5.16 the results are shown by measurement number, unfolding the classic  $I$ - $V$  curve. By doing this, some notable and interesting features become visible. Firstly, it is clear that the rise to  $I_{max}$  is steeper on the up sweep, with similar onset at each dwell time, falling off more gently in the down sweep. This, in relation to sorption theories, shows desorption to be dependent on higher fields, which makes energetic sense. Secondly, the up sweeps remain similar in appearance, whilst the down sweeps show varying clusters of points in the low-mid field regions, and stop emitting at lower fields ( $E_{on(down)}$ ) as dwell time increases. Between 1 s and 10 s dwell time,  $I_{max}$  increases by 150 %. This increase in electron availability could account for the difference seen in  $E_{on(down)}$ . Adsorption is likely to occur quicker than desorption, assuming incommensurate states, owing to smaller energies required, thus explaining the initial steeper decline of current on the down sweep resulting in the consistently higher measured current of the up sweep compared to down sweep in the high-field region (positive  $\Delta I$ ). The clusters of points were also seen in the stability study at the same region on the down sweep and are responsible for the change in  $\Delta I$  from positive to negative. A possible filtering effect, bypassing potential current avenues that require an amount of time to activate, could be shown when the current sweep is faster (shorter dwell times). Adsorption processes enhanced by the more gradual decreasing current, compared to the faster 1 s dwell time, could explain the resulting increase of clustering effect with increasing dwell time allowing more species to re-adsorb onto the surface, resulting in a deviation from pure CNT behaviour. This assumes that adsorbed species enhance the field emitting properties of CNT by the creation of additional tunnelling states, or indeed the lowering of the surface  $\phi$ . Resulting intermediate states could also be reasonably responsible for this, even if the surface  $\phi$  is increased by adsorbates including H, O<sub>2</sub> and H<sub>2</sub>O as previously discussed.

## 5. Hysteretic Behaviour of Carbon Nanotube Field Emitters

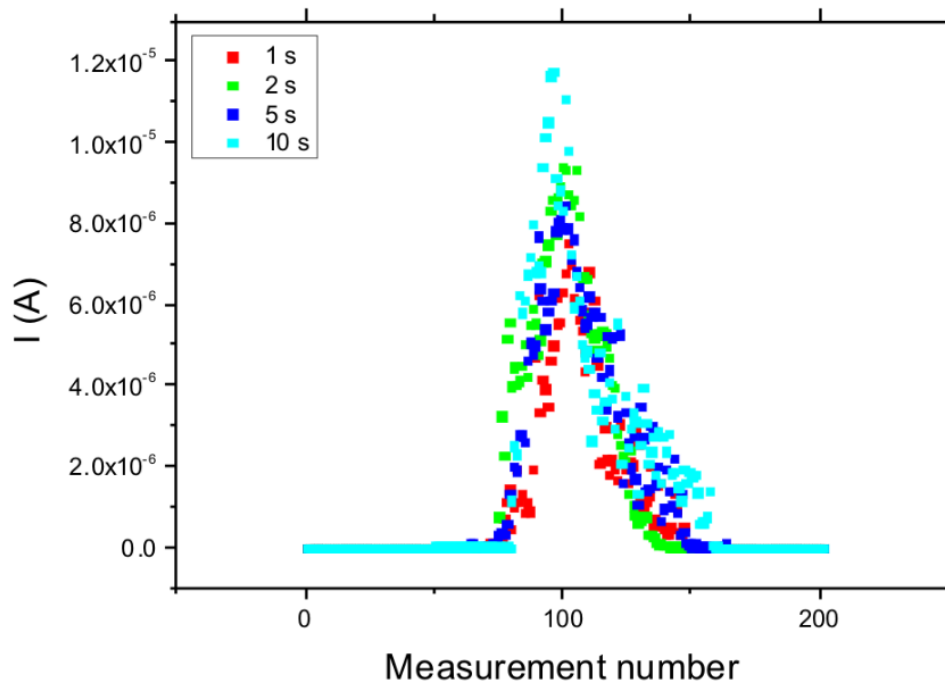


**Figure 5.16 | Sweep Speed: Unfolding the  $I$ - $V$  Curve.** Field emission as a function of measurement number from different sweep speeds.

The area under the graph is a further, and possibly better, way to measure the hysteresis. In each of the cases, the area under the graph is similar with  $203 \mu\text{A}$ ,  $295 \mu\text{A}$ ,  $283 \mu\text{A}$  and  $337 \mu\text{A}$  for 1, 2, 5 and 10 seconds respectively with an average of  $279 (\pm 56) \mu\text{A}$ .

### 5.8.1 Limitations and Future Work

Whilst this study gives some insight into the effects of varying the ramp rate of the electric field, more can be done to investigate the hysteretic behaviour. As it appears from the results that the amount of additional, clustered emission observed under downwards sweep of the electric field tends to minimisation with increased sweep speeds, further investigations could provide information on which dwell times result in no additional emission, and hence little observed hysteresis. The equipment may prove to be a limiting factor in ascertaining results with any dwell times less than 1 s, and the number of current measurements made would have to be cut to one when measuring the current, which could prove unstable.

Increasing the dwell times would be simpler to instigate using the current equipment, and as measurements, up to a few minutes at each voltage, could be performed. Exposing the same emitters over such long periods could prove challenging in continuity between results.

Hysteresis could, in fact, be inadvertently promoted by changes to the structure of emitters simply by prolonged exposure to emission conditions.

Typical sorption timescales of individual species are not known, nor have they been documented elsewhere, even under temperature studies. It is possible that sorption is not fully active within the timeframes measured, and that the observed effects are due to other factors. With currently undocumented sorption timeframes, it is difficult to assess whether the above dwell times sufficiently represent adsorption and desorption effects.

## **5.9 A Model Describing the Emission Process and Resultant Hysteretic Behaviour**

The contribution to hysteresis by a number of interlinked mechanisms, many of which may be caused by sorption processes, can be used to describe a suggested six step model of FE including why and how hysteresis occurs. Figure 5.17 outlines the points at which these steps occur within the FE cycle. It is based on the accumulation of data from the above experiments and is inspired also by the available literature on the subject.

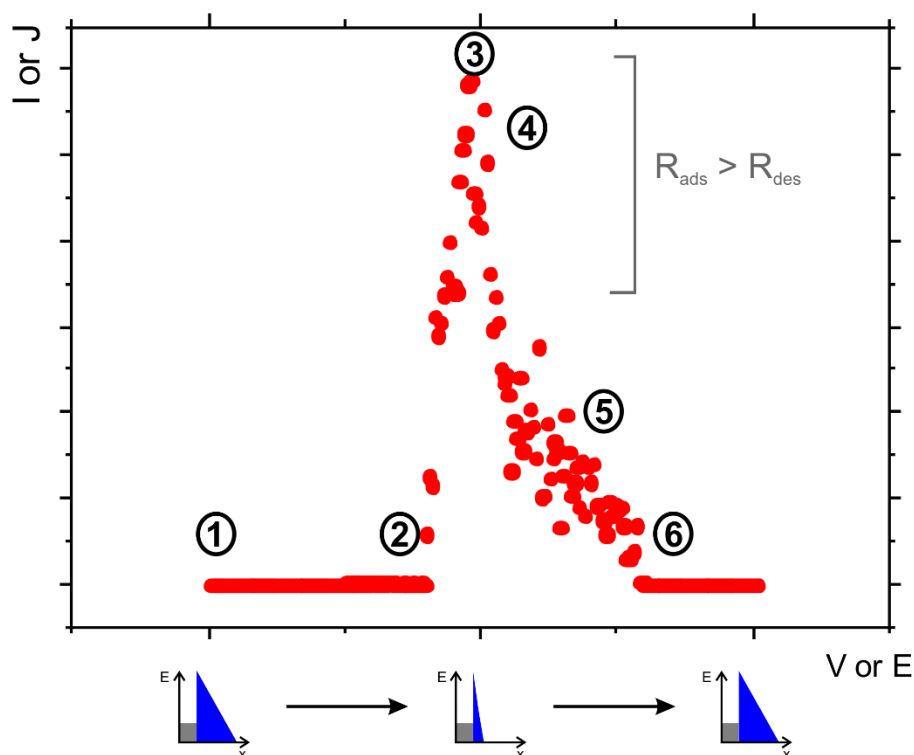


**Figure 5.17 | Field Emission Model.** Model illustrating the six steps in emission and the hysteretic behaviour.

**Step 1:** An electric field is applied to the anode inducing the potential barrier to become triangular. Due to the still quite large width of the potential barrier and insufficient electron energies, negligible current is measured. As increasing fields are applied the barrier thins further.

**Step 2:** Occurring at a voltage of 2500 V – 3000 V, corresponding field  $4.17 \text{ V}/\mu\text{m} - 5 \text{ V}/\mu\text{m}$ . The barrier sufficiently narrows to allow electrons to tunnel through at the Fermi energy to contribute to a significantly measurable current. Up to this point, electrons have steadily populated empty or intermediate states defined by adsorbates. The onset of a measurable current and liberation of electrons contributes to the increasing desorption of gas species on the CNT surface as well as contributions from increasing energy from the applied field. Removal of species is likely to follow the same order as seen in temperature studies: O and N, followed by  $\text{CO}_2$  and finally  $\text{H}_2\text{O}$ <sup>57</sup> and happens at a narrow field distribution. The energetic positions of adsorbed species (i.e. chemisorbed versus physisorbed, location on CNT surface etc.) is influential in determining the exact field at which the species are desorbed – though this is primarily seen in the mid-field region (approximately between 2000 V and 4000 V).

**Step 3:** Maximum applied field results in thinnest potential barrier seen here and corresponding maximum current. The electron surface states are fully populated.

**Step 4:** Located immediately after the maximum applied field in the high-field region of emission, where current is lower than at the same field in the up sweep. A decrease in applied field leads to destabilisation of desorbed molecules, previously kept from the surface by continually increasing electric fields, and molecules readily adsorb back onto CNT surface at energetically favourable locations. The rate of this re-adsorption is fast, beginning immediately as the field direction changes, altering the FE environment compared to that of the increasing field, where adsorbates were not present on the surface at high fields. This results in lower measured current at the same high fields due to increase of the surface  $\phi$  by adsorbates and formation of intermediate electron states.

**Step 5:** Taking place in the mid-field region typically between 4750 V to 2250 V (7.92 V/ $\mu\text{m}$  to 3.75 V/ $\mu\text{m}$ ), where the emission in the down sweep is higher than in the up sweep. This step is the most variable and is highly subject to emission conditions. This region is dominated by the effects of re-adsorption of species onto the CNT surfaces, the rate of which is dependent on the number of species already present on the surface, which in turn is dependent on the dwell time and species available. Immediately after adsorption (Step 4), intermediary states are created, which gradually populate and contribute to emission later (Step 5), increasing the emission compared to the same field in the up sweep.

**Step 6:** The system is returned to its previous original condition with desorbed molecules re-adsorbed, though not necessarily in the same location or at the same energy, contributing in part to the subsequent asymmetries in the emission profiles. The species of these molecules may change over time with relation to both the preferential adsorption of certain molecules and the direct species available.

### **5.9.1 Explaining the Causes of Hysteresis: Trapped, Surface and Intermediate States from Adsorbed Molecules**

The lack of continuity, as is particularly evident in Step 5, between cycles originates principally from the variation seen in adsorption site population and species as well as, of course, some contribution from statistical variation in the experiment. Over long time periods of exposure to a cycle, since water molecules are preferentially adsorbed compared to others<sup>54</sup> and the

## 5. Hysteretic Behaviour of Carbon Nanotube Field Emitters

percentage of these molecules within vacuum levels of this range is high, it is likely that adsorbed species tend towards increasing concentrations of water molecules. Contributing factors to the origin of the observed extra current could be caused by trapped states, potentially on the CNT surface, intermediate states caused by adsorption of molecules, induced changes to surface  $\phi$  and even potential surface morphological changes caused by adsorption.

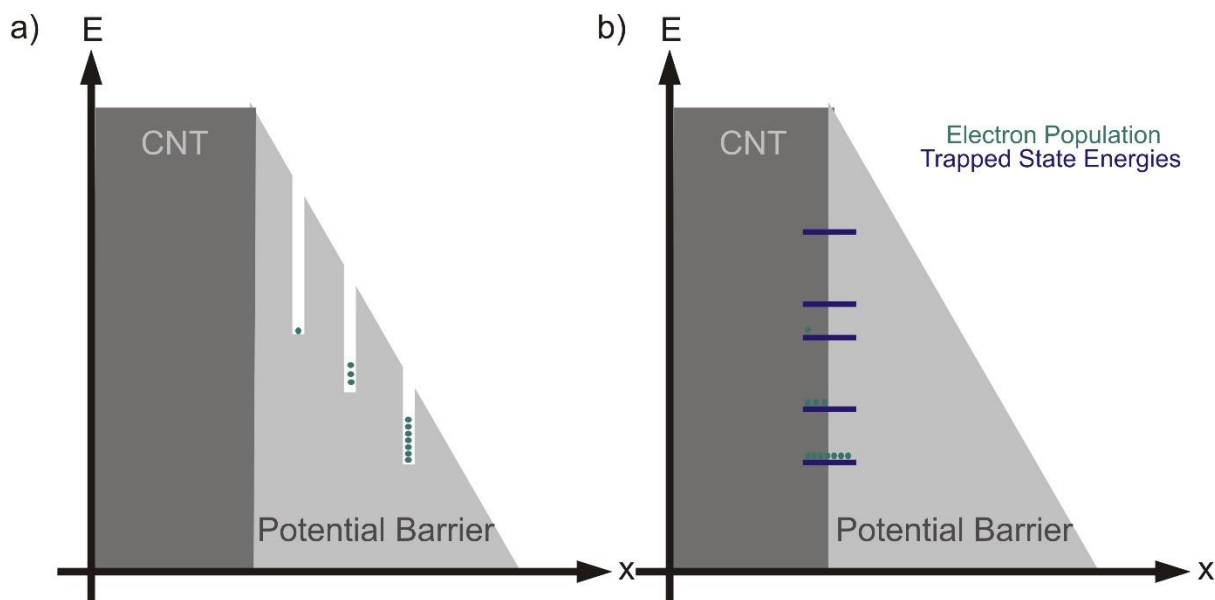


**Figure 5.18 | Sources of Additional Electrons.** a) Quantum wells induced by adsorbed species and b) trap state population caused through surface defects.

One potential mechanism contributing to hysteretic current is through trapped states, where additional electrons are released in the down sweep that became trapped in the up sweep. Population of potential trapped states, or any additional energy levels located at some energy above  $E_f$ , have a probability associated with the statistics of Fermi-Dirac distribution, where states with energy levels closer to the Fermi energy have higher probability of being filled, compared to those with higher energies. Electrons positioned furthest away from the Fermi level, near the top of the triangular barrier, have the highest likelihood of tunnelling, as the barrier is thinnest here and are the most unstable. Most electrons, however, are found at the minimum energy position where the triangular barrier is thickest, and have the lowest probability of tunnelling. This could explain the significant additional emission at the mid-to-low field region. The location, energy and prevalence of surface states is influenced by nanotube defects and adsorbed molecules, thus differing between emitters.

Figure 5.18 demonstrates the different ways in which electrons could be trapped, either by a) within the potential barrier in small quantum wells generated by adsorbates or b) as trapped states along the interface between the CNT and vacuum. The correctness of either of these suggestions is not known, they simply illustrate possible scenarios and explanations of both will follow. Lyth and Silva<sup>58</sup> suggest that adsorbates, particularly chemisorbed species, create quantum wells, as in Figure 5.18a, contributing to additional peaks in measured current due to distribution of electrons at resonant energies of the quantum wells. Step-like behaviour in the emission current has been studied by Filip *et al*<sup>59</sup>, which is described to originate from quantum well structures seen in nanotubes. Slow discharging of the trapped electrons in quantum wells could explain the behaviour seen in Step 5, where a number of electrons are released at low fields. Lee *et al*<sup>60</sup>, however, studied the effect of treatment of CNTs with an oxygen plasma, nitric and hydrofluoric acids, and attribute defects at opened CNT tips to causing trap states, represented by sites of electron population along the interface between the CNT surface and potential barrier in Figure 5.18b. Again, the slow release of electrons is purportedly responsible for improvements in FE in this case. They found that trap sites, dominating tunnelling at low fields, can reduce  $E_{on}$ . This is consistent with my results (Sections 5.4.3 and 5.4.4). Surface states were also found to contribute to emission in this model. Kan *et al*<sup>61</sup> describe these trap states, as illustrated in Figure 5.18b, as defect induced energy bands that allow electrons to climb up the energy ladder. Emission in this case is said to originate from discrete energy states.

The effect of the different adsorbed species has been studied by a number of authors. The CNT tips are modelled using density functional theory in explaining emission behaviour as they are thought to be the most likely place for adsorption to occur because of dangling bonds and defects seen there<sup>62</sup>. Hata *et al*<sup>63</sup> suggest that the size of the adsorbed molecules relates to changes in tunnelling ability. Oxygen molecules are commonly attributed to inhibiting the emission because of an increased  $\phi$  due to its electronegativity<sup>64</sup>, which draws the Fermi level towards the valence band (the opposite effect has been seen for other species  $N_2$ ,  $H_2O$ )<sup>62</sup>. A small gap is induced between the carbon derived valence band and bottom of the unoccupied oxygen derived states essentially increasing  $\phi$ . Weak hybridisation between C and O molecules is responsible for a change in the DOS at Fermi energy, though there is some dispute about this<sup>65</sup>. Studies have shown that  $O_2$  is physisorbed. However, in molecular form, O is chemisorbed onto a SWNT surface with binding energy 0.19 eV<sup>66</sup>.  $O_2$  binds to a semi-conducting SWNT at 2.7 Å from the surface with a binding energy of 0.25 eV. A large activation barrier exists for chemisorption<sup>66</sup>, though it has been shown that excited electronic

## 5. Hysteretic Behaviour of Carbon Nanotube Field Emitters

states have been caused in chemisorption on metal surfaces<sup>67</sup>. Some cases have shown an increase in FE with oxidative etching supposedly increasing current by the creation of new states when molecular oxygen is adsorbed<sup>68</sup>, though this is an unusual case, and the increased emission effects could be dominated by etching effects on the CNT rather than adsorbed oxygen.

Water molecules are arguably the most interesting in terms of the effect on FE because of their polar nature and the resulting related increase in current. This has been attributed to an adsorbate tunnelling state induced between the molecule and CNT tip<sup>69</sup>. Electrons are transferred from other occupied states to fill the HOMO on the CNT cap and tunnel, contributing to the current<sup>70</sup>. Chen *et al*<sup>65</sup> attribute enhanced FE to changes in the effective work function,  $\phi_{eff}$ , caused by charge redistribution and accumulation at the tip under an applied electric field. Adsorption of water molecules is reportedly fairly unstable under no external electric field, leading to ease of desorption, however, under FE conditions, adsorption energies are higher and molecules become stable, chemisorbing onto the surface of the CNT<sup>71,72</sup>. A dipole moment is induced, directed from H<sub>2</sub>O molecule to the CNT tip that strengthens with increasing number of molecules as they also show greater probability of adsorbing in clusters, and bonds the molecule to the tip<sup>62,71</sup>. The chemisorbed molecule is likely to remain more stable, continuing to contribute to hysteresis. Electrostatic interactions lower the ionisation potential, a measure of the ease of electron extraction, by moving the conduction band downwards under an applied field and increasing the local DOS. Interestingly, current saturation has been attributed to an effect caused by H<sub>2</sub>O adsorption<sup>70</sup>.

Chen *et al*<sup>65</sup> report the importance of the difference between physisorbed and chemisorbed species. Physisorption of polar molecules results in strong interactions with the surface by increasing the DOS at the Fermi level, which act as tunnelling states. Chemisorbed molecules, on the other hand, forming chemical bonds, redistribute the charge resulting in a variation of the surface dipole and surface  $\phi$ . The adsorption energies of molecules differ, with N<sub>2</sub> requiring the least energy followed by H<sub>2</sub>O, then H<sub>2</sub> and finally O<sub>2</sub> requiring the most. H<sub>2</sub>, which similarly to H<sub>2</sub>O molecules, are physisorbed onto the CNT surface show little difference to the FE, whilst H<sub>2</sub>O show marked improvement. Chemisorbed species, including O, with weak dipoles are not seen to greatly affect ionisation potential. Both H<sub>2</sub> and N<sub>2</sub> are found to not greatly influence FE because of an absence of DOS at the Fermi energy (H<sub>2</sub>). Adsorption was found to be an endothermic reaction, except in the case where no field was present, i.e. ambient

adsorption. It seems likely that H<sub>2</sub>O in both chemisorbed, from ambient, and physisorbed forms, from vacuum environment, contribute to the hysteresis cycle.

Applying this knowledge to the results found, it can be anticipated that the most likely cause of hysteresis can be attributed to the effects of water molecule adsorption on CNTs. Knowing both that H<sub>2</sub>O molecules are more readily adsorbed compared to other species<sup>54</sup> and being the overwhelmingly dominant gas species within the vacuum chamber, as seen in RGA analysis in Section 5.5, there is some confidence in assuming that this species is favourably adsorbed. To bolster this assumption, the effects seen in the experiments match previous findings. These are: continued hysteresis by stability of molecules on the surface, enhanced emission in down sweep through tunnelling states at the tip, potential increase in  $\phi$  leading to reducing  $I_{max}$  with desorption (potentially of physisorbed species), and current saturation. Dean *et al*<sup>73</sup> attempted to introduce the nanotubes to individual gas species by heating the nanotubes to over 900 °C then leaked gases into the chamber. In this process they discovered that water vapour had the greatest effect on emission, with adsorbate states strongly correlated to the existence of water vapour adsorption. This supports the findings claimed here.

### 5.9.2 Evidence from Results

The sweep speed is significant in determining whether additional electron sources, from trapped, surface or intermediate states, are present. If we assume that the higher energy states take longer to fill with electrons, hence longer to contribute to emission, we can essentially filter them out by increasing the sweep speed. Similarly, using a long dwell time at given electric field values, electrons from an increased number of states can be activated and contribute to higher emission current. From the results in Section 5.8, see Figure 5.16, it can be seen that there is a significant increase (150%) in current when the field dwells for ten seconds at an electric field value compared to one second, and that the contribution to additional emission (Step 5) for a one second dwell time is minimal. Electrons, therefore, must take some time,  $\tau$ , to fill the available states and tunnel. If  $t < \tau$ , the states are not filled and, therefore, do not contribute to electron emission. If the electric field is ramped up and down sufficiently quickly, with dwell times less than a second, it is possible hysteresis could be filtered out altogether. Future projects to study the ramp rate and the possibility of hysteresis filtration could be performed using high voltage pulsing. Determining the nature of the states (energy

## 5. Hysteretic Behaviour of Carbon Nanotube Field Emitters

levels and filling time constants) induced by specific molecular species and signatures of their sorption cycles is possible, potentially more achievable through modelling, at least initially.

In stability studies in Section 5.6, see Figure 5.10, a single emitter is measured at the same dwell time (3 seconds) over fifty cycles of voltage increasing from 0 V – 5000 V and back. It can be seen that the maximum current achieved remains approximately consistent, with only a small decrease from 14.0  $\mu\text{A}$  on the first measurement loop, to 13.4  $\mu\text{A}$  on the 50<sup>th</sup>, 96% of the original value. This suggests that the species contributing to emission are either repeatedly re-adsorbed or remain on the surface. In contrast, the difference in maximum current for an emitter with a dwell time of ten seconds is 1.5 times higher at 11.8  $\mu\text{A}$ , compared with 7.5  $\mu\text{A}$  for the same emitter with a dwell time of one second, where the emitter has been used only twice in between these measurements (one second measured first). It is important to realise that the two emitters were different, and it is not the value of the current that is noteworthy; the difference in value is of higher significance here. Primarily, we can deduce that the higher current seen at ten seconds is not due to emitter degradation, since it was measured after one second readings. It is not expected that the number of uses dramatically affects the maximum current (from Figure 5.10 a), though a steady decrease would be predictable. This result, therefore, further supports the theory that certain electron states require some time to fill and therein contribute to emission. We could conclude that, with voltage sweep rates faster than the reactions of sorbates, fewer molecules are removed from the surface in addition to fewer extra states being filled, resulting in a more symmetrical emission and ensuing removal of hysteretic behaviour.

We can also argue that over time trapped, surface or intermediate states can be removed by permanent desorption of gas molecules from the surface. Permanent removal could be achieved by replacement of molecules with other molecules, which quench the hysteretic behaviour over time, or by escape upon desorption to be pumped away. Quenching could be achieved by preferential adsorption of a single molecular species. Regarding Figure 5.11c in Section 5.6, it can be seen that the emission current narrows over time when displayed in a novel way that opens up the results by measurement number as opposed to the traditional field value. If we assume that the more trapped states there are, the greater the measured current, and we see that the current is decreasing with number of uses, we could conclude that there are fewer trapped states for electrons to occupy in the  $n + 50^{\text{th}}$  loop than the  $n + 1^{\text{st}}$ , with lower emission seen. However, the number of trapped states, on the CNT surface, might be expected to increase over time with emitter degradation. This would, therefore, suggest that adsorbed species are a more likely candidate in causing changes to measured current. Other factors are likely to add to the

degradation of the emitter, however, the perceived reduction of the FWHM from 2145 V to 853 V between the 50 loops strongly suggests there are fewer channels for electron tunnelling (and therefore measured current) throughout the measurement loop. Another factor that could have this effect, or indeed enhance it, is the morphology, which could be changing (becoming less perturbed) via burn out or arcing. Post experimental SEMs revealed little obvious damage, however. A few signs of arcing were observed covering approximately 4% of the emitting area.

Onset of hysteresis and repeatable measured difference between up and down sweeps is shown in Section 5.7. This suggests that the amount of current measured is directly related to the applied field and the relation to when species are desorbed from the surface. The rapid desorption between 3500 V and 4000 V suggests that either just one species is desorbed, or that the ranges of the energies required are similar for all species.

### **5.10 Summary**

In this chapter, a six step model of the emission and resulting cause of hysteresis were determined following a range of experiments. The vacuum environment was found to be predominantly made up of water vapour molecules, though other influential species were also present. The profile of hysteresis was calculated by measuring the difference in measured current in the up versus down sweep, which showed different regions of domination linked to the kinetics of the sorption process detailed in the emission model. Whilst desorption, with higher activation energies, affects the later onset of emission in the up sweep, fast re-adsorption at high fields can be attributed to a lower initial measured current on the down sweep, with later contributions increasing the current when newly formed states, shaped by re-adsorbed species, emit.

The stability over a long exposure to emission cycles showed larger changes in FWHM compared to the maximum emitted current, which showed a gradual decrease. The maximum applied electric field was found to be of little significance in determining the amount of hysteresis seen, however, highlighting the dependence of desorption on the applied field. In examining the structure of hysteresis, by varying dwell time at each applied field, the significance of an effective filtering was seen and increasing contribution to current from re-adsorbed states was determined.

## References

- 1 Parmee, R., Collins, C., Milne, W. & Cole, M. X-ray generation using carbon nanotubes. *Nano Convergence* **2**, 1 (2015).
- 2 Collins, C. M., Parmee, R. J., Milne, W. I. & Cole, M. T. High Performance Field Emitters. *Advanced Science* **3** (2015).
- 3 Baca-A, R., Paredes-R, G. R., Pena-Sierra, R. & Ieee. *Study of materials to synthesize vacuum electron nanoemitters*. (2006).
- 4 Zhao, Z. G., Liu, S. H., Liu, C., Bai, J. B. & Cheng, H. M. A comparison between field-emission properties of three one-dimensional carbon materials. *Physica B-Condensed Matter* **396**, 44-48 (2007).
- 5 Arkhipov, A. V., Mishin, M. V., Sominski, G. G. & Parygin, I. V. Hysteresis of pulsed characteristics of field emission from nanocarbon films. *Technical Physics* **50**, 1353-1359 (2005).
- 6 Gorodetskiy, D. V. *et al.* Memristive model of hysteretic field emission from carbon nanotube arrays. *Journal of Nanophotonics* **10** (2016).
- 7 Cahay, M., Murray, P.T., Back, T.C., Fairchild, S., Boeckl, J., Bulmer, J., Koziol, K.K.K., Gruen, G., Sparkes, M., Orozco, F. and O'Neill, W. Hysteresis during field emission from chemical vapor deposition synthesized carbon nanotube fibers. *Applied physics letters* **105**, 173107 (2014).
- 8 Filippov, S. V., Popov, E. O., Kolosko, A. G., Romanov, P. A. & Iop. in *2nd International School and Conference Saint-Petersburg Open on Optoelectronics, Photonics, Engineering and Nanostructures* Vol. 643 *Journal of Physics Conference Series* (2015).
- 9 Chen, J. *et al.* The hysteresis phenomenon of the field emission from the graphene film. *Applied Physics Letters* **99**, 173104 (2011).
- 10 Zuo, Y., Ren, Y., Wang, Z., Han, X. & Xi, L. Enhanced field emission and hysteresis characteristics of aligned carbon nanotubes with Ti decoration. *Organic Electronics* **14**, 2306-2314 (2013).
- 11 Li, C. *et al.* Effect of adsorbates on field emission from flame-synthesized carbon nanotubes. *Journal of Physics D-Applied Physics* **41**, 195401 (2008).
- 12 Okotrub, A. V., Bulusheva, L. G. & Gusel'nikov, A. V. Effect of purification on the electron structure and field emission characteristics of a carbonaceous material containing single-wall carbon nanotubes. *Journal of Experimental and Theoretical Physics* **99**, 1244-1252 (2004).
- 13 Filippov, S. V. *et al.* in *29th International Vacuum Nanoelectronics Conference (IVNC)*. (2016).
- 14 Eswaramoorthy, M. A study of micropores in single-walled carbon nanotubes by the adsorption of gases and vapors. *Chemical physics letters* **304**, 207-210 (1999).
- 15 Yan, X. M. *et al.* Adsorption and desorption of atrazine on carbon nanotubes. *Journal of Colloid and Interface Science* **321**, 30-38 (2008).
- 16 Takagi, H. Adsorptive hydrogen storage in carbon and porous materials. *Materials science & engineering. B, Solid-state materials for advanced technology* **108**, 143-147 (2004).
- 17 Burgess, C. G. V. Adsorption hysteresis in porous materials. *Pure and applied chemistry* **61**, 1845 (1989).
- 18 Donohue, M. D. Adsorption Hysteresis in Porous Solids. *Journal of colloid and interface science* **205**, 121-130 (1998).
- 19 Striolo, A. Water in carbon nanotubes: Adsorption isotherms and thermodynamic properties from molecular simulation. *The Journal of chemical physics* **122**, 234712 (2005).
- 20 Kuznetsov, A. A., Lee, S. B., Zhang, M., Baughman, R. H. & Zakhidov, A. A. Electron field emission from transparent multiwalled carbon nanotube sheets for inverted field emission displays. *Carbon* **48**, 41-46 (2010).
- 21 Cheng, Y. Electron field emission from carbon nanotubes. *Comptes rendus. Physique* **4**, 1021-1033 (2003).
- 22 de Jonge, N. & Bonard, J. M. Carbon nanotube electron sources and applications. *Philosophical Transactions of the Royal Society a-Mathematical Physical and Engineering Sciences* **362**, 2239-2266 (2004).
- 23 Zhao, J. Gas molecule adsorption in carbon nanotubes and nanotube bundles. *Nanotechnology* **13**, 195-200 (2002).
- 24 [Webpage] *2.3 Adsorption Kinetics - The Rate of Adsorption*, <[http://www.chem.qmul.ac.uk/surfaces/scc/scat2\\_3.htm](http://www.chem.qmul.ac.uk/surfaces/scc/scat2_3.htm)> (2017).
- 25 Zhu, X. Y. Adsorption and Desorption of an Molecule on Carbon Nanotubes. *Physical review letters* **85**, 2757-2760 (2000).
- 26 De, H. A carbon nanotube field-emission electron source. *Science (New York, N.Y.)* **270**, 1179 (1995).
- 27 Zhu, W. Defect-enhanced electron field emission from chemical vapor deposited diamond. *Journal of applied physics* **78**, 2707-2711 (1995).

- 28 Bonard, J.-M. Degradation and failure of carbon nanotube field emitters. *Physical review. B, Condensed matter* **67**, 115406 (2003).
- 29 Bower, C. Fabrication and Field Emission Properties of Carbon Nanotube Cathodes. *MRS proceedings* **593**, 215 (1999).
- 30 Okano, K. Fabrication of a diamond field emitter array. *Applied physics letters* **64**, 2742-2744 (1994).
- 31 Katayama, M., Lee, K. Y., Honda, S., Hirao, T. & Oura, K. Ultra-low-threshold field electron emission from pillar array of aligned carbon nanotube bundles. *Japanese Journal of Applied Physics Part 2-Letters & Express Letters* **43**, L774-L776 (2004).
- 32 Cole, M. T. *et al.* Deterministic Cold Cathode Electron Emission from Carbon Nanofibre Arrays. *Scientific Reports* **4** (2014).
- 33 Costa, S., Borowiak-Palen, E., Kruszynska, M., Bachmatiuk, A. & Kalenczuk, R. J. Characterization of carbon nanotubes by Raman spectroscopy. *Materials Science-Poland* **26**, 433-441 (2008).
- 34 Graupner, R. Raman spectroscopy of covalently functionalized single-wall carbon nanotubes. *Journal of Raman spectroscopy* **38**, 673-683 (2007).
- 35 Ferrari, A. C. Raman spectroscopy of graphene and graphite: Disorder, electron-phonon coupling, doping and nonadiabatic effects. *Solid state communications* **143**, 47-57 (2007).
- 36 Ni, Z. Raman spectroscopy and imaging of graphene. *Nano research* **1**, 273-291 (2008).
- 37 Das, A. Monitoring dopants by Raman scattering in an electrochemically top-gated graphene transistor. *Nature nanotechnology* **3**, 210-215 (2008).
- 38 Lehman, J. H. Evaluating the characteristics of multiwall carbon nanotubes. *Carbon (New York)* **49**, 2581-2602 (2011).
- 39 Hart, A. J. Growth of conformal single-walled carbon nanotube films from Mo/Fe/Al<sub>2</sub>O<sub>3</sub> deposited by electron beam evaporation. *Carbon (New York)* **44**, 348-359 (2006).
- 40 Beams, R. Raman characterization of defects and dopants in graphene. *Journal of physics. Condensed matter* **27**, 083002 (2015).
- 41 DasA *et al.* Monitoring dopants by Raman scattering in an electrochemically top-gated graphene transistor. *Nat Nano* **3**, 210-215 (2008).
- 42 Kang, D. Oxygen-induced p-type doping of a long individual single-walled carbon nanotube. *Nanotechnology* **16**, 1048-1052 (2005).
- 43 Bell, R. A., Payne, M. C. & Mostofi, A. A. Does water dope carbon nanotubes? *Journal of Chemical Physics* **141** (2014).
- 44 Lekawa-Raus, A. Influence of atmospheric water vapour on electrical performance of carbon nanotube fibres. *Carbon (New York)* **87**, 18-28 (2015).
- 45 Kittel, C. & McEuen, *Introduction to Solid State Physics* (Wiley, 1953) 6<sup>th</sup> Edition, p.680.
- 46 Curran, S. A. Defect-induced vibrational response of multi-walled carbon nanotubes using resonance Raman spectroscopy. *Journal of materials research* **20**, 3368-3373 (2005).
- 47 Chen, M.-L. & Oh, W.-C. Synthesis and highly visible-induced photocatalytic activity of CNT-CdSe composite for methylene blue solution. *Nanoscale Research Letters* **6**, 398 (2011).
- 48 Zhang, X., Cui, X. & Ebrahimi, F. in *Nanocomposites - New Trends and Developments* Ch. 10 (InTech, 2012).
- 49 Rezania, H. & Taherkhani, F. Effect of electron phonon interaction on the optical conductivity of zigzag carbon nanotubes. *Applied Physics a-Materials Science & Processing* **109**, 343-347 (2012).
- 50 Horastani, Z. K., Hashemifar, S. J., Sayedi, S. M. & Sheikhi, M. H. First-principles study of H<sub>2</sub> adsorption on the pristine and oxidized (8,0) carbon nanotube. *International Journal of Hydrogen Energy* **38**, 13680-13686 (2013).
- 51 Li, J., Yan, X., Gou, G., Wang, Z. & Chen, J. Engineering the field emission properties of graphene film by gas adsorbates. *Physical Chemistry Chemical Physics* **16**, 1850-1855 (2014).
- 52 Pinto, H. Electronic and electrochemical doping of graphene by surface adsorbates. *Beilstein journal of nanotechnology* **5**, 1842-1848 (2014).
- 53 Wei, Q. Nitrogen-Doped Carbon Nanotube and Graphene Materials for Oxygen Reduction Reactions. *Catalysts* **5**, 1574-1602 (2015).
- 54 Rossi, M. *Carbon nanomaterials for gas adsorption*. (Pan Stanford Publishing, 2012).
- 55 Yue, G. *et al.* Generation of continuous and pulsed diagnostic imaging x-ray radiation using a carbon-nanotube-based field-emission cathode. *Applied Physics Letters* **81**, 355-357 (2002).
- 56 Semet, V. *et al.* Field electron emission from individual carbon nanotubes of a vertically aligned array. *Applied Physics Letters* **81**, 343-345 (2002).
- 57 Ulbricht, H., Zacharia, R., Cindir, N. & Hertel, T. Thermal desorption of gases and solvents from graphite and carbon nanotube surfaces. *Carbon* **44**, 2931-2942 (2006).
- 58 Lyth, S. M. Resonant behavior observed in electron field emission from acid functionalized multiwall carbon nanotubes. *Applied physics letters* **94**, 123102 (2009).

## 5. Hysteretic Behaviour of Carbon Nanotube Field Emitters

- 59 Filip, L. D., Palumbo, M., Carey, J. D. & Silva, S. R. P. Two-step electron tunneling from confined electronic states in a nanoparticle. *Physical Review B* **79** (2009).
- 60 Lee, S., Oda, T., Shin, P. K. & Lee, B. J. Chemical modification of carbon nanotube for improvement of field emission property. *Microelectronic Engineering* **86**, 2110-2113 (2009).
- 61 Kan, M. C., Huang, J. L., Sung, J. & Chen, K. H. Thermally activated electron emission from nano-tips of amorphous diamond and carbon nano-tubes. *Thin Solid Films* **447**, 187-191 (2004).
- 62 Kim, C. The Effect of Gas Adsorption on the Field Emission Mechanism of Carbon Nanotubes. *Journal of the American Chemical Society* **124**, 9906-9911 (2002).
- 63 Hata, K. Field emission from multiwall carbon nanotubes in controlled ambient gases, H<sub>2</sub>, CO, N<sub>2</sub> and O<sub>2</sub>. *Ultramicroscopy* **95**, 107-112 (2003).
- 64 Akdim, B. The Effects of O Adsorbates on Field Emission Properties of Single-Wall Carbon Nanotubes: A Density Functional Theory Study. *Nano letters* **3**, 1209-1214 (2003).
- 65 Chen, C. W., Lee, M. H. & Clark, S. J. Gas molecule effects on field emission properties of single-walled carbon nanotube. *Diamond and Related Materials* **13**, 1306-1313 (2004).
- 66 Giannozzi, P., Car, R. & Scoles, G. Oxygen adsorption on graphite and nanotubes. *Journal of Chemical Physics* **118**, 1003-1006 (2003).
- 67 Kasemo, B., Tornqvist, E., Norskov, J. K. & Lundqvist, B. I. Photon and electron-emission as indicators of intermediate states in surface-reactions. *Surface Science* **89**, 554-565 (1979).
- 68 Park, N. Effects of oxygen adsorption on carbon nanotube field emitters. *Physical review. B, Condensed matter* **64**, 125401 (2001).
- 69 Dean, K. A. The environmental stability of field emission from single-walled carbon nanotubes. *Applied physics letters* **75**, 3017-3019 (1999).
- 70 Qiao, L. First-principles density-functional investigation of the effect of water on the field emission of carbon nanotubes. *Nanotechnology* **18**, 155707 (2007).
- 71 Grujicic, M., Cao, G. & Gersten, B. Enhancement of field emission in carbon nanotubes through adsorption of polar molecules. *Applied Surface Science* **206**, 167-177 (2003).
- 72 Maiti, A. Effect of Adsorbates on Field Emission from Carbon Nanotubes. *Physical review letters* **87**, 155502 (2001).
- 73 Dean, K. A., von Allmen, P. & Chalamala, B. R. Three behavioral states observed in field emission from single-walled carbon nanotubes. *Journal of Vacuum Science & Technology B* **17**, 1959-1969 (1999).



# **6. Conclusions and Summary**



## 6.1 Conclusions

A review of the literature covering field emission, carbon nanotubes and their related histories was presented, with a review of potential applications, the problems and the difficulties limiting commercial realisation at present. It became apparent, through studying the available literature, that the physics underpinning the emission process in nanomaterials was not sufficient to explain their field electron emission behaviour, which deviated significantly from traditional Fowler Nordheim.

To address this, focus on the important, and more uncertain, characteristics determined in Fowler Nordheim of work function,  $\phi$ , and field enhancement factor,  $\beta$ , were investigated. An exhaustive comparison of materials previously exploited in field emission studies, documented in close to 130 published works, was performed. It was predicted that when arranged according to  $\phi$ , some dependency between materials and emission performance would be seen. However, this was not the case. An unpredicted outcome evidenced that 1D and 2D materials demonstrated a turn on field,  $E_{on}$ , for the measured current density of 0.01 mA/cm<sup>2</sup>, half that of 3D and bulk materials. Whilst dimensionality of material may be of influence, it was generally concluded that emitter material, and surface  $\phi$ , are not the most significant factors in determining the success of a material as a field emitter. CNTs, and indeed the nanocarbons in general, were shown to exhibit the required characteristics for use in applications of low  $E_{on}$  and high measured current density,  $J$ .

Uncertainties in the field came to light including the ambiguities surrounding performance metrics  $E_{on}$ ,  $E_{thr}$  (threshold electric field) and the previously mentioned  $\beta$ . For clarity,  $E_{on}$  was defined at 0.01 mA/cm<sup>2</sup>, as this appeared the most commonly accepted, whilst  $E_{thr}$ , with lack of clear meaning or purpose, was disposed of. The total number of different  $\beta$  definitions totalled nine throughout the studied literature. In an attempt to generate a morphology metric,  $\alpha$ , a number of approaches were trialled. Difficulties in determining a mathematically strong  $\alpha$  from such a wide range of materials and images prevented a definition from being completed, however.

The surface morphology of the emitter has been implicated in strongly affecting field emission, though lack of clarity and definition previously seen, particularly regarding  $\beta$ , have inhibited confidence in explicit determination of how and why. To better understand this, a number of

## 6. Conclusions and Summary

different CNT geometries patterned in triangular, square, hexagonal and octagonal varieties were fabricated using a combination of electron beam lithography, sputtering and chemical vapour deposition. Further investigations into the importance of surface geometry were performed in a parallel plate set up when a custom built SAFEM proved insufficient in providing useful data. The obtainable results of these experiments suggested that aspects of particular importance in determining the maximum achievable current and lowest activation energy were linked to the reduction of the screening factor and emitter surface area coverage as well as increased length of exposed perimeter. Future studies, with a fully functioning SAFEM, exploring the different scales and area coverage of CNT patterns on emitters already fabricated may reveal more insightful conclusions about the emitter morphology and effect on field emission. One clear finding made, however, was the verification of an obvious deviation from linear behaviour when plotted on a Fowler Nordheim graph. Three areas of roughly linear correlation were seen, however, defined as the low, mid and high field ranges.

Hysteretic behaviour was identified in field electron emission from CNTs. The vacuum environment was found to be predominantly made up of water vapour molecules, though other species also considered to be important were also present, namely oxygen, carbon dioxide and nitrogen. The effects of the different molecules (including surface  $\phi$  changes, increased or decreased measured current, added tunnelling states, etc.) were considered, the outcome of which expressed the likelihood that the main participant in the observed hysteresis was due to water molecule adsorption. This was determined by characteristics such as: an increased propensity for water to adsorb compared to other molecules in the first place; some stability of molecules, likely chemisorbed, on the CNT surface contributing to continued hysteresis observed; enhanced emission, possibly from physisorbed species, with additional tunnelling states in the mid-low field regions caused by adsorption recovery at the tip where the fields are strongest; potential gradually increasing surface  $\phi$  resulting in reduced maximum emission current; and saturation of the current in the high field.

The profile of the hysteresis seen on an  $I$ - $V$  curve was calculated by measuring the difference in measured current in the up sweep versus down sweep,  $\Delta I$ , showing different regions of domination linked to the kinetics of the sorption process detailed in the emission model. In high and mid field regions,  $I_{up} > I_{down}$ , this was reversed at low fields. Plotting of the data points by measurement number, as opposed to the usual field values, on the  $x$ -axis proved insightful. In stability studies, where the emitter was exposed to fifty repeated loops, plotting by measurement number revealed a narrowing of the FWHM, which was attributed to the removal

of adsorbates from the system. This narrowing was more pronounced than the decline in maximum current, suggesting adsorbates have more effect on the emission profile, and hysteresis, than on the maximum output current.

Varying the exposure time to each electric field before measuring the current revealed a filtering of the additional emission seen in the down sweep, one source of hysteresis. Longer exposures also resulted in higher measured currents. By varying the sweep speed, it was thought that the adsorbates were activated (or bypassed in the case of less exposure to an electric field) and their effect on the emission became distinctive. Primarily, the effects of hysteresis were observed on the down sweep, with little change to the up sweep dynamics seen.

A six step model of the emission and resulting cause of hysteresis to explain this phenomenon was made following a number of revelations from the experiments performed on the emitters. The higher activation energies of desorption affect the later, and more predictable, onset of emission in the up sweep of the voltage loop compared to the field at which the emitter stops producing a measurable current on the down sweep. Fast re-adsorption at high fields can be attributed to a lower initial measured current on the down sweep, at high fields, with later contributions to emission increasing the current when newly formed states, shaped by re-adsorbed species, form and emit in the low field.

### ***Future Work***

The next stages, following on from these studies are the further investigation into: the effects of emitter morphology using the already fabricated samples containing different geometries; careful fabrication of emitters with controlled exposures to ambient and other gas species and different vacuum levels to further probe the hysteresis and specific species effects; and the eventual coupling of this research with applications including miniaturised X-ray sources in a demountable X-ray tube, working towards commercial viability.

To better understand the effect of the geometry, particularly whether the number of edges on a unit cell has an impact on performance, repeating the experiments of Chapter 4 with bulk materials could be performed. At present, it is possible that the fabricated shapes are blurred by the CNTs, which can fold over. It would also be beneficial to include a pentagonal and/or septagonal variation.

To complete the work began in Chapter 4, studying the geometries including different heights, widths and spacing, would be easily undertaken if the SAFEM was to be fixed to work properly.

## 6. Conclusions and Summary

Being able to use this machine to its full potential would give greater insight into the workings and effects of the surface geometry and build emission maps in 3D. In order for this to happen, greater tip stability is required, possible use of a melted PtIr wire could be one way towards a solution to this.

To further probe the hysteresis, repetition of the stability study, with measurements over 50 loops should be repeated at lower vacuum, around  $10^{-9}$  mbar, in order to see the effects of the vacuum. Further tests could also be performed over longer periods of time. This may reveal a point at which the hysteresis ceases to exist. These stability studies could be used in conjunction with the morphology studies used in the previous chapter to analyse the different geometries and their resistance to change and destructive events over long exposures.

In Chapter 5 the hysteresis was tested under different time scales by varying the dwell time. Increasing the dwell times would be simpler to instigate using the current equipment, and as measurements, up to a few minutes at each voltage, could be performed, however, surface kinetics of adsorbates are likely quicker than one second. Exposing the same emitters over such long periods could also prove challenging in continuity between results. Hysteresis could, in fact, be inadvertently promoted by changes to the structure of emitters simply by prolonged exposure to emission conditions.

Further studies that can be undertaken to probe the hysteresis further are temperature studies and analysis into the supply function of the electrons to the cathode. Varying the temperature at which the measurements are taken will give greater insight into the gas species involved in the emission process and their reactivity.

Empirical modelling of the six step model presented in Chapter 5 describing the hysteresis would further improve the theory and make it more quantitative.

### **6.2 Summary**

This thesis has presented the development of understanding of the field emission process from nanomaterials, with particular focus on CNTs, and the relation of influential factors including work function and local enhancement factor, as well as determining the cause of hysteresis.